Solid-Liquid Phase Equilibria of Chiral Molecules
- Theory and Experiment -

Dissertation
zur Erlangung des akademischen Grades

Doktoringenieur
(Dr.-Ing.)

von Dipl.-Ing. Hannes Konrad Buchholz

geb. am 22.11.1983 in Heidelberg

genehmigt durch die Fakultät für Verfahrens- und Systemtechnik
der Otto-von-Guericke-Universität Magdeburg

Promotionskommission:	Prof. Dr. Heike Lorenz (Vorsitz)
	Prof. Dr. Andreas Seidel-Morgenstern (Gutachter)
	Prof. Sarah L. Price (Gutachterin)
	Prof. Dr. Sergey Verevkin (Gutachter)
	Dr. Matthias Stein (Mitglied)

eingereicht am:	28.03.2018
Promotionskolloquium am:	14.06.2018

Schriftliche Erklärung

Ich erkläre hiermit, dass ich die vorliegende Arbeit ohne unzulässige Hilfe Dritter und ohne Benutzung anderer als der angegebenen Hilfsmittel angefertigt habe. Die aus fremden Quellen direkt oder indirekt übernommenen Gedanken sind als solche kenntlich gemacht.

Insbesondere habe ich nicht die Hilfe einer kommerziellen Promotionsberatung in Anspruch genommen. Dritte haben von mir weder unmittelbar noch mittelbar geldwerte Leistungen für Arbeiten erhalten, die im Zusammenhang mit dem Inhalt der vorgelegten Dissertation stehen.

Die Arbeit wurde bisher weder im Inland noch im Ausland in gleicher oder ähnlicher Form als Dissertation eingereicht und ist als Ganzes auch noch nicht veröffentlicht.

(Heidelberg, 25.11.2018)

Erklärung zur strafrechtlichen Verurteilung

Ich erkläre hiermit, nicht wegen einer Straftat verurteilt worden zu sein, die Wissenschaftsbezug hat.

(Heidelberg, 25.11.2018)

Acknowledgements

Kurzfassung

Die Kristallisation ist ein wichtiges Verfahren zur Trennung und Aufreinigung chiraler Substanzen. Für die Entwicklung eines Kristallisationsprozesses ist jedoch eine detaillierte Kenntnis über die zugrundeliegenden Fest/Flüssig-Phasengleichgewichte von essentieller Bedeutung. Insbesondere in frühen Stadien der Prozessentwicklung können computerbasierte Methoden helfen, die dafür benötigten substanzspezifischen Daten zu generieren, um langwierige und stoffintensive Experimente zu ergänzen und zukünftig möglicherweise sogar zu ersetzen.

In dieser Arbeit wurden rechnergestützte Methoden allein und in Kombination mit Experimenten verwendet, um die nötigen stoffspezifischen Energiebeiträge zur Ermittlung der freien Lösungsenergie zu berechnen. Dafür wurden zwei thermo-dynamisch konsistente Wege entwickelt, der *Schmelzzyklus* und der *Sublimationszyklus*, mittels derer die Löslichkeiten organischer Kristalle berechnet werden können. In beiden Zyklen werden die Unterschiede zwischen chiralen Kristallen aufgelöst. Sie sind ferner in der Lage, sowohl reine als auch gemischte Lösungsmittelsysteme zu beschreiben und sind nicht auf verdünnte Lösungen beschränkt. In dieser Arbeit wurde untersucht, ob Löslichkeitsvorhersagen unter Verwendung moderner quantenchemischer Methoden für die Entwicklung von Kristallisationsprozessen anwendbar sind. Weiterhin wurde analysiert, welchen Einfluss Phasenübergangsenergien und deren thermische Korrekturbeiträge sowie Wechselwirkungen in der Lösung auf die Berechnung absoluter und relativer Löslichkeiten chiraler Substanzen haben.

Exakte Gitterenergien sind sowohl zur Berechnung von absoluten Sublimationsenergien als auch von Energieunterschieden zwischen verschiedenen chiralen Kristallen erforderlich. Wenn diese mittels periodischer Dichtefunktionaltheorie (DFT) berechnet werden, hängt die Genauigkeit maßgeblich von der Wahl des Dichtefunktionals, der Größe des Basissatzes und der Dispersionskorrektur ab. Es konnte weiterhin gezeigt werden, dass die präzise Berechnung thermischer Korrekturen zu den elektrostatischen Energien gleichermaßen wichtig und zudem stark methodenabhängig ist. Obwohl sie in der Literatur oft vernachlässigt werden, tragen thermische Korrekturen zu Energieunterschieden zwischen dem Enantiomer und der racemischen Verbindung bei. Diese werden durch Wärmekapazitätsunterschiede zwischen den beiden chiralen Kristallen hervorgerufen, welche auf Unterschiede in Molekül- und Gitterschwingungen zurückzuführen sind. Zum Teil sind diese mittels Raman-Spektroskopie nachweisbar. Die Rechengenauigkeit hängt dabei stark von der Flexibilität des Moleküls und der Anordnung im Kristall (Packung) ab. Mit dem Sublimationszyklus konnten freie Lösungsenergien mit nahezu chemischer Genauigkeit bestimmt werden (1 kcal·mol^{-1}). Er bietet somit eine vielversprechende Alternative zum häufiger verwendeten Schmelzzyklus, für den substanzspezifische experimentelle Daten benötigt werden. Dennoch sind beide Zyklen noch nicht zuverlässig genug quantifizierbar, um in der frühen Prozessentwicklung Anwendung finden zu können. Dahingegen können präzise berechnete Energieunterschiede schon jetzt die Entwicklung von Trennverfahren von Enantiomeren unterstützen, indem sie zur Abschätzung der eutektischen Zusammensetzung der Lösung verwendet werden.

Abstract

Crystallization is an important separation process which is in particular attractive for chiral substances. Detailed knowledge on the underlying solid-liquid phase equilibria (SLE) is essential for the design of any crystallization process. Particularly in early stages of process development computational methods can supplement, or possibly replace tedious and material intensive experiments. For example, they can be used to generate substance-specific information which are required for solubility prediction.

Motivated by the above, this thesis uses a joint computational and experimental approach in order to evaluate the numerous energy contributions required for determining solid-liquid phase equilibria. A consistent computational framework is derived for calculating mole fraction solubilities of organic molecular crystals via the so-called *melt cycle* and the *sublimation cycle*. Both cycles can quantify the influence of the crystal structure on the solubility. They are further capable of handling pure as well as mixed organic solvent systems and are not restricted to infinite dilution. It was investigated whether solubility predictions using state-of-the-art quantum chemistry methods are applicable for crystallization process design. It was further analysed, to what extent calculated absolute and relative solubilities of chiral crystals are affected by phase transition energies and their thermal contributions as well as molecular interactions in solution.

For calculating absolute sublimation energies and differences between chiral crystals precise lattice energies are required. When determined by periodic density functional theory (DFT), calculations mainly depend on the choice of the density functional, the size of the basis set and the dispersion correction. It was further shown, that an accurate calculation of thermal corrections to the electrostatic energies are equally important and that their computation is strongly method-dependent. Even though they are often neglected, thermal corrections contribute to energy differences between the enantiomer and the racemic compound. They are related to heat capacity differences between the two chiral crystals which are evoked by differences in molecular and lattice vibrations. In parts, those are detectable experimentally by Raman spectroscopy. A precise calculation of heat capacity differences is dependent on the flexibility of the molecule and on the crystal packing. Finally, solution Gibbs energies can be calculated close to chemical accuracy ($1 \cdot$ kcal mol^{-1}) via the suggested sublimation cycle. It therefore competes well against the more commonly used melt cycle which requires substance specific experiments. However, both thermodynamic cycles are not reliable enough to be used for solubility prediction for an early stage crystallization process design. Nevertheless, precise sublimation Gibbs energy differences can already be used to support enantioseparation process design by estimating the eutectic composition in solution.

Content

List of symbols

Symbols	Description	Unit
a	activity	mol mol^{-1}
C_P	isobaric heat capacity	J mol^{-1} K^{-1}
C_V	isochoric heat capacity	J mol^{-1} K^{-1}
E	energy	kJ mol^{-1}
G	Gibbs free energy (free energy)	kJ mol^{-1}
H	enthalpy	kJ mol^{-1}
m	mass	kg
M	molar mass	g mol^{-1}
n	amount of substance	mol
p	pressure	Pa
Q, q	partition function	
R	ideal gas constant	J mol^{-1} K^{-1}
S	entropy	J mol^{-1} K^{-1}
T	temperature	K or °C
TS	entropy x temperature	kJ mol^{-1}
V	volume	m^3
w_i	weight fraction	g g^{-1}
x_i	mole fraction	mol mol^{-1}
μ	chemical potential / partial molar free energy	kJ mol^{-1}
γ	activity coefficient	
π	thermodynamic phase	
υ	stoichiometric constant	
$\hat{H}$	Hamiltonian operator	
Ψ	wave function	

Subscript	Description
conc	concentration-dependent quantity
corr	thermal correction
ep	enantiopure compound
eu	eutectic composition
i	constituent of a specific phase
inf	infinite dilution (often specified as ∞)
inter	intermolecular
intra	intramolecular
latt	lattice
melt	melting (fusion)
rac	racemic compound
ref	reference state
sat	saturation concentration
sol	solution
subl	sublimation
tp	triple point
vdW	van der Waals
ZPE	zero-point energy

Superscripts	Description
0	reference state: $T = 298$ K; $p = 1$ bar abbreviation for the bar/mol reference state
E	excess thermodynamic quantity
g	gas phase
ig	ideal gas phase
isg	ideal static gas phase
iss	ideal static solid
l	liquid phase
s	solid phase
scl	supercooled liquid / supercooled melt

Abbreviations	Description
CSD	Cambridge Structural Database
DHPC	direct heat pulse calorimetry
DFT	density functional theory
DZ	double-zeta basis set
FDA	Food and Drug Administration
GGA	generalized gradient approximation
GTO	Gaussian type orbitals
HF	Hartree-Fock
IR	infra-red
IUPAC	International Union of Pure and Applied Chemistry
LDA	local density approximation
LCAO	linear combination of atomic orbitals
MD	molecular dynamics
PCM	polarized continuum model
PD	equation of Prigogine and Defay, eq. (34)
PPMS	Physical Property Measurement System (Quantum Design Inc.)
QSPR	quantitative structure-property relationships
QZ	quadruple-zeta basis set
rac	50:50 mixture of (S) and (R)-enantiomers
RMSD	root mean square deviation
RRHO	Rigid Rotor Harmonic Oscillator
SLE	solid-liquid phase equilibrium
SV	split valence basis set
SVL	equation of Schröder and van Laar, eq. (35)
SVP	split valence plus polarization basis set
TPD	ternary solubility phase diagram
TZ	triple-zeta basis set
TZVP	split valence triple-zeta plus polarization basis set
XRD	X-ray diffraction
XRPD	X-ray powder diffraction
ψ_{crys}	computational method according to section 2.7.2
ψ_{mol}	computational method according to section 2.7.2

1   Introduction

1.1   Crystallization for purification and enantioseparation

Crystallization processes are one option of many separation and purification process strategies. Nowadays, the organic chemical industry is based to roughly 95 % on crude oil and natural gas products[1] and rectification processes are commonly used for their separation and purification. However, most fine chemicals which are often applied as starting chemicals for pharmaceuticals, agrochemicals and life science products[2] are solid at environmental conditions.[3] Hence, for the production of these low-volume, high-value products separation processes such as chromatography, membrane processes, liquid-liquid extraction and crystallization are preferable. Especially many active ingredients (such as pharmaceuticals) have high molar masses and form a crystalline solid under environmental conditions which is why a crystallization process is often the final step in the downstream process section. Furthermore, pharmaceuticals are often sensitive to elevated temperatures which makes the low temperature crystallization processes a preferable process option.

Besides their application to the separation and purification of speciality chemicals, crystallization processes are regarded as a cost-efficient way to separate enantiomers because of rather modest requirements in terms of technical equipment. In the pharmaceutical industry, the resolution of enantiomers by the formation of diastereomeric salts is still the most common way to separate a 50:50 (racemic) mixture of enantiomers and is thus called "classical resolution".[4] Besides that kinetically driven preferential crystallization processes are capable of "breaking the symmetry" and hence producing pure enantiomers from a racemic mixture. Furthermore, thermodynamically based enantioseparation can be used to generate pure enantiomers from a mixture which is enriched by one of the enantiomers.[5] All crystallization-based separation methods rely strongly on knowledge about the specific underlying solid-liquid phase equilibria and consequently on the solution thermodynamics of the target molecules.

1.2   Solution thermodynamics

A general description of solution thermodynamics includes details on the crystalline solid phases and on the composition of the liquid phase(s) and thus on the solubilities of the specific crystalline solid. The characteristics of these phases and their compositions are a function of temperature and the solvent system which results in a complex system with many unknown molecule-dependent parameters. A merely experimental determination of all unknown quantities is a tedious and substance, as well as equipment intensive procedure. As a consequence, it is expensive and should be accompanied or possibly replaced by computational methods.

A rather rigorous way to address this issue computationally is the field of solubility

prediction, which is the focus of this work. It is desirable to use a limited amount of experimental input for calculating solubilities or to solely apply computational methods which do not require substance specific experimental inputs. Solubility prediction is of interest in numerous fields for the chemical industry, such as pharmacy, drug and agrochemical design.[6] Applications within these fields are mainly focused on aqueous solubility and generally assume the solution to be infinitely diluted. For example, Quantitative Structure-Property Relationships (QSPR)[7] and data mining are capable to predict the solubility with limited input parameters but often lack physical insight.[8] However, a better understanding of physics for solid-liquid phase equilibria in order to develop molecular modelling methodologies has been defined as the most important research in the field of crystallization process design.[9] It has been shown that purely theoretical methods - where the only information needed is the experimental crystal structure - are capable of achieving slightly worse but promising levels of accuracy in comparison to empiric methods.[10] When integrated with computational methods to predict the crystal structure[11] knowing only the molecular structure a solely computational way becomes achievable.

In contrast to solubility prediction in the frame of drug design in the pharmaceutical industry, its application for crystallization processes should not be limited to aqueous media. Furthermore, for a cost-efficient crystallization process with high productivities, solid-liquid phase equilibria with high saturation concentrations are favourable. Hence, besides water as a solvent there is a broad spectrum of solvent systems which includes all classes of pure organic solvents as well as mixed organic-organic and mixed aqueous-organic solvent systems, where the choice in solvent may be of interest for enhancing the solubility or to find an anti-solvent that lowers the solubility disproportionally strong. These issues will be addressed in this work by studying various organic non-electrolyte systems while focussing on the field of solubility prediction for enantioseparation by crystallization.

1.3   Structure of the thesis

Chapter 2 ("Theory and Computational Methods") delivers the general thermodynamics of solid-liquid phase equilibria (SLE) and its specifics for modelling SLE of chiral molecules. Two thermodynamic approaches to calculate solubilities of crystalline organic substances are presented, the *melt cycle* and the *sublimation cycle*. The theoretical background for modelling molecular interactions in the crystalline solid and in solution as well as specifics on their computational implementation are presented.

Chapter 3 ("Experimental Methods") introduces all measurement methods that are used for a broad experimental investigation of the phase transition thermochemistry of three chiral molecules.

Chapter 4 ("Results and Discussion") contains all experimental and computational results of this work. The first part of chapter 4 (section 4.1 and 4.2) evaluates the accuracy of the melt and the sublimation cycle for two well studied model substances. Subsequently, the accuracy of state-of-the art electronic structure methods to calculate the dominant energy

contribution within the sublimation cycle, the lattice energy, is studied. In a second part of chapter 4 (section 4.3) the melting and sublimation phase transition is studied for three chiral representatives using experiment and theory; namely lactide, naproxen and 3chloromandelic acid. The absolute sublimation energies and energy differences between the enantiopure and corresponding racemic crystals are calculated and compared to experiment. The relative energies are subsequently used in section 4.5 to approximate the solution behaviour of mixtures of chiral molecules which have been determined as well experimentally. In a third part of Chapter 4 (section 4.4 and 4.6) the two thermodynamic cycles are used to calculate solubilities and their temperature dependency for selected chiral molecules which have been measured in a variety of pure and mixed solvent systems.

Chapter 5 ("Conclusion and Outlook") summarizes the main findings and suggests directions for future research.

The Appendix contains selected computational details and primary experimental data.

2 Theory and Computational Methods

This chapter presents the thermodynamic background of solid-liquid phase equilibria (SLE) and its specifics when modelling chiral system (section 2.1 and 2.2). The field of application is the design of crystallization processes for purification and enantio-separation. Two thermodynamic approaches to calculate solubilities of organic crystals are presented, the *melt cycle* and the *sublimation cycle* (section 2.3 to 2.5). The theoretical background for modelling molecular interactions in the crystalline solid using *ab-inito* quantum chemistry methods are presented (see section 2.6). Method specific computational details which have been used throughout this work are given in section 2.7.

2.1 Chirality and enantioseparation

A large number of molecules are chiral which means they exist in two constitutionally identical isomeric forms that are non-superimposable mirror images of one another. The two opposite counterparts are called enantiomers. They are commonly labelled according to their ability to rotate polarized light by (+) vs. (-) or by (*D*) vs. (*L*) for *dextro-* and *levo-* or by the molecular configuration around the chiral centre with (*S*) vs. (*R*) which stands for *sinister* and *rectus*.[12] On the one hand, all proteins and enzymes as well as their building blocks, amino acids, are chiral (except glycine). On the other hand, many fine chemicals such as pharmaceuticals, agrochemicals, flavours and fragrance are chiral as well. For example, 56% of the currently used drugs are chiral molecules.[13] Stereoisomers can have different effects on receptors in the human body which results in different pharmacological and toxicological properties of the two enantiomers of a drug molecule. One example is naproxen (see Figure 2.1) which is an example case of a chiral molecules within this work. Only the (*S*)-enantiomer of naproxen is used as a nonsteroidal anti-inflammatory drug while (*R*)-naproxen does not exhibit the wanted effects[14] but is suspected to act as liver toxin[15].
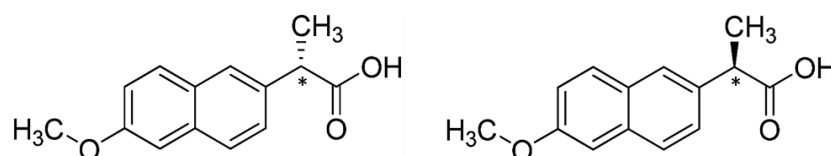
Figure 2.1: The two enantiomers of naproxen. (left) (*S*)-naproxen which is used a nonsteroidal anti-inflammatory drug and (right) the pharmacologically unwanted (*R*)-naproxen. The asymmetric carbon molecule - the chiral centre - on the propionic acid side chain is marked.

Until recently, roughly 90 % of all chiral pharmaceuticals are still marketed as "racemates" which consist of an equimolar mixture of the two enantiomers.[13] Racemates are denoted with the prefix (±)- or rac- (or racem-) or by (*RS*) which is used within this work.[16] Nowadays the U.S. Food and Drug Administration (FDA) requires that drugs have to be distributed as pure enantiomers or the mixture has to be proven to be

harmless.[17] Hence, most newly introduced drugs today are single enantiomers rather than racemic mixtures.[18]

Enantiomers have the same molecular structures and thus identical physical and chemical properties in an achiral environment which aggravates their separation. Pure enantiomers can be provided by preferentially synthesizing one of the enantiomers in an asymmetric synthesis[19]. On the other hand, a racemic or slightly enriched synthesis mixture can be as well separated in a downstream process. Focussing on post synthesis processes, frequently applied methods to separate enantiomers are chromatography, crystallization and membrane processes.[5] Further process options are available but less common because of a smaller field of application like preferential sublimation[20] which requires the crystal to sublimate at process relevant conditions.

Enantioseparation by crystallization is a downstream process option which is highly selective and comparably cheap on industrial scale as it requires only basic technical equipment.[21] It exploits the high selectivity when the crystalline solid that contains only one enantiomer is formed from a solution that consists of a mixture of both enantiomers. It is of special relevance if a product is marked as a solid and a crystallization or precipitation step is required anyhow as a final process step.[5] Furthermore, pharmaceuticals are often sensitive to elevated temperatures and hence decompose above their melting temperature which mostly ranges in between 50 °C to 250 °C[22]. For these temperature sensitive molecules low temperature crystallization processes are the preferable process option.

2.1.1   Classification of chiral substances

For the design of a crystallization process in order to separate enantiomers it is of fundamental importance to elaborate what types of crystalline phases the pure enantiomers and their mixtures form. As shown in Figure 2.2, chiral substances are typically divided into three distinct classes: conglomerates, racemic compound-forming systems and solid solutions (pseudoracemates). Roughly 90 % of all chiral substances form a racemic compound which contains both enantiomers in an equimolar ratio within the crystal structure.[23] However, there are molecular compounds with other stoichiometric ratios.[24, 25] In contrast to that around 10 % of all chiral molecules form a mechanical mixture of the enantiopure crystals, a so-called conglomerate (Figure 2.2 a). Both cases form a minimum melting temperature in the binary system and a maximum solubility at a given T in the TPD, the so-called eutectic composition x_{eu}. In rare cases molecules within the enantiopure crystal can be substituted by the counter-enantiomer in an ordered or disordered manner affecting the crystal structure. As indicated in Figure 2.2 (c) the melting temperature and hence the solubility of such solid-solutions can be either lowered or increased by the counter enantiomer; in the ideal case it is a constant (straight line). The thermochemistry of chiral substances can be complicated by featuring characteristics of more than one of the three distinct classes as shown for example in the case of malic acid.[26] There are as well systems that form a metastable conglomerate while thermodynamically belonging to the class of compound-forming systems.[27]
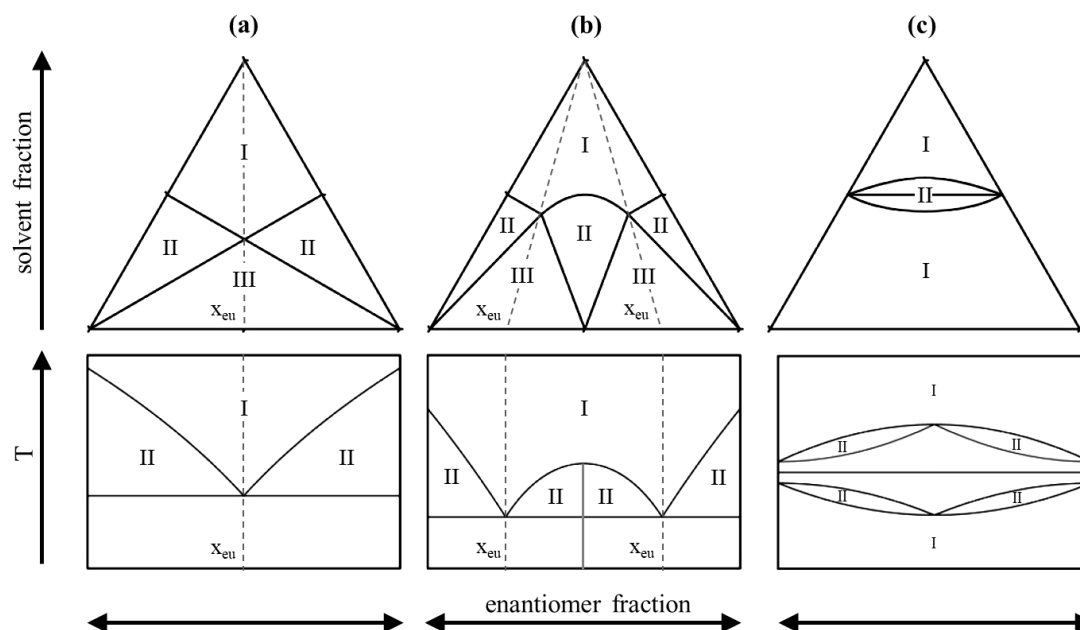
Figure 2.2: Illustrations of solid-liquid phase diagrams of the three most common classes of chiral systems: (a) conglomerates, (b) racemic compounds and (c) solid solutions or pseudo racemates; (bottom) binary melt phase diagram (top) ternary solution phase diagram –TPD. The number of coexisting phases is labelled in roman numbers. The eutectic composition is denoted by x_{eu}.

Structural clarification of a chiral system can be done by investigating the binary solvent free system using a combination of caloric measurements (DSC) and X-ray diffraction (XRPD or single crystal XRD). For unravelling the TPD solubility, measurements are combined with diffraction methods of equilibrated crystalline solid. The phase behaviour and hence the type of chiral system are often the same in the melt and in solution but there are as well exceptions. The hydrochloric salt of histidine for example forms a conglomerate in the binary system and a racemic compound in presence of water.[23]

Even though polymorphism (the ability of a given compound to crystallize in more than one crystal form) is less frequently observed for chiral molecules[28], structural clarification and, hence, the generation of the binary melt and ternary solution phase diagrams can be further complicated by polymorphism or the formation of solvates. Polymorphs can be either formed exclusively when crystallized from the melt or they can be solvent mediated and hence appear only in the TPD. Statistically, one out of three organic molecules in the Cambridge Structural Database (CSD) are polymorphic.[28] In any case the crystalline solid phase plays a crucial role for SLE and thus has to be characterized with case. The following section presents specifics about the characterization and classification of organic crystals.

2.1.2   Crystal structure

A perfect crystal can be described as a system that is build up by a periodic arrangement of a specific well-defined entity, the unit cell. The unit cell is defined as the smallest material portion which can be parallelly displaced in three dimensions to form the

crystal.[16] The unit cell is characterized by the length of the cell vectors a, b and c as well as the angles between the cell vectors α, β and γ (see Figure 2.3).[29]
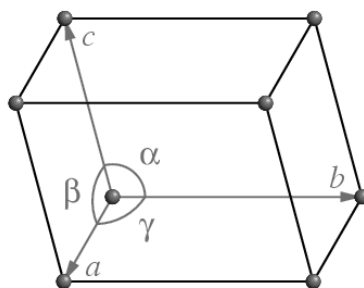
Figure 2.3: Unit cell (or primitive cell) and unit cell parameters, where a, b and c are the cell vectors and *α, β and γ* the angles between the cell vectors.

Crystal structures are grouped into one of the 14 Bravais lattices containing seven main crystal systems which differ in the way the cell vectors and angles are organized. The simplest crystal system is the cubic system where $a = b = c$ and $\alpha = \beta = \gamma = 90°$. In the most complex triclinic crystal system all lattice vectors differ in length and there is no vector at a right angle to another vector. Additionally, to the Bravais lattice groups the internal symmetry of the molecules within the unit cell is captured by its space group. There are exactly 230 space groups that can describe the three-dimensional symmetry of crystals. Roughly 85 % of all organic crystals organize in a monoclinic, orthorhombic or triclinic crystal system which form in 70 % of all cases a $P2_1/c$ (30 %), P1, $P2_1$, C2/c, $P2_12_12_1$ and Pbca space group.[30] Inorganic crystals, on the other hand, mostly (~66 %) organize in one of the three other crystal systems, which are tetragonal, trigonal / hexagonal and cubic.[30] Another characteristic quantity of a crystal structure is the number of molecules, Z, or the number of independent molecules, Z', within the unit cell. In 88 % of the cases Z' is smaller or equal to one[31] while the absolute number, Z, can be significantly larger.

Information about crystals structures, like its unit cell parameters, atomic coordinates and internal symmetry, is most commonly obtained from single-crystal X-ray crystallography.[32] Besides an experimental determination of the most thermodynamically stable crystal structure and experimental screening of possible polymorphs and solvates computational methods have been developed in the last decades. So-called crystal structure prediction (CSP) methods deliver computational counterparts to predict the most stable crystalline structure and possible polymorphic crystal forms from the structural formula only.[11] Significant progress has been made in the last years to predict the molecular structure of small rather rigid molecules[33] but the methods are nowadays as well capable to handle larger, more flexible molecules as well as salts and hydrates[34].

Experimental as well as computational investigation are related to one specific temperature. Computations are performed for the static crystal at zero Kelvin. As well experiments are most accurately performed below room temperature.[35] However, temperature and pressure can have several effects on the crystal structure. On the one hand a specific molecule can pack in multiple ways into a crystalline, which is called

polymorphism, where one specific crystal structure is stable only in a certain temperature and pressure range.[32] On the other hand the unit cell parameters (and hence the volume) of one specific crystal structure are functions of temperature and pressure. The temperature dependency of the density (reciprocal of specific volume) has been shown to be approximately a linear function with a slope of in between 0.15–0.35 mg cm^{-3} K^{-1} for most organic moelcules.[35] This aggravates a comparison of experimental data and computations which are commonly performed using quantum chemistry methods and thus for the static crystal at 0 K. Furthermore, the thermal expansion effects the temperature-dependent thermochemistry of crystals by effecting the heat capacity of the crystal.[36]

2.1.3   Enantioseparation by crystallization

Conglomerates can be separated from a racemic mixture by preferential crystallization. This kinetically driven resolution of a racemic mixture has been advanced over the last decade[21] and was applied as well for continuous process strategies[37, 38]. Unfortunately, these process strategies are not directly transferable to racemic compound-forming systems but concepts have been developed to separate their enantiomeric enriched solutions.[39,40] There are other process strategies which exploit the solution thermodynamics of mixtures of enantiomers to separate enantiomerically enriched solutions. For example, a shift of the eutectic composition with temperature and/or the solvent can be exploited to separate enantiomers of a racemic compound-forming system.[41] Besides that industry relies on the availability of a chiral agent that can form diastereomeric salts and thus on a separation of the racemic mixtures by "classical resolution".[4]

This work focuses on the most common class of chiral molecules, the racemic compound-forming systems. The thermodynamic feasibility and yield of a crystallization process depends on the solubilities of pure enantiomers, the racemic compound and their mixtures and thus on the ternary phase diagram. Of special importance is the solubility and enantiomeric composition of the eutectic mixture, the eutectic composition x_{eu}, which confines the area where pure enantiomer can be crystallized. The illustration in Figure 2.2 (b) shows the TPD of a racemic compound-forming system containing two symmetric eutectic compositions, x_{eu}, which are the points of maximum solubility at a certain T. In contrast to conglomerate type systems (Figure 2.2 a), the enantiomeric ratio at the eutectic lies in between the racemic mixture and that of the pure enantiomer. In the binary solvent free system, the eutectic composition is often regarded as an invariant point. However, it can depend on pressure as shown for binary mixtures of achiral organic substances.[42] Within the TPD, it depends on the solubility behaviour of the enantiomer and the racemic compound and their mixtures. As a consequence, it is not an invariant point but instead is a function of temperature and the solvent.[43, 44]

For an infinitely diluted system, the solubility is independent from the number of dissolved molecules and hence as well from the enantiomeric ratio in solution. Industrial crystallization processes, however, are preferably operated at high solution

concentrations to enable high productivities. In concentrated solutions solute-solute interactions can evoke non-ideal solution behaviour within the TPD. Two particularly non-ideal TPD are shown in Figure 2.4 including guaifenesin[45] and mandelic acid[46]. Both systems exhibit a strong increase in solubility when both enantiomers are present in solution. Hence, for an accurate description of solid-liquid equilibria such effects have to be incorporated within the model framework.
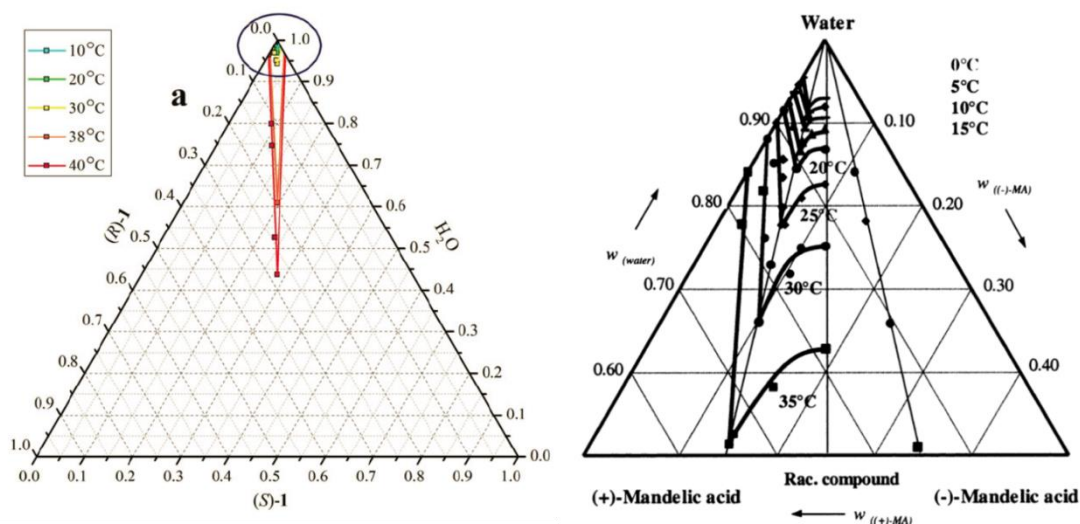
Figure 2.4: Two examples of the ternary solution phase diagram of mixtures of enantiomers that both exhibit strong deviations to an ideal solution. (left) TPD of the conglomerate forming system guaifenesin[45] in water. (right) TPD of the racemic compound-forming system mandelic acid[46] in water.

2.2   Thermodynamics of solid-liquid phase equilibria (SLE)

There are three fundamental thermodynamic states of matter (phases) that are relevant for modelling the solid-liquid phase equilibria (SLE): the gas phase (g), liquid phase (l) and solid phase (s). For a given composition, the number and types of phases depend on the temperature and pressure of the system and are usually plotted in a phase diagram. Figure 2.5 (left) shows the temperature vs. pressure phase *p-T*-diagram of a single component system where the straight lines are the phase boundaries between two phases which are functions of temperature and pressure.

For solid-liquid phase equilibria, the melting line represents the phase boundary. If the melting temperature is assumed to be independent of pressure the melting line is a vertical line in the *p-T*-diagram. The binary system which corresponds to the SLE of a crystalline solid and a solvent is depicted in Figure 2.5 (right) at one specified pressure. The melting line is split up into the solidus line and the liquidus line. In between these two-phase boundaries one solid phase and one liquid phase are in equilibrium. The liquidus line represents the temperature dependency of the higher melting component A within the lower melting component B (in this case referred to as the solvent) and is named "solubility line" throughout this work.

The solubility of a solute in a designated solvent is defined as the analytical composition

of a saturated solution and is expressed in terms of the proportion of that solute in the solution. Hereby, a saturated solution is regarded as a solution which is in thermodynamic equilibrium with un-dissolved solute at specified values of the temperature and pressure.[47]
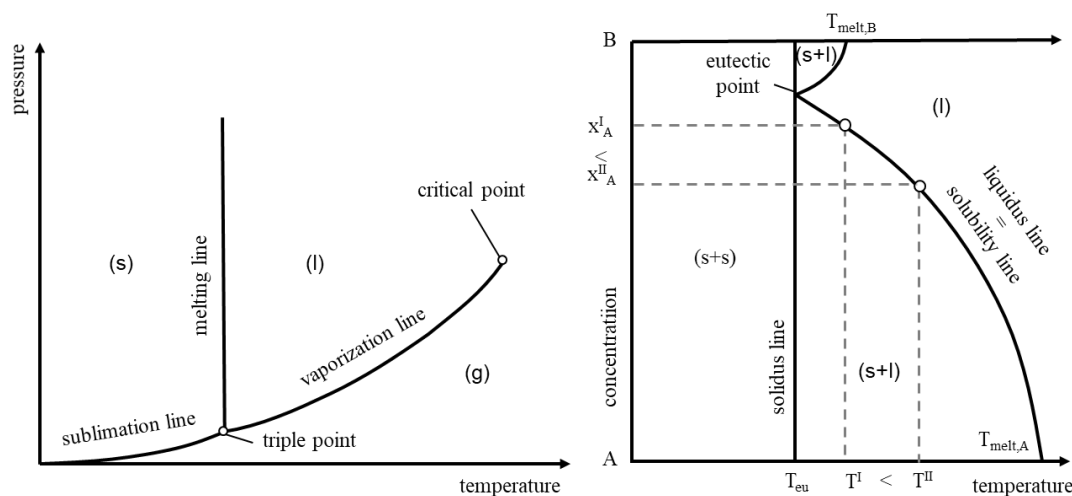
Figure 2.5: (left) Schematic single component *p-T*-diagram which shows the dependency of the melting, sublimation and vaporization phase transition on temperature and pressure. (right) The binary melt phase diagram of mixtures of two arbitrary components A and B. T^I and T^{II} are two choices of temperatures on the liquidus line which refer to two different saturation concentrations (solubilities) of A in B, x^I_A and x^{II}_A.

Hence, the solubility of an organic molecule depends on the chemical structure of the solute and the solvent as well as on the temperature. In rare cases it is as well a function of pressure which is neglected throughout this work. It is of relevance for exceptionally high pressures and special cases like highly diluted solutions of carbonates, alkaline earths and heavy metals in water[48] but it can have an effect on the melting temperature of a solvent free system[26]. The solubility is commonly quantified by the mole fraction, the mass fraction, molality, mole ratio, mass of the solute per volume of the solvent etc. In this work the solubility of the solute, *i*, is expressed as either the mole fraction, x_i, or mass fraction, w_i, of the solute in a solvent (eq. (1)). Hereby, *n* and *m* are the amount of substance and the mass of the constituents *i…N*, respectively. A solution is called an infinite dilution or dilute solution if the sum of the mole fractions of solutes is small compared with unity.[16]

$$ x_i = \frac{n_i}{n_i + n_{i+1} + ... + n_N} \quad or \quad w_i = \frac{m_i}{m_i + m_{i+1} + ... + m_N} \tag{1} $$

2.2.1   Fundamental thermodynamics for modelling SLE

Following nomenclature conventions from *IUPAC* (International Union of Pure and Applied Chemistry), throughout this work capital letters represent molar quantities (e.g the Enthalpy *H*). In a closed system with more than one phase, each phase can be treated as an open system that can exchange energy as well as matter via the phase boundaries.

The fundamental equation of the Gibbs energy of an open system relates the Gibbs free energy, G, to the enthalpy, H, and entropy S (n_i = amount of substance of component i, n = the total amount of substance, T = temperature and p = pressure)[49]

$$nG = nH - nTS = f(T, p, n_i ... n_N)$$ (2)

A system consisting of $i...N$ components and $\pi...\Pi$ phases is in thermodynamic equilibrium if the relevant variables of state, T, p and n_i, are constant in each phase. Hence, a system that is in equilibrium has to re-establish equilibrium in the case one of those variables of state is changed. The relation between the variables of state during a change of a persisting thermodynamic equilibrium is described by the Gibbs-Duhem relation, eq. (3), which has to be valid for each phase π at equilibrium.[50]

$$S^\pi dT^\pi - V^\pi dP^\pi + \sum_{i=1}^N x_i^\pi d\mu_i^\pi = 0$$ (3)

Eq. (3) uses the definition of the chemical potential $\mu_i^\pi = f(T, p, x_i ... x_N)$ of component i in within phase π. The chemical potential is defined as the partial molar Gibbs free energy and is related to the activity a^π_i, the *effective concentration*, of a compound in a certain phase (see eq. (4)).

$$Z_i = \left(\frac{\partial G}{\partial n_i} \right)_{P,T,n_{j\neq i}}^\pi = \mu_i^\pi = \mu_i^0 + RT \ln a_i^\pi \quad \text{with} \quad a_i^\pi = x_i^\pi \cdot \gamma_i^\pi (T, p, x_i)$$ (4)

Hereby, μ_i^0 is the chemical potential of that species under some defined set of standard conditions and is commonly related to the pure component in the same state of matter. The activity coefficient, γ_i, is a dimensionless quantity which describes the deviation of the real system from an ideal mixture. It lumps all non-ideal molecular interactions of component i in the mixture into one quantity that is a function of temperature, pressure and composition. The difference between the chemical potential of a real system (eq. (4)) and that of an ideal system under the same conditions is called the excess chemical potential. It is equal to the partial molar excess Gibbs free energy as shown in eq. (5).

$$\mu_i^E = G_i^E = RT \ln \gamma_i^\pi$$ (5)

The excess chemical potential is closely related to the pseudo-chemical potential, μ_i^*, which has been introduced by Ben-Naim[51] and which is frequently used in computational chemistry. The pseudo-chemical potential is defined as the change in the Gibbs energy for the process of placing component i at some fixed position in the phase with a fixed temperature, pressure and composition.[51] For modelling of mixtures it has the advantage that it can be calculated at any molar concentration within the solution. As a consequence, it is not restricted to infinite dilution. Like the excess chemical potential, it is the chemical potential in solution minus the ideal entropic contribution (see eq. (6)).[52] It is thus only different from the excess chemical potential if the internal partition function of the molecule is affected by the phase transfer.[53]

$$\mu_i^{\pi,*} = \mu_i^\pi - RT \ln x_i$$ (6)

The total differential of the chemical potentials (eq. (7)) is needed to derive the dependency of the phase equilibrium to the variables of state and thus the thermodynamic relation for modelling solid-liquid phase equilibria with $\pi = s, l$. The three parts represent the thermal, mechanical and chemical potential, respectively.

$$d\mu_i^\pi = -S_i^\pi dT^\pi + V_i^\pi dP^\pi + \sum_j^{N-1} \left(\frac{\partial \mu_i^\pi}{\partial x_j^\pi} \right)_{T.P} d\mu_j^\pi \qquad (7)$$

The total differential of the chemical potential combined with the Gibbs-Duhem relation (eq. (3)) can be used for deriving the dependency of temperature, T, and composition, x_i, of a binary system (A and B) with two coexisting phases (s and l) at thermodynamic equilibrium.[50, 54] For SLE this results in eq. (8) where $[x_A^s(H_A^l - H_A^s) + (1-x_A^s)(H_B^l - H_B^s)]$ is the solution enthalpy ΔH_{sol} of A.

$$\frac{dT}{dx_A^l} = \frac{T(x_A^s - x_A^l)}{(1 - x_A^l) \left[x_A^s (H_A^l - H_A^s) + (1 - x_A^s)(H_B^l - H_B^s) \right]} \left(\frac{\partial \mu_i^l}{\partial x_i^l} \right)_{T,p} \qquad (8)$$

There are several variants of SLE which are relevant for modelling solubilities of chiral molecules and their mixtures. In the following, two selected variants are derived which are most relevant for modelling SLE of chiral compound-forming systems.

2.2.2   SLE of a binary or pseudo-binary system

The simplest case of a binary SLE is set up by two components which are both present in the liquid phase (A^l and S^l) but where only one component (A^s) is present in the equilibrated solid phase (see Figure 2.6). This type of SLE perfectly describes the solubility of a single component crystalline solid which is in contact with a solvent. In a more complex form S^l can be a representative for a solvent mixture $S_i^l...S_N^l$ of N constituents within a pseudo-binary system.
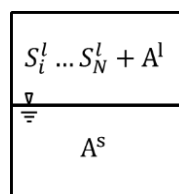
Figure 2.6: Illustration of a binary, two phase solid-liquid equilibria (SLE) - The dissolution of a component A in a second compound S which stays in the liquid phase (e.g. a solvent).

The solubility of a single component solute can be either derived via the fundamental equation of two binary coexisting phases (eq. (8)) or directly from the necessary conditions of a thermodynamic equilibrium which needs the thermal, mechanical and chemical potential to be identical in both phases.[51] Neglecting the influences of pressure and assuming that the temperature in all phases is identical the necessary condition for thermodynamic equilibrium of one solid (s) and one liquid (l) phase is given by eq. (9).

$$\mu_i^s(T,p,x_i^s) = \mu_i^l(T,p,x_i^l) \tag{9}$$

In combination with the definition of the chemical potential from eq. (4) one gets a relation of the molar concentration of compound i in the liquid phase, the solubility x_i, to the difference in the chemical potential of compound i in the pure solid phase and the liquid phase that is saturated with compound i, the pseudo-chemical potential $\mu_i^{l,*}$ which has been defined previously in eq. (6).

$$-RT \ln x_i^l = \mu_i^{l,*} - \mu_i^s = \Delta G_{sol,i} \tag{10}$$

The difference in chemical potential of compound i in the pure solid phase and the saturated liquid phase is defined as the partial molar Gibbs free energy of solution, $\Delta G_{sol,i}$. It includes all interactions of the solute with the solution and thus as well non-ideal solution quantities. Equation (10) will be used in this work for the calculation of the solubility, x_i, of single component solids which are commonly referred to as simple eutectic systems.

2.2.3   SLE of a ternary or pseudo-ternary system

There are two possible multicomponent systems that are of relevance for modelling solid-liquid phase equilibria systems that contain two components in one liquid phase but only two components in the solid phase(s). The two variants are illustrated in Figure 2.7. The two SLE models are capable to describe the ternary solution phase diagram of chiral compound-forming systems.
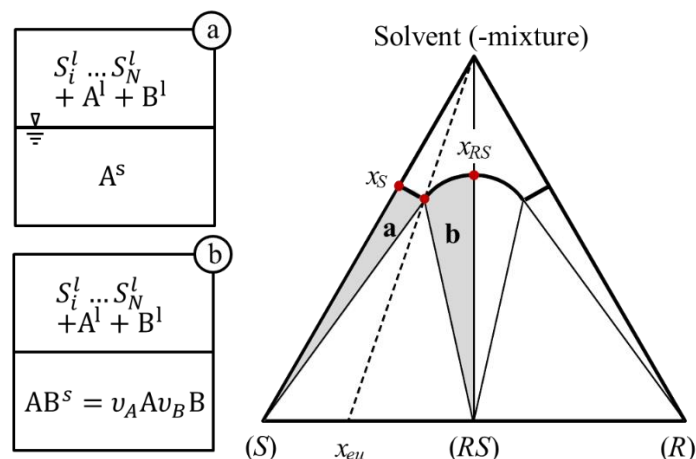
Figure 2.7: (left) Illustration of a ternary solid-liquid equilibria (SLE) - The solution contains one or more solvents S_i^l which stay only in the liquid phase and two solutes (A^l and B^l) that (a) crystallize into two solid phases (A^s or B^s) or (b) into a molecular compound (AB^s). (right) Illustration of a TPD of a chiral compound-forming system. Grey shaded areas within the TPD correspond to the two SLE variants (a) and (b).

The two variants in Figure 2.7 (left) are sufficient to describe the ternary solution phase diagram (TPD) of chiral compound-forming system. Hereby, A and B represent the two

enantiomers (R) and (S) and AB represents the racemic compound (RS) (Figure 2.7 (left)). System (a) in Figure 2.7 can be described in a similar way as binary two phase SLE (Figure 2.6). Thus, eq. (10) can be equivalently used but the pseudo-chemical potential of component i is now a function of the concentration of both solutes (A^l and B^l). A system referring to type (b) in Figure 2.7 requires a model for the crystallization or dissolution of compound AB. The formation or dissociation of AB can be modelled analogous to a chemical reaction where v_i is the stoichiometric coefficient (see eq. (11)).

$$\vartheta_A A + \vartheta_B B \Leftrightarrow AB \tag{11}$$

The solid-liquid phase equilibria of a stoichiometric compound-forming system is commonly derived via the fundamental equation of two binary coexisting phases (eq. (8)) by adjusting the molar concentrations within the solid phase with the stoichiometry of the dissociation reaction of eq. (11). If one mole of compound AB is formed by v_A and v_B mole of component A and B, respectively, the molar concentrations within the solid phase are:[50]

$$x_A^s = \frac{\vartheta_A}{\vartheta_A + \vartheta_B}, \quad 1 - x_A^s = \frac{\vartheta_B}{\vartheta_A + \vartheta_B} \tag{12}$$

Combining the above formulated stoichiometry with the fundamental equation of two binary coexisting phases (eq. (8)) and the definition of the pseudo chemical potential (eq. (6)) gives the general equation of the solid-liquid phase equilibria of a stoichiometric molecular compound which is equivalent to the equation of proposed by Prigogine and Defay[54].

$$\Delta G_{sol,AB} = -RT \ln \left[\left(\frac{x_A^l}{x_A^s} \right)^{\vartheta_A} \left(\frac{x_B^l}{x_B^s} \right)^{\vartheta_B} \right] \tag{13}$$

The molecular compound of a chiral system nearly exclusively consists of an equimolar "racemic" mixture of the two enantiomers (see Figure 2.7, right). If we assume that 1 mol of racemic compound ($AB = RS$) is formed by ½ mol of each enantiomer ($A = R$ and $B = S$) the resulting stoichiometric constants are $v_R = v_S = 0.5$. Furthermore, both the solid and the liquid phase can be expressed as binary mixtures of R and S. Hence, eq. (13) can be reformulated with $x_R^l = (1-x_S^l)$ and $x_S^s = x_R^s = 0.5$ as the solid phase comprises racemic mixture of both enantiomers. This results in a relation between the molar concentration of S and the Gibbs free energy of solution of compound RS which is equivalent to the equation derived by Prigogine and Defay[54] and which will be used in this work for modelling mixtures of chiral compound-forming systems.

$$2\Delta G_{sol,RS} = -RT \ln \frac{x_R^l \left(1 - x_R^l\right)}{\left(0.5 \cdot 0.5\right)^2} = -RT \ln 4 x_R^l \left(1 - x_R^l\right) \tag{14}$$

At the racemic (50:50) mixture $x_R = x_S = 0.5 \cdot x_{RS}$ where x_{RS} represents the total solubility of the racemic compound. This way, equation eq. (14) can be reformulated and coincides with the equation (10) which has been formulated for a single solute SLE.

$$-RT \ln x_{RS}^{l} = \Delta G_{sol,RS} \tag{15}$$

2.2.4 Thermodynamic description of the eutectic composition

Regarding racemic compound-forming systems, the design of an enantioselective crystallization process not only depends on the solubility of the pure enantiomer and racemic compound (eqs. (10) and (15)). It requires knowledge on the complete ternary phase diagram (Figure 2.7) and hence on the SLE of mixtures of the two enantiomers in solution (see eq. (14)). The width of the region where either a pure enantiomer or the pure racemic compound can be crystallized by thermodynamic control (marked in grey) is defined by the eutectic composition.[44] Consequently, the eutectic composition is a key information which is required for crystallization process design of racemic compound-forming systems. The eutectic composition and the enantiomeric excess *ee* are defined by

$$x_{eu} = \frac{x_{S}^{eu}}{x_{S}^{eu} + x_{R}^{eu}} \quad \text{or} \quad ee = \frac{x_{S}^{eu} - x_{R}^{eu}}{x_{S}^{eu} + x_{R}^{eu}} \tag{16}$$

x_{eu} is the maximum in solubility of the ternary system and its composition is a function of temperature and the solvent.[44, 55] Variations of the eutectic composition with temperature can be potentially used for enantioseparation. The productivity of such a process is defined by the magnitude of the shift and the eutectic composition itself.[44] In this section, a thermodynamic model is derived which relates the difference in Gibbs free energy of solution between the racemic compound and the enantiomer, $\Delta_{RS-S}\Delta G_{sol}$, to the eutectic composition. It will be used in the following sections to predict x_{eu} with different thermodynamic approaches to model $\Delta_{RS-S}\Delta G_{sol}$.

At the eutectic point, three phases are in equilibrium with each other, the pure solid enantiomer in excess, the solid racemic compound and the liquid phase with the eutectic composition. Assuming an excess of the (*S*) enantiomer and using the common definition which refers 1 mol of racemic compound to ½ mol of each enantiomer the phase equilibria are defined by:

$$\text{equil. 1: } S_{crystal} \quad \leftarrow \boxed{\Delta G_{sol,S}} \rightarrow \quad S_{solution}$$

$$\text{equil. 2: } RS_{crystal} \quad \leftarrow \boxed{\Delta G_{sol,RS}} \rightarrow \frac{1}{2} S_{solution} + \frac{1}{2} R_{solution} \tag{17}$$
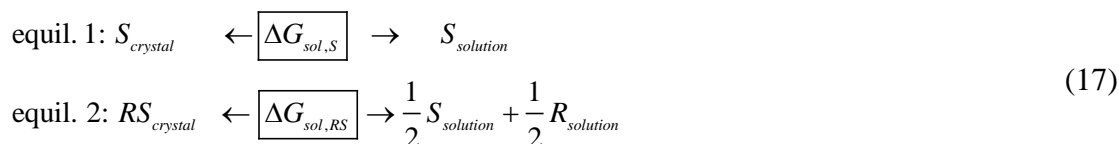
The solubility of a pure enantiomer and a racemic compound-forming system are described by eqs. (10) and (14) which are summarized below:

$$\text{enantiomer:} \qquad\qquad RT \ln x_{S} = -\Delta G_{sol,S}$$

$$\text{racemic compound:} \qquad RT \ln 4 x_{R} x_{S} = -2\Delta G_{sol,RS} \tag{18}$$

As illustrated in Figure 2.8, the phase equilibria that are present at the eutectic system can be established for the solid enantiomer (equil. 1b) as well as for the solid racemic compound (equil. 2b) which are in equilibrium with the same liquid phase.
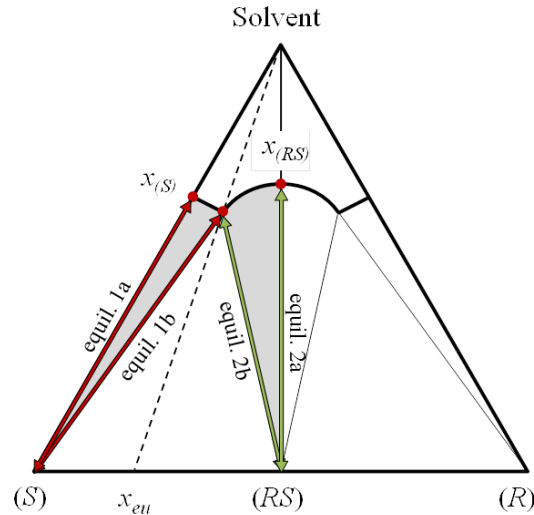
Figure 2.8: Illustration of the TPD of a racemic compound. The phase equilibria are shown which are relevant for the derivation of a thermodynamic model relating the eutectic composition to the difference in Gibbs free energy of solution between the racemic compound and the enantiomer.

Via equation (18) the four phase equilibria within Figure 2.8 are formulated:

$$
\begin{aligned}
&\text{equil. 1a: } RT \ln x_S = -\Delta G_{sol,S} && \text{equil. 2a: } RT \ln x_{RS} = -\Delta G_{sol,RS} \\
&\text{equil. 1b: } RT \ln x_S^{eu} = -\Delta G_{sol,S}^{eu} && \text{equil. 2b: } RT \ln 4 x_R^{eu} x_S^{eu} = -2\Delta G_{sol,RS}^{eu}
\end{aligned}
\tag{19}
$$

Equil. 2a in eq. (19) implies that the liquid phase in equilibrium with the pure racemic compound has a known composition of $x_S = x_R = 0.5 \cdot x_{RS}$. Assuming an infinitely diluted system, the Gibbs free energy of solution of the enantiomer and the racemic compound within eq. (19) are the same for the eutectic system and for the pure system:

$$
\begin{aligned}
\Delta G_{sol,S} &= \Delta G_{sol,S}^{eu} \\
\Delta G_{sol,RS} &= \Delta G_{sol,RS}^{eu}
\end{aligned}
\tag{20}
$$

Combining eq. (19) and (20) two equations can be derived that relate the solubility of each enantiomer at the eutectic system to the solubilities of the pure systems:

$$
\begin{aligned}
x_S^{eu} &= x_S \\
x_R^{eu} &= \frac{x_{RS}^{\;2}}{4 x_S}
\end{aligned}
\tag{21}
$$

Using the definition of the eutectic composition and the enantiomeric excess *ee* (eq. (16)) in combination with equation (21) forms a relation between the solubility ratio $\alpha = x_{RS}/x_S$ and the eutectic composition or the enantiomeric excess:

$$x_{eu} = \frac{x_S^{eu}}{x_S^{eu} + x_R^{eu}} = \frac{1}{1 + 1/4\left(x_{RS}/x_S\right)^2} = \frac{1}{1 + 1/4\,\alpha^2}$$

or

$$ee = \frac{x_S^{eu} - x_R^{eu}}{x_S^{eu} + x_R^{eu}} = \frac{1 - 1/4\left(x_{RS}/x_S\right)^2}{1 + 1/4\left(x_{RS}/x_S\right)^2} = \frac{1 - 1/4\,\alpha^2}{1 + 1/4\,\alpha^2}$$

(22)

Equation (22) is equivalent to a model that was proposed in literature[55] to estimate the eutectic composition from measured solubility ratios $\alpha = x_{RS}/x_S$. Finally, we can combine equation (22) and (19) to relate the solubility ratio α to the difference in Gibbs free energy between the racemic compound and the enantiomer, $\Delta_{RS\text{-}S}\Delta G_{sol}$:

$$x_{eu} = \frac{1}{1 + 1/4\left(x_{RS}/x_S\right)^2} = \frac{1}{1 + 1/4\exp\left(-2\dfrac{\Delta_{RS-S}\Delta G_{sol}}{RT}\right)}$$

(23)

In case of no enantiomeric excess, $x_{eu} = 0.5$ and the corresponding relative solubility $\alpha_{min} = 2$. The Gibbs free energy of solution difference is then $\Delta_{RS\text{-}S}\Delta G_{sol} = -RT\ln(2)$. This corresponds to an ideal conglomerate, a mechanical mixture of both enantiopure crystals. An alternative derivation[56], using a reference state of a mole of molecules, independent of chirality, leads to to eq. (24). In that case $x_{eu} = 0.5$ is related to $\Delta_{RS\text{-}S}\Delta G_{sol} = 0$.

$$x_{eu} = \frac{1}{1 + \alpha^2} = \frac{1}{1 + \exp\left(-2\dfrac{\Delta_{RS-S}\Delta G_{sol}}{RT}\right)}$$

(24)

2.2.5 Temperature dependence of solid-liquid equilibria

The solubility of organic crystalline substances always increases with increasing temperature. There are some salts, however, whose solubility in water does not change or even decreases with increasing temperature. The temperature dependence of the solubility can be described by the enthalpy of solution, ΔH_{sol}, via the Van't Hoff equation:

$$\frac{\partial \ln x^l}{\partial(1/T)} = -\frac{\Delta H_{sol}}{R}$$

(25)

Eq. (25) is frequently used to extract ΔH_{sol} from solubility measurements using a linear relation between the logarithmic mole fraction solubility and the inverse absolute temperature (in Kelvin). However, it was shown that a temperature and concentration independent solution enthalpy is often not valid, if solution temperatures are close to the melting temperature or if saturation concentrations are high.[57-59] Besides determining the solution enthalpy indirectly from the temperature dependence of the molar solubility, it can be determined by isothermal solution calorimetry methods with high accuracy.[60] If operated precisely, these methods are capable of quantifying influences of temperature and solution concentration on the solution enthalpy of organic non-electrolytes.[61-63] Solution calorimetry is a common method in pharmaceutical science to investigate polymorphism and molecular interactions in solution.[64]

2.3   Solubility prediction

In early stages of crystallization process design, for example in pharmaceutical development[65-67], the amount of substance available for experimental work is limited. In consequence, rather than intensively determining solid-liquid phase diagrams through direct solubility measurements, computational methods can be used to support or possibly replace experimental investigations. Popular and fast computational methods which are commonly used in industry are empirical Quantitative Structure–Property Relationship (QSPR)[7] methods. . Those however lack in physical insight and are often limited to water as a solvent.[68, 69] Most other approaches are based on computing the Gibbs free energy of solution, ΔG_{sol}, in order to predict solid-liquid phase equilibria via eq. (10).[70] In this section two thermodynamic approaches for calculating ΔG_{sol} are presented which require a limited amount of substance-specific experimental data or ultimately rely exclusively on first-principle computational methods.

2.3.1   Thermodynamic cycles for solubility prediction

Before introducing the specific thermodynamic approaches to determine the Gibbs free energy of solution which have been applied in this work, the conceptual approach of so-called "thermodynamic cycles" is elaborated. Analogously to the Hess' Law of constant heat (enthalpy) summation, a so-called *Bordwell thermodynamic cycle*[71] can be constructed in order to make a specific Gibbs free energy difference accessible - e.g. ΔG_{sol} from eq. (10). In the following, the term *thermodynamic cycle* will be used when referring to a Bordwell type thermodynamic cycle. A conceptual illustration of a thermodynamic cycle is depicted in Figure 2.9. Two exemplary ways are set up in order to bypass a non-accessible (or hard-to-reach) transition between two distinct states S1 and S2 by introducing a limited amount of intermediate state I1-I5. These intermediate states should be either easily and precisely accessible by experiment or by computational methods.
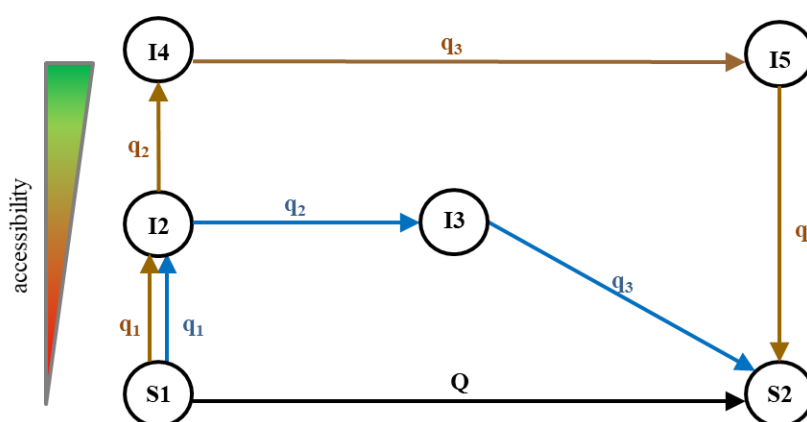
Figure 2.9: Conceptual illustration of a thermodynamic cycle which is constructed in order to detour the transition from the state S1 to S2 via intermediate states, I, by introducing a distinct set of auxiliary transition quantities, q_i, that in sum describe the seeked quantity, Q.

For the description of any thermodynamic quantity, q_i, is accompanied by the addition of uncertainties of determining the auxiliary quantities, δq_i, which contributes to the total uncertainty δQ. As every uncertainty δq_i is assumed to be uncorrelated, we can describe the total uncertainty by the square root of the sum of squares of the uncertainties of the N auxiliary quantities:

$$\delta Q = \sqrt{\left(\delta q_1\right)^2 + \ldots + \left(\delta q_i\right)^2 + \ldots + \left(\delta q_N\right)^2} \tag{26}$$

For solubility prediction, the Gibbs free energy of solution has to be modelled in order to access solubilities via eqs. (10) and (14). Two thermodynamic pathways have been proposed in literature in order to access the Gibbs free energy of solution, ΔG_{sol}.[72] Both concepts are illustrated in Figure 2.10. In the upper cycle, which will be referred to as the *melt cycle*, the solution free energy is approximated by the free energy difference when transferring a molecule from the solid crystal via the super-cooled melt into the solution. The lower cycle, which will be called the *sublimation cycle*, describes ΔG_{sol} by the energy differences needed to transfer one molecule from the crystal to the gas phase and subsequently into the solution.
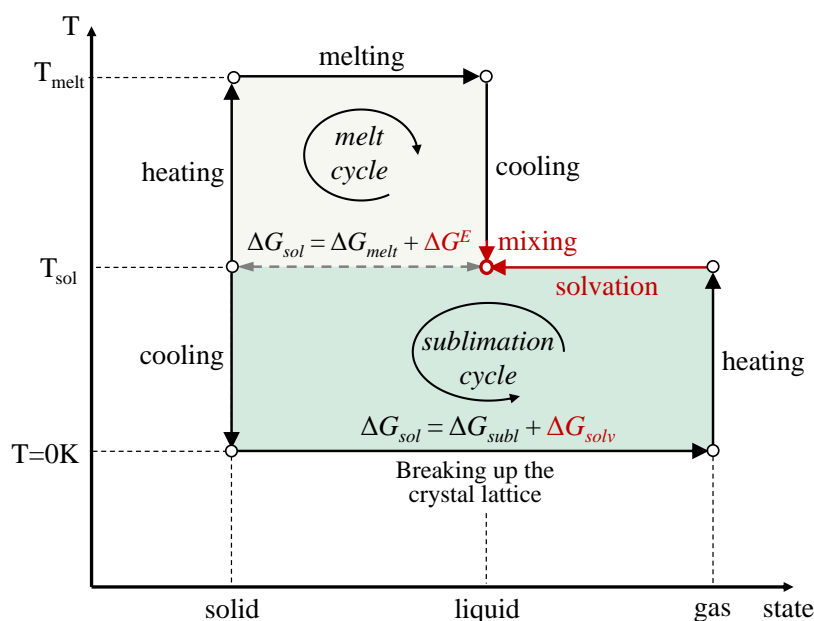
Figure 2.10: Illustration of two thermodynamic cycles to describe the free energy of solution, ΔG_{sol}. The *melt cycle* (top) relies on the free energy of melting, ΔG_{melt}, and on the partial molar free energy of mixing, ΔG^E. The *sublimation cycle* uses the free energies of sublimation, $\Delta G_{subl,}$ and the solvation free energy, ΔG_{solv}. Both cycles rely on specific solvent/molecule properties (indicated in red).

More specifically, the *melt cycle* relates the solution Gibbs free energy, ΔG_{sol}, by the Gibbs free energy of melting, ΔG_{melt}, and the excess Gibbs free energy of mixing the supercooled melt with a solvent, ΔG_i^E.

$$\Delta G_{sol} = \Delta G_{melt} + \Delta G^E \tag{27}$$

Variants of the melt cycle are used by classical solubility prediction methods such as the

general solubility equation (GSE)[73-75] and other QSPR methods[7, 76]. The popular GSE for example relates the aqueous solubility to the melting temperature and the case specific octanol-water partition coefficient and is frequently used to calculate drug solubilities. It empirically correlates ΔG_{melt} to the melting temperature and ΔG^E to the octanol-water partition coefficient.

The *sublimation cycle* alternatively uses an energetically less direct route via the gas phase by expressing ΔG_{sol} by the Gibbs free energy of sublimation, ΔG_{subl}, and the Gibbs free energy of solvation, ΔG_{solv}, of component *i*:

$$\Delta G_{sol} = \Delta G_{subl} + \Delta G_{solv} \tag{28}$$

The sublimation cycle was suggested by Grant and Higuchi[72] and first evaluated by Palmer et al.[10, 77] for predicting the aqueous solubility of organic molecules. For exclusively predicting the solubility, the sublimation cycle appears to be favourable as it uses the most computationally accessible solid-state quantity that can be derived directly from the crystal structure, the lattice energy.

Both thermodynamic cycles (Figure 2.10) incorporate thermodynamic quantities (melting or sublimation free energy) that are related to the crystalline solid and are specific quantities of one crystal structure (see section 2.1.2). As a result, they are capable to model solubility differences of polymorphs or chiral crystals. The two thermodynamic cycles are discussed in more detail in the following sections. The relevant energy quantities are specified and their experimental and/or computational determination are presented.

2.4   Melt cycle

The melt cycle requires the determination of the Gibbs free energy of melting, ΔG_{melt}, which is related to the melting temperature and melting enthalpy. An exclusively computational determination of these melting thermodynamics is still not precise enough for solubility prediction[78, 79] or limited to group contribution methods that cannot distinguish between polymorphs or chiral molecules.[76, 80, 81] Hence, this work focuses on the experimental investigation of, ΔG_{melt}, which is limited to substances that do not decompose or sublimate before or during melting.

2.4.1   Melting

The Gibbs free energy of melting, ΔG_{melt}, is comprised of the melting enthalpy, ΔH_{melt}, and the melting entropy, ΔS_{melt}.

$$\Delta G_{melt} = \Delta H_{melt} - T\Delta S_{melt} \tag{29}$$

The melting enthalpy is accessible by experiment at melting temperature using calorimetric methods like differential scanning calorimetry (DSC). The free energy difference between the melt phase and the crystalline solid is zero per definition at

thermodynamic equilibrium, $\Delta G_{melt} = 0$. Hence, at melting temperature the entropy of melting can be obtained via the melting enthalpy and the melting temperature, $\Delta S_{melt} = \Delta H_{melt} / T_{melt}$. Based on the above, the free energy of melting that can be calculated merely from the melting enthalpy and melting temperature:

$$\Delta G_{melt} = \Delta H_{melt}\left(1 - T/T_{melt}\right) \tag{30}$$

However, the melting thermodynamic functions, ΔH_{melt} and ΔS_{melt}, are functions of temperature and have to be corrected from the melting point to a given temperature, such as the solution temperature T_{sol}, as illustrated in Figure 2.11.
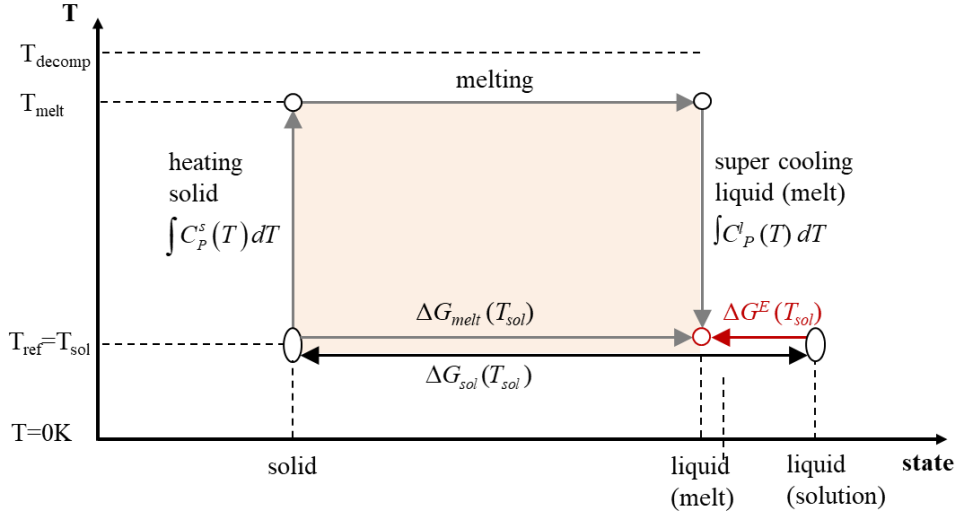
Figure 2.11: Scheme of the *melt cycle* which relates the Gibbs free energy of solution to the Gibbs energy of melting and the excess Gibbs energy of mixing (eq. (27)). It is experimentally accessible only when the decomposition (or sublimation) temperature is above the melting temperature. Solvent dependent properties are indicated in red.

Integrals of the heat capacity differences, $\Delta C_P^{l-s} = C_P^l - C_P^s$, between the supercooled melt (*l*) and the solid (*s*) from T_{melt} to $T_{ref} = T_{sol}$ add thermal corrections to the measured values determined at melting temperature:

$$H_{melt}\left(T_{sol}\right) = \Delta H_{melt}\left(T_{melt}\right) + \int_{T_{melt}}^{T_{sol}} \Delta C_P^{l-s}\left(T\right)dT \tag{31}$$

$$\Delta S_{melt}\left(T_{sol}\right) = \Delta S_{melt}\left(T_{melt}\right) + \int_{T_{melt}}^{T_{sol}} \frac{\Delta C_P^{l-s}\left(T\right)}{T}dT \tag{32}$$

Hence, the higher the melting temperature and the larger the difference in heat capacity between the crystal and the melt the larger the thermal corrections. Combining eq. (29) with eq. (31) and (32) results the general expression of the free energy of melting:

$$\Delta G_{melt} = -\frac{\Delta H_{melt}}{RT}\left(1 - \frac{T}{T_{melt}}\right) + \int_{T_{melt}}^{T} \Delta C_P^{l-s}dt - T\int_{T_{melt}}^{T} \frac{\Delta C_P^{l-s}}{t}dt \tag{33}$$

In literature thermal corrections are often neglected. In the most simplified case this

results in the equation of Schröder and van Laar which gives the "ideal" solubility of a single solute SLE if additionally the excess Gibbs free energy of mixing is set to zero $(\Delta G^E = 0)$:[49]

$$\ln x = -\frac{\Delta H_{melt}}{RT}\left(1 - T/T_{melt}\right) \tag{34}$$

For a racemic compound the equivalent to the Schröder van Laar equation is the equation of Prigogine and Defay:[54]

$$\ln 4x\left(1 - x\right) = -\frac{2\Delta H_{melt}}{RT}\left(1 - T/T_{melt}\right) \tag{35}$$

However, it has been shown that thermal corrections can influence melting free energies and subsequently the logarithmic solubility significantly by $\delta \ln x_i = 0.5$ to 1.7 and thus should not be neglected for solubility prediction.[82] Several methods are proposed in the literature to incorporate temperature corrections which rely on different amounts of experimental input.[59, 82, 83] The crudest methods do not require direct measurements but use an empirical temperature independent value for heat capacity difference. For example, the average ΔC_P^{l-s} of 117 organic molecules can be used which was shown to be $\Delta C_P^{l-s} = 84$ J·mol^{-1}K^{-1} but has a large standard deviation of 57 J·mol^{-1}K^{-1}.[83] A further temperature independent empirical simplification is to approximate the heat capacity difference by the entropy of melting, $\Delta C_P^{l-s} = \Delta S_{melt} = \Delta H_{melt}/\Delta T_{melt}$.[49] Experimentally costlier are substance specific measurements of heat capacity difference (for example at melting temperature) which are in its simplest form assumed to be temperature-independent.[59] An experimentally more demanding method requires experimental heat capacities of the crystal from reference temperature to melting temperature and measurements of the heat capacity of the melt above and if accessible below melting temperature. However, heat capacities of the supercooled melt are often not accessible due to recrystallization. Alternatively, they can be linearly extrapolated from T_{melt} to T_{ref} in order to approximate a temperature-dependent heat capacity difference. Any of the before described way to model ΔC_P^{l-s} can be used within eq. (33) to calculate temperature corrected Gibbs free energy of melting.

2.4.2   Mixing

In order to allow the solution to exhibit non-ideal behaviour and hence the solubility to be affected by the solvent and by the number of dissolved molecules (concentration dependence), the excess Gibbs free energy of mixing, ΔG^E, is introduced:

$$\Delta G^E = RT \ln \gamma_i \tag{36}$$

The activity coefficient, γ, which has been defined earlier in eq. (4) incorporates all deviations from the ideal solution. As a consequence, it is a function of temperature and composition of the solution. Most activity coefficient based thermodynamic methods, so-called g^E-models, are used in combination with the simplified description of the free

energy of melting of eq. (34) which neglects the contribution of the heat capacity difference. Further information on available g^E-models are given later on in section 2.7.3. According to the melt cycle (27) the enthalpic solution non-idealities, the excess enthalpies H^E, are related to the solution and melting enthalpies. More precisely, the excess enthalpies of the solution describe the difference between the solution enthalpy at T_{ref} and the corrected melting enthalpy at T_{ref} according to eq. (37). Like the excess Gibbs free energy of mixing H^E is related to the activity coefficient and thus is a function of the temperature and the solution concentration.

$$\Delta H_{sol} = \Delta H_{melt} + H^E \tag{37}$$

2.5   Sublimation cycle

The sublimation cycle in eq. (28) substitutes the melting thermodynamic quantities by introducing the gaseous state. This is based on the idea that the separated molecule (ideal gas) and the perfect crystal are two idealized thermodynamic states that are computationally well accessible using *ab-initio* quantum chemistry methods[84-86]. As a result, it offers an option for calculating solubility using solely computational methods. However, the sublimation thermodynamic quantities are as well accessible experimentally with high accuracy from sublimation vapor pressures.[87] Experimental data is required as reference quantities for predictive methods to work out sources of the computational errors. The experimental and computational routes are illustrated in Figure 2.12.
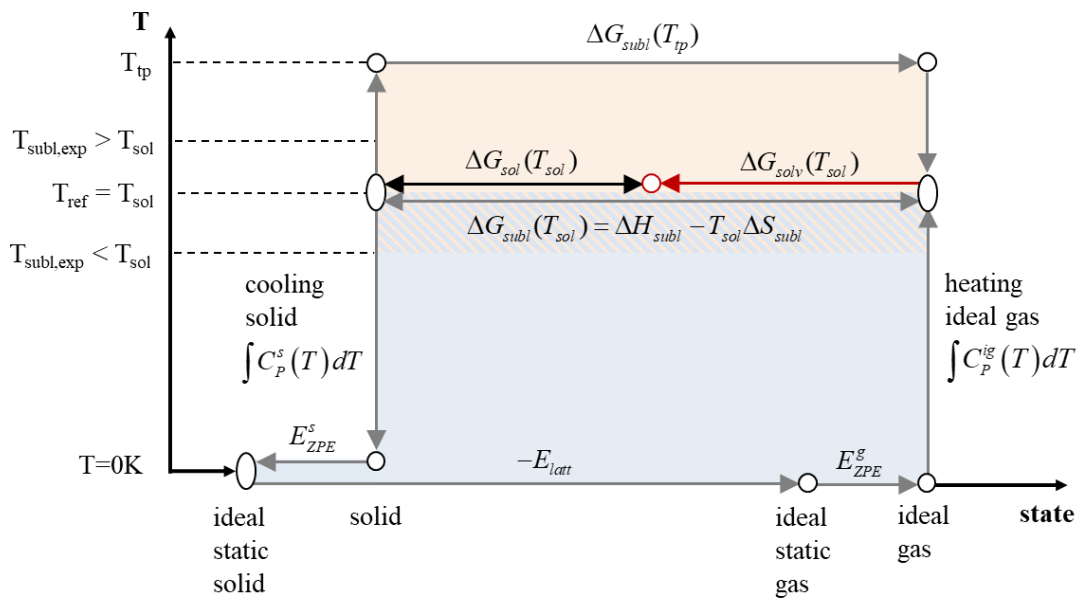
Figure 2.12: Illustration of the *sublimation cycle* which describes the Gibbs free energy of solution, ΔG_{sol}, with the Gibbs free energy of sublimation, ΔG_{subl}, and solvation, ΔG_{solv}, (eq. (28)). The red area indicates the accessibility of ΔG_{subl} by experiment and the light blue area indicates the route via the lattice energy, E_{latt}, that is accessible by ab initio quantum chemistry. Solvent-dependent properties are indicated in red.

Both routes thermodynamically connect the Gibbs free energy of solution, ΔG_{sol}, with the free energy of sublimation, ΔG_{subl}, and the Gibbs free energy of solvation, ΔG_{solv}. The experimental route is limited to cases where the sublimation temperature is below decomposition temperature.

2.5.1 Sublimation

The highest temperature a crystalline solid can sublimate is the triple point temperature, T_{tp}, which is equal to the melting temperature if the melting of the crystal is independent of the pressure (see Figure 2.5). This temperature defines the limit for an experimental investigation if the specific substance does not decompose before. Experimentally, the Gibbs free energy of sublimation, ΔG_{subl}, is directly accessible via the sublimation vapor pressure of a crystalline solid:[88]

$$-RTln\left(p_i \,/\, p_0 \right) = \Delta G_{subl} \tag{38}$$

Hereby, p_i is the absolute vapor pressure of substance i and p_0 is the reference pressure which is defined as 1 bar throughout this work. ΔG_{subl} is comprised of the sublimation enthalpy ΔH_{subl}, and the sublimation entropy ΔS_{subl}.

$$\Delta G_{subl} = \Delta H_{subl} - T\Delta S_{subl} \tag{39}$$

Analogously to the connection of solution enthalpy to the temperature dependency of the solubility via the Van't Hoff relation (see eq. (25)), the sublimation enthalpy is related to the temperature dependence of the vapor pressures. It is accessible via the so-called Clausius–Clapeyron equation[88]:

$$\frac{\partial \ln p_i}{\partial T} = -\frac{\Delta H_{subl,i}}{RT^2} \tag{40}$$

Due to the low vapor pressures of organic crystalline substances, sublimation measurements are usually performed at elevated temperatures as indicated in Figure 2.12 (light red area). Hence, the extracted sublimation enthalpy should be corrected to a reference temperature in order to ensure comparability between various experimental data.[82, 87] Similar to melting enthalpies (see eq. (31)) Kirchhoff's law can be used to adjust the heat of sublimation to the desired temperature. Assuming that sublimation is determined at the triple point (tp), ΔH_{subl} can be adjusted according to eq. (41) if no solid-solid phase transition occurs within that temperature range.[88]

$$\Delta H_{subl,i}\left(T_{ref} \right) = \Delta H_{subl,i}\left(T_{tp} \right) + \int_{T_{ref}}^{T_{tp}} \left(C_P^s - C_P^g \right) dT \tag{41}$$

There are simplified empirical methods to determine $\Delta C_P^{g-s} = C_P^g - C_P^s$ which are molecule-independent: $\Delta C_P^{g-s} = 2R$ (~9.6 J·mol^{-1}K^{-1}) or $\Delta C_P^{g-s} = 6R$ (~28.9 J·mol^{-1}K^{-1}).[82] An experimental dataset of 117 molecules suggests ΔC_P^{g-s} to be 32.7±45.5 J mol^{-1} K^{-1}.[83] Besides that, measured solid-state heat capacity and calculated ideal gas heat capacities can be combined to approximate a substance-specific ΔC_P^{g-s}.[87]

In contrast to an experimental determination at elevated temperatures, the sublimation

thermodynamics are computationally accessible via the static crystal at zero Kelvin (see blue area in Figure 2.12). At zero Kelvin, the equivalent to the sublimation free energy is the lattice energy, E_{latt}, which is the energy needed for breaking up the static crystal lattice. More specifically, it is defined as the energy difference between a static perfect infinite crystal (ideal static solid – iss) and its related ideal static gas (isg) phase of infinitely separated molecules in their lowest energy conformation both at 0 K:

$$E_{latt} = \frac{E^{iss}}{Z} - E^{isg} = E_{inter} + \Delta E_{intra} \tag{42}$$

Where E^{isg} is the energy of the static separated molecule (ideal static gas), E^{iss} is the energy of the ideal static solid crystal and Z is the number of molecules within the unit cell. The lattice energy can be separated into two contributions.[89] The dominant contribution is the intermolecular energy, E_{inter}, which includes all electrostatic as well as polarization, dispersion and repulsion contribution (see Figure 2.13). They all depend on intermolecular distances and hence on the crystal packing.[90] ΔE_{intra} is the difference in energy for a single molecule in the crystal conformation and in its lowest energy conformation in the ideal gas. ΔE_{intra} is zero for rigid molecules and typically in the order of a few kJ·mol^{-1} unless intramolecular hydrogen bonding is involved.[11]

Advance in computer technology enables a fast and reliable calculation of the lattice energy and lattice vibrations of an organic compound.[91] Nowadays, E_{latt} can be calculated with increasing accuracy with DFT shown for benzene, which has been computed with an accuracy of better than 1 kJ mol^{-1}.[86] Recent benchmarks of larger sets of molecules show an increase in accuracy of better[92, 93] or equal[85] to 4.9 kJ·mol^{-1} which is the statistical uncertainty of measurements of ΔH_{subl}[94]. Hence, the precision of computational methods is converging to the level of relatively small polymorphic or enantiopure/racemic energy differences. For example, the lattice energy differences between observed polymorphs are usually less than 4 kJ·mol^{-1} (80% of the cases)[28], which is in the same range as the energy difference between homochiral and racemic crystals[95].

Besides the lattice energy, various thermal corrections contribute to the Gibbs free energy of sublimation. They are required to close the large gap between the ideal static states and a real system at solution temperature as illustrated in Figure 2.12. Corrections include enthalpy and entropy terms, ΔH_{corr} and ΔS_{subl}, which all contribute to ΔG_{subl} as shown in eq. (43). Following the concept of absolute entropy, the entropy contribution to the sublimation free energy is not labelled as an entropy correction but as an absolute value ($\Delta S_{corr} = \Delta S_{subl}$) within eq. (43).

$$\Delta G_{subl} = -E_{latt} + \Delta G_{corr} = -E_{latt} + \Delta H_{corr} - T\Delta S_{subl} \tag{43}$$

Thermal corrections are comprised of contributions of zero-point vibrational energy and thermal corrections between zero Kelvin and reference temperature (see Figure 2.12). The zero-point vibrational energy is the lowest energy a quantum mechanical system can have. It describes the energy gap between an idealized static thermodynamic state to a system at zero Kelvin. Hence, the difference in zero-point energy between the crystal and the gas, $\Delta E_{ZPE} = E_{ZPE}^{g} - E_{ZPE}^{s}$, shifts energy difference between the idealized static solid (iss)

and the ideal static gas (isg) to an energy difference between the crystalline solid (s) and the ideal gas (g) at zero Kelvin. The difference in heat capacity on the other hand, $\Delta C_P^{g-s} = C_P^g - C_P^s$, levitates the energy difference between the gas and the solid from zero K to the reference temperature by introducing an enthalpy correction, ΔH_{corr}, and the sublimation entropy, ΔS_{subl}, as shown in eq. (44).

$$H_{corr} = \left(E_{ZPE}^g - E_{ZPE}^s \right) + \int_{T'=0}^{T} \Delta C_P^{g-s} \left(T' \right) dT'$$

$$\Delta S_{subl} = \int_{T'=0}^{T} \frac{\Delta C_P^{g-s} \left(T' \right)}{T'} dT'$$

(44)

Unlike for the thermal corrections to the experimental sublimation enthalpies (see eq. (41)), in eq. (44) ΔC_P^{g-s} are required for a significantly larger temperature range. Yet still, there is a substance independent method to approximate ΔH_{corr} by -2RT within the so-called 2RT-approximation[96]. However, there is no equivalent simplified method for determining ΔS_{subl}. Therefore, calculated (or measured) solid-state heat capacities and calculated ideal gas heat capacities have to be acquired.[87] Computations require details on the molecular and lattice vibrational frequencies[97]. Further details on the computation of thermal corrections to the lattice energies are given in more detail in section 2.6.5.

2.5.2 Solvation

The Gibbs free energy of solvation is needed to transfer the gas phase molecule into the solution after its sublimation from the crystal structure to close the sublimation cycle (Figure 2.12). It is defined as the change in Gibbs free energy when a molecule (or an ion) is transferred from a vacuum (the ideal gas) into a solvent and is required at solution temperature. It can be computed as the difference between the chemical potential of component i in the solution, μ_i^l, and its chemical potential in the ideal gas, μ_i^{ig}:

$$\Delta G_{solv} = \mu_i^l - \mu_i^{ig}$$

(45)

According to the sublimation cycle in eq. (28) the solvation enthalpy ΔH_{solv} which is the heat that is released when transferring the molecule from the gas phase into solution is related to the solution and sublimation enthalpies. More precisely, the solvation enthalpies is the difference between the solution enthalpy at T_{sol} and the corrected melting enthalpy at T_{sol} according to eq. (46). Like the excess Gibbs free energy of solvation, ΔG_{solv} it is related to the activity coefficient and thus is a function of the temperature and the solution concentration.

$$\Delta H_{sol} = \Delta H_{subl} + \Delta H_{solv}$$

(46)

2.5.3   Standard states for sublimation and solvation thermodynamics

There are two commonly used standard states which use different sublimation and solvation free energies and result in different units for the calculated solubilities. Both approaches are introduced in the following while one standard state system is chosen which is used throughout this work.

Computations of solvation free energies are often quoted in the Ben-Naim standard state[51] (suffix *) which refers to 1 mol of gas that is solvated in 1 litre of solvent. Alternatively, the gas phase is related to 1 bar of ideal gas which is solvated in 1 mol of solvent (suffix ^{0}). The solvation free energies of the two different reference states can be converted into one another with knowledge with the molar volume of the solvent (or the solution), V^l, and of the ideal gas, V^{ig}:

$$\Delta G^*_{solv} = \Delta G^0_{solv} - RT \ln\left(\frac{V^{ig}}{V^l}\right) \tag{47}$$

Experimental sublimation free energies are commonly referred to 1 mol of substance that is transferred to 1 bar or 1 atm of ideal gas. Hence, for an application within the sublimation cycle the bar/mol standard state (suffix ^{0}) directly leads to a mole fraction solubility, x_i, while mol/l standard state (suffix *) results in a mol/l solubility, S_i, and needs the Gibbs free energy of sublimation to be converted using the molar volumes of the crystal and the gas, V^s and V^{ig}, via eq. (48).

$$\Delta G^*_{subl} = \Delta G^0_{subl} - RT \ln\left(\frac{V^s}{V^{ig}}\right) \tag{48}$$

In this work, the bar/mol standard state system (suffix ^{0}) is used for the solvation and sublimation free energies. It results in the wanted mole fraction solubility (see eq. (1)) without the need of unit conversions requiring molar volumes of the crystal when choosing the mol/l reference state[77]. Furthermore, the bar/mol reference state is the standard reference state within the COSMO-RS model which is used in this work for calculating ΔG_{solv} as discussed later in section 2.6.6 and 2.7.2.

2.6   Modelling molecular interactions

All interactions in atoms and molecules are fundamentally electric in nature.[90] To be able to differentiate between intermolecular forces they are commonly divided into different classes. Figure 2.13 illustrates the commonly used classification of non-covalent molecular interactions, dividing them into Coulombic (often referred to as electrostatic) interactions which incorporate the undistorted and directed interaction energies and van der Waals (vdW) interactions which originate from induction and dispersion. The various intermolecular potentials differ in strength and their dependency on the distance of the contributing charges. Ion-Ion interactions for example are strong and long-range interaction energies while vdW interactions deplete quickly with intermolecular distances and are weak in comparison. Hydrogen bonds are strong and directed dipole-dipole

interactions where the proton acceptor and proton donator only have a very short distance. They play an exclusively important role for modelling interactions the crystal lattice as well in solution. More detailed information on intermolecular forces and modelling approaches can be found refs. [90, 98].
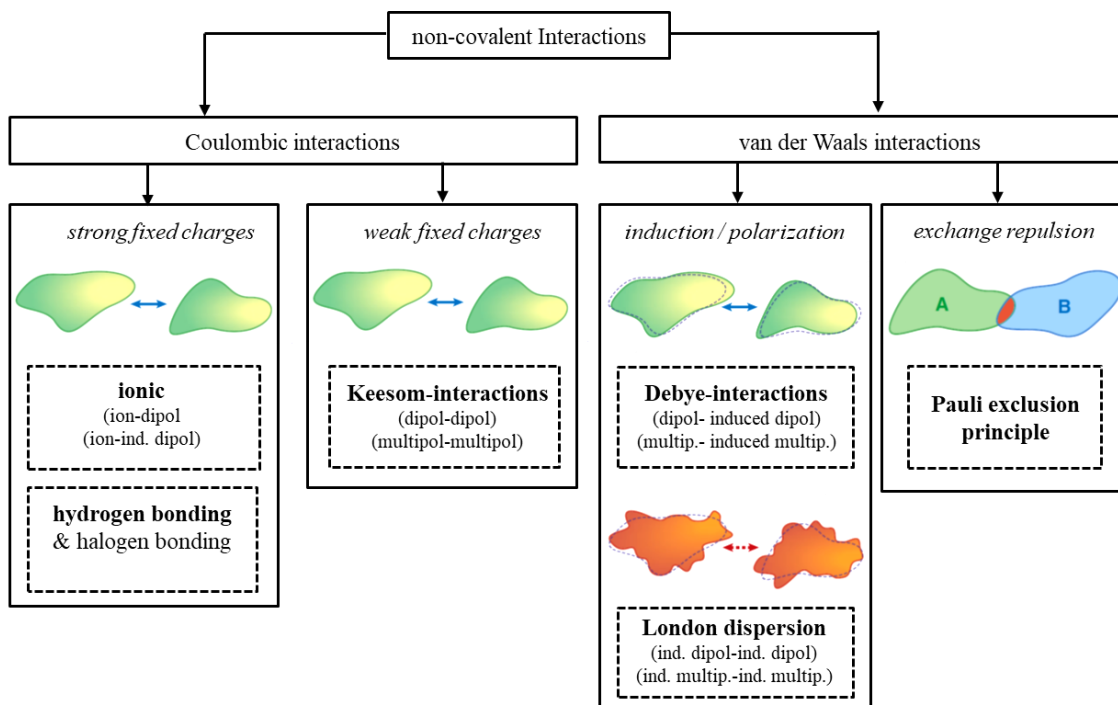
Figure 2.13: Classification of non-covalent molecular interactions. The coloured clouds schematically illustrate intermolecular interactions based on interactions of electron densities which were adapted from ref. [99].

2.6.1 Density Functional Theory (DFT)

This section provides a brief insight into the theory behind quantum chemistry methods based on Density Functional Theory (DFT), focussing on those methods that have been used within this work. The interested reader is referred to additional literature for a more detailed representation.[100-102]

Electronic structure calculations – such as DFT – are frequently used to determine the lowest-energy state of a many-electron system (e.g. a molecule), the so-called *ground state*. For that, they try to solve the *time independent, non-relativistic Schrödinger equation* shown in eq. (49) in a numerically efficient way.[100]

$$\hat{H}\Psi(r_i...r_N) = E\Psi(r_i...r_N) \tag{49}$$

$\hat{H}$, the Hamiltonian, is the quantum mechanical operator and r_i is the coordinate of an electron i of a system containing N elections. The Hamiltonian is constructed to extract the energies from a system that is described by Ψ, the wave function. $\hat{H}$ consists of a sum of three terms, the kinetic energy, the interaction energy with the external potential and the electron-electron interaction energy. Methods that provide solutions of eq. (49) without the need of experimental data are called *ab initio* methods. Born-Oppenheimer

introduced an important simplification which states that firstly the motion of the nuclei and electrons can be separated and that secondly the relatively small velocity of the nuclei can be neglected in contrast to the motion of the electrons which reduces the complexity of the Hamiltonian and which made the Schrödinger equation accessible.

Two commonly used methods make use of the Born-Oppenheimer approximation by treating only the electrons as quantum mechanical objects. The so-called *Hartree-Fock* (HF) theory uses this assumption by averaging all electron-electron interactions.[100] Alternatively, the electron distribution can be described by its probability density which is related to the square of the wave function (Ψ^2). The basic theorem of Density Functional Theory (DFT) has been proposed by Hohenberg and Kohn[103] which states that the ground state electronic energy is directly correlated to the electron density and depends on only three spatial coordinates. Besides it theoretical accessibility it can be determined as well experimentally (see Figure 2.14) and hence is not merely a theoretical concept.
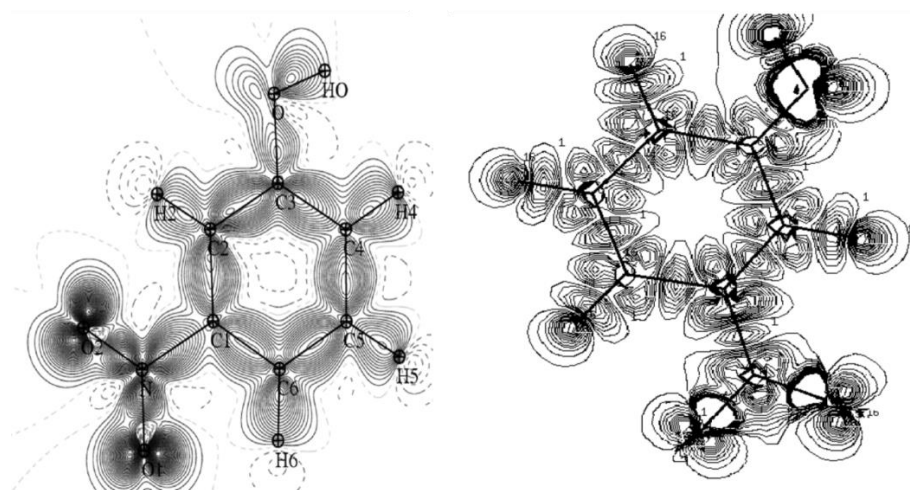
Figure 2.14: Comparison of an electron density map of m-nitrophenol that has been determined (left) experimentally by high-resolution X-ray diffraction and (right) computationally via Density Functional Theory.[104]

2.6.2   Density functionals

After Kohn-Sham proposed an approach in which the fully-interacting system is replaced by a system of non-interacting electrons it became obvious that there is a need to construct exchange-correlation functionals that are capable to model interactions between electrons.[102] The most well-known exchange-correlation functionals belong to the class of Local Density Approximation (LDA), Generalized Gradient Approximation (GGA), Meta-GGA and Hybrid Functionals. Until now, numerous exchange-correlation function have been proposed while most well known and most used functionals belong to the GGA, meta-GGA and Hybrid class.[105] Hybrid functionals mix LDA and GGA functionals with some part of Hartree-Fock exchange in a given ratio or by fitting the parameters to experimental data which makes them a semi-empirical method. The most well-known hybrid functional is the B3-LYP functional. Selected functionals that are used in this work are summarized and classified within Table 2.1.

Table 2.1: Summary of the exchange-correlation density functionals that have been used in this work. The corresponding literature referring to the respective functional can be found here[105].

Class	Functionals
GGA	B-LYP, B-P86, PBE, B97-D (semi-empirical)
Meta-GGA	M06
Hybrid	B3-LYP

A major drawback of DFT methods is related to their difficulties to accurately model the rather week vdW interactions (see Figure 2.13). Especially the long range attractive interaction tail of the London dispersion interactions are difficult for most functionals.[106] This is especially relevant for the computation of crystal structures, so-called periodic DFT methods (see subsequent section 2.6.4). Within a crystal, the molecules are closely packed and intermolecular interactions are in some cases dominated by van der Waals forces (e.g. naphthalene). To overcome this inherent limits of DFT methods, corrections terms, so-called *dispersion corrections*, are frequently used, which add an empirical correction term.[106, 107] Besides that, methods have been proposed that are parameterized by ab initio methods without the incorporation of experimental data.[108] It has been shown that the dispersion correction sometimes account for errors of up to 80 % depending on the functional used in weakly bound systems.[109] Hence, their precise incorporation is one of the key challenges in the development of new density functionals.[102]

2.6.3   Basis sets

All density functionals require a computational efficient framework to calculate the electronic wave function. Basis sets are used in quantum chemistry methods in order to approximate the wave function by a set of known functions which can be efficiently solved numerically. More specifically, a basis set is comprised of so-called basis functions using linear combinations of those to model the molecular orbitals of a system. This is not necessarily an approximation if the basis set is complete which would require an infinite number of basis functions. Hence, for practical applications the choice of the basis set is always a balance between accuracy and computational cost. Generally speaking, the smaller the basis set, the poorer is the resulting representation of the wave function. Most commonly a linear combination of atomic orbitals on each nucleus (LCAO), more specifically Gaussian-type orbitals (GTO), are used as they allow computationally efficient implementations of electronic structure calculations.[110] Within this work mainly GTO type basis functions are used. However, especially for the description of this three-dimensional systems, such as molecular crystals, plane-wave (PW) type basis functions[111, 112] or a hybrid of the Gaussian and plane-wave scheme[113] are used.

The smallest GTO type basis set for electronic structure calculations of a molecule contains just one function for each occupied orbital of each nucleus. For example, for

hydrogen the minimum basis (*Single Zeta*, SZ) set would require a single s-function representing the 1s orbital whereas at least four basis functions for carbon, oxygen and nitrogen (one s- and a set of p-orbitals). A better description of the wave function is obtained when taking twice as many basis functions as the minimal basis set that each can be fully optimized as done in a *Double Zeta* (DZ) basis set. Increasing the number of basis functions allows the electron distribution to be different in different directions which is for example important for chemical bonding. As chemical bonding and non-covalent intermolecular interactions occurs predominantly between valence electrons it is computationally more efficient to use the *Double Zeta* method only for the valence orbitals which is done by the so-called *Split-Valence* (SV) basis set. Adding more than two basis functions for each valence orbital leads to often used triple (TZV) and quadruple-zeta (QZV) basis sets. Additional flexibility can be built into the system to account for strong direction-dependent electron distribution by adding an additional higher orbital basis function which is denoted as *Polarization Function*. This leads to one of the most common basis sets, the SVP (Split Valence Double-Zeta plus Polarization) and the TZVP (Split Valence Triple-Zeta plus Polarization) basis set.

2.6.4   Modelling molecular interactions in the crystal

Especially in the field of solid-state chemistry, DFT has wide applications for the computation of structural, chemical, optical, spectroscopic, vibrational and thermodynamic properties.[84] This section focuses on the application of periodic DFT for modelling molecular interactions in a crystal in order to determine its lattice energy. More in-depth information are given in literature[84, 114].

To be able to calculate the electronic ground state and energy of a crystalline solid using DFT the symmetry and periodicity of a crystal structure can be exploited to reduce the computational cost. As introduced before a crystal structure can be described by its unit cell (see Figure 2.3). It is characterized by the length of the cell vectors *a, b* and *c* as well as the angles between the cell vectors α, β and γ. For periodic calculations a commonly used mathematical simplification is the concept of reciprocal space. Hereby, the unit cell vectors (*a, b* and *c*) are converted to forming a reciprocal lattice, which is named the 1st Brillouin zone. It is defined as the most symmetric unit cell (the Wigner-Seitz cell) for the reciprocal lattice.[29]

The periodicity of crystals can then be exploited by applying Bloch's theorem which expresses the wave function as a periodic Bloch function whose wave vector is constructed from the centre of the reciprocal lattice. Integrals over the Brillouin zone are approximated numerically, with so-called Bloch wave functions and sampled on a discrete mesh of wave vectors often referred to as *k*-points.[84] The Bloch wave function (also called Bloch state or Bloch function) represents the wave function for an electron in the periodically-repeating environment, e.g. the crystal, while the *k*-points represent the points where the system is evaluated.[115] The higher the number of *k*-points the better the approximated integral over the entire unit cell. In practice, the Brillouin zone can be constructed by considering a finite and relatively small number of *k*-points.[90] An

important *k*-point is the gamma point (Γ-point) where $k = 0$, which is the centre point of the 1st Brillouin zone. An important quantity which determines the complexity and time needed to calculate the lattice energy of an organic crystal is the number of independent molecules within the unit cell, Z'. In 88 % of the cases molecular crystals incorporate only one independent molecule in the unit cell (Z' $\leq$ 1) while the cases where Z' $\geq$ 2 is rare and accounts to less than 1 % of the crystals in the Cambridge Crystal Database (CSD).[31] However, if internal symmetry within the unit cell cannot be exploited by a computational method the total number of molecules, Z, defines the number molecules within the unit cell which is often significantly larger then Z'.

2.6.5   Thermal corrections to the lattice energies

Calculating electronic energies of a single molecule or of molecular crystals using above introduced DFT and periodic DFT methods gives the ground-state energies of hypothetical non-vibrating (static) molecules at zero Kelvin. This is a result of the underlying assumption that the atomic nuclei are static.[100] As discussed before (see Figure 2.12), in order to model solid-liquid phase equilibria via the sublimation cycle lattice, energies obtained from the static molecular interaction energies have to be adjusted to solution temperatures (hence to around 298 K). Of relevance are the gas phase as well as solid phase enthalpy and entropy contributions. In order to incorporate temperature and thus enthalpy and entropy corrections to the ground state energies statistical mechanics is applied to the quantum mechanical systems.[116] Besides calculating the total energies of a system, DFT methods can be used to calculate the second derivatives of these energies. The second derivatives give the molecular Hessian matrix which enable the calculation of vibrational frequencies within the harmonic approximation. Vibrational frequencies can subsequently be used to calculate the vibrational part of the partition function which is required for calculating the thermodynamic functions at temperatures other than 0 K. This will be discussed in more detail in the following.

Gas phase contributions

Excluding electronic excitations, thermal stimulation of a static ground state of an isolated molecule results in translational, rotational and vibrational motions of the molecule. The resulting thermodynamic functions are accessible via the molecular partition function, *Q*, which originates from statistical thermodynamics. Given the partition function the temperature-dependent heat capacities of the separated molecule (ideal gas) and its general thermodynamic functions can be calculated:[117]

$$C_P(T) = RT \frac{\partial}{\partial T}(T \ln Q) + R \tag{50}$$

$$S(T) = R + R \ln Q + RT \frac{\partial \ln Q}{\partial T} \tag{51}$$

$$H(T) - H(0) = \frac{RT^2}{Q}\frac{\partial Q}{\partial T} + RT \qquad (52)$$

where R is the ideal gas constant. A simplified way to model the partition function is to use the so-called *Rigid Rotor Harmonic Oscillator* (RRHO) approximation. First of all, it assumes that the translational, rotational and vibrational motions are decoupled. Secondly, the vibrational contributions to the thermodynamic functions are calculated as summations over all vibrational frequencies which are assumed to be harmonic. The molecular vibrational frequencies are accessible from the second derivative (Hessian matrix) of the ground state energies. Each molecule has 3N-6 harmonic vibrational frequencies where N specifies the number of atoms within the molecule. All parts of the partition function and the resulting thermodynamic functions are summarized in Table 2.2 according to literature[117].

Table 2.2: Classical approximation of the translational, rotational and vibrational parts of the partition function Q and the resulting thermodynamic functions C_P, $S(T)$ and $H(T)$-$H(0)$ of an ideal gas according to eqs. (50) to (52) and ref. [117].

	Translation	Rotation*	Vibration	Sum
Q	q_{tr} $= \left(\frac{2\pi mKT}{h^2}\right)^{3/2} V$	q_{rot} $= \frac{\sqrt{\pi}}{\sigma_r}\left(\frac{T^{3/2}}{\sqrt{ABC}}\right)$	q_{vib} $= \prod_i \left(1 - e^{-\frac{hv}{k_B T}}\right)^{-1}$	$Q = q_{tr}q_{rot}q_{vib}$
$C_P(T)$	$C_{P,tr} = \frac{5}{2}R$	$C_{P,rot} = \frac{3}{2}R$	$C_{P,vib}$ $= R \sum_i \left(\frac{hv_i}{k_B T}\right)^2 \frac{e^{-\frac{hv_i}{k_B T}}}{\left(1 - e^{-\frac{hv_i}{k_B T}}\right)^2}$	C_P $= C_{P,vib} + 4R$
$S(T)$	S_{tr} $= R\left(\ln q_{tr} + \frac{5}{2}\right)$	S_{rot} $= R\left(\ln q_{rot} + \frac{3}{2}\right)$	S_{vib} $= R \sum_i \ln\left(1 - e^{-\frac{hv_i}{k_B T}}\right)$ $+ R \sum_i \left(\frac{hv_i}{k_B T}\right)^2 \frac{e^{-\frac{hv_i}{k_B T}}}{\left(1 - e^{-\frac{hv_i}{k_B T}}\right)^2}$	S $= S_{tr} + S_{rot}$ $+ S_{vib}$
$\Delta_0^T H$	$\Delta_0^T H_{tr}$ $= \frac{5}{2}RT$	$\Delta_0^T H_{rot}$ $= \frac{3}{2}RT$	$\Delta_0^T H_{vib}$ $= RT \sum_i \left(\frac{hv_i}{k_B T}\right)^2 \frac{e^{-\frac{hv_i}{k_B T}}}{\left(1 - e^{-\frac{hv_i}{k_B T}}\right)^2}$	$\Delta_0^T H$ $= \Delta_0^T H_{vib}$ $+ 4RT$

* For a linear molecule the expressions change slightly as a result of rotational symmetry.

Thermal excitations are dependent on temperature and are zero at zero Kelvin. However, in classical quantum mechanics an oscillator is always in motion and has a residual Energy at zero Kelvin, the zero-point vibrational energy (ZPE). The ZPE is not accessible

by caloric measurements but can be calculated from measured or calculated vibrational frequencies of the molecules. Within the RRHO approximation the ZPE in the gas phase equals one-half the sum of the $3N$-6 harmonic vibrational frequencies:[117]

$$E_{ZPE}^{g} = \frac{h}{2} \sum_{i}^{3N-6} \nu_i \qquad\qquad (53)$$

Crystalline phase contributions

Molecular motions within the crystal can be divided into two types. Similarly, as for molecules in the ideal gas, molecules within the crystal can be thermally exited which results in *molecular vibrations*. However, as they are packed within a crystal lattice molecular motions are limited to only vibrations while translational and rotational movements are inhibited. It is often assumed that the vibrational motions of each molecule are independent of the surrounding molecules. This would lead to the same molecular vibrational thermodynamic functions as for a separated molecule (see Table 2.2). However, besides the motions of each molecule the molecules within the lattice can uniformly oscillate at a specific frequency resulting in *lattice vibrations*. These vibrational modes are often called phonon modes. A phonon is a quantum mechanical description of such a vibrational motion of the lattice. Phonon modes can be divided into optical and acoustic modes where acoustic modes relate to motions that are in phase within the unit cell while optical modes to out of phase motions. There are models that assume the phonon modes to be independent from the molecular modes and others that allow interactions between the molecular and lattice vibrations. Within this work both assumptions are compared for chiral molecular crystals and are introduced later on in section 2.7.2 along with further computational details.

Thermal corrections to the lattice energy

According to eq. (44), the resulting overall thermal enthalpy and entropy corrections (ΔH_{corr} and ΔS_{corr}) to the lattice energy are related to the difference between the aforementioned gas phase contributions and those of the crystalline solid. In the costliest form, all thermal enthalpy and entropy contributions are determined independently for the ideal gas and the crystalline solid. Hereby, the solid-state heat capacities between zero Kelvin and reference temperature can either be determined experimentally or by computational methods. Together with the ideal gas thermodynamic functions (see Table 2.2) the overall thermal corrections are accessible via eq. (44). However, frequently assumptions are made in order to reduce the computational effort. If molecular and lattice vibrations are assumed to be decoupled, the molecular (zero-point and thermal) vibrational energy contributions, ΔE_{vib}^{mol}, are identical in the crystal and for the separated (ideal gas) molecule.

As a consequence, they cancel out which results in a simplified expression of the overall vibrational contributions ($\Delta E_{vib}^{g\text{-}s} = \Delta E_{vib}^{mol} + \Delta E_{vib}^{latt}$) and finally of ΔH_{corr}:

$$\Delta H_{corr} = -\Delta E_{vib}^{latt} + 4RT \tag{54}$$

where ΔE_{vib}^{latt} is the total (thermal and zero-point) vibrational energy which is related to lattice vibrations. This expression can be further simplified resulting in a simple molecule independent model, the so-called $2RT$-approximation[101]. This requires on the one hand to neglect all remaining zero-point vibrational energy differences between the crystal and the gas. Secondly, the temperature is assumed to be high enough to treat intermolecular vibrations as if they were at the high-temperature limit. Together, this gives a ΔE_{vib}^{latt} of $6R$. Hence, the overall thermal correction enthalpy correction is given by the $2RT$-approximation:

$$\Delta H_{subl} = -E_{latt} - 2RT \tag{55}$$

Entropy contributions to the sublimation free energy, $T\Delta S_{subl}$, is not accessible by an equivalent simplified expression such as the $2RT$-approximation. As a consequence, vibrational frequencies within the separated molecule and the crystal lattice have to be modelled explicitly.

2.6.6 Modelling molecular interactions in solution

The two thermodynamic cycles shown in Figure 2.10 both incorporate molecular interaction energies between the solute molecules and the solution in a different way. Within the melt cycle parts of solution process (the liquefaction) are incorporated within the Gibbs free energy of melting which can be independently used to model "ideal" solutions via the equation of Schröder and van Laar, eq. (34).[49] Deviations to an ideal solution are added via the activity coefficient and thus the excess Gibbs energy of mixing ΔG^E (see eq. (5)). ΔG^E can be approximated by a thermodynamic model of the activity coefficient, a so-called g^E-model[118, 119]. Famous representatives are the NRTL, UNIQUAC and the PC-SAFT model.[49, 120] These methods however require substance specific experimental solubilities to which their internal parameters are correlated to. There are as well methods that do not rely on solubility measurements of the specific substance but instead have been calibrated with a set of molecular interactions energies which are not necessarily solubilities. These models are commonly called predictive g^E-models. The UNIFAC model for example approximates interactions of the solvated molecule with the solution by interactions between the various functional groups of the solute and the solvent. Thus, it relies on a set of binary interaction energies between the various functional groups. The COSMO-RS[121] model and the subsequently published comparable COSMO-SAC[122] model use the partial charges of the molecular surface of the solute and solvent molecule to calculate their intermolecular interaction energies. Hereby, the surface charges which are obtained from the polarizable continuum model (PCM[123]) COSMO[124] are divided into segments with a specific partial charge. The binary interaction between these segments give the excess chemical potential in solution and hence the activity coefficient.
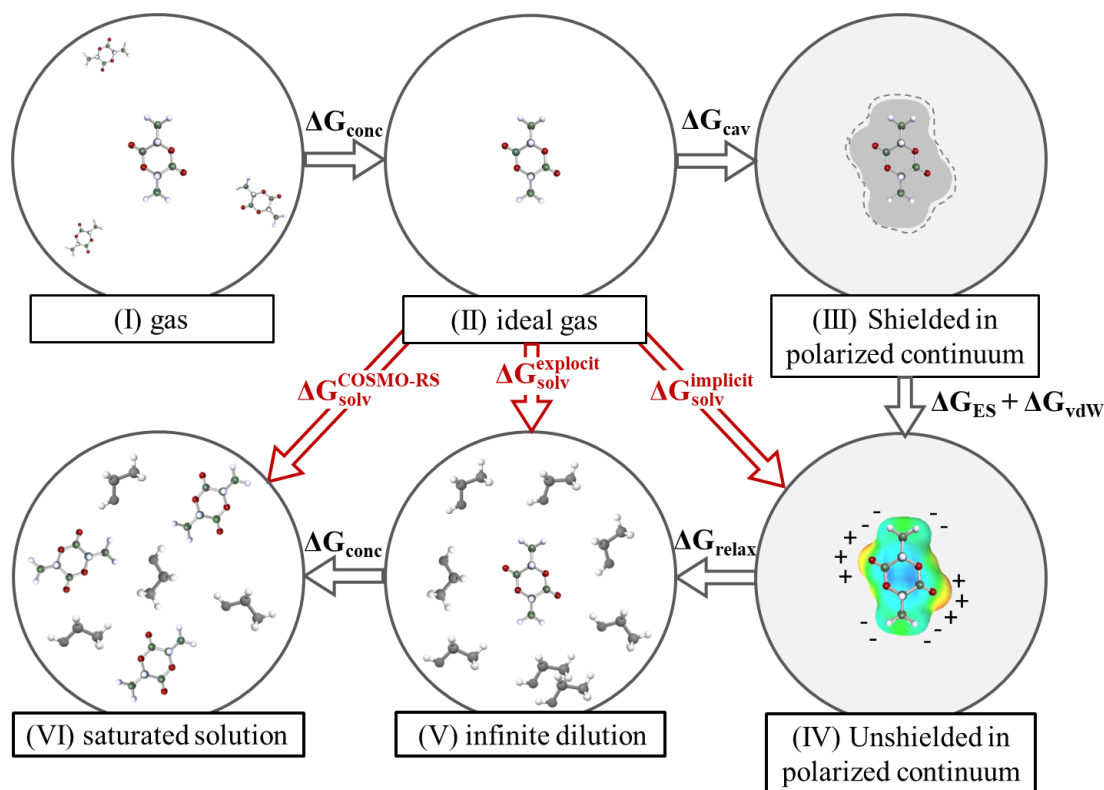
Figure 2.15: Computational approaches to model the Gibbs free energy of solvation, ΔG_{solv}. Explicit models treat the solvent by individual solvent molecules while implicit models approximate the solvent as a continuum. Many computational models are restricted to infinite dilutions. The COSMO-RS model uses statistical thermodynamics to model non-dilute solutions.

Within the sublimation cycle the transition from the gas phase into solution, the Gibbs free energy of solvation, incorporates the solvent specific interaction energies (see eq. (28)). Computational ways to model the solvation free energy can be split up into explicit and implicit models which differentiate mostly in the way the solvent is implemented. In contrary to an explicit description of the solvent by a cluster of independently modelled solvent molecules, implicit models express the solvent as a continuous field with no explicit solvent coordinates (see Figure 2.15). The main contributions are (1) the cavitation energy, ΔG_{cav}, which is the energy needed to form a hole in the solvent for the dissolved molecule; (2) the isotropic as well as anisotropic fixed charge electrostatic interaction energies (e.g. dipole-dipole interactions and hydrogen bonds) and the van der Waals interaction energies, ΔG_{vdW}, and ΔG_{ES}, originating from induction and polarization; (3) the reorientation energy due to relaxation of the solute and solvent molecules, ΔG_{relax}, which possibly change ΔG_{vdW}, and ΔG_{ES}.[125] State of the art explicit and implicit solvation models are summarized in a recently published overview.[70]

The COSMO-RS solvation model

In this work the COSMO-RS model[121] is used for modelling molecular interactions in solution. It is beneficial as it enables the calculation of the solvation terms from both thermodynamic cycles, ΔG^E and ΔG_{solv} (see Figure 2.10). As a consequence, it allows a

consistent evaluation of both thermodynamic cycles. In the following the theoretical background of the COSMO-RS model is briefly given. Additional information can be found in ref. [52].

The so-called Conductor-like Screening Model for Real Solvents (COSMO-RS) combines the implicit COSMO model[124] with statistical thermodynamics of pairwise interacting surface segments from the computed COSMO cavity. It is hereby assumed that the surfaces are in close contact and that 3D geometry information can be neglected. It incorporates eight empirical model as well as element specific parameters, a radius constant and a dispersion constant for H, C, N, O and Cl, which are correlated against experimental data. For parameterization free energy of hydration data as well as experimental vapor pressures and the partition coefficients for octanol/water, benzene/water, hexane/water, and diethyl ether/water have been used.[126] Hence, COSMO-RS can be classified as an extended continuum model which approximates the transition from a polarized continuum to the concentrated saturated solution (step IV to VI in Figure 2.15) using a parameterized statistical thermodynamics model. In order to account for conformational variation in solution the interaction energies of various molecular conformations can be weighted according to a Boltzmann distribution. It should be mentioned that the different conformers are weighted according to their chemical potential in solution and not their ground state ideal gas energies. Hence, the weighting is affected by the molar concentration of the solute in solution and hence as well by solute-solute interactions. The accuracy of COSMO-RS to model solvation free energies for small and medium sized molecules is around 2.1 kJ mol^{-1} when using the TZVPD-FINE parameterization.[127][128] In the standard case the free energy of solvation is calculated assuming an infinitely diluted system. There are some limitations for applications of the COSMO-RS model as well as most above mentioned predictive g^E-models and implicit solvation models. Due to the neglect of explicit solvent coordinates they cannot distinguish between enantiomers. Hence, strong interactions between one enantiomer and the counter enantiomer caused by the three-dimensional geometry cannot be resolved. However, there are some suggestions to incorporate three-dimensional contact information into implicit polarized continuum solvation models that in principle should be able to resolve interactions of enantiomers.[128, 129]

To be able to evaluate computed solvation energies (ΔG_{solv} or ΔG^E) experimental reference data is required. Experimentally determined ΔG_{solv} are rare and often restricted to solvation in water (hydration).[130] Solvation free energies can be calculated from either Henry's law constants which is the partition coefficient between an infinitely diluted solution and the gas phase. Alternatively, it can be recursively calculated from vapor pressures and solubilities and hence the Gibbs free energy of sublimation and solution, respectively, using eq. (28).[130] In the same way experimental ΔG^E can be recursively calculated via eq. (27) the Gibbs energy of melting and solution. If ΔG_{solv} or ΔG^E are recursively determined from measured solubilities they are related to the saturated solution and are thus not necessarily equal to calculations at infinite dilution (see Figure 2.15).

2.7 Computational details

The previous section 2.6 provided the theoretical background to the computational methods use in this work. In this section general details to the computational methods are summarized. If required, additional details are given directly in the related subsections of Chapter 4 "Results and Discussion".

2.7.1 Gas phase energies and vibrations

If no three-dimensional information on the molecular structure was available 2D representations of the molecular structure have been used, so-called SMILES (Simplified Molecular-Input Line-Entry System)[131]. The isolated (ideal gas phase) molecular structures were geometry optimized using TURBOMOLE (V6.5-V7.1)[132]. Def2-type basis sets by Weigand and Ahlrichs[133] and in most cases the B-P86[134, 135] and PBE[136] density functional have been used. They have been corrected (if not further specified) with the 'D3'[137] dispersion correction. Calculations have been accelerated using the resolution of identity approximation[138]. Harmonic molecular vibrations were calculated on top of the optimized structures in the RRHO approximation using the *aoforce*-module in TURBOMOLE. If imaginary frequencies were obtained the molecular structure was re-optimized. The thermodynamic functions have been calculated using the *freeh*-module as implemented in TURBOMOLE. This uses the harmonic vibrational frequencies from the *aoforce*-module for evaluating the ideal gas thermodynamic functions via the RRHO approximation according to Table 2.2.

2.7.2 Crystal lattice energies and vibrational frequencies

Lattice energies, E_{latt}, have been determined via eq. (42). E_{latt} requires the calculation of the ideal gas energies, E^{isg}, and the average energy of a molecule within the unit cell, E^{iss}/N, where N is the total number of molecules in the unit cell (see Figure 2.3). It is essential that both energies are calculated in the same level of theory. Sublimation thermodynamics at temperature other than 0 K (ΔH_{subl}, ΔS_{subl} and ΔG_{subl}) additionally incorporate thermal corrections according to eqs. (43) and (44). They require the calculations of molecular and lattice vibrational frequencies. In the following, all computational methods that have been used in this work are presented.

The riper framework

For the computation of lattice energies, E_{latt}, periodic DFT calculations are performed using the riper module within TURBOMOLE software package (V7.1)[139]. The riper module is an implementation of Kohn-Sham DFT using Gaussian-type basis functions that can compute periodic systems in three dimensions. A detailed description of its implementation is provided in refs [140, 141]. Experimental unit cell geometries were taken from literature and are not computationally optimized. For the periodic DFT calculations

as well as the corresponding ideal gas energies def2-type basis sets by Weigand and Aldrichs[133] and the B-P86[134, 135] and PBE[136] density functionals have been. They have been corrected (if not further specified) with the "D3"[137] dispersion correction. Dispersion corrections are especially relevant for the computation of crystalline solid state structures and lattice energies.[142] Thermal corrections to the ground state energies cannot be calculated within the riper framework.

The ψ_mol model

All energies within the ψ_{mol} model have been determined within a collaboration with Professor Sarah L. Price, Rebecca Hylton and Jan Gerit Brandenburg from the Physical Chemistry Section at University College in London. Additional information on the computational method is given in the electronic supplementary information of ref. [41].

lattice energies have been determined using the *CrystalOptimizer* algorithm[143] which refines the crystal structure by a distributed multipole model for the intermolecular electrostatic forces while allowing any torsion angles that have been determined to be flexible to change in response to the crystal packing forces to minimize the lattice energy. The intramolecular energies, ΔE_{intra}, (eq. (42)) were evaluated using Gaussian 09[144]. The charge densities are subsequently analysed by GDMA to give the distributed multipoles.[145, 146] Those are used in combination with an empiric model for the repulsion-dispersion term in order to calculate the intermolecular lattice energy, E_{inter}, (eq. (42)) using DMACRYS.[89] Temperature effects to the static crystal lattice were calculated from the Γ-point $k = 0$ phonon modes[147] using the DMACRYS[89] model. The isolated molecular vibrations were calculated at the PBE/def2-TZVP level of theory using the D3 dispersion correction[137] as described in section 2.7.1. As the molecular vibrations and lattice vibrations are treated to be independent, a combination of a Debye-Einstein model can be used to model the Helmholtz free energy of the system.[148] As thermal expansion is neglected the same model directly gives the thermal Gibbs energy contributions of the crystal by eq. (56).

$$\Delta G_{vib}\left(T\right) = k_B T \sum_i \ln\left[1 - e^{-\frac{\hbar\omega_{E,i}}{k_B T}}\right] + k_B T \sum_j \ln\left(1 - e^{-\frac{\hbar v_i}{k_B T}}\right)$$

$$+ 3k_B T \ln\left[1 - e^{-\frac{\hbar\omega_D}{k_B T}}\right] - k_B T \frac{3}{\left(\hbar\omega_D / k_B T\right)} \int_0^{\hbar\omega_D/k_B T} \frac{t^3}{e^t - 1} dt \tag{56}$$

Within eq. (56) the $i = 3 ... 6Z\text{-}3$ (Z is the number of molecules within the unit cell) optic frequencies, $\omega_{E,i}$, are modelled with an Einstein model as well as the $j = 3 … 6N\text{-}3$ (N is the number of atoms in the molecule) molecular vibrational frequencies, v_i. A Debye model is used to account for the acoustic modes by using one extrapolated Debye cut-off frequency, ω_D. The last part of eq. (56) is the Debye function which is integrated from 0 to $\hbar w_D/kT$. As molecular and lattice vibrations are decoupled, the zero-point energy difference between the gas and the solid, ΔE_{ZPE}, can be calculated from optic lattice vibrational frequencies ($\omega_{E,i}$) and the Debye cut-off frequency, ω_D, via (57):[148]

$$\Delta E_{ZPE} = \frac{N_A}{N} \left(\frac{1}{2} \sum_{i>3} \hbar \omega_{i,E} + \frac{9}{8} \hbar \omega_D \right) \tag{57}$$

Eq. (56) together with eq. (57) and the ideal gas translational and rotational enthalpy and entropy contributions from Table 2.2 gives the overall Gibbs energy correction, ΔG_{corr}, to the lattice energy within eq. (43) according to eq. (58) (N = number of molecules in the unit cell; N_A = Avogadro number).

$$\Delta G_{corr} = -\Delta E_{ZPE} + N_A k_B T - T \left(S_{trans}^{ig} + S_{rot}^{ig} \right) - \Delta G_{vib} N_A / N \tag{58}$$

The isochoric heat capacities can be separately calculated via eq. (59) where ω_i comprises all optic lattice ($\omega_{E,i}$) and all molecular vibrational frequencies (v_i) while (ω_D) is the extrapolated Debye cut-off frequency.[149]

$$C_V^s(T) = k_B \sum_i \left(\frac{\hbar \omega_i}{k_B T} \right)^2 e^{\frac{\hbar \omega_i}{k_B T}} \left[e^{\frac{\hbar \omega_i}{k_B T}} - 1 \right]^{-2} +$$

$$+ \frac{36 k_B}{(\hbar \omega_D / k_B T)^3} \int_0^{\hbar \omega_D / kT} \frac{t^3}{e^t - 1} dt - 9 \frac{\hbar \omega_D}{T} \left[e^{\frac{\hbar \omega_i}{k_B T}} - 1 \right]^{-1} \tag{59}$$

The ψ_{crys} model

All energies within the ψ_{mol} model have been determined within a collaboration with Professor Sarah L. Price, Rebecca Hylton and Jan Gerit Brandenburg from the Physical Chemistry Section at University College London. A more detailed description is given in the ESI of ref.[150].

The computations were conducted with a developer version of the CRYSTAL14 program.[151] which can exploit full point and space group symmetry of the unit cell.[152] The semi-empirical HF-3c[153, 154] method is used in combination with the "D3-BJ"[137, 155] dispersion correction while basis set superposition errors are and basis set incompleteness effects are corrected by gCP[156, 157] and SRB[153], respectively. Vibrational frequencies from HF-3c are globally scaled by 0.86 as common for Hartree-Fock methods and recommended in literature.[153] Heat capacity calculations require integration over all phonons using the phonon density of states $F(\omega)$ and a numerical integration over the Brillouin zone at each temperature:

$$C_V^s(T) = k_B \sum_{k,i} \left(\frac{\hbar \omega_{k,i}}{k_B T \left(\exp\left(\frac{\hbar \omega_{k,i}}{k_B T} \right) - 1 \right)} \right)^2 \exp\left(\frac{\hbar \omega_{k,i}}{k_B T} \right) \tag{60}$$

The zero-point energy of a molecule in the crystal is given by eq. (61).

$$E_{ZPE}^s = \frac{N_A}{N} \sum_{k,i} \left(\frac{\hbar \omega_{k,i}}{2} \right) \tag{61}$$

Within the ψ_{cry} the Gibbs free energy of the crystalline solid is related to the phonon density of states by equation eq. (62) (N = number of molecules in the unit cell; N_A = Avogadro number).

$$G^s(T) = \frac{N_A}{N} \sum_{k,i} \left(\frac{\hbar \omega_{k,i}}{\exp\left(\frac{\hbar \omega_{k,i}}{k_B T} \right) - 1} \right)$$

$$- \frac{N_A T}{N} \sum_{k,i} \left(\frac{\hbar \omega_{k,i}}{T\left(\exp\left(\frac{\hbar \omega_{k,i}}{k_B T} \right) - 1 \right)} - k_B \ln\left[1 - \exp\left(-\frac{\hbar \omega_{k,i}}{k_B T} \right) \right] \right) \tag{62}$$

Eq. (62) together with zero-point energies of the ideal gas and of the crystal (eqs. (53) and (61)), as well as the ideal gas enthalpy and entropy contributions from Table 2.2 gives the overall free energy correction, ΔG_{corr}, to the lattice energy by eq. (63):

$$\Delta G_{corr} = \left(E_{ZPE}^{ig} - E_{ZPE}^s \right) + H^{ig} + TS^{ig} - G^s \tag{63}$$

The mixed "exp/theory" model

In order to replace computed solid-state heat capacities with experimental $C_{P,exp}^S$, a mixed "exp/theory" model can be constructed. This combines numerical integrations of the experimental solid-state heat capacities with calculated gas phase heat capacities (see section 2.7.1) to quantify the heat capacity corrections within eq. (44). For integrating experimental solid-state heat capacities they were extrapolated from the lowest measurement point to 0 K using Debye's cubic law, $C_P = A \cdot T^3$. Finally, the heat capacities are integrated numerically from 0 K to 298 K using spline functions using MATLAB (Mathworks®). The "exp/theory" method has to be combined with calculated zero-point energies as well as lattice energies to calculate ΔG_{subl}.

This has been done within section 4.3 where the "exp/theory" method is combined with the aforementioned ψ_{mol} and ψ_{crys} in order to evaluate experimental heat capacities of lactide, naproxen and 3ClMA. In case of naproxen and 3ClMA experimental heat capacities are not completely available in the full temperature range. To close the temperature gap between the (later discussed) low temperature DHPC measurements and high temperature DSC measurements, the heat capacity data was linearly interpolated between 200 K and 300 K. Finally, the heat capacities were integrated numerically from 0 K to 298 K. The resulting enthalpy was subtracted from the thermal corrections of the ideal gas which gives a heat capacity related thermal correction H_{th} and $T\Delta S_{subl}$. They

were combined with the ψ_{mol} and ψ_{crys} zero-point energies to calculate sublimation thermal corrections according to eq. (44). When further combined with the lattice energies, the sublimation enthalpies and sublimation free energies of the ψ_{mol} (exp/theory) and ψ_{crys} (exp/theory) method can be calculated according to eq. (43).

Calculation of sublimation thermodynamic from experimental solubilities

As an alternative "experimental" reference quantity, sublimation enthalpies were calculated from experimental solubility data via the sublimation cycle (see (28))). This results in a sublimation Gibbs energy of $\Delta G_{subl,solub} = -RT \ln x_{exp} - \Delta G_{solv}$ and a sublimation enthalpy of $\Delta H_{subl,solub} = -RT \ln x_{exp} - \Delta G_{solv} + T\Delta S_{subl}$. The entropy of sublimation is obtained from integrals of the experimental solid state and calculated ideal gas C_P/T from 0 K to 298 K. As a consequence, they are equivalent to the sublimation entropy of the aforementioned "exp/theory" method. The Gibbs free energy of solvation ΔG_{solv} was calculated with the COSMO-RS model as described in the following section 2.7.3.

2.7.3   Solution thermodynamics

This section gives computational details for calculating ΔG^E and ΔG_{solv} with the COSMORS model. The theoretical framework has been described before in section 2.6.6. The excess Gibbs free energy of mixing (see (36)) and the Gibbs free energy of solvation (see (45)) were calculated using the COSMO-RS[121, 126] model within the COSMOthermX program (version C30_1301) from COSMOlogic GmbH & Co KG. In all cases the BP_TZVPD_FINE_HB2012_C30_1301 (TZVPD-FINE) parameterization was used. The TZVPD-FINE method is based on a COSMO single-point calculation in TURBOMOLE (V6.5)[139] , using the B-P86/def2-TZVPD level of theory on top of a COSMO calculation using the B-P86/def-TZVP level of theory. This works solvation free energies ΔG_{solv} are calculated in the bar/mol reference state system (see section 2.5.3). In case the molecular structure of the solute is flexible, energy contributions of selected low energy conformations are weighted according to a Boltzmann distribution (eq. (64)); where E is the ground-state COSMO energy of the molecule j which is part of the conformational ensemble k. As the chemical potential of j in solution, μ_j^l, contributes to the weighted overall chemical potential of j, π_j^l, the solution concentration as well as the solvent affects the conformational weighting.

$$\pi_j^l = \frac{\exp\left(-\dfrac{E_j + \mu_j^l}{k_B T}\right)}{\sum_k \exp\left(-\dfrac{E_k + \mu_k^l}{k_B T}\right)} \tag{64}$$

Conformational treatment is of special importance if there are multiple molecular conformations within a small energy window that have significantly different surface partial charges (e.g. if intramolecular hydrogen bonding occurs). An iterative procedure

has been used to calculate the energy differences between an infinite solution and a concentrated solution. Hereby, the concentration of the solute in the solution is at first calculated using the Gibbs energy solvation at infinite dilution, $\Delta G_{solv,inf}$. In a second step the solvent composition is adjusted according to the calculated fractions from the previous step. As a result, the subsequently calculated solvation terms incorporate binary surface interactions energies between the solute and the solute, so-called solute-solute interactions. These steps are repeated until the calculated mole fractions in solution converge. This iterative procedure is implemented within the COSMOthermX program (version C30_1301) for the calculation of the activity coefficient and thus ΔG^E and has been separately adapted for the computation of ΔG_{solv}.

2.7.4   Implementation of the sublimation and melt cycle

Within this section, a general implementation routine of the two thermodynamic cycles is presented. As discussed within section 2.7.3, the solvent specific thermodynamic quantities of the two cycles, The Gibbs energy of solvation ΔG_{solv} as well as the excess Gibbs energy of mixing ΔG^E, are both calculated within the COSMO-RS framework. However, in contrast to the melt cycle which relies on the experimental determination of the melting temperature and enthalpy by e.g. DSC (see section 3.2.5) the sublimation cycle is based on an exclusively theoretical approach. It combines periodic DFT and calculated molecular and lattice vibrations (see section 2.7.2) in order to calculate ΔG_{subl} using exclusively first-principle methods. A flow chart of both thermodynamic cycles is illustrated within Figure 2.16.

The sublimation cycle is accessible using two input quantities, the molecular structure and the unit cell parameters of the crystal structure. Molecular structures are available from the Simplified Molecular-Input Line-Entry System (SMILES)[131] which are 2Drepresentations of the molecular structure. Unit cell dimensions of the crystal structure and the atomic coordinates of the molecules within the unit cell are taken from experimental Crystallographic Information Files (CIF) which originate from experiment. The main steps from determining the solubility from these input parameters via the sublimation cycle is marked in blue in Figure 2.16.

The ground state energy, E^{isg}, of the lowest energy molecular conformation is determined within a conformational screening. Depending on the number of rotatable bonds this can be laborious process. Together with the total energy of the optimized crystal unit cell, E^{iss}, the lattice energy, E_{latt}, is calculated via eq. (42). To calculate the effect of temperature to the ground state energies, solid-state heat capacities have to be calculated via the lattice and molecular vibrational frequencies, alternatively, they can be determined by experiment. For determining the ideal gas thermal energies, the molecular vibrational frequencies can be used within the RRHO approximation (see Table 2.2). Several methods have been used in this work to calculate the ground state energies and thermodynamic functions which are presented in section 2.7.2. Summarized, the ideal gas and crystalline solid thermal corrections within eq. (44) together with the lattice energy give the sublimation free energy, ΔG_{subl}, via eq. (43).

The melt cycle takes significantly less steps to access the Gibbs energy of melting, ΔG_{melt}. It uses the melting properties, T_{melt} and ΔH_{melt}, which can be determined by DSC, in case enough crystalline sample substance is available which does not decompose before melting. ΔG_{melt} (T_{melt}) can be optionally corrected to solution temperature using eq. (33). This requires the heat capacity differences between the solid and the melt to be experimentally determined or approximated by an empiric model[60, 83, 84].

For both thermodynamic cycles the COMSO-RS model is used to calculate the solvation thermodynamics. Selected low energy molecular conformations are weighted according to eq. (64). If available solvent molecular structures and surface charge distributions can be taken from the COSMOtherm data base. The solvation free energy, ΔG_{solv}, and the excess free energy of mixing, ΔG^E, are first calculated at infinite dilution using the COMSO-RS model. They are subsequently combined with the aforementioned ΔG_{subl} and ΔG_{melt}, to calculate solution free energy, ΔG_{sol}, via the sublimation and melt cycle via eqs. (27) and (28), respectively. Consequently, the solubility can be calculated via eqs. (10) or (13). Concentration dependency of the solvent specific terms, ΔG_{solv} and ΔG^E, can be calculated by an iterative procedure as described in section 2.7.3.

The two thermodynamic cycles have been investigated in detail for two non-chiral model substances as well as three representatives of chiral compound forming systems. All results are presented and discussed in the following chapter 4 "Results and Discussion".
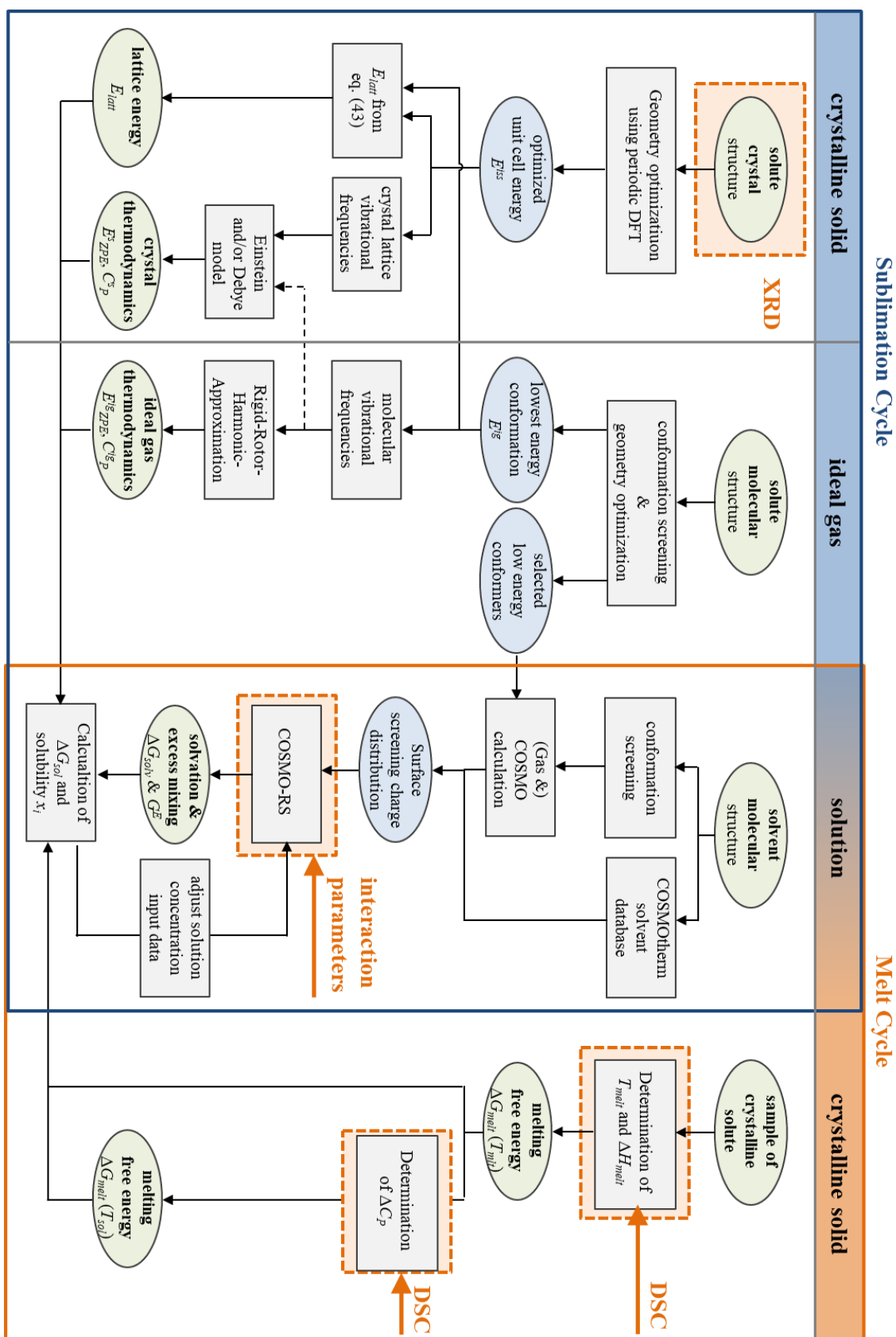
Figure 2.16: Illustration of the computational implementation of the melt as well as the sublimation cycle for solubility calculation.

3   Experimental Methods

This chapter provides detailed insight into the experimental methods that have been used within this work. Field of application is the experimental investigation of the phase transition thermochemistry of the three chiral molecules lactide, naproxen and 3chloromandelic acid. Furthermore, specifics on origin and purity of the materials which have been used w the experiments are briefly given. If required, additional case specific experimental details are given directly in the respective subsections of Chapter 4 ("Results and Discussion").

3.1   Materials

Samples of (*S*)-lactide, (*S,S*)-3,6-Dimethyl-1,4-dioxan-2,5-dion, and (*RS*)-lactide, (*S,S-R,R*)-3,6-Dimethyl-1,4-dioxan-2,5-dion, were obtained from Purac Biochem with a purity of > 99.5 % and were used without further purification.

(*S*)-naproxen, (*S*)-(+)-2-(6-Methoxy-2-naphthyl)propionic acid, and (*RS*)-naproxen, (*RS*)-(±)-2-(6-Methoxy-2-naphthyl)propionic acid, were purchased from TCI-Europe with specified purities of 99 % and 98 %.

(*RS*)-3ClMA, (*RS*)-3-chloromandelic acid, has been purchased from Alfa Aesar (purity > 97 %). (*R*)-3ClMA, (*R*)-(-)-3-chloromandelic acid was purchased from Sigma Aldrich (purity > 97 %) and further purified by recrystallization from water.

(*R*)- and (*RS*)-mandelic acid were purchased from Merck with a specified purity > 99 % and used without further treatment.

3.2   Experimental details

3.2.1   Measurements of the solubility and the eutectic composition

Solubilities, x_i, and the eutectic composition in solution, x_{eu}, were measured by means of a classical isothermal method. The experimental setup consisted of a tempered jacketed vessel which was filled with water and a Pt-100 resistance thermometer with a resolution of 0.01 K for ensuring stable equilibrium temperatures. A vial with a stirred (magnetic stirrer) suspension of 5 to 10 ml was equilibrated within the jacketed vessel at a constant temperature (±0.1 K) for 48 h up to 72 h. A minimum of two samples of 1-2 ml of solid free solution were taken using a syringe and a filter (PET - membrane, pore size 45 μm) for determination of the saturation concentration.

The solid phases in equilibrium with the solution were analysed by XRPD for structural clarification (see section 3.2.3). When measuring the eutectic composition in solution, XRPD was further used in order to examine if both the enantiopure and racemic crystals were present in the precipitate.

The extracted solution samples were dried at ambient condition and optionally for 3-5 h in a vacuum oven. Solubilities were calculated from the weight of the solution and the weight of the sample after drying via eq. (1) or by calibrated HPLC in cases where solubilities were low. When measuring the eutectic composition, the enantiomeric ratio of mixtures of the two enantiomers has been determined by HPLC method. Further details are given in the subsequent section 3.2.2.

3.2.2   Characterization of liquid phases

High-performance liquid chromatography (HPLC) has been used to either quantify absolute solution compositions in case of low solubilities or to determine the enantiomeric ratio for investigating the enantiomeric purity and when measuring the eutectic composition.

For the chiral discrimination of naproxen a Chiralpak AD-H column (Chiral Technologies) was used in combination with mobile phase consisting of n-Hexane/IPA/TFA in a ratio of 80:20:0.1. The flow rate was 1 ml/min and the temperature 25°C. For naproxen HPLC has been used in order to determine enantiomeric ratios in the frame of measuring the eutectic composition and further when measuring absolute solubilities. Therefore, solution concentration was linearly correlated against the peak area as shown within Figure 3.1.
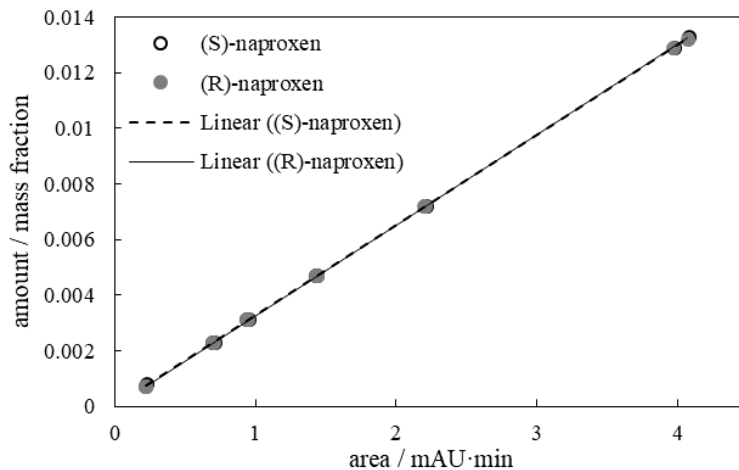
Figure 3.1: Calibration of the concentration of (*S*)- and (*R*)-naproxen in solution using HPLC.

For lactide HPLC has been used in order to determine the enantiomeric purity or in the frame of measuring the eutectic composition. The enantiomeric ratio has been determined from the concentration dependence of the peak areas within the chromatograms. A Chirobiotic T column (Daicel Corporation) has been used along with a mobile phase containing a 80/20 vol% mixture of methanol and ethyl acetate as well as 1% triethylammonium acetate as buffering agent for adjusting a pH-value of 4.02. The flow rate was 0.5 ml·min^{-1} and the temperature 20 °C.

3.2.3   Characterization of solid phases

Crystal forms have been analysed by X-ray powder diffraction (XRPD) in an X'Pert Pro apparatus (PANanalytical GmbH, Germany) using CuK-α radiation and scanning diffraction angles (2θ) from 3-40° with as step size of 0.017° and a duration of 50s.

Solid-state Raman analysis of the powdered crystals was performed with a commercial MultiRAM spectrometer from Bruker, Germany. The system employs a laser beam at 1064 nm. If not further specified, the laser was operated at 500 mW and the analyses were carried out at ambient temperature averaging over 32 scans with a spectral resolution of 1 cm^{-1} between 10 cm^{-1} and 3500 cm^{-1}.

3.2.4   Solution enthalpy

The solution enthalpy measurements were carried out in a C80 calorimeter from Setaram Instrumentation (France). The device consists of two measurement chambers which are both surrounded by a Calvet-type sensor which has been calibrated calorically from the manufacturer using the Joule-effect method. Two identical standard membrane mixing cells have been used for the reaction and reference side. Both measurement cells consist of two chambers which are separated by a 0.05 mm thick Teflon membrane. Weighted crystalline solid was placed into the lower chamber of the reaction cell. The upper chamber of both the reaction and reference cell was filled with the solvent in the same amount. The sample and the solvent were weighted with a balance with an accuracy of ±0.01 mg.

After an initial equilibration period of around 2 h both Teflon membranes were pierced through simultaneously and the solution was stirred by hand for around 3 min on both sides. To ensure complete dissolution the cells were stirred a second time after another 5 min. If no thermal reaction was detected complete dissolution was assumed. Additionally, the vessels were checked after the experiment for non-dissolved substance. The differential heat-flux was recorded as a function of time and integrated to give the heat change during mixing. The thermal effect of the stirring was determined to be smaller than 0.1 $kJ \cdot mol^{-1}$ and was neglected in the following. Figure 3.2 depicts a characteristic thermal response for the dissolution of the enantiopure and racemic crystalline solid of lactide in toluene. The caloric measurements are performed for final concentrations which are significantly lower than saturation concentration but large enough to give an accurate heat response. To obtain the solution enthalpy at infinite dilution, $\Delta H_{sol,inf}$, several measurements at different concentrations are performed which are then linearly extrapolated to infinite dilution (x = 0) using a linear least squares regression. Concentrations were changed by varying the amount of dissolved solute while keeping the amount of solvent constant in all measurements. The accuracy of the system was tested with KCl (Merck, purity > 99.99%) in deionized water at 30°C. Measurements were performed in triplicate and gave a solution enthalpy of 16.34±0.33 $kJ \cdot mol^{-1}$ which is in agreement with data from literature[158] which is $\Delta H_{sol,inf}$ (303.15 K) = 16.42 $kJ \cdot mol^{-1}$. Furthermore, it has been shown before that solution enthalpies of organic crystals can be measured within the C80 calorimeter with high accuracy.[63]
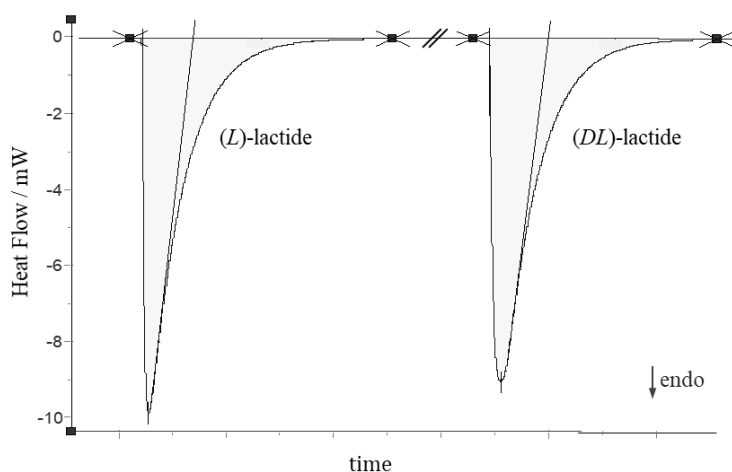
Figure 3.2: Caloric measurement of the dissolution of 30mg of (*L*)-lactide (left) and (*DL*)-lactide (right) in 2000 mg of toluene.

3.2.5   Melting properties

Thermodynamics of fusion were measured using a Setaram DSC 131. Temperature and enthalpy calibration are regularly performed on this device using indium, tin, and lead reference material. Samples with typical masses of ~10 mg (±10 μg) were weighed into Al-pans (30 μl, purchased from Setaram), closed with a lid, and heated with a constant heating rate of 0.5 to 2 K·min^{-1} while purging with highly pure helium (99.999 Vol. %) at a constant flow rate of 35 mL min^{-1}.

Melting temperatures have been determined from the extrapolated initial (onset) temperature which is determined from the intersection of the tangent of the peak with the extrapolated baseline using the accompanying software from Setaram. Melting enthalpies have been determined from the integrated areas of the melting peaks using either a linear integration routine or a sigmoid integration routine in case of a shift of the baseline before and after melting. For measuring the binary melt phase diagram of mixtures of two enantiomers the corresponding solidus temperatures were determined via the onset temperature while the liquidus temperatures (see Figure 2.6) were determined from the maximum peak temperature. More detailed information on the determination of the binary melt phase diagram of chiral substances is given in ref. [159].

3.2.6   Sublimation thermodynamics

Sublimation vapor pressures were measured in the frame of a collaboration with Prof. Sergey P. Verevkin and Vladimir N. Emel̀yanenko from the Physical Chemistry department of the University of Rostock. Vapor pressures were measured using the transpiration method, which was described before in literature.[160, 161] About 0.5 g of solid sample was dissolved in acetonitrile and mixed with small glass beads in a glass beaker. The solvent was slowly evaporated while stirring producing uniformly covered glass beads with crystalline solid. A well-defined nitrogen gas stream was passed through a

thermostated ($\pm$0.1 K) U-shaped saturator filled with the glass beads and the sublimated material was collected in a cold trap. The amount of condensed sample was determined by weighing with microbalances of 0.1 mg resolution. The absolute vapor pressure p_i of substance i was calculated from the amount of the product collected within a definite period of time per Volume $V = V_{N2} + V_i$ at temperature T using ideal gas law ($p_i V = m_i R T$). Uncertainties of absolute vapor pressures measured by the transpiration method were estimated to in between 1% and 3% as described in detail in literature.[161]

Additionally, enthalpies of sublimation were measured in the same collaboration by TGA with a Perkin Elmer Pyris 6 calorimeter. Before TGA measurement about 70 mg of a sample was melted and cooled inside a platinum crucible and analysed by FT-IR to ensure that the sample did not decompose. Isothermal TGA curves were measured just below melting temperature at a nitrogen flow rate of 200 mL·min^{-1} using the same crucible with the recrystallized sample. Measurements of the mass loss rate were performed in a few consequent series of steps of increasing and decreasing temperature. The detailed procedure was described elsewhere.[162]

3.2.7   Heat capacities

Low-temperature heat capacities of the crystalline solid were measured by means of direct heat pulse calorimetry (DHPC) from 2 to 200 K. A commercially available relaxation calorimeter has been used in cooperation with Prof. Cornelius Krellner and Natalija van Well from the Institute of theoretical Physics at the Goethe-University in Frankfurt, the Physical Property Measurement System (PPMS) from Quantum Design. The PPMS provides a high-vacuum environment, around 10^{-8} bar. For the measurement the sample powder is pressed to a pellet and placed on a 3 mm x 3 mm measurement platform. Thermal grease (Apiezon® N) is used to enhance thermal coupling between the pellet and the platform as described in literature.[163] Figure 3.3 (left) shows the pressed pellet and the measurement platform of the PPMS system. The platform has a weak thermal link with known thermal resistance to a constant heat sink. Further technical details of the system are given in detail elsewhere.[164]

The temperature response of a discrete heat pulse of heating and subsequent relaxation is evaluated using an analytical curve-fitting procedure which includes two time constants, τ_1 and τ_2.[165] In the case of ideal thermal coupling τ_2 becomes zero. In all cases however, thermal coupling is slightly less than 100 % and both time constants are used in the fitting procedure. An example response from a discrete heat pulse is depicted within Figure 3.3 (right). One experiment comprises an 'addenda run' where only the platform and the thermal grease is measure and a second 'sample run' where the heat capacity of the whole ensemble is observed. The net heat capacity of the sample is then given by the difference between both measurements.
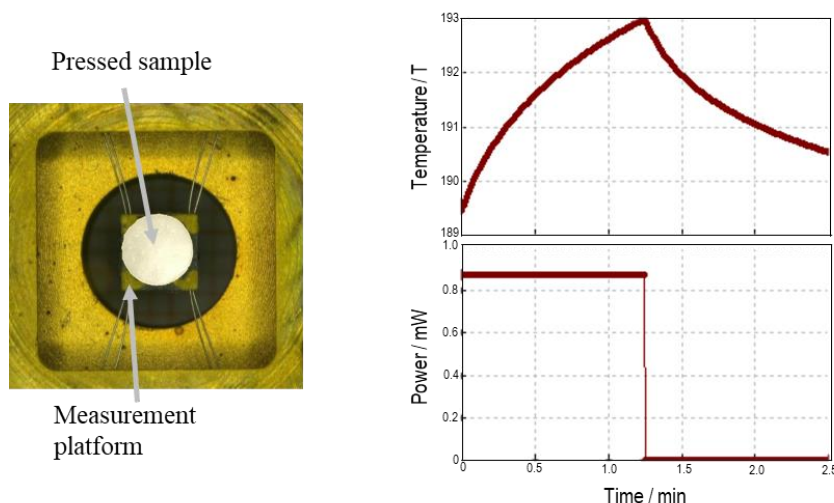
Figure 3.3 (left) Pressed tablet of the crystalline sample on the measurement platform of the PPMS. (right) Temperature response of the system from a discrete heat pulse consisting of heating and subsequent relaxation.

Heat capacities above room temperature were measured using a DSC 111 calorimeter from Setaram which operates with a Tian-Calvet sensor.[166] Temperature calibration was conducted using indium, tin and lead as reference material. Since the Calvet detector was absolutely calibrated calorically by Joule effect, the heat capacity was not measured against a reference material. The calorimetric resolution of the instrument is 0.4 µW, and the detection limit 5–15 µW. Measurements were performed using the temperature step method while purging with highly pure helium at a flow rate of 35 ml·min^{-1}. Samples with typical masses of 60 to 80 mg ($\pm$10 µg) were weighted into aluminium crucibles (150 µl, purchased from Setaram) and closed with an aluminium lid. The heat capacity measurements were performed at 10 K temperature steps, a heating rate of 5 K min^{-1} and subsequent equilibration time of 600 s. One experiment comprises two consecutive runs measuring the empty crucible (blank run) and subsequently the crucible containing the sample (sample run). The net heat capacity of the sample is then calculated from the difference between both measurements using the accompanying software from Setaram. A typical measurement routine is depicted within Figure 3.4 showing the blank run, the sample run, the temperature of the sample during the sample run and the resulting heat capacities. Sapphire and benzoic acid were used as calibration standards. Average deviations to published data were 1.4% for sapphire[167] and 2.6% for benzoic acid[168].
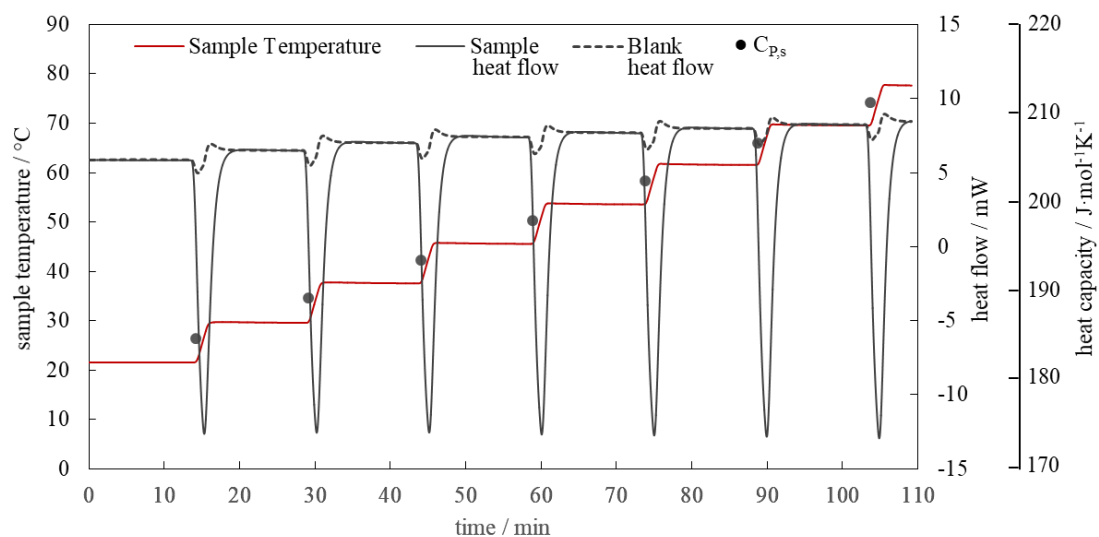
Figure 3.4: Experimental routine of the high temperature heat capacity measurements using the step-wise method. Exemplarily, measurement results for crystalline (*RS*)-mandelic acid are shown.

4   Results and Discussion

This chapter comprises all experimental and computational results. In each sub-section results are first presented and discussed and subsequently summarized to draw conclusions. Parts of the computational work has been compiled within a cooperation with Prof. Sarah L. Price, Dr. Rebecca Hylton and Dr. Jan Gerit Brandenburg from the Physical Chemistry Section at University College London. In the course of this project, low-temperature heat capacities have been measured at the Institute of theoretical Physics at the Goethe-University in Frankfurt in cooperation with Prof. Cornelius Krellner and Dr. Natalija van Well. Furthermore, measurements of the sublimation thermodynamics have been conducted at the Physical Chemistry department at University of Rostock in cooperation with Prof. Sergey P. Verevkin and Dr. Vladimir N. Emel'yanenko. All results that were published beforehand in the frame of this work can be found in refs.[41, 44, 150, 169, 170].

In **section 4.1 and 4.2** the melt and the sublimation cycle are used for solubility prediction of two well-studied model substances, naphthalene and benzoic acid. Subsequently, the accuracy of state-of-the art electronic structure methods to calculate the dominant energy contribution within the sublimation cycle, the lattice energy, is evaluated.

In **section 4.3** the melting and sublimation phase transition is studied for chiral lactide, naproxen and 3ClMA using experiment and theory. The numerous energy contributions to Gibbs free energy of sublimation are calculated using *ab-inito* quantum chemistry methods. Calculations are accompanied by broad experimental investigations of the melting properties, the sublimation vapor pressures and sublimation enthalpies as well as the solid-state heat capacities of the racemic compound and the enantiomer.

In **section 4.4 and 4.6** the two thermodynamic approaches are used to calculate solubilities and their temperature dependence for the three chiral molecules in a variety of pure and mixed solvent systems. Furthermore, the energy differences between the enantiomer and the racemic compound are used in **section 4.5** to estimate the eutectic composition in solution and its temperature dependence. All calculations are compared to experimentally determined solubilities, the solution enthalpies as well as the specific eutectic composition in solution.

4.1   Solubility prediction of non-chiral model substances

Within this section, the melt and the sublimation cycle (eqs. (27) and (28)) are evaluated for their applicability to calculate solubilities of two well-studied reference substances, namely naphthalene and benzoic acid, in a variety of organic solvents. Main focus is to compare the accuracy of the two thermodynamic cycles and to evaluate relevance and accessibility of the various energy contributions to the solution free energy.

4.1.1   Experimental reference data

To be able to assess the sources of computational errors, experimental thermodynamic reference quantities are required. For naphthalene as well as benzoic acid a wide range of and reliable experimental data on solubilities, melting and sublimation as well on solid state heat capacities is available in literature.

The Gibbs free energy of sublimation, ΔG_{subl}, has been calculated for naphthalene and benzoic acid from published experimental sublimation vapor pressures from refs. [171, 172] via eq. (38). These are recommended averaged values of several independent studies and both give particularly reliable ΔG_{subl} with an uncertainty of ± 0.1 kJ·mol^{-1} (see Table 4.1). Experimental sublimation enthalpies have been studied extensively for both naphthalene and benzoic acid resulting in approximately 50 published values for both molecules between 1925 until today.[173] However, the sublimation enthalpy is function of temperature and the various literature data[173] was determined at different temperatures or even lacks in information about this essential detail. For this work the ten most recent fully specified sublimation enthalpies from ref. [173] have been extrapolated to 298 K via eq. (41) using experimental solid state heat capacities[168, 174] and calculated ideal gas heat capacities using a mixed "exp/theory" method as introduced in section 2.7.2. Further details on the calculation of the ideal gas thermodynamics are given in the subsequent section where they are used for correcting the calculated lattice energies from zero Kelvin to 298 K (see Table 4.3). Obviously, the sublimation free energies are more reliable in terms of the experimental error compared to the sublimation enthalpies making ΔG_{subl} an especially reliable experimental reference quantity.

Table 4.1: Experimental melting and sublimation thermodynamic quantities. Averaged sublimation enthalpies have been taken from ref.[173]. Sublimation free energies have been determined from experimental sublimation vapor pressures from refs. [171, 172] via eq. (38).

	ΔH_{subl}	$T\Delta S_{subl}{}^a$	$\Delta G_{subl}{}^b$	T_{melt}	ΔH_{melt}	$\Delta G_{melt}{}^c$
	kJ·mol^{-1}	kJ·mol^{-1}	kJ·mol^{-1}	K	kJ·mol^{-1}	kJ·mol^{-1}
naphthalene	73.0 ($\pm$ 1.7)	50.4 ($\pm$ 1.7)	22.6 ($\pm$ 0.1)	354.0 ($\pm$ 1.0)	19.0 ($\pm$ 0.4)	3.0 ($\pm$ 0.1)
benzoic acid	90.6 ($\pm$ 2.9)	56.3 ($\pm$ 2.9)	34.3 ($\pm$ 0.1)	395.0 ($\pm$ 0.7)	17.4 ($\pm$ 1.2)	4.3 ($\pm$ 0.1)

^{a} calculated via $\Delta G_{subl} = \Delta H_{subl} - T\Delta S_{subl}$ where $T = 298.15$ K.
^{b} calculated according to eq. (38) via $\Delta G_{subl} = -RT \ln (p/p_0)$ where $T = 298.15$ K and $p_0 = 1$ bar.
^{c} calculated according to eq. (30) via $\Delta G_{melt} = \Delta H_{melt} (1 - T/T_{melt})$ where $T = 298.15$ K.
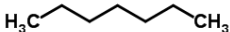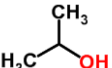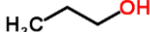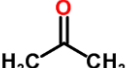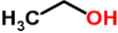
Additionally, Table 4.1 contains the melting temperatures and enthalpies which are required in order to calculate the Gibbs free energy of melting via eq. (30). Precise experimental data from various sources is available in literature[173]. An average value of the ten most recent fully specified values has been taken for this work.

Reliable experimental solubilities are available for both substances in a large variety of

pure and mixed organic solvent systems from the IUPAC Solubility Data Series a series of reviews containing published data for solubilities of gases, liquids and solids in liquids or solids.[175] Unfortunately, most experimental solubility data lack information on the specific polymorphic form which is in equilibrium for a given solvent and temperature. They have been assumed to belong to a single experimental structure which is introduced later in Figure 4.2.

For a comprehensive examination of the accuracy of the COSMO-RS model to determine the excess Gibbs free energy of mixing, ΔG^E, and the solvation free energy, ΔG_{solv}, a set of pure solvents with different polarity have been chosen. Mole fraction solubilities according to eq. (1) have been taken for both substances from refs. [176, 177]. In cases where more than one data point is available, an averaged value was taken. Aqueous solubilities have been taken from refs. [178, 179] as they are missing within the large solubility data series. The experimental solubilities are summarized in Table 4.2, sorted by the polarity of the specific solvent which is expressed by the dielectric constant. They cover a broad spectrum ranging from $x_i = 1.6 \cdot 10^{-6}$ up to $x_i = 0.5$.

Table 4.2: Mole fraction solubilities, x_i, according to eq. (1) from literature of naphthalene[176] and benzoic acid[177] in various organic solvents with different polarity - expressed by the dielectric constant.

Name	Molecular structure	Dielectric constant[180]	Mole fraction solubility of naphthalene	Mole fraction solubility of benzoic acid
Heptane		1.9	0.081	0.012
Cyclohexane		2.0	0.149	0.011
Benzene		2.3	0.297	0.073
1-octanol		10.3	0.126	0.199
2-propanol		18.3	0.045	0.194
1-butanol		17.8	0.066	0.202
1-propanol		20.1	0.0461	0.180
Propanone		21.0	0.226	0.196
Ethanol		24.6	0.034	0.183

Methanol	H₃C—OH	32.6	0.023	0.163
Dimethyl-formide		47	0.281	0.491
Water	H_2O	78.5	$4.1 \cdot 10^{-6}$	$1.6 \cdot 10^{-6}$

4.1.2   Lattice energies and thermal correction

Within this section the determination of the sublimation free energy from periodic DFT in combination with the mixed "exp/theory" method is discussed. The resulting ΔG_{subl} are subsequently used for predicting solubilities via the sublimation cycle. As lattice energies are calculated by DFT for the static crystal lattice and the static ideal gas, zero-point energy as well as thermal enthalpy and entropy corrections are required and will be discussed first. Assuming that the vibrational lattice and molecular modes are decoupled the zero-point energy difference between the crystal and the gas, ΔE_{ZPE}, can be derived from the lattice frequencies as molecular vibrations cancel out. Experimental vibrational lattice frequencies, ν_i, from literature[147, 181] were used to calculate the zero-point energy contribution by $\Delta E_{ZPE} = E_{ZPE}^g - E_{ZPE}^s = -h/2 \sum \nu_i$. The obtained ΔE_{ZPE} (see Table 4.3) is in excellent agreement with published calculated values for naphthalene[147] and benzoic acid[182].
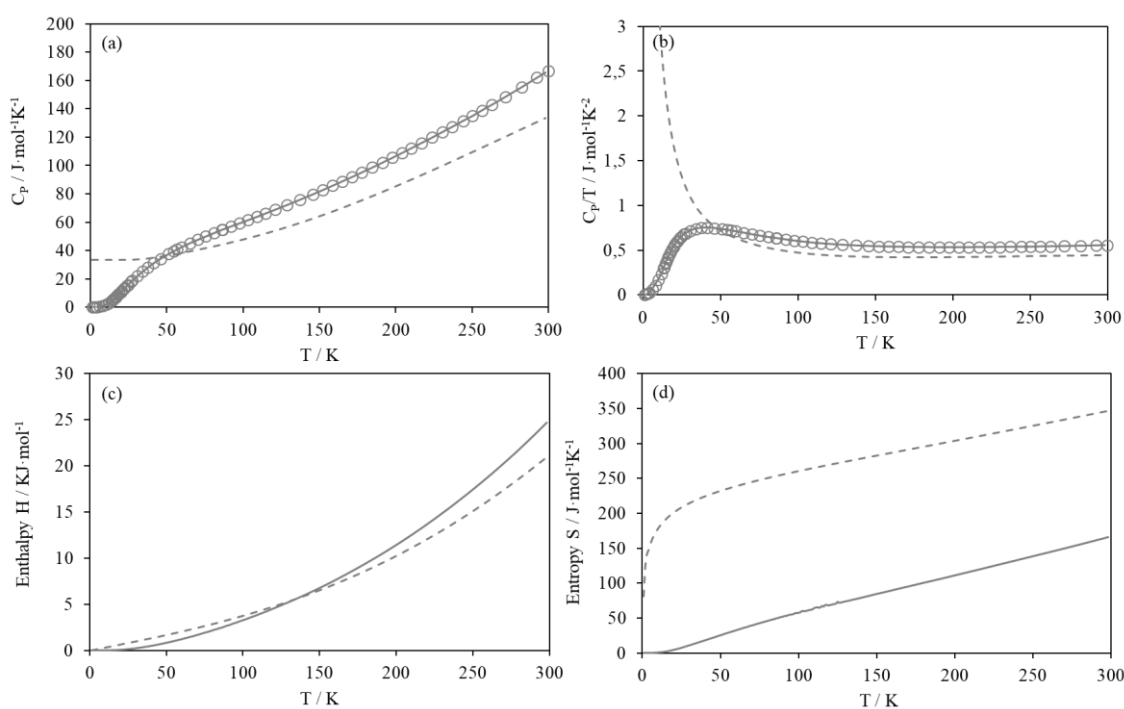
Figure 4.1: Temperature-dependent solid state (experiment[183] - ○; calculations via the "exp/theory"-method - straight line) and calculated ideal gas (dashed line) (**a**) heat capacities C_P and (**b**) C_P/T as well as the corresponding thermodynamic (**c**) enthalpy and (**d**) entropy functions of naphthalene.

Thermal enthalpies, entropies and Gibbs energies are related to the integrals of the heat capacities in the specific state of matter. Integrals of C_P from zero Kelvin give the enthalpy while thermal entropies are related to integrals of C_P/T. Within the mixed "exp/theory" method the experimental solid state heat capacities from literature[168, 183] were interpolated using while ideal gas heat capacities and thermodynamic functions have been calculated via the RRHO (Table 2.2) as described in section 2.7.1 using the def2-TZVP-BP86-D3 level of theory for calculating the harmonic vibrational frequencies. This is exemplarily shown in Figure 4.1 for the crystalline solid and ideal gas of naphthalene in the whole temperature range from 0 K to 298 K.

Integrals of the experimental solid state[168, 174] and calculated ideal gas heat capacities between zero Kelvin and 298 K were combined with the ΔE_{ZPE} to give the final thermal enthalpy correction, H_{corr}, and the sublimation entropy, $T\Delta S_{subl}$, via eq. (44) which are summarized in Table 4.3 for both molecules. There are only minor differences of the calculated H_{corr} to the 4.9 kJ·mol^{-1} of the frequently used $2RT$-approximation (see eq. (55)). The calculated sublimation entropies via the mixed "exp/theory" method are in good agreement with the primary experimental data from measured vapor pressures (Table 4.1) with absolute deviations of 3.3 and 0.4 kJ·mol^{-1} for naphthalene and benzoic acid, respectively. However, when used to calculate solubilities these relatively small errors can affect the predictions accuracy due to the exponential relation within eq. (10).

Table 4.3: Summary of all zero-point, thermal enthalpy and entropy corrections which are required to calculate the sublimation free energy, ΔG_{subl}, via eq. (44).

		Naphthalene	Benzoic acid
1	ΔE_{ZPE}	2.30^a	2.75^a
2	$H^{ig} \pm$ stdev	20.67 ± 0.30^b	21.41 ± 0.29^b
3	$\int C_{P,exp}\, dT$	24.79^c	24.03^c
4	H_{corr}	-6.42 ± 0.30^d	-5.37 ± 0.29^d
5	$TS^{ig} \pm$ stdev	102.91 ± 0.57^b	106.09 ± 0.51^b
6	$\int (C_{P,exp}/T)\, dT$	49.44^c	49.34^c
7	$T\Delta S_{subl}$	53.47 ± 0.27^e	56.74 ± 0.23^e

a Calculated from experimental lattice vibrational frequencies[147, 181] via $\Delta E_{ZPE} = -h/2 \sum \nu_i$. b Average of BP86-, B3LYP- and MO6-def2-TZVP method together with the standard deviation. c Calculated from integrals of the solid-state heat capacities[168, 174]. d Sum of 1, 2 and 3 according to eq. (44). e Sum of 5 and 6 according to eq. (44).

Lattice energies have been determined via eq. (42). Geometry optimizations of the ideal gas molecules as well as of crystalline solid have been performed within the TURBOMOLE software package (V7.1)[139]. Further details are given in section 2.7.2. Calculations have been performed using three GGA type density functionals, B-P86[134, 135], BLYP[135, 184] and PBE[136] as well as the semi-empirical GGA-type B97-D[185]. They are

combined with various Gaussian def2-type basis sets by Weigand and Ahlrichs[133] and the D3 dispersion correction by Grimme et al.[137]. A k-point sampling was performed from k = 1 to k = 21 using uniform k-points in all three dimensions and no significant change for $k > 3$ was observed in test runs for benzoic acid and naphthalene (see Table 7.22 in the appendix). Hence, lattice energies have been calculated using a uniform k-points mesh of k = 3x3x3 for all calculations.

Lattice energies have been calculated for the experimental crystal structures. They contain the necessary information of the dimensions of the unit cell as well as starting atomic coordinates for the periodic DFT calculations. Two representatives of crystal structures of benzoic acid and naphthalene, NAPHTA04[186] and BENZAC02[187], have been used (see Figure 4.2). Details on the unit cell dimensions are given in Appendix Table 7.16.
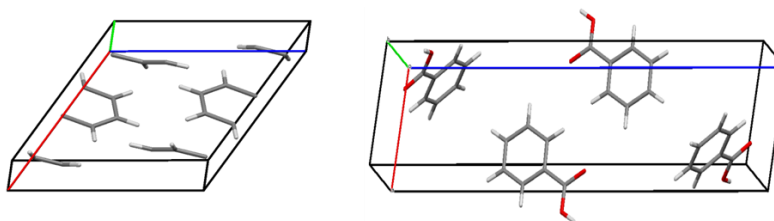
Figure 4.2: Crystal structures of (left) naphthalene – NAPHTA04[186] and (right) benzoic acid – BENZAC02[187].

The molecular crystals differ in the type of molecular interactions that dominate. In case of benzoic acid cyclic hydrogen-bonds between the carboxylic acid groups form strong dimer structures.[96] In contrary, naphthalene forms a layered structure which is dominated by van der Waals interactions.[188]

Sublimation free energies can be determined via eq. (43) from calculated lattice energies when combined with thermal and entropy corrections from Table 4.3. Figure 4.3 (a) and (b) show the absolute deviations of the calculations from the experiment summarized in Table 4.1. All calculations overestimate the sublimation Gibbs energies in comparison to experiment. For both substances (NAPHTA04[186] and BENZAC02[187]) there is a drastic increase in accuracy when using the *split valence triple-zeta* (TZV) basis set (def2-TZVP) over the smaller *split valence double-zeta* (SV) one (def2-SVP). An inclusion of a second polarization term for all hydrogen atoms does not change the overall quality of the calculation. This trend is consistent for all three functionals and slightly larger for benzoic acid. It is related to the strong anisotropic electrostatic interactions of the hydrogen bonds between the valence electrons of the carboxyl groups which are more likely to be affected by basis set superposition errors (BSSE).[189] This issue will be discussed in more detail later on in section 4.2 for a larger set of molecular crystals.

For both molecules, the PBE and the semi-empirical B97-D functional perform best whereas the BLYP functional leads to the largest deviation from experiment. In case of the weakly bound naphthalene, the differences between the functionals are significantly larger than for the hydrogen-bonded benzoic acid. Even though for naphthalene the PBE functional performs best, the semi-empirical B97-D functional gives the best overall performance whereas the BLYP functional leads to the largest deviations to experiment.

For def2-TZVP/B97-D3 deviations are 2.9 kJ mol^{-1} for naphthalene and 1.6 kJ mol^{-1} for benzoic acid. Based on the above, the B97-D method in combination with a def2-TZVP basis set will be used in the following for solubility predictions.
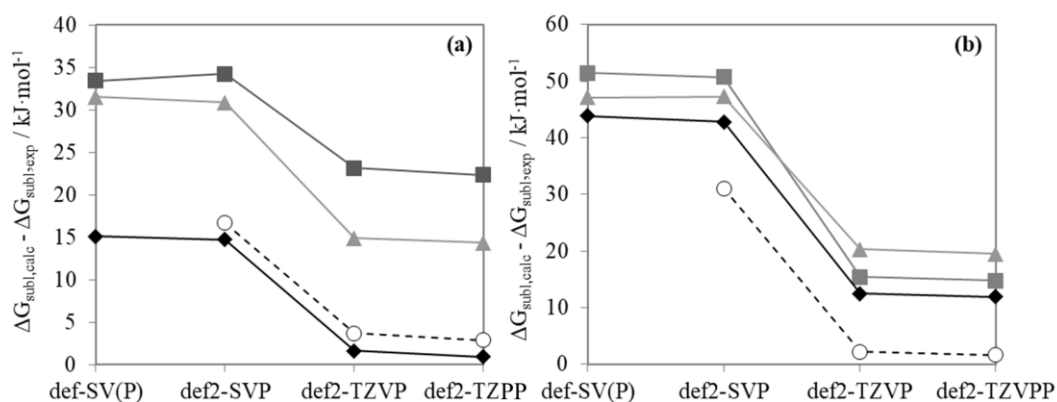
Figure 4.3: Differences in the calculated sublimation Gibbs energies and experiment from Table 4.1 of **(a)** naphthalene (NAPHTA04) and **(b)** benzoic acid (BENZAC02). $\Delta G_{subl,calc}$ combines calculated lattice energies with thermal corrections from Table 4.3. For E_{latt} BLYP (■), B-P86 (▲), PBE (◆) and B97 (○) were used in combination with the "D3" dispersion correction def2-type basis sets with increasing size from left to right.

As the unit cell geometry is not optimized, the quality of the result is depending on the experimental unit cell parameters. Lattice energies of two structurally related experimental unit cell geometries for naphthalene (NAPHTA04[186] and NAPHTA23[190]) as well as benzoic acid (BENZAC01[191] and BENZAC02[187]) give energy difference that are smaller than 1.5 kJ mol^{-1}. Further details are given in Appendix Figure 7.2. These rather minor differences can be minimized when optimizing the unit cell parameters in addition to the molecular geometries. A combined optimization of the unit cell and molecular geometries, however, significantly increases computational times.

4.1.3   Solubility prediction

The experimental melting free energies, ΔG_{melt}, from Table 4.1 and calculated sublimation free energies, ΔG_{subl}, from Figure 4.3 ("exp/theory" + def2-TZVP/B97-D) were combined with the solvent specific excess Gibbs free energy of mixing, G^E, and the Gibbs free energy of solvation, ΔG_{solv} in order to calculate ΔG_{sol} via eqs. (27) and (28), respectively. The resulting ΔG_{sol} from both thermodynamic cycles were used to calculate mole fraction solubilities from Table 4.2 via eq. (10). ΔG^E and ΔG_{solv} have been both determined using the COSMO-RS[121, 126] model in combination with the TZVPD-FINE parameterization. For both cycles an iterative procedure was applied in order to calculate ΔG^E and ΔG_{solv} at saturation concentration (see Figure 2.16). Further information on the calculation of the solvation terms with COSMO-RS are given within section 2.7.3.

Results and discussion

Figure 4.4 (left) compares the experimental solubilities, ln x_i, to calculations via the two thermodynamic cycles. The melt cycle gives slightly better results for both substances however seem to systematically overestimate the solubilities. It has an error of RMSE = 0.57 and 2.13 (in ln$x$ – units) for naphthalene and benzoic acid, respectively. In comparison, the sublimation cycle has an overall error of RMSE = 1.78 and 2.84 (in ln$x$ – units) for naphthalene and benzoic acid, respectively. The sublimation cycle systematically underestimates the solubilities which is in parts due to the overestimation of the sublimation Gibbs energies (see Figure 4.3). Calculations errors affect the final mole fraction solubilities x_i significantly more if solubilities are large due to the exponential relation between the free energy of solution and x_i (see Figure 4.4, right).
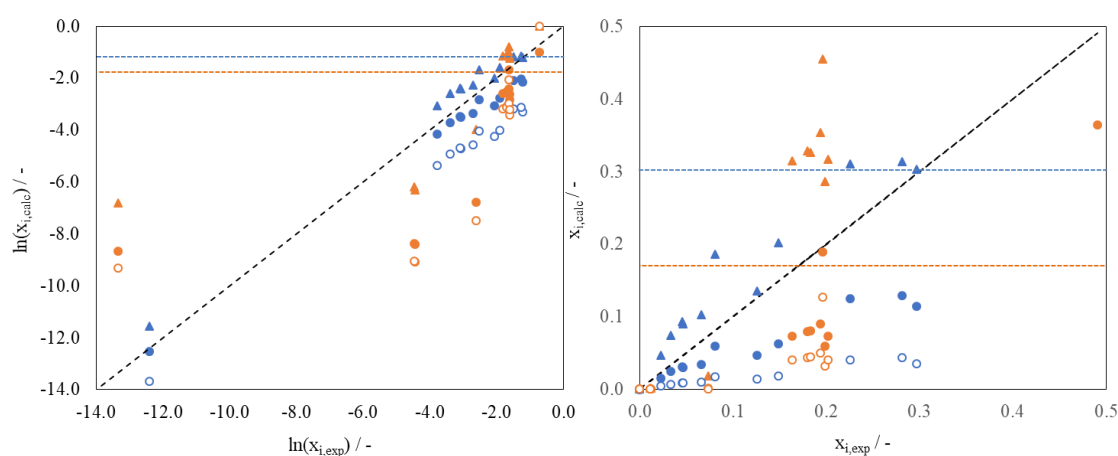
Figure 4.4: Calculated mole fraction solubilities, (**left**) ln(x_i) and (**right**) x_i, via the two thermodynamic cycles (Figure 2.10) for naphthalene (blue symbols) and benzoic acid (orange symbols) in a variety of organic solvents with varying polarity (see Table 4.2). The melt cycle (▲) is compared to the sublimation cycle (○). The coloured horizontal lines corresponds to the SVL equation (eq. (34)) representing the solvent-independent "ideal" solubility.

In order to evaluate error sources, "experimental" solvation quantities, $\Delta G_{solv,exp}$ and ΔG^E_{exp}, have been recalculated from the experimental solubilities in Table 4.2 and the experimental melting and solvation Gibbs energies from Table 4.1 via the two thermodynamic cycles (eqs. (27) and (28)). They are compared to the calculated solvation terms within Figure 4.5. For most of the cases ΔG_{solv} is larger compared to ΔG^E due to the cavitation energy, ΔG_{cav}, the energy needed to form space in the solvent for the dissolved molecule (see Figure 2.15). Both ΔG_{solv} and ΔG^E are accurately modelled by the COMSO-RS model for naphthalene while errors for benzoic acid are larger and systematically underestimate the solvation free energies. The benzoic acid results are significantly worse than the suggested 2.1 kJ mol^{-1} accuracy of COSMO-RS in combination with the TZVPD-FINE parameterization.[127] Especially for the unipolar solvents deviations between calculations and experiment are large by to 10 kJ mol^{-1}. Benzoic acid dissociates in water which is not explicitly included in the model resulting in a large computational error when calculating the solubility in water. It can be summarized that errors within the sublimation cycle for naphthalene are mainly related to the calculation of ΔG_{subl} while for benzoic

acid the solvation terms are responsible for most of the deviations in Figure 4.4.
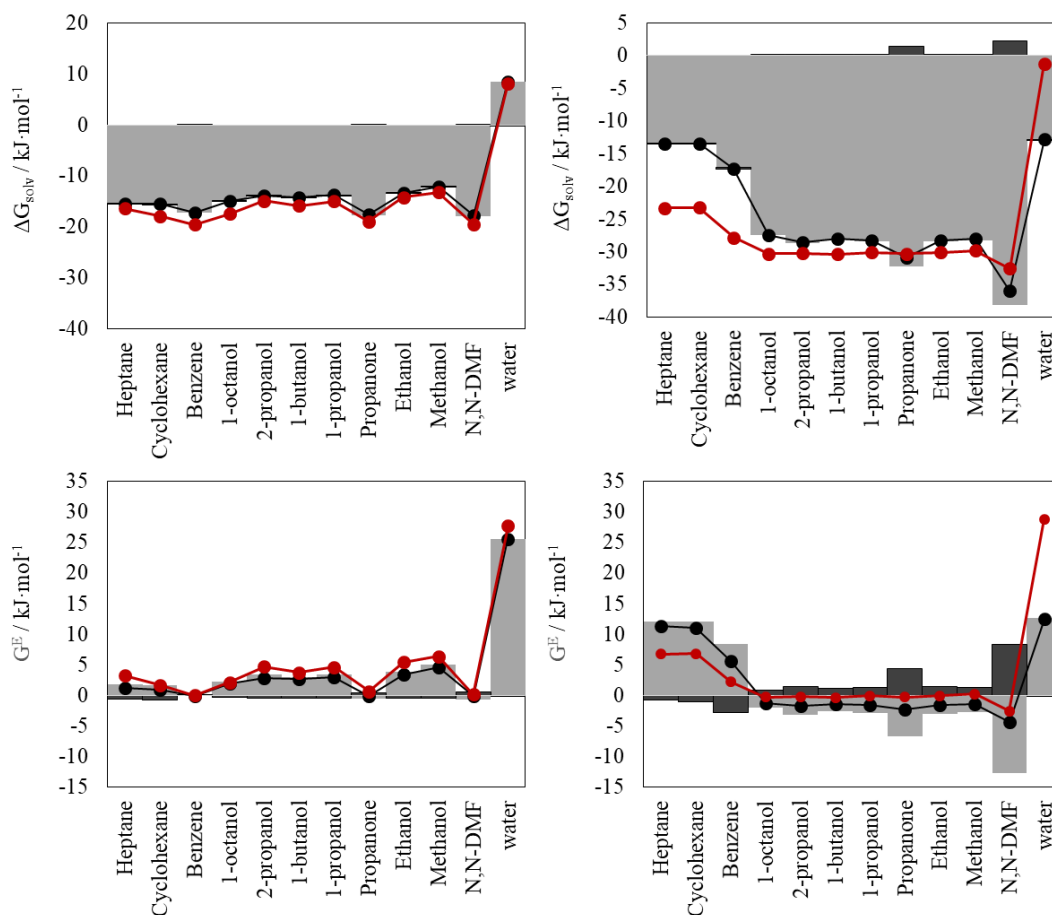
Figure 4.5: Calculated COSMO-RS solvation free energies, ΔG_{solv}, and the excess free energies of mixing, G^E, for the sublimation and melt cycle, respectively: (**left**) naphthalene; (**right**) benzoic acid. Light grey bars are the free energies at infinite dilution and the black bars energy contributions due to solute-solute interactions. The final free energies at saturation concentration (black ●) are compared to the experimental values (red ●) which are obtained from recalculating $\Delta G_{solv,exp}$ via experimental $\Delta G_{sol,exp}$ (Table 4.2) and $\Delta G_{subl,exp}$ (Table 4.1).

Both solvation quantities are comprised by concentration-independent terms, $\Delta G_{solv,inf}$ and ΔG^E_{inf}, as well as energy contributions that incorporate solute-solute interactions (see Figure 4.5). $\Delta G_{solv,inf}$ and ΔG^E_{inf} are significantly larger than the concentration-dependent counterparts for both substances. As suspected, the latter are larger for systems with high solubilities, such as propanone and DMF. As a consequence, the concentration-dependent terms are larger for the melt cycle which overestimates most of the solubilities (see Figure 4.4). For naphthalene, concentration-dependent terms are mostly smaller than 0.6 kJ·mol^{-1} even in cases where solubilities are large but for benzoic acid they can be significantly larger and vary between -3 and 4 kJ·mol^{-1}. The hydrogen bonding capability of the benzoic acid carboxylic acid group is responsible for the strong association energies at high solubilities. The overall accuracy for calculating the solvation Gibbs energy is only slightly improved if concentration-dependent terms are included. Within the melt cycle concentration effects are larger due to the larger solubilities but only improve the overall calculations for benzoic acid while for naphthalene slightly less accurate ΔG^E are

calculated. Hence statistically, the modelling of concentration-dependent solvation terms does not significantly improve the overall calculations accuracy.

Figure 4.6 compares all major *absolute* energy contributions to ΔG_{sol} when calculated via the sublimation cycle. The solvation free energy is solvent-depending and varies, for the solvents from Table 4.2, between 8 and 17 kJ·mol^{-1} for naphthalene and between 19 and 32 kJ·mol^{-1} for benzoic acid. For both substances the lattice energy is the dominant energy contribution while the entropy correction is the second largest term. Hence, thermal enthalpy and entropy corrections and solvation make up around 40 to 50 percent of the total *absolute* energies. In summary, an accurate determination of the sublimation free energy is especially relevant for predicting solubilities via the sublimation cycle. Within the following section the accuracy of state-of-the-art methods to calculate the major energy contribution to ΔG_{subl}, the lattice energy, is discussed for a benchmark set of molecular crystals.[85]

	E_{latt}	ΔH_{corr}	$T\Delta S_{subl}$	ΔG_{solv}
benzoic acid	97.9	5.2	56.7	19 to 32
naphthalene	85.3	6.4	53.5	8 to 17
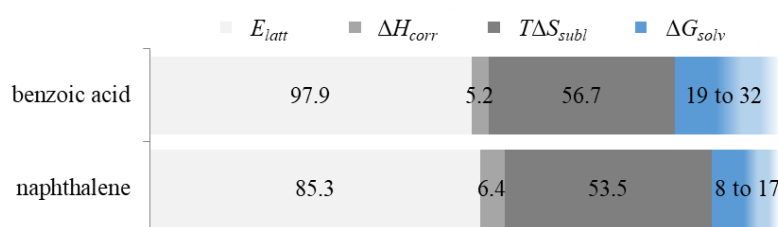
Figure 4.6: Absolute energy contributions to the free energy of solution within the sublimation cycle. For ΔG_{solv} an energy range is given which corresponds to the solvation in various solvents (Table 4.2).

4.1.4   Conclusions

Calculations of lattice energies consequently of sublimation Gibbs energies are more accurate using the larger def2-TZVP basis set due to effects of basis set superposition errors (BSSE) when using def2-SVP (see Figure 4.3). The sublimation cycle has an overall accuracy of RMSE = 1.8 to 2.8 (ln *x*-units) when used for solubility prediction of naphthalene and benzoic acid, respectively (see Figure 4.4 a). This is only slightly worse in comparison to the melt cycle results. The modelling of concentration-dependent solvation terms does not significantly improve the overall calculations accuracy. However, the absolute mole fraction solubilities, x_i, from both cycles are not accurate enough to be used for crystallization process design due to the summation of errors and the exponential relation between ΔG_{sol} and x_i (see Figure 4.4 b). Errors in the naphthalene calculations are mainly related to the calculation of ΔG_{subl} while for benzoic acid the solvation terms are responsible for most of the computational errors (see Figure 4.5). The main energy contribution within the sublimation cycle is the lattice energy but thermal corrections as well as solvation make up around 40 to 50 percent of the total energies (see Figure 4.6). Hence, combining periodic DFT and the COSMO-RS model within the sublimation cycle provides a consistent framework for calculating mole fraction solubilities. Moreover, its accuracy is comparable to the melt cycle which requires substance specific experimental melting parameters.

4.2   Lattice energies of organic molecular crystals

The lattice energy has been identified as being the dominant energy contribution to the solution free energy of naphthalene and benzoic acid (see Figure 4.6). Within this section, the accuracy of state-of-the-art methods to calculate lattice energies of organic molecular crystals is evaluated and compared to own calculations using a consistent framework to model the separated ideal gas molecules and periodic crystal.
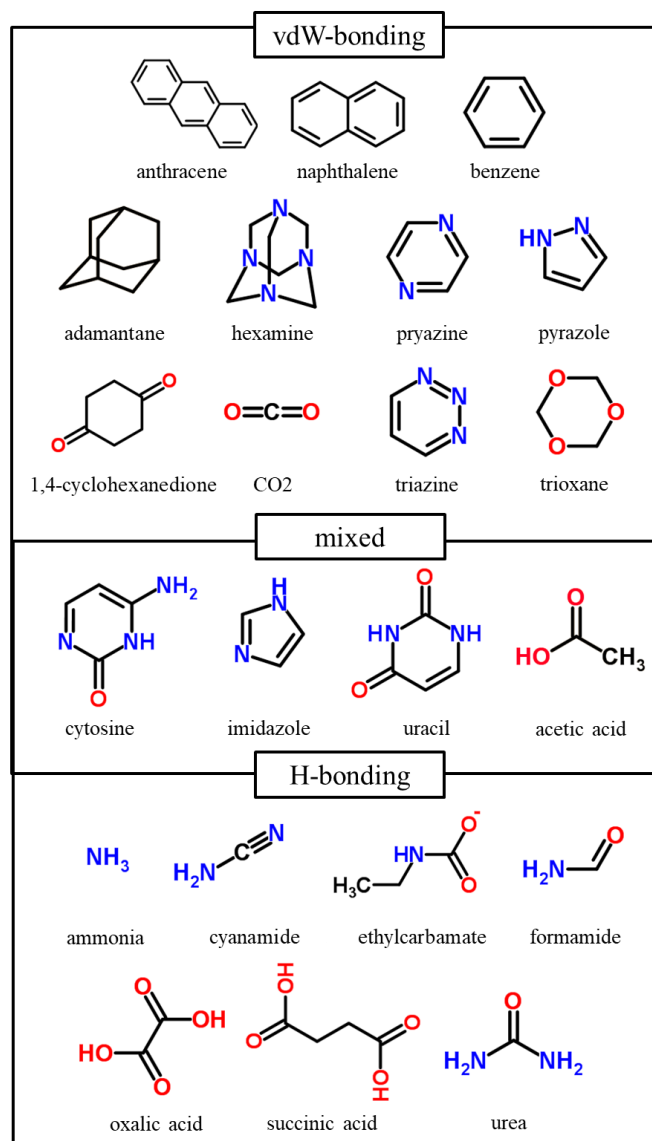
Figure 4.7: Molecular structures of the molecules within the X23 benchmark set for non-covalent interactions in solids suggested by Otero-de-la-Roza et. al.[85] and extended Reilly et. al.[97]. The molecular structures are classified by the dominant intermolecular interactions within the crystal.

A set of well-studied molecular crystals is used in order to generate a reliable framework for evaluating the accuracy of computations. The set of molecules is bases on the "C21" benchmark set by Otero-de-la-Roza et. al.[85] which has been suggested for studying non-covalent interactions in solids of 21 crystal structures, including one polymorphic system (α- and β-oxalic acid). The C21 set was extended to include hexamine (HXMTAM09[192]) and succinic acid (SUCACB02[193]) by Reilly et. al.[97] and subsequently named "X23". The

X23 benchmark set consists of rather small and rigid molecules which are depicted in Figure 4.7. The various molecules are classified into systems that are dominated by hydrogen bonding or van der Waals interactions in the solid state.

4.2.1   Lattice energy calculations

Lattice energies of the full X23 benchmark set have been calculated and compared to recalculated "experimental" values that have been extracted from experimental sublimation enthalpies. "Experimental" lattice energies, $E_{latt,exp}$, can be extracted from measured sublimation enthalpies via eq. (44) using calculated thermal and zero-point energies. For parts of the molecular crystals from the X23 set, which are solid at room temperature, the suggested thermal corrections from literature[85, 97, 194] can be compared to the frequently used molecule independent $2RT$-approxmation (eq. (55)) which reveals significant differences with an overall RMSE of 2.5 kJ mol^{-1} (see Figure 4.8).
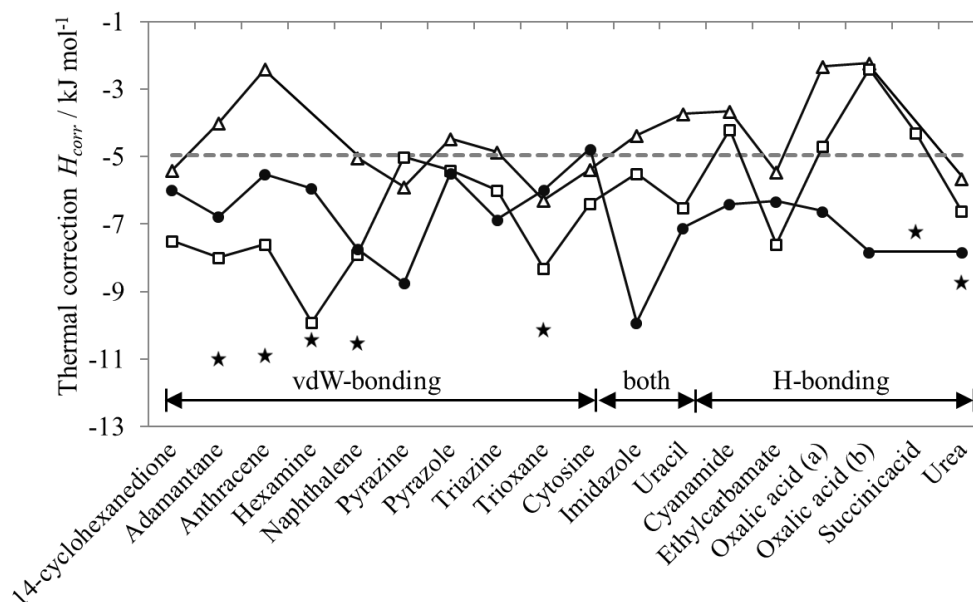
Figure 4.8: Calculated thermal contributions ΔH_{corr} to the sublimation energy at 298 K for selected crystals of the X23 benchmark set that are solid at 298 K. Corrections in the harmonic approximation from different electronic structure methods are given: PBE-XDM (open triangles [85]), PBE-TS (filled squares [97]), and DFTB3-D3 (filled circles [194]) and compared to the $2RT$-approximation (horizontal line). For six systems more demanding calculations which include anharmonic contributions have been performed (filled stars [97]).

Based on the above, the average of the suggested thermal corrections from the three studies[85, 97, 194] have been used to extract $E_{latt,exp}$ from the experimental sublimation enthalpies while the standard deviation between the three ΔH_{corr} values gives the uncertainty of $E_{latt,exp}$. The final values and their corresponding uncertainty are summarized in Appendix Table 7.23.

For the computation of lattice energies, E_{latt}, periodic DFT calculations have been

performed using the riper[140, 141] module in TURBOMOLE software package (V7.1)[139] as described in section 2.7.2. For all calculations, the def2-type basis sets by Weigand and Ahlrichs [133] have been used in varying size in combination with the PBE[136] density functional and the "D3"[137] dispersion correction. If possible, all calculations were performed with *m3* grid size, which has been increased to *m5* in case of convergence issues. As space group symmetry options cannot be exploited within the riper framework, computational effort is directly related to the size of the molecules, as well as the total number of molecules, Z, within the unit cell. The number of molecules within the crystal structures vary in between $2 \leq Z \leq 8$ which significantly scales the computational time of the periodic calculations in comparison to that of the single gas phase molecules. Lattice energies have been calculated via eq. (42) from the ground state energies of the 22 molecular structures in the gas phase and energies of the 23 distinct crystal structures. For succinic acid, the lowest energy conformation has been used for lattice energy calculations as suggested in literature.[97] The experimental unit cell parameters are summarized in Table 7.18 in the appendix and remain unchanged during the calculations while molecular coordinates within the unit cell are optimized. This work's calculation results are summarized in Figure 4.9 and compared to $E_{latt,exp}$. For anthracene, the standard TZP basis set was used to avoid convergence difficulties with the too diffuse triple-zeta valence basis sets.

A major influencing variable on the quality of the computed lattice energies is the choice of the dispersion model. In Figure 4.9 (top), calculations from ref. [85] using the uncorrected PBE functional are compared to this works def2-TZVP / PBE-D3 results. Obviously, the uncorrected PBE functional underestimates the binding energies drastically. They are smaller for crystals which are dominated by H-bonding interactions and especially large for crystals that are dominated by van der Waals interactions.

Figure 4.9 (bottom) compares the absolute deviations to the "experimental" lattice energies of this works PBE-D3 results. There is a clear increase in accuracy when using the larger basis set in comparison to the def2-SVP results. This is consistent with the previously discussed calculations of benzoic acid and naphthalene (see Figure 4.3) where the most significant difference in accuracy for modelling the crystal binding energies was between the def2-SVP and def2-TZVP results. Furthermore, there is a clear tendency of the lower size def2-SVP basis set to overestimate binding energies of the predominantly hydrogen bonded crystals while differences are smaller if van der Waals interactions prevail (see Figure 4.9, bottom). The strong dependence on the size of the basis set to accurately model hydrogen bonding interactions is consistent with previous findings.[156, 195] These accuracy issues of the small basis set have been assigned to superposition errors when using small basis sets (BSSE) which are more severe for crystals that are dominated by hydrogen bonding interactions.[189]
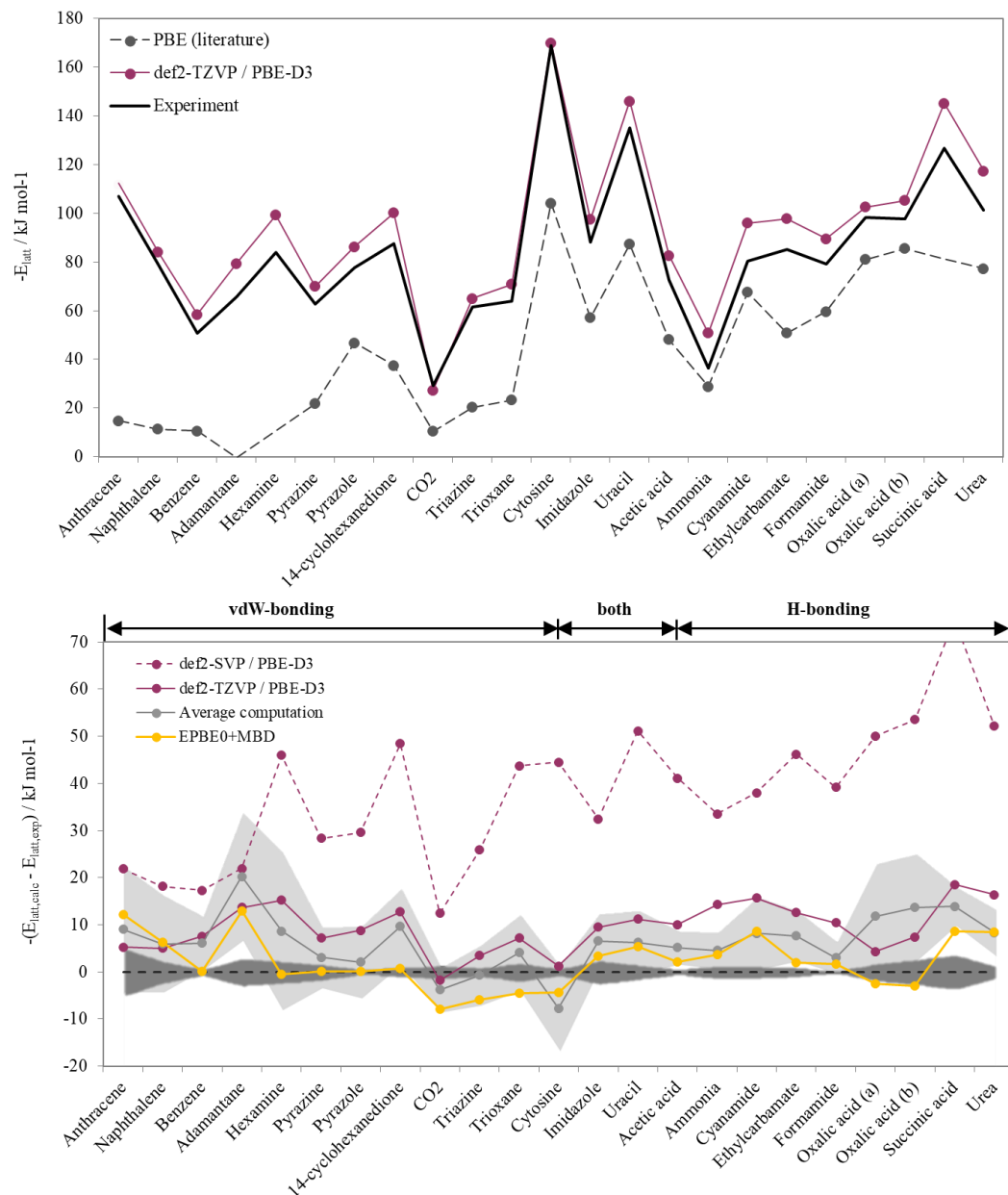
Figure 4.9: Calculated lattice energies for molecules from the X23 benchmark. PBE-D3 results are compared with experimental values and (top) results from uncorrected PBE calculations according to literature[87], and (bottom) an average computational value from various methods in literature[85, 97, 194, 196]. The light grey area indicates the standard deviation of the literature values (see Table 7.24). The dark grey area indicates the uncertainty in calculating $E_{latt,exp}$ from experimental sublimation enthalpies via eq. (43).

Figure 4.9 (bottom) further compares this works results to the "average computation" value which has been determined from several dispersion corrected electronic structure methods to calculate lattice energies from literature[85, 97, 194, 196]. The light grey area indicates the standard deviation between the 12 different methods. Primary data for the average computational value is given in Table 7.24 in the appendix. This work's def2-TZVP method gives binding energies that are comparable to the literature results (def2-TZVP / PBE-D3: RMSE = 10.6 kJ·mol^{-1}; Average literature: RMSE = 8.6 kJ·mol^{-1}) and

mostly within the standard deviation of those methods (grey shaded area). Deviations of this work's def2-TZVP method can, on one hand, be evoked by the combination of the PBE functional and the D3 dispersion correction. On the other hand, the non-complete basis set def2-TZVP can be responsible for parts of the deviations to experiment. Errors caused by missing geometry optimizations of the unit cell are suspected to contribute only minor to the absolute error as shown before for naphthalene and benzoic acid (see section 4.1.2). Hence, further calculations with a def2-QZVP basis set could improve the overall accuracy.

The various electronic structure methods tend to overestimate the binding energies. Especially for crystals that are predominantly dominated either by hydrogen bonding or van der Waals interactions, deviations to experiment are large and calculated binding energies are too large. To amplify this common calculation scheme, the result of the EPBE0+MBD[36] method from literature, which gives the best overall representation of $E_{latt,exp}$ is shown Figure 4.9 (top).

Even though the EPBE0+MBD method has an overall accuracy of RMSE = 5.8 kJ mol^{-1}, it produces a similar substance-dependent trend compared to the other computational methods. In order to be able to work out sources of the computational errors we compared the computational errors of the various methods for each substance to the density of the related crystal. Figure 4.10 plots the calculations error over the density for each of the 23 substances of the benchmark set which ranges from 0.8 g·cm^{-1} to 2.0 g·cm^{-1}. The density has been calculated from published[97] volumes of the unit cell, V, the molar Mass of the molecule, M, the number of molecules in the unit cell, Z, and the Avogadro number via $\rho_{cryst} = Z \times M / (V \times N_A)$. Computational errors in Figure 4.10 appear to be not directly correlated to the density of the crystal for any of the computational method shown. Even though density is a characteristic value of one specific crystal packing, crystals with different crystal structures can have the same density.
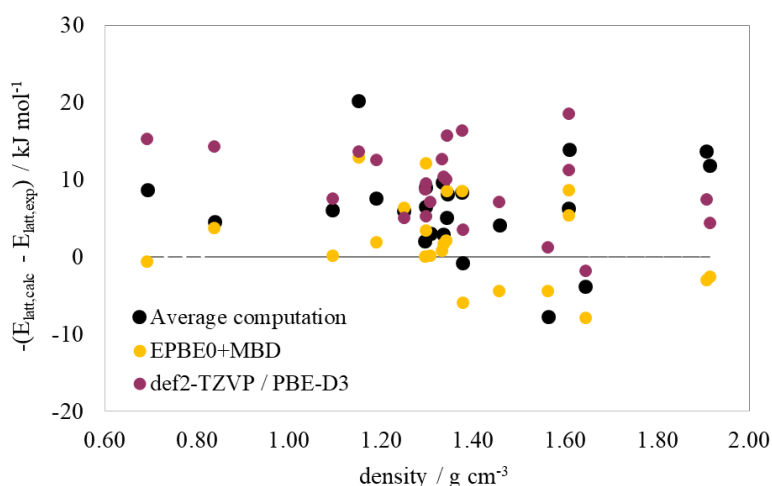
Figure 4.10: Dependence of the absolute computational errors of the lattice energy calculations of the X23 benchmark set in comparison to the density of the molecular crystals. This works def2-TZVP / PBE-D3 results are compared to the average literature values[85, 97] and results of the method with the lowest RMSE to experiment (EPBE0+MBD[97]).

Thus, the conclusion that computational errors are less dependent on the density of crystals then on the types of interactions within, is not directly transferrable to the crystal structure in general.

Based on the above considerations, it can be suspected that the dominant parts of the errors when calculating the absolute binding energies are more likely to be connected to the specific molecular structure and the types of binding energies (H-binding and van der Waals interactions) that are present in the crystal (see Figure 4.9) rather than to the density of the crystal. This could be of advantage for calculations of energy differences between polymorphs or different types of chiral crystals – for example an enantiopure crystal and a racemic compound. Absolute errors that are connected to molecular specific binding energies potentially cancel out when aiming for energy differences as both chiral crystals contain the same molecules. This is studied in section 4.3 for three chiral model substances.

4.2.2   Benchmark set for calculation of sublimation Gibbs energies

Besides lattice energies, thermal and zero-point energy contributions are needed for modelling sublimation free energies. Thermal corrections are related to the integrals of the solid state and ideal gas heat capacities from zero Kelvin to reference temperature via eqs. (43) and (44). The previously introduced X23 benchmark set of molecular crystals has been designed in order to test the accuracy of electronic structure methods for calculating the total non-covalent binding energies to determine E_{latt} (see Figure 4.9). Less frequently, thermal enthalpy corrections, ΔH_{corr}, to the lattice energy have been studied (see Figure 4.8). Information on the sublimation entropies which are required for determining ΔG_{subl} are missing. In order to extend the X23 benchmark set for evaluating all energy contributions to ΔG_{subl} it is useful to exclude those substances that are liquid (acetic acid benzene and formamide) or gaseous (ammonia and CO_2) at environmental conditions and are thus irrelevant for modelling phase equilibria such as SLE at 298 K.

Hence, experimental data was gathered for the remaining 18 molecular crystals. Sublimation enthalpies were taken from the original publications[85, 97] of the X23 benchmark set and have been used without further adjustments of the X23 benchmark set and were used without further adjustments with the exception of cytosine which was taken from ref. [197]. Sublimation free energies haven been calculated via eq. (38) from published sublimation vapor pressures from various literature sources. They are summarized together with ΔH_{subl} and $T\Delta S_{subl}$ in Table 4.4. $T\Delta S_{subl}$ was calculated from the sublimation enthalpies and free energies via eq. (39). Wherever possible experimental uncertainties are given. Those are generally smaller for ΔG_{subl} in comparison to ΔH_{subl} as the free energies are related by logarithm to the experimental vapor pressures. Sublimation free energy values within the reduced set of molecular crystals span from 13 kJ·mol^{-1} (triazine and 1,3,5-trioxane) up to 90 kJ·mol^{-1} (cytosine).

Table 4.4: Experimental sublimation enthalpies, entropies and free energies at 298 K of selected molecular crystals from the X23-benchmark set that are solid at environmental conditions.

Substance	ΔH_{subl}[a] kJ mol^{-1}	$T\Delta S_{subl}$[b] kJ mol^{-1}	ΔG_{subl} kJ mol^{-1}	reference
Anthracene	101.9	55.8	46.1 ± 0.5	[198]
Naphthalene	71.3	48.7	22.6 ± 0.1	[198]
Adamantane	58.4	37.0	21.4	[199]
Hexamine	75.8	40.5	35.3	[200]
Pyrazine	56.3	45.9	10.4	[201]
Pyrazole	72.4	51.6	20.8	[202]
1,4-cyclohexanedione	81.1	52.9	28.2	[200]
Triazine	55.7	42.5	13.2	[200]
1,3,5-trioxane	56.3	42.7	13.6	[200]
Cytosine	156.4[197]	65.7	90.7	[197]
Imidazole	81.4	49.7	31.7	[202]
Uracil	129.2	58.8	70.4 ± 0.2	[203]
Cyanamide	75.5	46.9	28.6	[200]
Ethylcarbamate	78.7	53.7	25.0 ± 0.5	[204]
Oxalic acid (a)	93.7	55.1	38.6 ± 0.6	[205-207]
Oxalic acid (b)	93.6	55.6	38.0	[207]
Succinic Acid	123.1	70.3	52.8 ± 1.3	[200, 205, 208]
Urea	93.8	48.4	45.4 ± 0.2	[206, 209]

a. Taken from refs. [85, 97] except for cytosine which was taken from ref. [197].
b. Calculated via $\Delta G_{subl} = \Delta H_{subl} - T\Delta S_{subl}$.

As discussed before, the sublimation enthalpy consists of the lattice energy as well as thermal corrections. Figure 4.11 compares all energy contributions when calculating ΔG_{subl} via eq. (43). The "experimental" lattice energies, $E_{latt,exp}$, have been used as discussed before, which are based on recalculations from the sublimation enthalpies using the average of the suggested thermal corrections, ΔH_{corr}, from the three studies[86, 98, 196] (primary data in Appendix Table 7.23). For all substances the lattice energy is the dominant energy contribution to the Gibbs free energy of sublimation. However, the heat capacity related thermal enthalpy corrections and especially the sublimation entropy are responsible for a relevant part accounting for 39±4 % of the sum of all energy contributions. *Ab-initio* quantum chemistry methods have been shown to be capable to determine the sublimation entropy, $T\Delta S_{subl}$, with accuracies of around 9 kJ·mol^{-1} resulting in an overall accuracy for calculating ΔG_{subl} of around 17 kJ·mol^{-1}.[210] Thus, precise methods for determining the thermal corrections are a key requirement for the applicability of the sublimation cycle for solubility prediction. As a consequence, two distinct methods are used in the next section to calculate the thermochemistry of chiral molecules. The two methods differ particularly in the way thermal corrections are modelled.
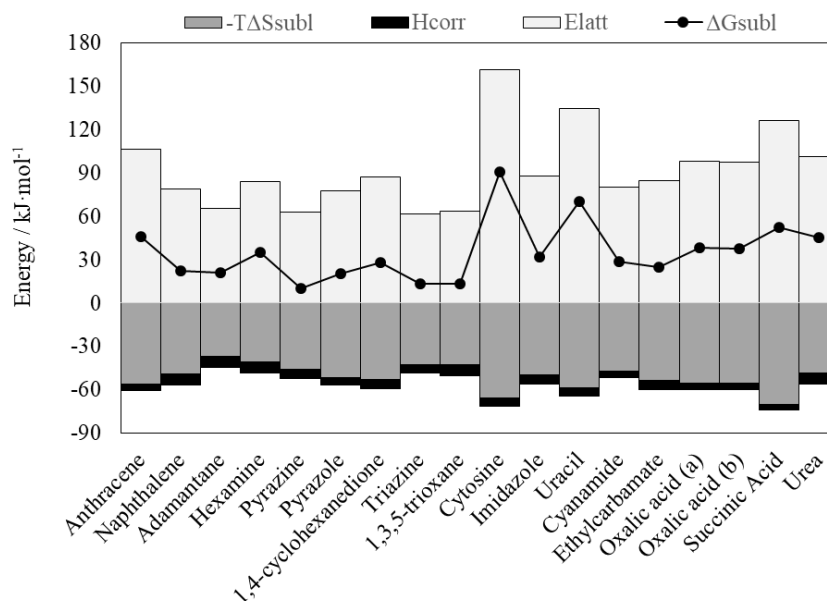
Figure 4.11: Energy contributions to the ΔG_{subl} for selected molecules from the X23-benchmark set that are solid at 298 K.

4.2.3 Conclusions

This work's def2-TZVP / PBE-D3 method has an overall accuracy of around 10 kJ·mol[1] but there are some methods in literature that are close to the chemical accuracy limit of 4.2 kJ·mol^{-1} (see Figure 4.9). Even though, the def2-TZVP is superior to the def2-SVP basis set parts of the remaining errors of this work's calculations are likely to be caused by the non-complete triple-zeta basis set. Influenced by the missing optimizations of the unit cell were comparatively small. The accuracy of state-of-the art electronic structure methods for determining the lattice energy was shown to be strongly dependent on the types of prevalent intermolecular interactions within the crystal. There were no obvious correlations between the calculations error and the density of the crystal (see Figure 4.10). As a consequence, errors are related to the type of intermolecular interaction (H-bonding and van der Waals interactions) that is dominating in the crystal rather than to the density of packing and the specific crystal structure. Molecule specific errors potentially cancel out when aiming for energy differences, e.g. between an enantiomer and the racemic compound. This is studied for three representatives of chiral substances in the following section 4.3.

Finally, a modified set of molecular crystals was suggested which can be used in order to test computational methods to calculate ΔG_{subl} rather than merely E_{latt} or ΔH_{subl} (see Table 4.4). Thermal corrections are shown to contribute by around 40 percent to the absolute energy contributions to ΔG_{subl}. As a consequence, two distinct methods are used in the next section to calculate the thermochemistry of chiral molecules which differ particularly in the way thermal corrections are modelled.

4.3   Phase transition thermodynamics of chiral molecules

Within this section the melting and sublimation thermochemistry of a diverse set of chiral compound-forming systems are evaluated by means of experimental and computational methods. The molecular structures of the three molecules are depicted in Figure 4.12. They incorporate an almost rigid molecule, lactide, a molecule with intermediate flexibility, naproxen, and the fully conformational flexible 3-chloromandelic acid (3ClMA).
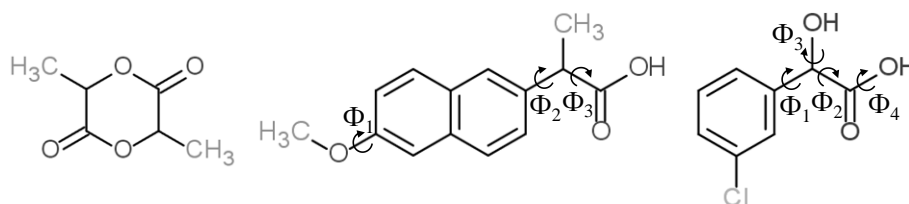
Figure 4.12: Molecular structures of the three representative chiral molecules: (a) 3,6-dimethyl-1,4-dioxane-2,5-dione (lactide $C_6H_8O_4$), (b) naproxen $C_{14}H_{14}O_3$, (c) 3-chloromandelic acid (3ClMA, $C_8H_7O_3Cl$). Relevant flexible torsion angles are marked.

The lactides are internal cyclic esters of lactic acid, and the racemic compound is used in the preparation of polylactide, a biologically decomposable polymer which is used, among others, for medical applications[211]. Naproxen is marketed in the enantiopure form as a non-steroidal anti-inflammatory drug as only (*S*)-naproxen has the desired effects. [14, 15] 3-chloromandelic acid (3ClMA) is used as an intermediate for pharmaceutical products and a resolving agent and has complex polymorphic crystallization behaviour.[212, 213] Experimental sublimation and melting thermodynamics[41] as well as studies on the polymorphic behaviour of naproxen[214, 215] have been reported before. Solubility data and a shift of the eutectic composition with temperature in certain solvent systems have been reported for lactide and 3-chloromandelic acid.[212, 213, 216]

The three molecules represent prototypes of frequently occurring organic crystalline racemic compound-forming systems. In the following, the phase transition thermochemistry which is relevant for calculating solubilities via the melt and the sublimation cycle is investigated for the enantiomer as well as the racemic compounds. This includes experimental investigations of the melting thermodynamics as well as combined experimental and computational studies of the sublimation thermodynamics the three chiral systems. Furthermore, a detailed experimental as well as computational investigation of the solid-state heat capacities have been conducted which is relevant for adjusting the measured and calculated thermodynamic phase transition quantities to one common reference temperature.

4.3.1   Structural clarification

This section provides information on the crystalline solid form of the three pairs of chiral crystals of lactide, naproxen and 3ClMA. Information on the origin and purity of the

crystalline substance that have been used throughout this work is given in section 3.1 "Materials".

Structures of (*S*)- and (*RS*)-lactide relate to the published NAHNOZ[217] (Z′=3, Z=12, P212121) and BICVIS[218] (Z′=1, Z=4 P21/c) crystal structures. The (*S*)- and (*RS*)-naproxen crystal forms which have been investigated after recrystallization of the purchased substance are identical with the computed patterns of the COYRUD[219] (Z′=1, Z=2, P21) and PAPTUX[215] (Z′=1, Z=8, Pbca), respectively.

For 3-chloromandelic acid (3ClMA) five polymorphic forms of each the enantiopure and racemic crystals have been found by experiment.[212] The commercial substance of (*RS*)-3ClMA contained a mixture of two polymorphic forms, form 2[220] and form 3[212]. The metastable form could be completely transformed into the stable form 3 (FIZPEL03, Z'=1, Z=4, P21/c) by recrystallization in water and subsequent equilibration of the stirred suspension for more than 24h. Recrystallized (*R*)-3ClMA was confirmed by PXRD to correspond to 3ClMA (S)-form 1[212] (TUYBIA, Z′=2, Z=4, P21, with a 2:1 disorder in the phenyl ring orientation). To model this disordered crystal, the two disorder components can be modelled separately and the results combined in a 2:1 ratio.

The experimental crystal structures of the enantiomer and racemic compound of lactide, naproxen and 3ClMA are depicted within Figure 4.13. They significantly differentiate, regarding the size of the unit cell which comprise two up to 12 molecules, as well as the types of molecular interactions within. The lactide crystals are dominated by isotropic and rather weak vdW-interactions whereas the two 3ClMA crystals form strong hydrogen bonding motifs.[212] Naproxen structures, on one hand, exhibit weak vdW-type C-H·π interactions between the naphthalene rings and, on the other hand, strong hydrogen bonding interactions between the carboxylic acid groups.[215]
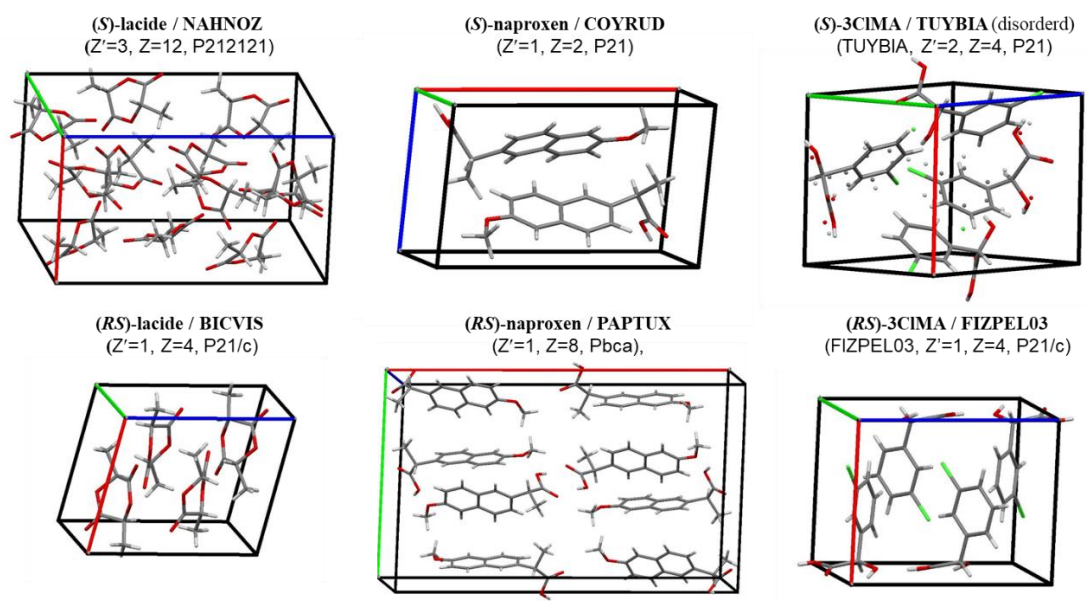
Figure 4.13: Experimental crystal structures of the enantiomer and racemic compound of lactide, naproxen and 3ClMA.

The XRPD-patterns of the three pairs of enantiopure and racemic crystalline substances are summarized in Figure 4.14. They have been measured by XRPD as described in section 3.2.3. Comparing the experimental and theoretical XRD-patterns which have been calculated via Mercury CSD 2.4 (Build RC5) confirms the aforementioned crystal structures as single polymorphs. XRPD measurements have been performed at room temperature while calculations refer to structures at much lower temperatures. This explains slight shifts in some cases.
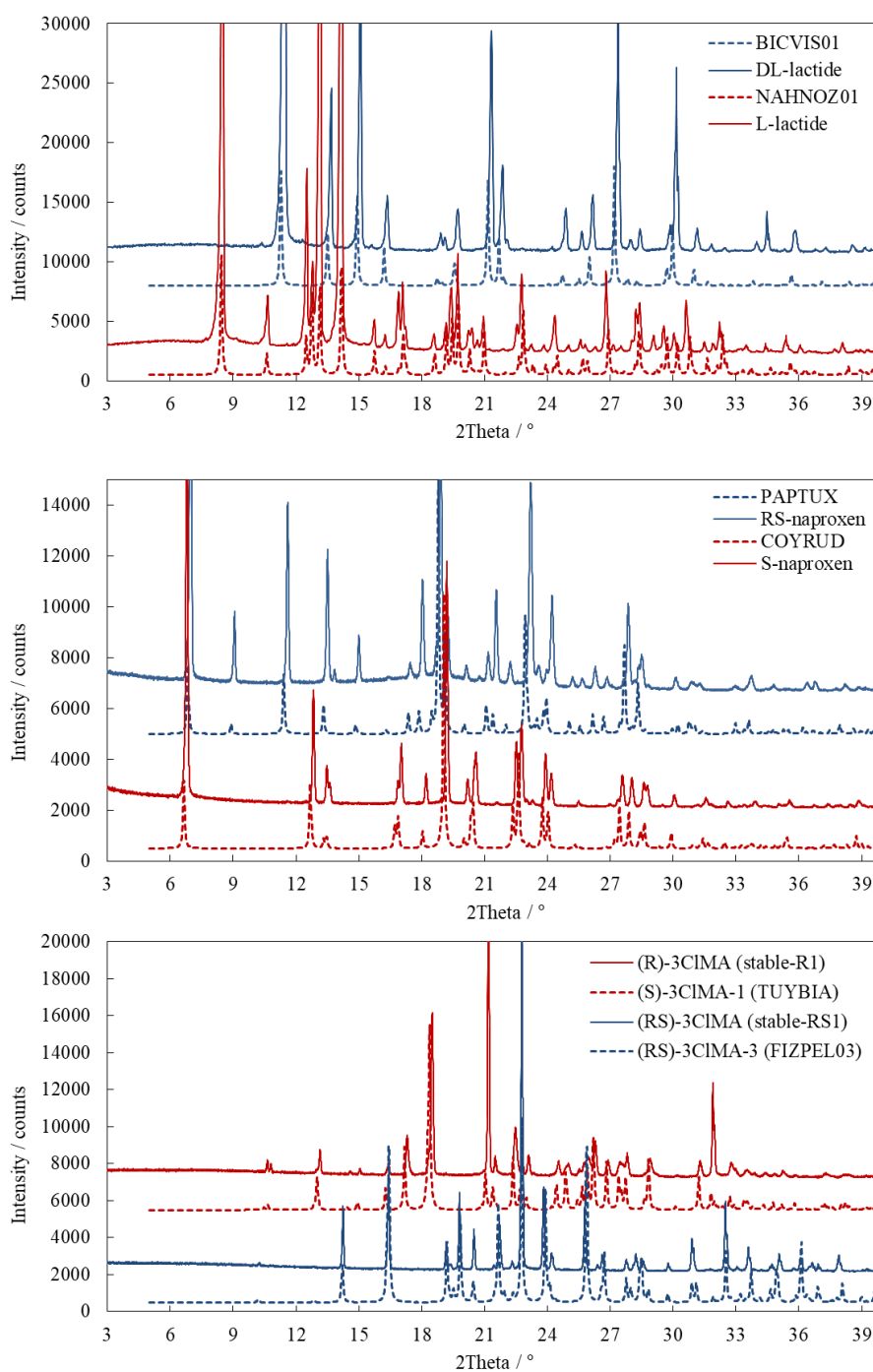
Figure 4.14: Experimental and computed XRPD-patterns of the crystal forms of (*S*)- and (*RS*)-lactide (NAHNOZ[217] and BICVIS[218]), (*S*)- and (*RS*)-naproxen crystal forms (COYRUD[219] and PAPTUX[215]) and (*S*)- and (*RS*)-3ClMA (TUYBIA and FIZPEL03)[212].

4.3.2 Melting thermodynamics

The melting thermodynamics of the three chiral molecules are investigated for structural clarification of binary mixtures of the two chiral species as well as in order to precisely determine melting temperatures and melting enthalpies. The latter are used later on within the melt cycle for calculating solubilities. Detailed information on the experimental procedures for measuring melting thermodynamics, as well as, the binary melt phase diagram, is given in section 3.2.5.

Pure compound melting properties

Melting temperatures and enthalpies of the pure enantiomer and racemic compound of lactide, naproxen and 3ClMA are summarized in Table 4.5. They are used in the following for calculating ideal solubilities via ΔG_{melt} and the ideal binary melt phase diagram via the SVL and PD equation, eqs. (34) and (35) respectively.

Table 4.5: Experimental melting temperatures and enthalpies. The Gibbs free energies of melting are calculated from $\Delta G_{melt} = \Delta H_{melt} - T \cdot \Delta H_{melt} / T_{melt}$, with T = 298.15 K.

Compounds	source	T_{melt}	ΔH_{melt}	ΔG_{melt}
		-	T_{melt}	298 K
unit		K	kJ mol^{-1}	kJ mol^{-1}
(RS)-lactide	this work	397.6 ± 0.4	25.3 ± 1.8	6.3
	[221]	397.1	24.7	6.2
(S)-lactide	this work	369.2 ± 1.0	14.2 ± 1.0	2.7
	[221]	366.6	16.9	3.2
Δ(RS-S)	this work	28.4 ± 1.1	11.1 ± 2.1	3.6
	[221]	30.5	7.8	3.0
eutectic mixture	this work	363.3 ± 1.8 (x_{eu} = 83.5 %)	12.8 ± 0.2	
(RS)-naproxen	this work[41]	429.0	32.8 ± 0.2	10.0
(S)-naproxen	this work[41]	429.2	31.6 ± 0.1	9.6
Δ(RS-S)	this work[41]	-0.2	1.2 ± 0.3	0.4
eutectic mixture	this work	419.6 ± 0.5 (x_{eu} = 87.5 %)	28.7 ± 0.2	
(RS)-3ClMA	[222]	391.1	27.9	6.6
	[223]	395.4	28.0	6.9
(R)-3ClMA	[222]	376.4	22.6	4.7
	[223]	383.8	26.2	6.4
Δ(RS-R)	[222]	13.7	5.3	1.9
	[223]	11.6	1,8	0.5
eutectic mixture	[222]	368.3 (x_{eu} = 84 %)	18.6	

For lactide and 3ClMA the racemic compound melts at a higher temperature than the enantiomer. For naproxen both melting temperatures are identical. Additionally, as well the melting enthalpy and consequently the Gibbs free energy of melting are larger for the racemic form which makes is more stable and results, in the ideal case, in a lower solubility for the racemic compound. For lactide, this work's measurements are in good agreement with literature[221]. For naproxen the averaged values from ref. [41] indicate a good reliability of the melting thermodynamic quantities. For 3ClMA however, disagreements between two literature sources[222, 223] result in a difference in ΔG_{melt} of 1.8 kJ mol^{-1} which would result in large deviations when used for calculating ideal solubilities. As a consequence, a careful experimental evaluation of the melting thermodynamic quantities is important as errors can lead to significant deviations of the predicted solubilities. Possible sources of errors are impurities of other substances or polymorphs of the same substance as well as decomposition or sublimation and/or vaporization during melting.

The melting temperatures of the three chiral substances are in the medium to lower range of common drug-like substances as shown in Figure 4.15. Most drug-like compounds[22] have a melting point of around 80°C to 200°C but can spread between 30°C and 300°C. This is relevant to know as melting enthalpies and entropies are temperature-dependent quantities as thermal corrections to ΔH_{melt} and $T\Delta S_{melt}$ are related to the integral of the heat capacity difference between solution temperatures and melting. The thermal correction terms are scaled by the temperature difference to the melting temperature. Effects of the melting temperature to the Gibbs free energy of melting at 298 K according to eq. (33) if a temperature-independent heat capacity difference of $\Delta C_p = 84 \pm 57$ J·mol^{-1}K^{-1} is assumed, as suggested in literature[83], is shown in Figure 4.15. For melting temperatures of larger than 150 °C the resulting thermal corrections, ΔG_{corr}, are larger than 2 kJ·mol^{-1} and, thus, are relevant when utilizing the melt cycle for solubility prediction.
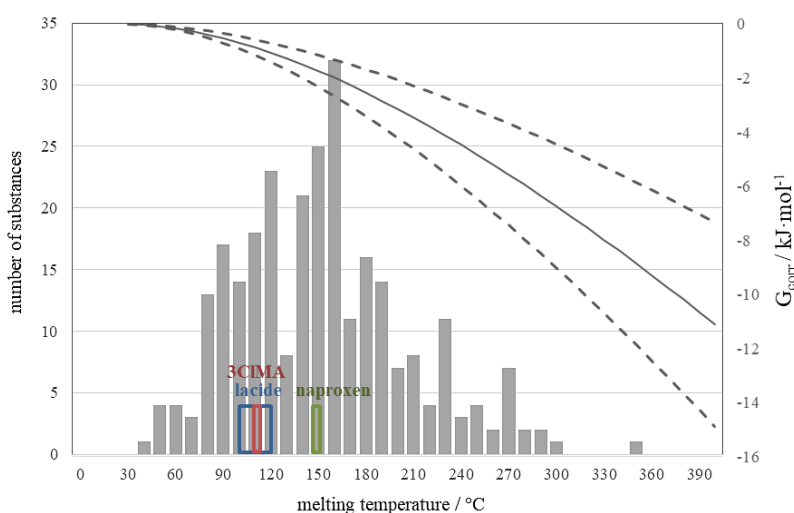
Figure 4.15: Distribution of melting temperatures of the 276 organic drug-like compounds plotted in a 10 K resolution as suggested by Bergström et. al.[224]. The range of the melting temperatures of lactide (blue), naproxen (green) and 3ClMA (red) is indicated. The solid line corresponds to the free energy corrections to the Gibbs free energy of melting at 298 K via eq. (33) assuming the temperature independent heat capacity difference of $\Delta C_p = 84 \pm 57$ J·mol^{-1}K^{-1} (solid line) from ref. [83]. The dashed lines show the influence $\varepsilon_{\Delta Cp} = \pm (57/2)$ J·mol^{-1}K^{-1} on ΔG_{corr}.

Binary melt phase diagrams of lactide, naproxen and 3ClMA

Determinations of the melting temperatures of the pure enantiomer and racemic compound as well as their mixtures are used in combination with X-ray diffraction in order to classify the chiral substance into one of the three major classes of chiral molecules via their respective binary melting phase diagram (see Figure 2.2). In the following, the binary melt phase diagram of lactide, naproxen and 3ClMA are presented and discussed.

For 3ClMA detailed information is available from previous studies[222, 225]. The binary melt phase diagram of 3ClMA (see Figure 4.16) is complicated by the formation of a metastable form of (R) as well as (RS)-3ClMA.[222] This work's crystal forms correspond to the higher melting enantiopure and racemic forms as shown in Figure 4.14.
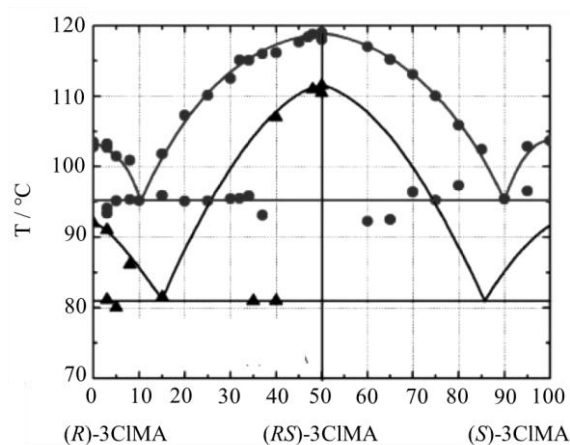
Figure 4.16: Binary melt phase diagram of polymorphic 3ClMA as suggested in ref. [222].

The binary melting phase diagram of lactide is depicted in Figure 4.17. Published data[225] has been extended with additional measurements within this work that agree well with one another and confirm a racemic compound-forming system. Furthermore, no indication for the formation of polymorphic forms or any signs of miscibility in the solid state have been found. At first sight, measurements seem to correlate well with the ideal phase behaviour from the SVL and PD equation using the pure component data from Table 4.5. However, there are deviations of the eutectic composition; the eutectic temperature is found $T_{eu} = 90.1 \pm 1.8$ °C. As the two melting peaks of the solidus and liquidus line are hardly distinguishable close to the eutectic composition even at low heating rates, an additional experimental method has been used to locate the eutectic composition. A mixture of (S)- and (RS)-lactide close to the expected eutectic composition has been heated above melting temperature and cooled down from the homogeneous melt to 91°C which is slightly above the melting temperature of the eutectic. The suspension has been kept at that temperature for around 5 minutes before two samples of the melt have been taken. Measurements via HPLC gave an enantiomeric ratio of $x_{eu} = 83.5 \pm 0.2$ % which is significantly different as for the ideal system (see Figure 4.17) but agrees well with the previous suggested value[225] of $x_{eu} = 84$ %. The extracted samples were additionally measured after solidifaction via DSC and one sharp

single melting peak confirmed the eutectic composition which is marked in Figure 4.17 in red.
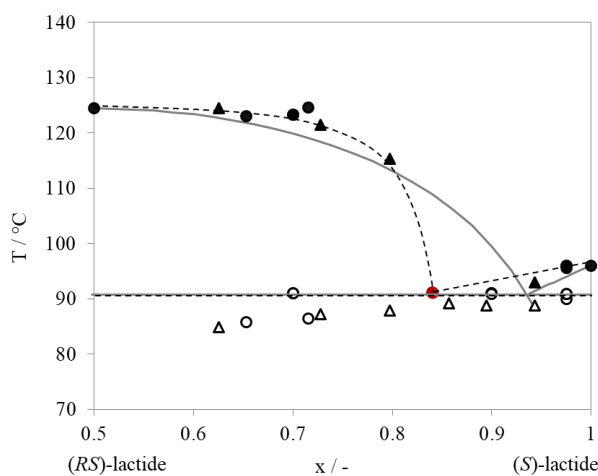
Figure 4.17: Binary melt phase diagram of lactide. Circles correspond to this works result while triangles have been taken from literature[225] (Open symbols - solidus line; solid symbols - liquidus line). The eutectic point is marked in red (Dashed lines - guide to the eye; Straight lines - calculations via the SVL and PD equation using melting properties from Table 4.5).

In case of naproxen melting temperatures of mixtures of the two enantiomers have been studied before suggesting the presence of an ordinary racemic compound-forming system.[215] Additional measurements have been performed in this work to complement previous findings. Slight modifications of the standard measurement procedure from section 3.2.5 have been conducted which are given in more detail here.
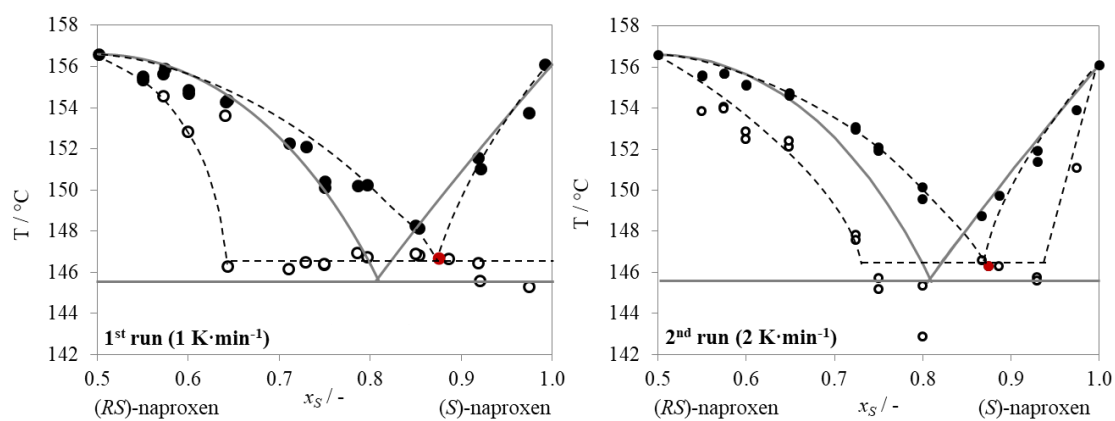
Figure 4.18: Binary melt phase diagram of naproxen: (**left**) first run of the recrystallized mixture from acetone; (**right**) second run after recrystallization from the melt. Open circles represent the solidus line and solid circles correspond to the liquidus line. The eutectic point is marked in red. Dashed lines are a guide to the eye. Straight are the calculations via the SVL and PD equation using the melting properties from Table 4.5.

This work's measurements give a eutectic temperature of $T_{eu} = 146.4 \pm 0.5$ °C which is in good agreement with earlier findings ($T_{eu} = 145.5 \pm 0.5$ °C)[215]. The eutectic composition was found[215] to be close to the ideal value which can be calculated with the

SVL and PD equation, $x_{eu,id} = 80.5$ %. This work's results, however, suggest the eutectic composition to be significantly closer to the pure enantiomer side, $x_{eu} = 87.5$ %, as marked in Figure 4.18 in red. Furthermore, the results of both runs suggest a more complex melting behaviour of the mixtures in between concentrations of the eutectic point and the racemic mixture as well as close to pure (S)-naproxen. In the first run (Figure 4.18, left) the eutectic melting peak (solidus line) disappears at concentrations of $x_S \leq 0.65$. At the same time the melting peak corresponding to the liquidus line exhibits a shoulder. The inflection point has been evaluated via the first derivative of the thermal response unveiling a lense-shaped solidus line. The effect is more pronounced in the second run after recrystallization from the melt (Figure 4.18, right). This indicates the formation of partial solid-solutions at concentrations of $x_S \leq 0.75$ and if recrystallized from the melt as well close to pure (S)-naproxen.

For additional information XRPD measurements have been performed of the samples once after recrystallization from acetone (Figure 4.19) and a second time after recrystallization from the melt (Figure 4.20). Figure 4.19 shows the XRPD patterns of selected mixtures after recrystallization from acetone. While the XPRD pattern of the $x_S = 75$ % mixture contains peaks of both (S)- and (RS)-naproxen and suggesting a mechanical mixture of both chiral crystals the pattern of the $x_S = 60$ % mixture only contains peaks of (RS)-naproxen. In between the 16 ° and 26 ° some of the peaks of the $x_S = 60$ % mixture are shifted compared to those of the pure racemic molecular crystal (blue arrows in Figure 4.19, b). At the same time the dominant peaks 2Theta < 16 ° are identical between the two mixtures and pure (RS)-naproxen indicating the dissolution of excess (S)-enantiomer within the crystal structure of (RS)-naproxen. These findings are consistent with the disappearing eutectic melting peak for mixtures of $x_S < 70$ % (see Figure 4.18, left). After recrystallization from the melt certain shifts of (RS)-naproxen, peaks become more pronounced (see Figure 4.20). Furthermore, the concentration range where partial solid solutions appear broadens by covering as well the $x_S = 75$ % mixture which prior formed a mechanical mixture before melting (Figure 4.19).

Close to pure (S)-naproxen ($x_S = 0.98$) a similar behaviour can be observed. While the recrystallized mixture from acetone clearly shows a mechanical mixture of the enantiopure and racemic crystals (see Figure 4.19), (R)-naproxen is able to crystallise within the crystal structure of (S)-naproxen when recrystallised from the melt. Most peaks of the $x_S = 0.98$ mixture in Figure 4.20 are identical to the ones of the pure enantiomer while certain peaks are merged or shifted after crystallisation form the melt (marked with red arrows in Figure 4.20, b). This is consistent with the melting temperatures from the DSC measurement where the eutectic melting peak of the $x_S = 0.98$ mixture disappears only in the second run and thus after recrystallisation from the melt (see Figure 4.18).
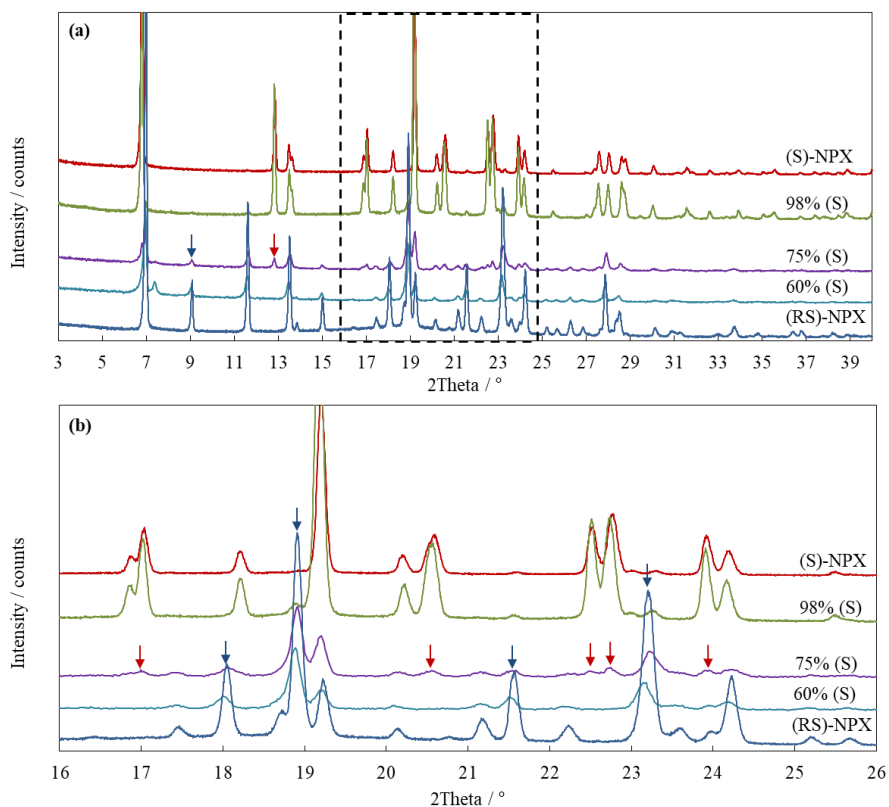
Figure 4.19: (a) The full XRPD-patterns and (b) a close-up of mixtures of (*S*)- and (*RS*)-naproxen after recrystallization from acetone in comparison to the pure components. Red arrows highlight selected peaks of (*S*)-naproxen while blue arrows those of (*RS*)-naproxen.
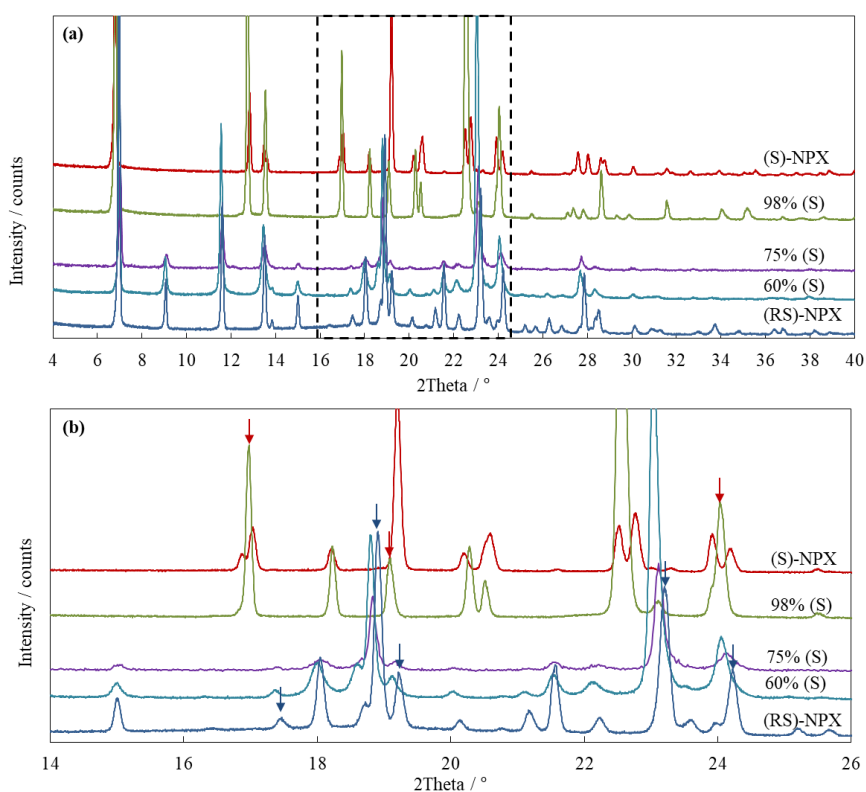
Figure 4.20: (a) The full XRPD-patterns and (b) a close-up of mixtures of (*S*)- and (*RS*)-naproxen after recrystallization from the melt in comparison to the pure components. Red arrows highlight relevant peaks of (*S*)-naproxen while blue arrows those of (*RS*)-naproxen.

In summary, the formation of a partial solid-solution close to the racemic compound and the pure enantiomer is more likely to occur when recrystallised from the melt and is more pronounced for mixtures close to the racemic compound. However, as well certain mixtures that have been recrystallised from solution (acetone) are as well able to form solid-solutions close to the racemic mixture. As a consequence, care should be taken when studying the solution behaviour of mixtures of (S) and (R)-naproxen. Furthermore, the purification of (RS)- and possibly as well (S)-naproxen by recrystallisation could potentially be complicated by miscibility in the solid phase close to the pure substances.

4.3.3 Heat capacities from room temperature to the melt

Heat capacities for the two chiral species of lactide, naproxen and 3ClMA where measured by DSC from room temperature until above the melting temperature. They are used in the following sections to adjust measurements of the melting enthalpy, entropy and Gibbs free energy from melting temperature (see Table 4.5) to one reference temperature, e.g. to solution temperature, via eqs. (31) - (33). They are further required in order to adjust experimental sublimation thermodynamics to one reference temperature as measurements are commonly performed at elevated temperatures (see Figure 2.12).

Experimental details

Heat capacities above room temperature were measured by DSC as described in section 3.2.7. A minimum of four measurements were carried out for each crystalline form using typical masses of 60 to 80 mg ($\pm 10\ \mu g$). The lactide measurements had an average relative deviation of 0.08 % for the racemate and 0.25 % for the enantiomer. For naproxen, the average relative deviation was 0.4 % for the racemate and 1.2 % for the enantiomer; for 3ClMA the average relative deviation was around 0.7 % for both compounds. To support the experimental high temperature 3ClMA heat capacities additional DSC measurements of the related (R)- and (RS)-mandelic acid molecules were performed in between 298 K and 370 K using the same measurement procedure. The relative deviation of three independent measurement series was 0.2% (R)- and (RS)-mandelic acid.

Results and discussion

Measurement results of the heat capacities of (S)- and (RS)-lactide, (S)- and (RS)naproxen as well as (R)- and (RS)-3ClMA from room temperature to above melting temperature are summarized in Figure 4.21 (a-c). The experimental uncertainty is displayed with black bars but is most of the time smaller than the symbols. Primary data is summarized in Appendix (Table 7.1 to Table 7.4).
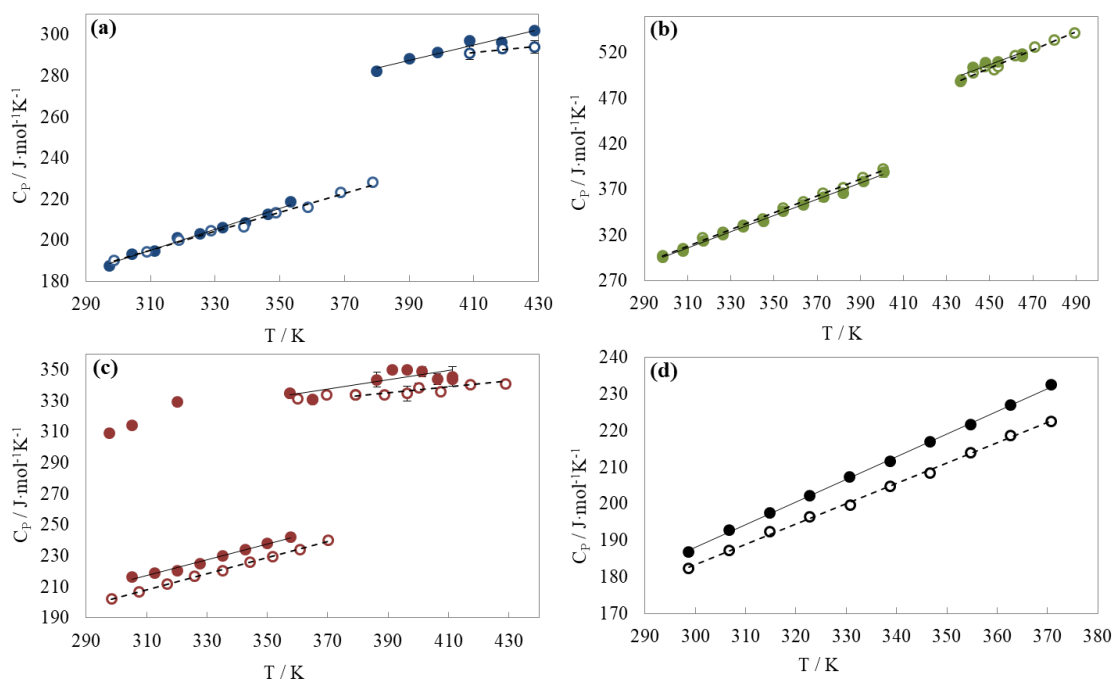
Figure 4.21: Experimental heat capacities of **(a)** (*S*)- and (*RS*)-lactide, **(b)** (*S*)- and (*RS*)-naproxen and **(c)** (*R*)- and (*RS*)-3ClMA from room temperature to above melting temperature. In addition, solid-state heat capacities of **(d)** (*R*)- and (*RS*)-mandelic acid are shown. Full circles (●) correspond to the enantiomers and open circles (○) to the racemic compounds.

This work's result of lactide (Figure 4.21 a) is in good agreement with literature[221, 226] with deviations of 2 to 3 % and thus within the 1 %-5 % accuracy of DSC[227] heat capacity measurements. Heat capacities of the two solid forms are indistinguishable by eye but there are small differences in the melt phase which have a smaller temperature dependency in comparison to the crystalline solid.

In case of naproxen, slightly different experimental heat capacities have been reported in literature for temperatures above 90°C.[82] Literature values are around 5 % smaller when compared to this work's (*S*)-naproxen (Figure 4.21 b). As details on the sample are missing[82], the reported data is not further discussed in this work. Temperature dependency of the heat capacities of the melt and the solid are, unlike for the lactides, very similar.

3ClMA is the only substance studied where heat capacities of the solid racemate and enantiomer differ significantly. To strengthen these findings additional measurement of the related (*S*)- and (*RS*)-mandelic acid (see Figure 4.21 d) have been performed which give similar results. Even though it has been suggested that 3ClMA decomposes at 92 °C[222], caloric measurements of the melt could be performed. Furthermore, the subcooled melt of 3ClMA could be measured as recrystallization from the melt has been found to be kinetically hindered. Hence, one measurement series of the subcooled melt between room temperature and 360 K for the enantiomer has been performed. Unrealistic large heat capacities in between 340 K and 350 K (not shown in Figure 4.21 c as they are out of scale) indicate an additional slow phase transition in between 330 K and 360 K which is possibly related to vitrification from the subcooled melt into an amorphous form.

Table 4.6: Heat capacities of the solid and molten enantiomer and racemic compound and their differences for lactide, naproxen and 3ClMA. Given values correspond to the linear regression of the primary measurement data using eq. (65). Thermal corrections between melting temperature and 298 K have been determined via eqs. (31) and (32) using ΔC_P^{l-s} at T_{melt}. Heat capacities and entropies are given in J mol^{-1}K^{-1} while enthalpies and Gibbs free energies are given in kJ mol^{-1}.

Compounds	C_P^s		C_P^l	ΔC_P^{l-s}	ΔH_{corr}	ΔS_{corr}	ΔG_{corr}
	298 K	T_{melt}	T_{melt}	T_{melt}	298 K	298 K	298 K
(S)-lactide	189.0	225.5	279.8	54.2	-5.4	-15.6	-0.7
(S)-lactide[221]	181.5	219.5	317.0	97.5			
(RS)-lactide	189.3	235.4	289.7	54.3	-3.9	-11.6	-0.4
(RS)-lactide [226]	184.3	243.7	297.1	53.4			
(RS)-(S)	0.4	9.9	9.9	0.0	-1.5	-4.0	-0.3
	2.8	24.2	-19.9	-44.1			
(S)-naproxen	295.6	412.5	482.6	70.1	-9.2	-25.5	-1.6
(RS)-naproxen	296.9	417.8	488.9	71.1	-9.3	-25.9	-1.6
(RS)-(S)	1.3	5.2	6.2	1.0	0.1	0.4	0.0
(S)-3ClMA	211.1	251.0	339.6	88.6	-8.2	-24.0	-1.1
(RS)-3ClMA	201.9	250.0	335.4	85.4	-6.7	-19.9	-0.7
(RS)-(S)	-9.2	-1.0	-4.2	-3.2	-1.6	-4.1	-0.4

Detailed discussions on the heat capacity differences between the racemic and enantiopure crystals of all three substances can be found in section 4.3.4 together with the results of the low-temperature heat capacity measurements which are presented in the following section. The absolute molar heat capacities of the solid and the melt at 298 K and T_{melt} are required in order to adjust melting enthalpies and entropies to the solution temperature. The temperature-dependent behaviour of the molar heat capacities of both states were assumed to be linear in between reference temperature and the melt and have been correlated by equation (65):

$$C_P = A + B \cdot T / K \tag{65}$$

The resulting heat capacities of the crystalline solid and liquid melt are summarized in Table 4.6. Heat capacity differences between the solid and the melt, ΔC_P^{l-s}, at melting temperature have been used to determine the thermal corrections that are required to adjust melting enthalpies and entropies from melting temperature to 298 K. ΔC_P's are in good agreement with literature[226] for (RS)-lactide while there are significant differences for (S)-lactide[221]. The measured ΔC_P^{l-s} of the four molecules are in between 54 to 88 J mol^{-1}K^{-1} which agrees with an average ΔC_p value for 117 organic molecules[83] of $\Delta C_P^{l-s} = 84 \pm 57$ J·mol^{-1}K^{-1}. The resulting thermal corrections are summarized in Table 4.6 and can be used to calculate the corrected melting enthalpies, entropies and Gibbs free energies when combined with the melting properties of Table 4.5. Influences of the thermal corrections are small for lactide, around -1 kJ·mol^{-1} for 3ClMA but especially significant for naproxen which hast the highest melting temperature where $\Delta G_{corr} = -1.6$ kJ·mol^{-1}. For 3ClMA and naproxen thermal corrections lower the Gibbs energies of

melting by around 17 % compared to the ΔG_{melt} at melting temperature. Hence, they are of relevance for both substances when calculating solubilities via the melt cycle.

4.3.4 Low-temperature heat capacities

In addition, the high temperature heat capacities discussed before, low-temperature heat capacities for the two chiral crystals of lactide, naproxen and 3ClMA where measured by direct heat pulse calorimetry (DHPC) from cryogenic temperatures (from ~1.8 K) until 200 Kelvin. They are essential in order to correct calculations of the lattice energy, which are usually performed for the static lattice at 0 K, to room temperature via the sublimation cycle (see Figure 2.12 and eqs. (43) - (44)). In comparison to this works experimental investigations, calculations using two different computational approaches have been performed. In a first approximation, molecular vibrations are assumed to be the same in the gas and in the solid phase. This approximation is computationally less demanding since the separated rigid-body lattice modes can be computationally efficient modelled for the crystal and electronic structure calculations are only required for the isolated molecule only.[147, 228] This will be referred to as the separated model, ψ_{mol}. Within the second model the crystal packing can modify both molecular and phonon modes.[229] Calculating the coupled vibrational modes requires the use of periodic electronic structure calculations of the whole crystal. This method will be referred to as the electronic model, ψ_{crys}. Further computational details on the ψ_{mol} and ψ_{crys} model are given in section 2.7.2.

Experimental details

Low-temperature heat capacities for enantiopure and racemic naproxen and 3ClMA crystals were measured by means of direct heat pulse calorimetry (DHPC) from 2 K to 200 K. A commercially available relaxation calorimeter has been used the Physical Property Measurement System (PPMS) from Quantum Design. The measurement method is described in section 3.2.7. Experiments were performed at 42 temperature points between 2 K and 200 K including three replicates at each temperature. Naproxen heat capacities were measured in samples of (S)-naproxen and (RS)-naproxen with sample masses of 3.16±0.01 mg and 2.80±0.01 mg, respectively. Heat capacities of 3ClMA were measured in samples of (R)-3ClMA and (RS)-3ClMA with sample masses of 3.02±0.01 mg and 1.99±0.01 mg, respectively. For both substances relative deviations between the three consecutive measurements are smaller than 1% for temperatures below 50 K and smaller than 0.5% for temperatures between 50 K and 200 K. Heat capacities of lactide could not be measured in the PPMS due to the high vapor pressures of lactide[230] and thus possible sublimation within the low-pressure environment. Instead, published experimental data for (S)-lactide and (RS)-lactide measured in an adiabatic low-temperature calorimeter have been taken from literature.[221, 226]

Results and discussion

Figure 4.22 (a-c) shows the measurement results of the temperature-dependent heat capacities of both chiral species of lactide, naproxen and 3ClMA. Primary experimental data is given in Appendix (Table 7.5 and Table 7.6). The low-temperature heat capacities are complemented by the before discussed DSC results (see Figure 4.21) of the crystalline solids. For all substances the heat capacities follow Debye's cubic law ($C_P \sim A \cdot T^3$) at very low temperatures then increase linearly for temperatures greater than 100 K. Naproxen has a significantly larger heat capacity than 3ClMA and lactide, reflecting the larger number of atoms per molecule, though the specific heat of the molecular crystals are all in the range of 1-1.3 $J \cdot g^{-1} K^{-1}$ at 298 K.

Figure 4.22 also contains calculated temperature-dependent heat capacities from the ψ_{mol} method. The heat capacities are calculated via a hybrid Einstein-Debye model (eq. (59)) using computed molecular and lattice vibrational frequencies. Contributions of the lattice and molecular vibrational frequencies are independently displayed for all six crystalline solids which in sum give the total calculated isobaric heat capacity, as thermal expansion is neglected. The calculations nicely reproduce the temperature dependence up to 300 K and also display the differences in magnitude between the different organic molecules. Calculated heat capacities of the ψ_{crys} model where molecular and lattice vibrations are not decoupled are very similar to those of ψ_{mol} model and thus not additionally displayed in Figure 4.22. Further information and numeric values of both computational methodscan be found in ref. [150]. Furthermore, the ψ_{mol} and ψ_{crys} heat capacities are compared in detail when discussing heat capacity differences between the enantiomer and the racemate in the following section 4.3.5.

With increasing temperature, the calculations appear to systematically underestimate the heat capacities. This is consistent with a recent study where experimental solid state heat capacities for small molecule crystals were underestimated in 85% of the cases.[231] At temperatures above 150 K the lattice modes are almost completely saturated resulting in final values of $C^s_{P,lattice} = 49.4 - 49.6$ kJ mol^{-1}K^{-1}. This is close to the assumption of mode saturation in the 2RT-correction (eq. (55)) which is $C^s_{P,lattice} = 6$ R $= 49.9$ kJ mol^{-1}K^{-1}. Hence, only the molecular vibrations are responsible for the temperature dependency at elevated temperatures.
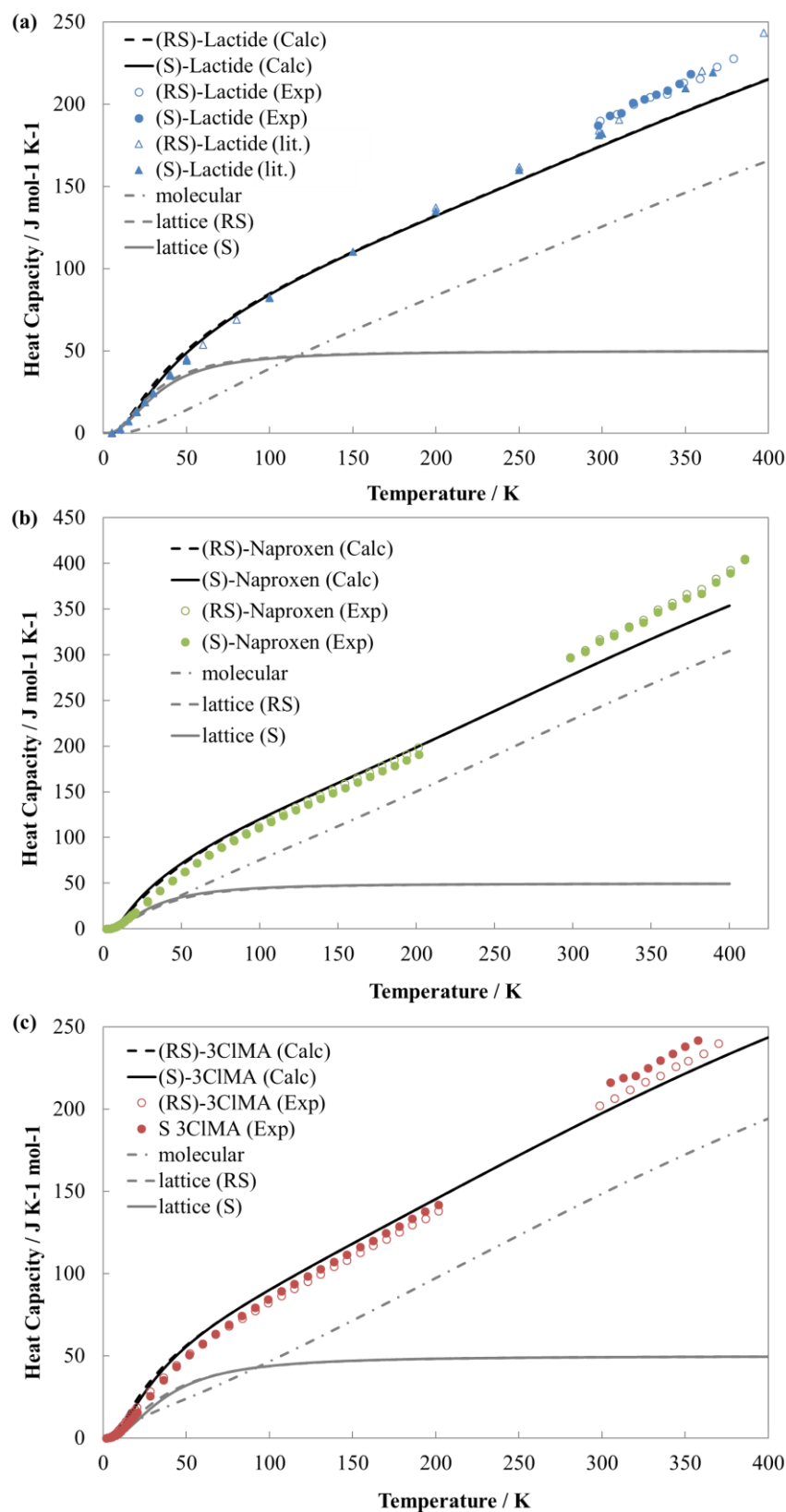
Figure 4.22: Experimental (exp) heat capacities at constant pressure (ΔC_P^s) compared with calculated heat capacities at constant volume (ΔC_V^s) by the ψ_{mol} model (calc) of the racemic (*RS*) and enantiopure (*S*) crystalline solid of **(a)** lactide, also including additional data from references[221, 226], **(b)** naproxen with inclusion of experiments for an unspecified form of naproxen[82] and **(c)** 3-chloromandelic acid. Experimental errors are too small to be visible in this plot but are given in Appendix (Table 7.1 to Table 7.6).

However, the systematic underestimation of the high temperature heat capacities might be as well partially attributed the experimental results as there is a systematic gap between the low temperature DHCP and the high temperature DSC measurements. For DHCP measurements, thermal coupling between the sample and the measuring platform is essential. However, for measurements of naproxen and 3ClMA thermal coupling never fell below 90% which has to be guaranteed for a DHCP measurement in a PPMS system.[232] Benzoic acid has been used as a test substance in order to investigate systematic errors in DHCP results and only a slight underestimation at room temperature compared to literature data could be observed. There is a general trend of PPMS measurements on small powdered samples to slightly underestimate heat capacities.[233] Simultaneously, the DSC measurement method tends to slightly overestimate heat capacities of the test measurements with benzoic acid and sapphire. It can be summarized that both effects could cause a systematic error in experimental methods when extrapolating the low temperature results to high temperature and vice versa. The systematic gap between the DHCP and DSC measurements is in total around 4 % and hence still within the range of precision for heat capacity measurements.[227] This deviation is most apparent at high temperature and also detectable for lactide data from literature[221, 226]. Hence, the systematic experimental error contributes to differences between experiment and theory but is unlikely to be responsible for the entire calculations error.

Another reason for an underestimation of the calculations is the neglect of thermal expansion within eq. (59). Even though thermal expansion can be neglected at low temperatures, in the high temperature region the neglect of thermal expansion can make an error of order 20 J mol^{-1} K^{-1}. This would lower the calculated heat capacity by roughly ~ 5 %. As a consequence, it could account for much of the underestimation of the calculations heat capacities.[150] This is consistent with a recent computational study on acetic acid and imidazole which concluded that zero-point energy and thermal expansion can affect the final free energy corrections by a few kJ mol^{-1}.[234]

4.3.5 Heat capacity differences

In this section the heat capacity differences between the racemic and enantiopure substances, $\Delta_{RS\text{-}S}C_P^s$, are discussed as they affect the difference in Gibbs free energy of sublimation between both chiral species, $\Delta_{RS\text{-}S}\Delta G_{subl}$, and thus as well the eutectic composition (see eq. (23)). Figure 4.23 shows the experimental and computed heat capacity differences between the enantiopure and racemic crystals for the three substances between 2 K and 200 K. Below 100 K, experimental $\Delta_{RS\text{-}S}C_P^s$ are between -1 and 3 kJ mol^{-1} K^{-1} and differ markedly between the three molecules. Even the sign of the heat capacity differences is temperature-dependent, with 3ClMA showing the largest differences from +3 kJ mol^{-1} K^{-1} at ~20 K to -4 kJ mol^{-1} K^{-1} at T > 150 K. The heat capacities for naproxen above 100 K have significant error bars which may be attributed to a loss in thermal coupling.[232] For all substances the calculated heat capacities qualitatively reproduce the differences between enantiomer and racemate at the lowest temperatures.
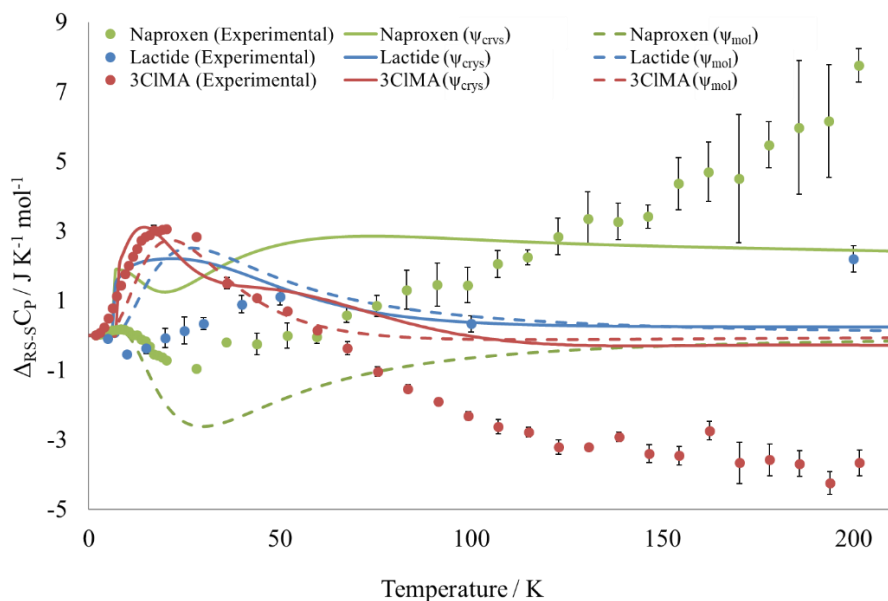
Figure 4.23: Low temperature heat capacity differences, $\Delta_{RS\text{-}S}C_P^s$, between racemic compound and the enantiomer for the three chiral molecules. Experimental results are shown with experimental uncertainty (dots) and compared with calculated values from the ψ_{crys} (solid lines) and the ψ_{mol} method (dashed lines).

The high temperature heat capacity differences in the range of 300-370 K are shown in Figure 4.24. They correspond to the experimental DSC measurement which have been extrapolated using linear correlations (see Figure 4.21) to obtain the capacity differences at 298 K which are given in Table 4.7. Differences are pronounced only for 3ClMA. The heat capacity of the enantiomer at 298 K is 9.2±2.2 J·mol^{-1}·K^{-1} which is 4.5% larger than that of the racemic crystal. A significant heat capacity difference has been reported in literature as well for the structurally related mandelic acid.[235] In order to confirm these findings and to compare them to the 3ClMA results measurement for (RS)- and (R)-mandelic acid have been repeated in this work (see Figure 4.21) using the same DSC method as for the other substances. This work's results are in good agreement with the previous results[235] and give a slightly smaller heat capacity difference at 360 K as shown in Table 4.7. The heat capacity difference between enantiopure and racemate changes with temperature for mandelic acid and is less severe at 298 K in comparison to the temperature independent heat capacity difference of 3ClMA (see Figure 4.24). The sign and magnitude is comparable between mandelic acid and 3ClMA. For lactide and naproxen, the heat capacity differences at room temperature are within experimental uncertainty. In case of lactide, the heat capacity of (RS)-lactide is only 0.6±0.6 J·mol^{-1}K^{-1} larger than that of the enantiomer, which is smaller than the published value of 2.8±0.3 J·mol^{-1}K^{-1}.[221, 226] The heat capacity differences of naproxen at room temperature are 1.3±4.9 J·mol^{-1}K^{-1} and within experimental uncertainty.
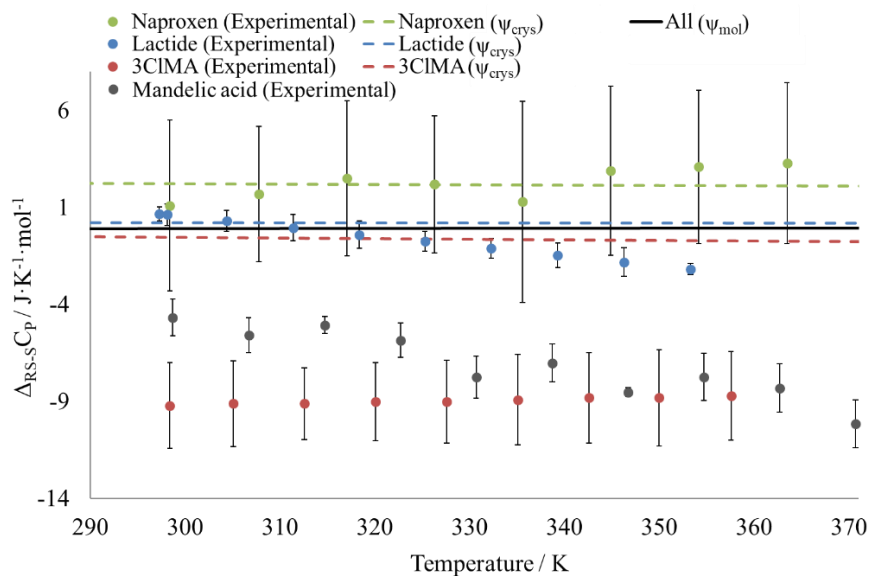
Figure 4.24: Experimental high temperature heat capacity differences, $\Delta_{RS\text{-}S}C_P$, between the racemic and enantiopure crystals. Computational results via the ψ_{crys} method are given by dashed lines in the same colour while results via the ψ_{mol} method are approximately zero for all substances (black straight line).

The computed harmonic rigid-molecule calculations (ψ_{mol} method) in Figure 4.24 all asymptotically approach zero for all compounds. The ψ_{crys} calculations show a difference in the heat capacities at process-relevant temperatures for naproxen which is independent of temperature. However, the overall effect of including the coupling between the molecular and lattice modes is relatively small. Clearly none of the two computational approaches is able to reproduce the heat capacity differences adequately. One reason might be the neglect of thermal expansion to the temperature dependency of the heat capacities of the enantiopure and racemic crystal. As they depend on the crystal structure they can affect as well the differences between the enantiomer and the racemate. However, it was recently shown for a large set of polymorphs, that the impact of thermal expansion on Gibbs energy differences is small in comparison to the effect of vibrational differences.[236]

Heat capacity differences are no rarity as shown in Table 4.7 where this work's measurements of lactide, naproxen, 3ClMA and mandelic acid are compared to literature data of several examples of chiral molecules. Literature data predominantly consists of studies of chiral amino acids which are zwitterionic in the solid state. Set aside both results from Leclercq et. al.[235], heat capacity differences are below 10 J·mol^{-1}K^{-1}. Usually the enantiopure crystal has the higher heat capacity, but for the lactide, naproxen and m-chloro-phenylhydracrylic acid, the racemic compound has the higher heat capacity compared to the enantiomer. The gathered data poses a challenge to computational methods as they have been shown in this work to fail to accurately (or at all in case of the separated ψ_{mol} method) compute high temperature heat capacity differences. A precise calculation of these differences from zero Kelvin to process relevant temperatures however is essential for the calculation of free energy differences between the enantiomer and the racemic compound and, thus, for enantioseparation process design.

Table 4.7: Compilation of heat capacity differences between the racemic compound (rac) and the enantiopure (ep) crystals, $\Delta_{RS\text{-}S}C_P = C_{P,rac} - C_{P,ep}$, from this work and literature.

		T / K	$C_{P,ep}$ (ep) / J·mol^{-1}·K^{-1}	$C_{P,rac}$ (rac) / J·mol^{-1}·K^{-1}	$\Delta_{RS-S}C_P$ / J·mol^{-1}·K^{-1}
Lactide	this work[41]	298.15	189.0±0.5	189.6±0.2	0.6±0.5
Lactide	[221, 226]	298.15	181.5±0.1	184.3±0.4	2.8±0.4
Naproxen	This work[41]	298.15	295.6±4.6	296.9±1.4	1.3±4.8
3ClMA	this work[41]	298.15	211.1±1.6	201.9±1.5	-9.2±2.2
Mandelic acid	this work[41]	298.15	186.9±0.4	182.3±0.8	-4.6±0.9
		360	225.4±0.4	216.6±0.8	-8.8±0.9
Mandelic acid	[235]	360	225.1±0.8	210.6±2.9	-14.1±3.0
Phenylglycine	[237]	298.15	179.1±0.1	177.7±0.1	-1.4±0.1
Valine	[238]	298.15	167.9±0.1	167.3±0.1	-0.6±0.1
Serine	[239]	298.15	134.9±0.1	130.3±0.1	-4.6±0.1
Alanine	[240]	298.15	122.3	121.6	-0.7
Cysteine	[241, 242]	273.15	142.4±0.1	135.6±0.1	-6.8±0.1
Erythro-phenylglyceric acid	[235]	350	279.7±3.3	251.0±5.4	-36.7±6.3
m-Chloro-phenylhydracrylic acid	[235]	305	222.6±2.1	224.7±0.8	2.1±2.3

Analysis of the origin of heat capacity differences

The absolute heat capacities are related to the integral of all vibrational movements of the molecules within the unit cell. The separated ψ_{mol} model assumes that the lattice modes are sufficiently separated from the molecular modes and thus are decoupled in the Einstein-Debye model in eq. (59). However, Figure 4.25 shows that some of the calculated molecular and lattice vibrational frequencies are similar in magnitude, which can affect one another. Even for the "rigid" lactide, there are some ring bending modes that are of similar frequencies to the lattice modes. For naproxen, the low frequency molecular modes correspond to rotations of the propionic acid side chain and bending of the naphthyl group. The low frequency molecular modes of 3ClMA are rotations of the flexible alpha-hydroxy acid sidechain and out-of-plane vibrations of the chlorine atom. The low frequency lattice modes determine the heat capacities at low temperatures. As a consequence, a coupling can affect the heat capacity differences in that temperature range (see Figure 4.23). Numeric values have of the molecular and lattice vibrations within the ψ_{mol} and ψ_{crys} can be found in ref. [150].
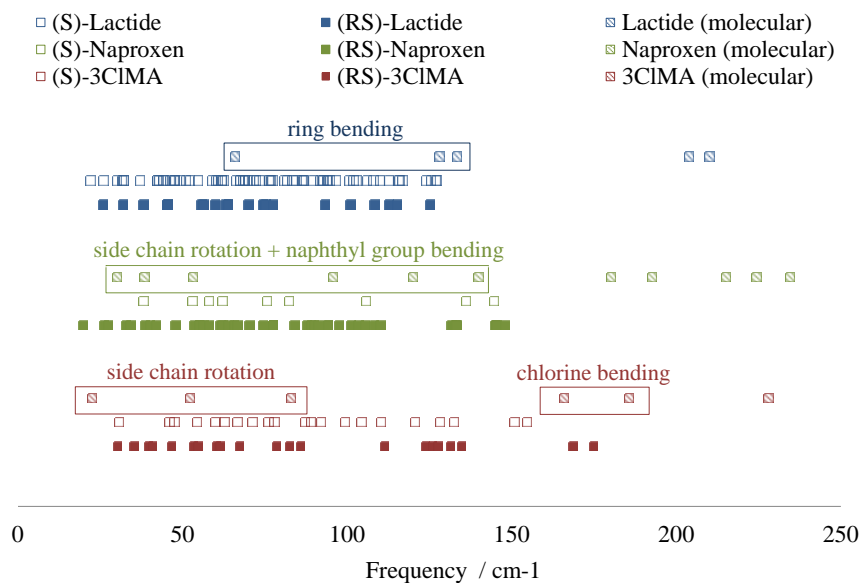
Figure 4.25: Comparison of the rigid-molecule lattice frequencies of the model ψ_{mol} model for the enantiopure and racemic crystals of lactide, 3ClMA and naproxen with their molecular low frequency modes.

All three molecules pack differently in the racemic and enantiopure structures (see Figure 4.13). This affects the lowest frequency modes which have been shown to be very sensitive to the choice of the computational method.[41] One source of errors comes from assuming that the molecule is rigid. Thus, the results of ψ_{mol} and ψ_{crys} are more consistent for the more rigid lactide, which has comparably isotropic and weak intermolecular interactions.

For the high temperature heat capacities, only the high frequency molecular modes are relevant, as the low frequency lattice modes have become saturated. Only the electronic ψ_{crys} calculations give small differences in the high frequency modes that lead to a small difference in heat capacities at process-relevant temperatures for naproxen and 3ClMA, but none for lactide (Figure 4.24). This can be experimentally resolved by the solid-state Raman spectra which can be distinct for polymorphs[243] and, thus, as well for the enantiomer and the racemic compound. Differences between the spectra of the enantiomer and the racemate are related to differences in vibrational frequencies of the crystal which can be responsible for differences in heat capacities. Solid-state Raman spectra were measured for enantiopure and racemic crystals of the three substances and are shown in Figure 4.26.

For naproxen and 3ClMA there are detectable differences between the crystal forms, in particular at higher frequencies i.e. the C=O around 1600-1800 cm^{-1} and O-H around 3000 cm^{-1}. On the contrary, for lactide the enantiopure and racemic crystals display an almost identical Raman spectrum. Such differences in the higher frequency molecular modes between the racemic and enantiopure crystals are one reason for the heat capacity differences at high temperatures shown in Figure 4.24. Thus, Raman spectra can be used to test whether heat capacity differences at high temperatures are likely before applying the costlier calorimetric measurements.
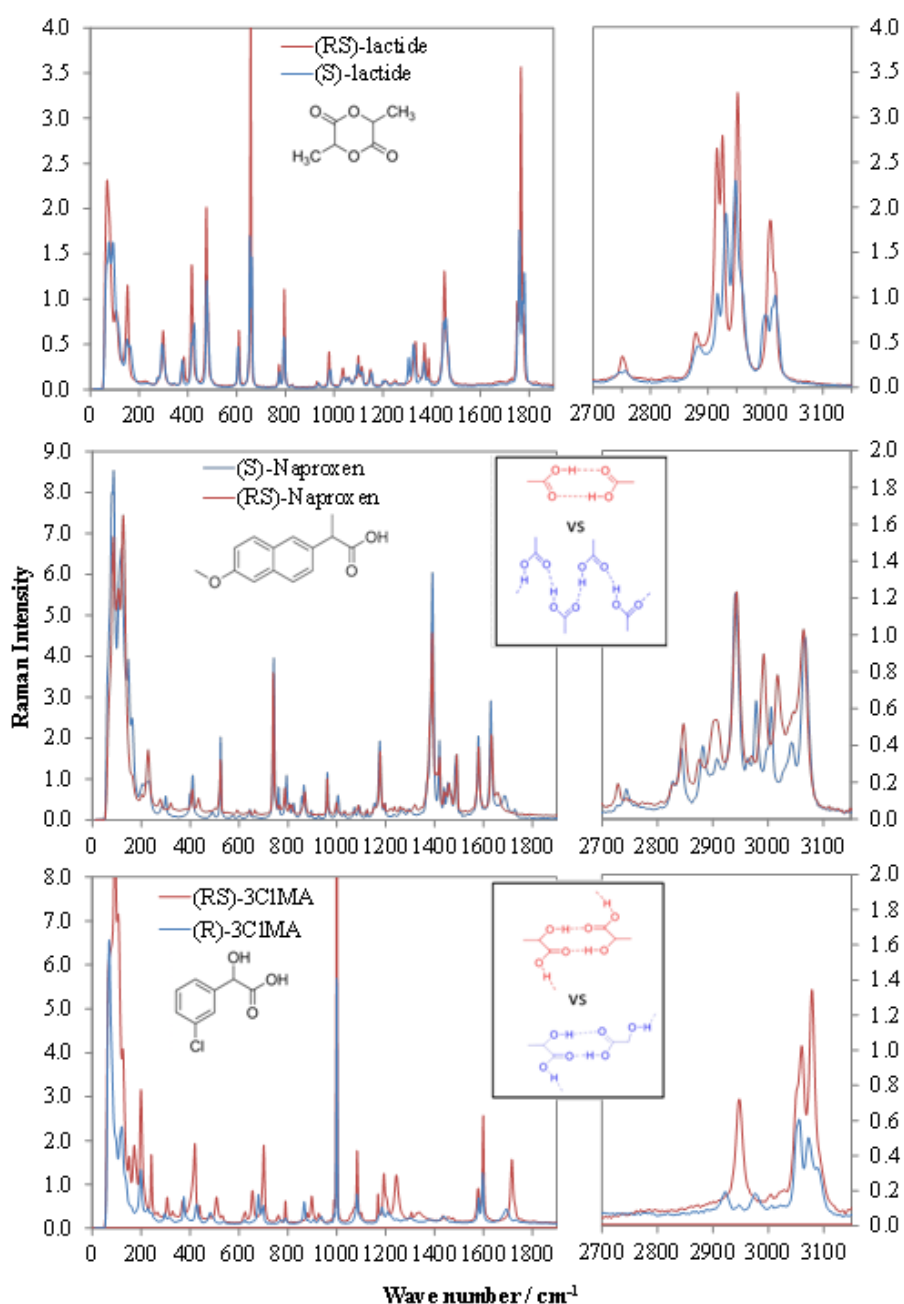
Figure 4.26: Overlay of the solid-state Raman spectra of the racemic and enantiopure species of the three compounds showing the relevant regions between 0-1800 cm^{-1} and 2700-3150 cm^{-1}. The inset illustrates the different hydrogen bonding motifs, responsible for the changes in the spectra at higher "molecular" frequencies i.e. the C=O around 1600-1800 cm^{-1} and O-H around 3000 cm^{-1}.

4.3.6   Sublimation Thermodynamics

In this section the sublimation thermodynamics of the three chiral model substances (Figure 4.12) are discussed. Experimental data is compared to calculations using *ab-initio* quantum chemistry methods. The Gibbs free energies of sublimation from experiment and computations are subsequently used in section 4.4 and 4.5 to calculate absolute and relative solubilities via the sublimation cycle, respectively.

Experimental sublimation thermodynamics

Sublimation enthalpies and Gibbs free energies are directly correlated to the sublimation vapor pressures via eq. (38) which are accessible by experiment. Experimental vapor pressures are available for enantiopure and racemic lacide in literature[230]. For naproxen, they have been determined in the frame of this work using the transpiration method according to section 3.2.6. For 3ClMA measurements have been conducted with the same experimental method. Unfortunately, measurements failed due to decomposition of the samples before sublimation.
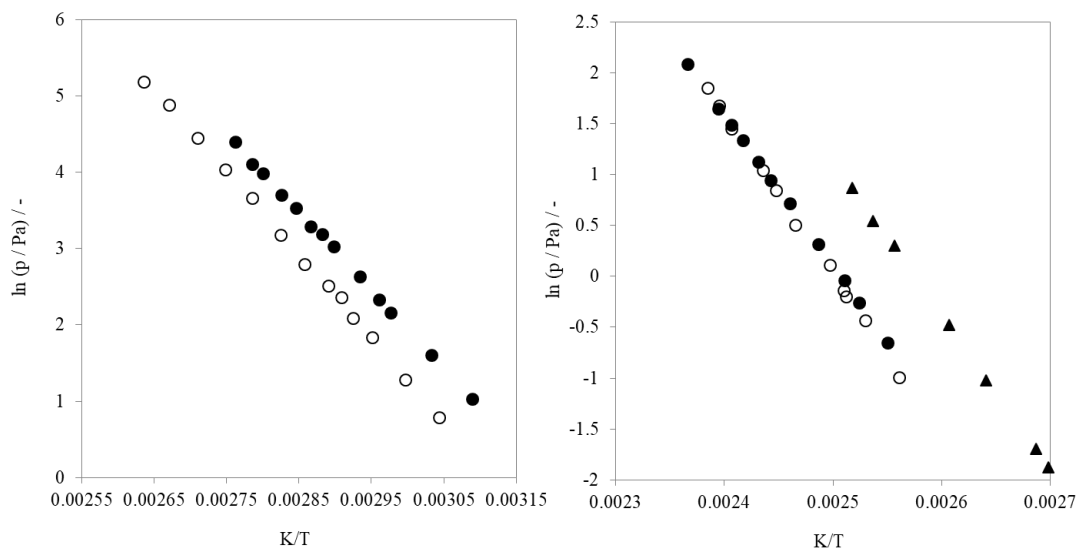
Figure 4.27: Experimental vapor pressures as a function of the reciprocal temperature of (●) the enantiomer and (○) the racemic compound of (left) lacide[230] and (right) naproxen[41]. This works naproxen results are compared to measurements of (▲) (S)-naproxen from literature[244].

For lactide, the vapor pressures of the racemic compound and the enantiomer differ significantly with the racemic compound having significantly larger vapor pressures. On the contrary, the absolute vapor pressures of (RS)- and (S)-naproxen (Figure 4.27, right) are very similar. However, they are still distinguishable especially at low temperatures where vapor pressures of the enantiomer are slightly higher in comparison to the racemic compound. Absolute vapor pressures from literature of (S)-naproxen[244] are substantially larger in comparison to this work's results but their temperature dependencies are comparable. Absolute vapor pressures p_i were correlated according to literature[160] via eq. (66).

$$\ln\left(\frac{p_i}{1\,\text{Pa}}\right) = \frac{a}{R} + \frac{b}{R \cdot T} + \frac{\Delta C_P^{g-s}}{R}\ln\left(\frac{T}{298\,K}\right) \tag{66}$$

where a and b are two adjustable parameters. The heat capacity differences between the gaseous and the crystalline phase ΔC_P^{g-s} for lactide and naproxen have been taken from literature[41, 230] where they have been determined at 298 K from the experimental solid-state heat capacities and calculated ideal gas heat capacities. The heat capacity differences

at 298 K are summarized in Table 4.8 together with the sublimation thermodynamic functions. They are qualitatively in agreement with a suggested averaged heat capacity difference of 117 molecules which was shown[83] to be $\Delta C_P^{g-s} = 32.7 \pm 45.7$ J mol^{-1} K^{-1}.

Gibbs free energies of sublimation are accessible via eq. (38) when referring the sublimation vapor pressures to a reference pressure of $p_0 = 1$ bar. Sublimation enthalpies have been taken from the dependency of ln p_i to the reciprocal temperature, 1/T, according to the Clausius-Clapeyron equation. They have been extrapolated using ΔC_P^{g-s} according to eq. (41). The resulting sublimation enthalpies, entropies and Gibbs free energies of lactide and naproxen are summarized in Table 4.8. Apart from their derivation from the experimental transpiration vapor pressures, ΔH_{subl} have been additionally determined experimentally by thermogravimetry (TGA) for the naproxens. The TGA results are in a good agreement with the results of the transpiration method. In Table 4.8 a mean average ΔH_{subl} (298 K) has been determined for the enantiomer and the racemate as discussed in more detail in literature[41].

Table 4.8: Experimental vapor pressures and sublimation enthalpies of lactide and naproxen at 298.15 K. The free energy of sublimation at T = 298.15 K was calculated by $\Delta G_{subl} = - RT$ $\ln(p^{298K}/p_0)$, where $p_0 = 1$ bar. Values in brackets have been derived from experimental solubilities at 298 K as described in section 2.7.2.

	$\ln(p^{298K}/p_0)$	ΔC_P^{g-s}	ΔH_{subl}	$T\Delta S_{subl}$[a]	ΔG_{subl}
	-	kJ mol^{-1} K^{-1}	kJ mol^{-1}	kJ mol^{-1}	kJ mol^{-1}
(RS)-lactide[230]	-14.10 ± 0.03	28.4	91.6 ± 0.4 (93.4)	56.6 (56.5)	35.0 ± 0.1 (36.8)
(S)-lactide[230]	-13.21 ± 0.03	28.4	86.3 ± 0.4 (91.8)	53.5 (57.1)	32.8 ± 0.1 (34.7)
(RS-S)	-0.9 ± 0.04		5.3 ± 0.6 (1.6)	3.1 (-0.5)	2.20 ± 0.1 (2.1)
(RS)-naproxen[41]	-25.26 ± 0.04	41.9	135.3 ± 1.3 (133.5)	72.7 (69.8)	62.6 ± 0.1 (63.7)
(S)-naproxen[41]	-24.28 ± 0.02	40.0	129.1 ± 0.9 (133.2)	68.9 (70.5)	60.2 ± 0.0 (62.7)
(S)-naproxen[244]	-23.7	-	128.3 ± 1.5	69.8	58.5
(RS-S)	-1.0 ± 0.04		6.2 ± 1.6 (0.2)	3.8 (-0.7)	2.41 ± 0.1 (1.0)
(RS)-3ClMA	n.a	-	(155.1)	(65.8)	(49.3)
(S)-3ClMA	n.a	-	(113.8)	(66.1)	(47.7)
(RS-S)	n.a	-	(1.3)	(-0.3)	(1.6)

[a] calculated from $\Delta G_{subl} = \Delta H_{subl} - T\Delta S_{subl}$, where T = 298.15 K.

Vapor pressure measurements of 3ClMA are not available due to decomposition before sublimation. As an alternative, experimental "reference" quantity sublimation enthalpies were calculated from experimental solubility data for all six crystals via the sublimation cycle (Figure 2.12) and thus via $\Delta G_{subl,solub} = -RT \ln x_{exp} - \Delta G_{solv}$ and $\Delta H_{subl,solub} = -RT \ln x_{exp} - \Delta G_{solv} + T\Delta S_{subl}$. Further details on the calculation of sublimation thermodynamics

from solubilities are given in section 2.7.2. The primary solubility data and resulting "experimental" sublimation free energies are summarized in Table 7.7 in the appendix. Further information on the calculation of the solvation free energies is given later in section 4.4 where they are used for solubility prediction. The sublimation free energies and sublimation enthalpies for lactide and naproxen that have been estimated from experimental solubilities are in good agreement with those from experimental vapor pressures. Based on the above, they are used in the following as an "experimental" reference for 3ClMA where direct sublimation data is missing.

Calculated sublimation thermodynamics

In this section, calculated sublimation thermodynamic quantities (ΔH_{subl}, $T\Delta S_{subl}$ and ΔG_{subl}) are discussed and compared to experimental reference data from Table 4.8. Calculated lattice energies, E_{latt}, were combined with the calculated zero-point vibrational energies (E_{ZPE}) as well as the calculated heat capacity corrections within the atomistic (ψ_{mol}) and electronic (ψ_{crys}) model in order to determine the sublimation thermodynamics at 298 K. Detailed information on the computational ψ_{mol} and ψ_{crys} methods are summarized in section 2.7.2. Both methods have been previously used for calculating the solid-state heat capacities (see Figure 4.22). The experimental solid-state heat capacities were evaluated within the mixed "exp/theory" model. They are combined with calculated ideal gas heat capacities of the ψ_{mol} method as well as the lattice energies and zero-point energies of the ψ_{mol} and ψ_{crys} methods resulting in the so-called ψ_{mol} (exp/theory) and ψ_{crys} (exp/theory) method. Further details of the integration of the experimental solid-state heat capacities and their combination with the exclusively computational ψ_{mol} and ψ_{crys} methods are given in section 2.7.2.

The final computational results of the absolute sublimation (a) enthalpies and (b) Gibbs free energies using the pure computational methods (ψ_{mol} and ψ_{crys}) and the mixed "exp/theory" methods are depicted in Figure 4.28. Selected data is given in Table 4.9 while all primary data is summarized in Table 7.19 in the appendix. Computations are compared to experiments[41, 230] and for 3ClMA to the recalculated values from experimental solubilities as discussed before in Table 4.8. For all molecules, absolute sublimation enthalpies depend strongly on the method used to calculate lattice energies which is the dominant quantity while thermal corrections H_{corr} play a minor role (see Figure 4.28a). The ψ_{mol} method gives worse enthalpies (RMSE = 10.1 kJ mol^{-1}) than the more sophisticated electronic method (RMSE = 5.2 kJ mol^{-1}) whose accuracies are close to the uncertainties of sublimation experiments (4.9 kJ mol^{-1})[94] (see Table 4.9). The utilization of experimental heat capacities only marginally improves the calculations for the atomistic (RMSE = 9.6 kJ mol^{-1}) as well as the electronic method (RMSE = 5.1 kJ mol^{-1}).
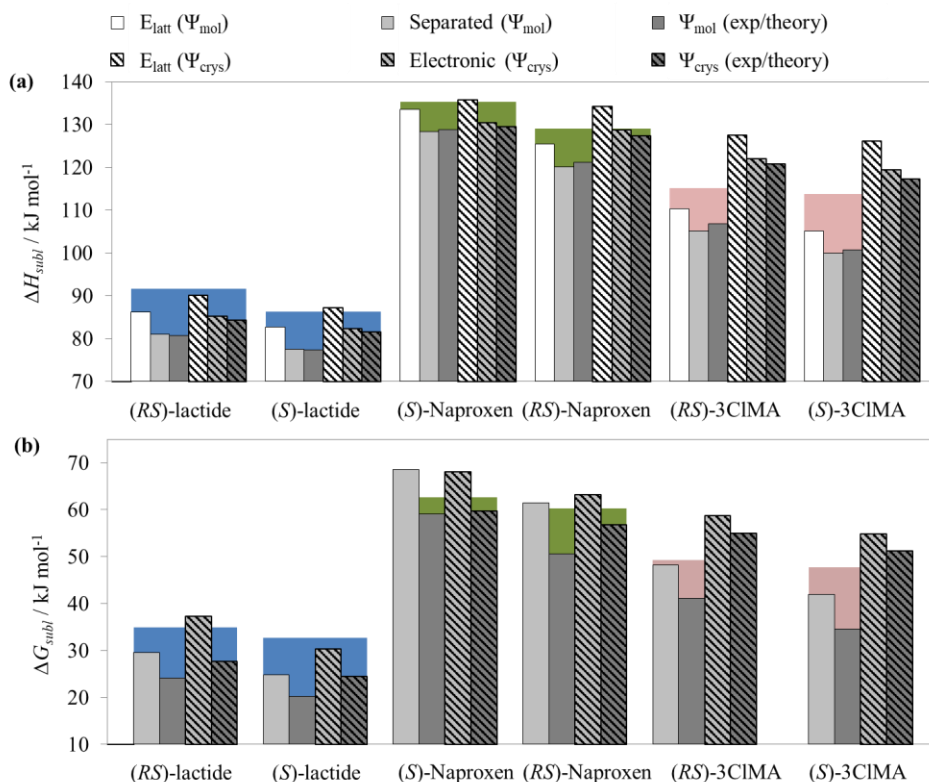
Figure 4.28: Calculated **(a)** Sublimation enthalpies, ΔH_{subl}, and **(b)** Gibbs free energies of sublimation, ΔG_{subl}, in comparison to the experimental data from Table 4.8 (blue = lactide[230]; green = naproxen[41]; red = 3ClMA – as 3ClMA decomposes estimations from experimental solubilities are used). The calculations are based on the pure ψ_{crys} and ψ_{mol} method and when combined with experimental solid-state heat capacities on the so-called mixed "exp/theory" methods.

The importance of a more complete model to determine the thermal corrections over the widely used 2*RT*-approximation becomes obvious in Figure 4.29 (a) where all absolute thermal corrections are summarized. Recently, this approximation has been queried for a set of smaller sized molecular crystals[85, 97, 194] where different calculations of ΔH_{corr} vary in between 1 to up to 9 kJ mol^{-1} and deviations to the 2*RT*-approximation are in the order of a few kJ mol^{-1} (see Figure 4.8). The literature data indicates that method related differences are largest in cases where vdW-interactions or H-bonding dominate in the crystal. However, there is a clear correlation between the differences in the thermal corrections with the molecular flexibility and packing in racemic and enantiopure crystal structures. The interactions in the crystals of rigid lactide are dominated by isotropic vdW-interactions. As a consequence, the ψ_{crys} and ψ_{mol} calculations seem to be independent to the method used and results are close to the 2*RT*-approximation. However, for naproxen and 3ClMA the different hydrogen bonding in the two crystals and increasing vibrational flexibility lead to larger differences in thermal corrections. For 3ClMA the largest deviations are observed and differences to the harmonic approximation are up to 4 kJ mol^{-1} while Naproxen results are somewhat in between the two extreme cases. In both cases the deviations come from the zero-point energies and thermal energies to a similar extent and hence do not only depend on the heat capacities

of the crystal. Based that it can be concluded that thermal corrections appear to be rather dependent on the complexity, on the molecules, and of the crystal packing, and is most apparent for the flexible 3ClMA.
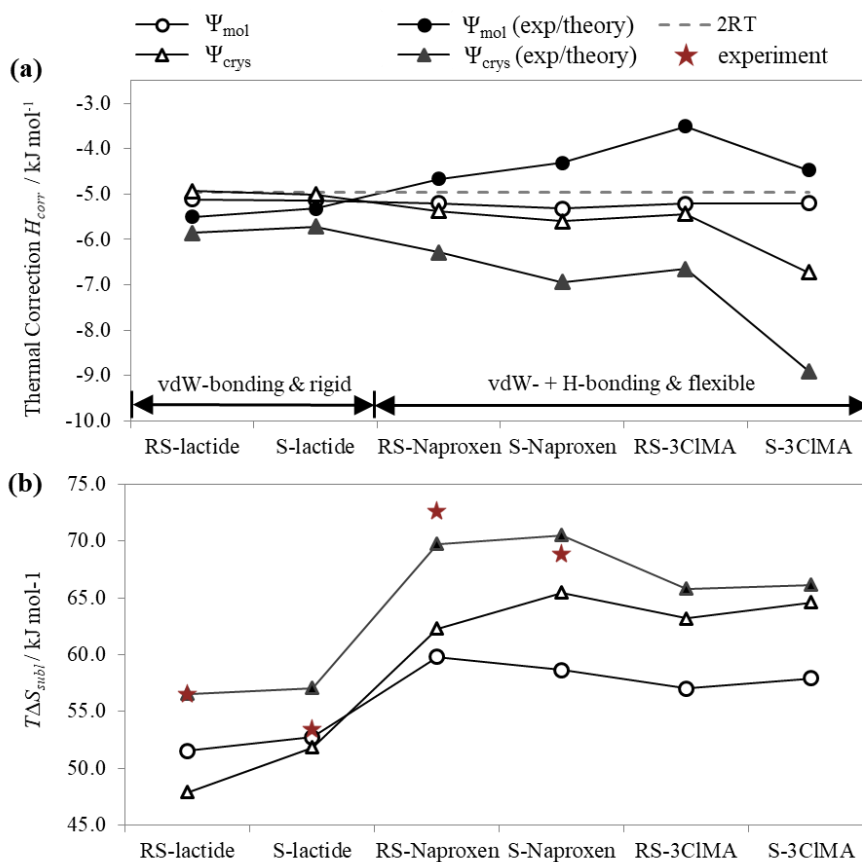
Figure 4.29: **(a)** Thermal enthalpy corrections, ΔH_{corr}, and **(b)** sublimation entropies, $T\Delta S_{subl}$, of the racemic and enantiopure crystals. The calculations are based on the pure ψ_{crys} and ψ_{mol} method and when combined with experimental solid-state heat capacities on the so-called mixed "exp/theory" methods.

In order to calculate the sublimation free energies of Figure 4.28 (b), besides the sublimation enthalpies, the sublimation entropies, $T\Delta S_{subl}$, are required. The latter are summarized Figure 4.29 (b) and compared to experimental data from vapor pressure measurements from Table 4.8. The electronic (ψ_{crys}) method gives slightly better results in comparison to the atomistic (ψ_{mol}) method except for lactide. However, deviations are above 7 kJ·mol^{-1} and thus significantly worse than the integrals from experimental solid-state heat capacities. Surprisingly, the integrals of the computed ideal gas and experimental solid-state heat capacities are not able to resolve the difference between the enantiomer and the racemate.

Table 4.9: Calculated absolute sublimation enthalpies, entropies and Gibbs free energies and energy differences between the racemic and enantiopure crystal $\Delta_{RS\text{-}S}$ of lactide, naproxen and 3ClMA in comparison to the experimental reference values from Table 4.8. All values are in kJ·mol^{-1}.

Method	lactide			naproxen			3ClMA			RMSE
	(RS)	(S)	$\Delta_{RS\text{-}S}$	(RS)	(S)	$\Delta_{RS\text{-}S}$	(RS)	(S)	$\Delta_{RS\text{-}S}$	abs.
Sublimation enthalpy ΔH_{subl}										
ψ_{mol}	81.1	77.5	3.5	128.3	120.1	8.2	105.2	99.9	5.3	7.9
ψ_{crys}	85.2	82.2	2.9	130.3	128.7	1.7	122.0	119.5	2.5	3.6
ψ_{mol} (exp/theory)	80.7	77.3	3.3	128.8	121.1	7.7	106.9	100.7	6.2	7.6
ψ_{crys} (exp/theory)	84.2	81.5	2.7	129.4	127.3	2.1	120.8	117.3	3.5	3.3
experiment	91.6	86.3	5.3	135.3	129.1	6.2	(115.1)	(113.8)	-	
Sublimation entropy $T\Delta S_{subl}$										
ψ_{mol}	51.6	52.7	-1.2	59.8	58.6	1.1	57.0	57.9	-0.9	8.6
ψ_{crys}	47.9	51.9	-4.0	62.3	65.4	-3.1	63.2	64.6	-1.4	7.1
"exp/theory"	56.5	57.1	-0.5	69.8	70.5	-0.7	65.8	66.1	-0.3	2.4
experiment	56.6	53.5	3.1	72.7	68.9	3.8	-	-	-	
Sublimation Gibbs energy ΔG_{subl}										
ψ_{mol}	29.5	24.8	4.7	68.5	61.5	7.0	48.2	42.0	6.2	5.2
ψ_{crys}	37.3	30.4	6.9	68.0	63.2	4.8	58.8	54.8	4.0	5.6
ψ_{mol} (exp/theory)	24.1	20.3	3.9	59.1	50.6	8.4	41.1	34.5	6.6	10.2
ψ_{crys} (exp/theory)	27.7	24.5	3.3	59.7	56.8	2.8	55.0	51.2	3.8	5.6
experiment	35.0	32.8	2.2	62.6	60.2	2.4	(49.3)	(47.7)	(1.6)	-

Calculations of the final sublimation free energies, ΔG_{subl}, (see Figure 4.28, b) give similar accuracies in comparison to the sublimation enthalpies. The atomistic method is comparably accurate (RMSE = 5.2 kJ mol^{-1}) than the more sophisticated electronic method (RMSE = 5.6 kJ mol^{-1}), even though it was less accurate for calculating ΔH_{subl} and $T\Delta S_{subl}$. Combining the atomistic results with experimental solid-state heat capacities within the ψ_{mol} (exp/theory) method drastically increases deviations to experiment (RSME = 10.2 kJ mol^{-1}). As the sublimation entropies, $T\Delta S_{subl}$, from the vapor pressure measurements (Figure 4.29, b) and from the "exp/theory" method are in good agreement for lactide and naproxen with an overall RMSE of 2.4 kJ mol^{-1} (Table 4.9) the calculation errors are more likely to come from the atomistic lattice and zero-point energies. As a result, the surprisingly accurate ψ_{mol}-results for ΔG_{subl} can only be explained by a fortunate compensation of errors.

Besides the absolute energies, the energy differences between the racemic and enantiopure crystal ($\Delta_{RS\text{-}S}E = E_{RS} - E_S$) are of great importance for enantioseparation process design as they can be related to the eutectic composition of chiral mixtures in solution (see section 2.2.4 and eq. (23)). Figure 4.30 shows the calculated sublimation (a) enthalpy and (b) Gibbs energy differences, $\Delta_{RS\text{-}S}H_{subl}$ and $\Delta_{RS\text{-}S}G_{subl}$, for the three

molecules in comparison to experiment. Only the sublimation Gibbs energy differences, which have been estimated from experimental solubilities via the sublimation cycle, are accurate enough for lactide and naproxen so that they can be used as an alternative experimental reference for 3ClMA.
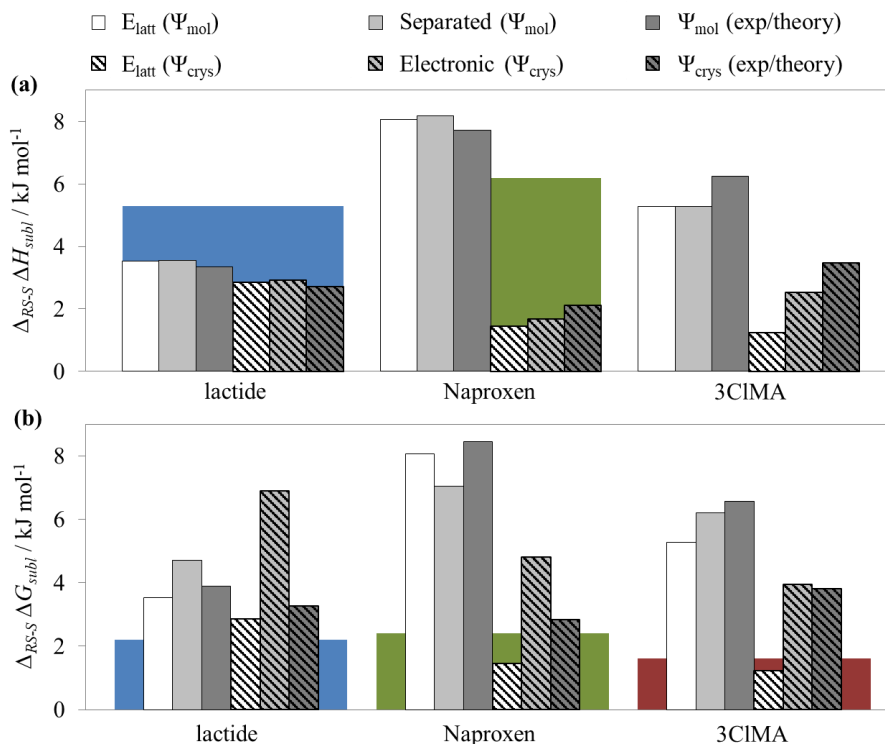
Figure 4.30: Energy differences between the racemic and enantiopure crystal. **(a)** Sublimation enthalpy differences, $\Delta_{RS-S}\Delta H_{subl}$, and **(b)** Gibbs free energies differences, $\Delta_{RS-S}\Delta G_{subl}$, using calculated and experimental solid state heat capacities in comparison to the experimental data from Table 4.8 (blue = lactide[230]; green = naproxen[41]; red = 3ClMA – as 3ClMA decomposes estimations from experimental solubilities are used). The calculations are based on the pure ψ_{crys} and ψ_{mol} method and, when combined with experimental solid-state heat capacities, on the so-called mixed "exp/theory" methods.

Similar to the absolute quantities (see Figure 4.28), enthalpy and free energy differences are in most cases dominated by the lattice energies. The variation between the computational methods depends markedly on the flexibility of the molecule. The lactides show the smallest dependence on the computational model (Figure 4.30) and also have almost complete cancellation of the thermal corrections (Figure 4.29, a). The thermal contributions have a major effect on the relative enthalpies of sublimation for 3ClMA, whereas the non-cancelling errors in calculation of the lattice energy dominates for naproxen. Nevertheless, for both 3ClMA and naproxen, there is a significant difference between the thermal contributions up to $\Delta_{RS-S}H_{corr} = 2.3 \ kJ \ mol^{-1}$, calculated from the experimental and computed heat capacities which equally come from the zero-point energies and thermal energies. Generally, the atomistic model shows less discrimination. Thus, the thermal contributions are significant, considering that enthalpy differences are below 6 kJ mol^{-1} for lactide and naproxen and probably as well for 3ClMA.

Similar results are obtained for the differences in sublimation free energies where experimental values are significantly smaller in comparison to the enthalpy differences (Figure 4.30, b). While the lattice energies of the ψ_{mol} method overestimate the free energy differences significantly for naproxen and 3ClMA, the $\Delta_{RS\text{-}S}E_{latt}$ of the ψ_{crys} method surprisingly reproduces the experimental free energy differences. However, adding the zero-point energies, thermal enthalpies and entropy corrections changes the $\Delta_{RS\text{-}S}\Delta G_{subl}$ on average by 1.6 ± 1.5 kJ·mol^{-1} up to 4.1 kJ·mol^{-1}. The method dependent variation of the various energy contributions to $\Delta_{RS\text{-}S}\Delta G_{subl}$ is illustrated additionally in Figure 4.31 for the pure ψ_{mol}, ψ_{crys} method and the combined "exp/theory" (ψ_{crys}) method. Regarding the small free energy differences of around 2 kJ·mol^{-1}, it is important to precisely determine the thermal correction for all three molecules. Especially if the free energy differences are used to calculate relative solubilities via the sublimation cycle since those are related exponentially (see eq. (23)).
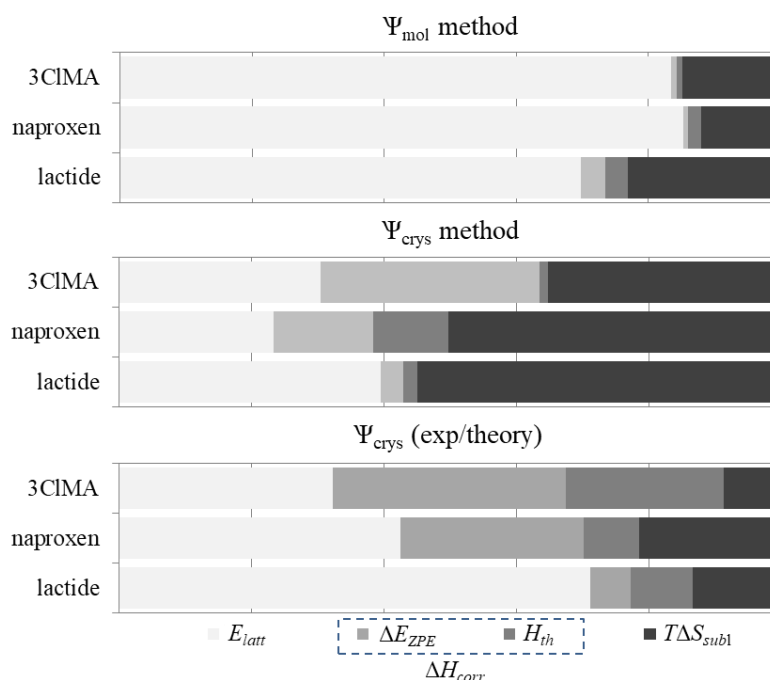
Figure 4.31: Share of the absolute energy contributions to the difference in Gibbs free energy of sublimation for lactide, naproxen and 3ClMA in percent. Calculations results of the ψ_{mol} and ψ_{crys} model and of the combined "exp/theory" (ψ_{crys}) method are compared. Total enthalpy correction ΔH_{corr} is comprised of the zero-point energies ΔE_{ZPE} and thermal heat capacity corrections H_{th}.

4.3.7   Conclusions

Lactide has been confirmed to belong to the class of simple racemic compound-forming systems (see Figure 4.17), whereas naproxen exhibits a more complex binary melting behaviour (see Figure 4.18). Combined DSC and XRPD analysis suggest the formation partial solid-solutions at concentrations close to (*RS*)-naproxen when crystallized from acetone (see Figure 4.19) and additionally close to (*S*)-naproxen if crystallized from the melt (see Figure 4.20). A presence of solvent mediated solid-solutions can lead to difficulties for enantiopurification by crystallization.

Thermal corrections are shown to affect ΔG_{melt} for up to 1.6 kJ·mol^{-1} in case of naproxen and are thus not negligible when used for solubility prediction (see Table 4.6). Within the sublimation cycle zero-point, as well as thermal enthalpy and entropy (see Figure 4.29), correction can make up to 40 % of the total energy contributions to ΔG_{subl}, due to the large temperature gap between 0 K and reference temperature (Table 4.9). Calculated heat capacities systematically underestimate the measured high temperature $C_{P,s}$. The underestimation of computational methods is consistent with literature results and partly due to a neglect in thermal expansion of the crystal structure (see Figure 4.22). Overall, the ψ_{crys} method gives significantly better results of the sublimation enthalpies in comparison to the ψ_{mol} method. However, both methods are close to chemical accuracy for calculating ΔG_{subl} (see Table 4.9). The surprisingly accurate ψ_{mol} results for ΔG_{subl} have been explained by a fortunate compensation of errors which mostly comes from the calculations of the lattice energies as well as the sublimation entropies.

At low temperatures there are detectable heat capacity differences between the racemate and the enantiomer in the DHCP experiments for all three molecules (see Figure 4.23). The high temperature DSC experiments show however only a significant ΔC_P for 3ClMA, which has been identified as well for the closely related mandelic acid (see Figure 4.24). Experimental data from literature shows that heat capacity differences are no rarity (see Table 4.7). This poses a challenge to computational methods as they have been shown in this work to fail to accurately compute high temperature heat capacity differences even if molecular and lattice vibrational frequencies are allowed to interact. The low frequency lattice modes determine the ΔC_P at low temperatures while for the high temperature heat capacities, only the high frequency molecular modes are relevant. Differences between the high frequency modes for naproxen and 3ClMA have been experimentally determined by Raman spectroscopy (see Figure 4.26) which can thus help to identify possible heat capacity differences at high temperatures. Zero-point energies as well as thermal enthalpies and entropies contribute on average by 1.6 ± 1.5 kJ·mol^{-1} and up to 4.1 kJ·mol^{-1} to the resulting free energy differences between the racemic and enantiopure crystals. The magnitude and method dependence appear to be related on the complexity on the molecules and of the crystal packing.

4.4   Solubility prediction of chiral model substances

Within this section, the phase transition thermodynamics from the previous section are combined with solvation terms from COSMO-RS in order to calculate solubilities via the melt and the sublimation cycle (eqs. (27) and (28)). Calculations of the solubility of the enantiomer, as well as the racemic compound of the three chiral model substances, lactide, naproxen and 3ClMA, are compared to experiment. The accuracy of the calculations via two thermodynamic cycles, the melt cycle and the sublimation cycle (Figure 2.10), are evaluated for solubility prediction in pure and mixed solvent system.

Experimental and computational details

In order to evaluate the subsequent calculations, solubilities have been gathered from literature and, if not available, determined in the frame of this work. Available solubility data of racemic and enantiopure lactide[225] has been extended in the frame of this work by means of isothermal solubility method (see section 3.2.1 for details). For naproxen, solubilities have been determined experimentally for both crystals in a variety of organic solvents. For 3ClMA, solubilities of both crystals have been studied thoroughly before[225] and thus have been used within this work. The primary experimental data is summarized in Table 7.7 in the appendix.

The melt cycle uses the Gibbs free energies of melting of Table 4.5 in combination with the thermal free energy corrections from Table 4.6 in order to determine the corrected ΔG_{melt} at 298 K (see eq. (33)). The sublimation cycle uses the Gibbs free energy of sublimation ΔG_{subl} from Table 4.9 that has been determined via the ψ_{crys} or ψ_{mol} method. ΔG_{melt} and ΔG_{subl} are combined with computed excess Gibbs free energy of mixing, ΔG^E, and the Gibbs free energy of solvation, ΔG_{solv} in order to calculate ΔG_{sol} via eqs. (27) and (28), respectively. ΔG^E and ΔG_{solv} have both been computed with the COSMO-RS model. Details on the theory behind COSMO-RS is given in section 2.6.6. All calculations have been performed at infinite dilution using the TZVPD-FINE parameterization. Further information on the computational details can be found in section 2.7.3. For the flexible naproxen and 3ClMA, several molecular conformations have been used which were treated with a Poisson-Boltzmann weighting as implemented in the COSMO-RS model. As lactide has a rigid molecular structure, only one conformation was used. All conformations that have been used are shown in Figure 4.32. The resulting ΔG_{sol} from both thermodynamic cycles are used to calculate mole fraction solubilities via eq. (10).
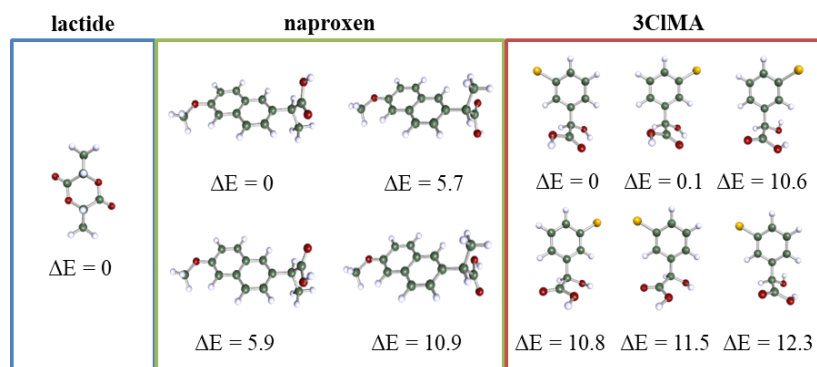
Figure 4.32: Molecular conformations of lactide, naproxen and 3ClMA that have been used for calculating solvation free energies and excess Gibbs free energies of mixing with the COSMO-RS model. The energy differences, ΔE, correspond to the difference in energy to the lowest energy conformation.

4.4.1 Solubility prediction

Figure 4.33 shows the calculation results of $\ln x_i$ via (a) the sublimation cycle and (b) the melt cycle in comparison to experiment. The Root-mean-square errors (RMSE) between calculations and experiment are given in Table 4.10. Calculations via the sublimation cycle using the ψ_{mol} and ψ_{crys} method in combination with COSMO-RS ($\psi_{mol+COSMO-RS}$ and $\psi_{crys+COSMO-RS}$) are generally in good agreement with experiment. The overall accuracy of the $\psi_{crys+COSMO-RS}$ method is slightly better compared to the $\psi_{mol+COSMO-RS}$ method with a RMSE of 1.9 and 2.6 in $\ln x$-units, respectively (see Table 4.10). Both *ab-initio* methods are more precise than calculations via the melt cycle if "ideal" solubility is assumed. In that case ΔG_{sol} is approximated by the solvent independent experimental ΔG_{melt} (see Table 4.10) resulting in the simple form of the SVL equation (see eq. (34)). If the solvent specific solution non-idealities within ΔG^E are calculated by COSMO-RS and added to ΔG_{melt}, the overall accuracy of the melt cycle is clearly increased (see Table 4.10). However, this is mostly due to a significantly better representation of the naproxen-heptane and 3ClMA-water system (marked with arrows within Figure 4.33) while the other systems are less effected.

Table 4.10: Accuracy of the calculated ΔG_{sol} and logarithmic mole fraction solubilities, $\ln x_i$, via the sublimation and the melt cycle.

RMSE	Sublimation cycle			Melt cycle	
	ψ_{mol} (+COSMO-RS)	ψ_{crys} (+COSMO-RS)	$\Delta G_{solv}{}^a$ (COSMO-RS)	SVL (ideal)	COSMO-RS
kJ·mol^{-1}	6.3	4.8	2.1	8.1	4.3 (3.3)[b]
$\ln \underline{x}$	2.6	1.9	-	3.3	1.7 (1.3)[b]

a. RMSE of the calculated solvation Gibbs energies of lactide and naproxen via COSMO-RS.
b. Calculated using the temperature corrected ΔG_{melt} from Table 4.5 and Table 4.6. Values in brackets use the uncorrected ΔG_{melt} from Table 4.5.

Interestingly, the addition of thermal corrections to ΔG_{melt} does not improve the melt cycle calculations, but instead slightly lowers the overall accuracy (see values in brackets in Table 4.10). As a consequence, even if solution non-idealities are determined by COSMO-RS the accuracy of the melt cycle for calculating ΔG_{sol} (RMSE = 4.3 kJ·mol^{-1}) is still comparable to that of the sublimation cycle in case the $\psi_{crys+COSMO-RS}$ method is used (RMSE = 4.8 kJ·mol^{-1}).
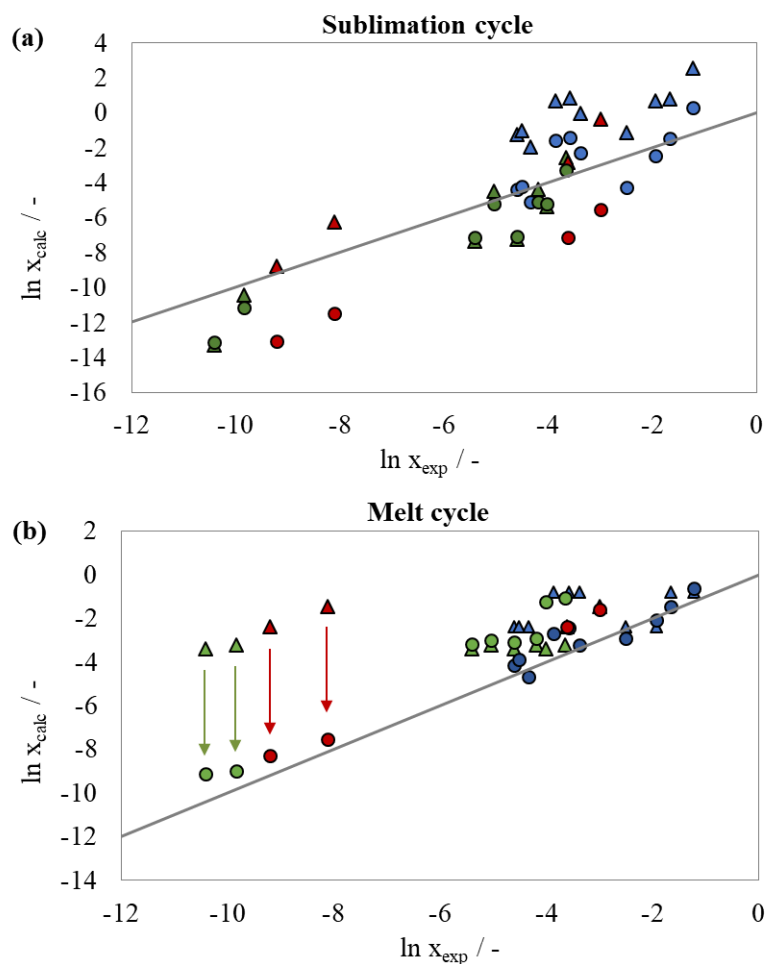
Figure 4.33: Calculated absolute solubilities of racemic and enantiopure lactide (blue), naproxen (green) and 3ClMA (red) in various organic solvent systems using **(a)** the sublimation cycle in combination with (Δ) the $\psi_{mol+COSMO-RS}$ and ($\circ$) the $\psi_{crys+COSMO-RS}$ method. Calculations of naproxen in heptane and 3ClMA in water are marked with arrows **(b)** Calculations assuming via (Δ) the SVL equation (eq. (34)) assuming "ideal" solubility and via ($\circ$) via the melt cycle combining ΔG_{melt} and the solvent specific ΔG^E from COSMO-RS. Calculations of naproxen in heptane and 3ClMA in water are marked with arrows.

In order to evaluate sources of computational errors, the accuracy of the COSMO-RS model for calculating the solvation Gibbs energies have been determined. For that purpose, experimental solvation Gibbs energies, $\Delta G_{solv,exp}$, have been recalculated from the experimental solubilities and experimental sublimation Gibbs energies, $\Delta G_{subl,exp}$, via $\Delta G_{solv,exp} = -RT \cdot \ln x_{i,exp} - \Delta G_{subl,exp}$. This is only possible for lactide and naproxen where experimental sublimation Gibbs energies, $\Delta G_{subl,exp}$, are available (see Table 4.8). The

extracted $\Delta G_{solv,exp}$ for lactide and naproxen in each of the studied solvent systems is summarized in Appendix (Table 7.7). The overall accuracy of the COSMO-RS model for calculating solvation free energies of lactide and naproxen is 2.1 kJ·mol^{-1} (see Table 4.10). This is in agreement with literature[245] where the COSMO-RS model was evaluated for a large benchmark set of small and medium sized molecules. As a consequence, within the $\psi_{crys+COSMO-RS}$ method calculations of the sublimation and solvation are equally contributing to the overall computational error. Within the $\psi_{mol+COSMO-RS}$ method, the computational error when calculating sublimation Gibbs energies prevails.

The magnitude of each energy contribution within the sublimation cycle is shown in Figure 4.34 (top). Exemplarily, the results for the solubility of the enantiopure crystals of lactide, naproxen and 3ClMA in toluene are compared. For all three substances the lattice energy is responsible for around half of the sum of all energy contributions which are largest for naproxen. Thermal enthalpy contributions only take a minor part within the sum of all energies while the entropy corrections to the static lattice are the second largest contributions which are around double the magnitude as the solvation free energies. The solvent specific energy contribution within the melt cycle, ΔG^E, is significantly smaller in comparison to the solvation free energy within the sublimation cycle. Nevertheless, it takes the largest share of the sum of all energies within the melt cycle (Figure 4.34, bottom), due to the significantly smaller energy contributions. The total energies are more than 10 times larger within the sublimation cycle. Based on the above, the good performance of the sublimation cycle (Figure 4.33 and Table 4.10) is surprising as the significantly larger energies are more prone to errors when adding all energy contributions.
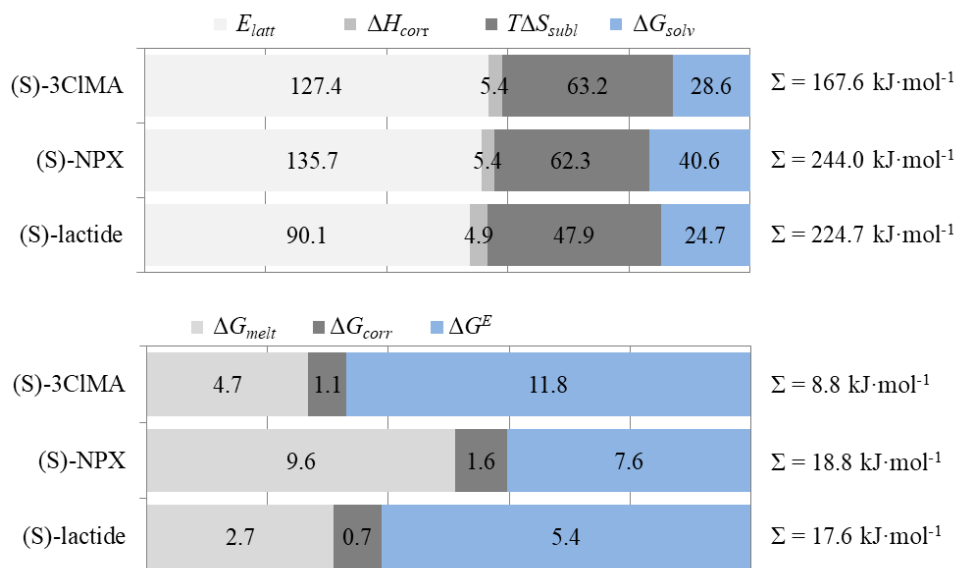
Figure 4.34: Absolute energy contributions to the Gibbs free energy of solution via (top) the sublimation cycle using the $\psi_{crys+COSMO-RS}$ model and (bottom) the melt cycle in combination with COSMO-RS. Exemplarily, the dissolution of lactide, naproxen and 3ClMA toluene is shown. The sum, Σ, of the absolute energies is given on the right.

In summary, the results of the $\psi_{mol+\text{COSMO-RS}}$ and $\psi_{crys+\text{COSMO-RS}}$ methods are promising, considering that both methods do not require substance specific experimental input data. Furthermore, the results are an improvement when compared to other solubility prediction methods from literature using first-principle calculations.[10] Around 40 % of the solubilities from the $\psi_{crys+\text{COSMO-RS}}$ are within the $\pm 0.5\log(x)$ limits which has been suggested as within a recent solubility challenge[246]. Secondly, the $\psi_{crys+\text{COSMO-RS}}$ model is not restricted to aqueous solution but can handle a large range of organic solvent systems. Besides that, the reliability is still not high enough so that any of the proposed method can be used for solubility predictions early stage crystallization process design.

4.4.2   Solubility calculations in mixed solvent systems

The solubility behaviour in mixed solvent systems is in particular relevant for crystallization process design. The addition of a second solvent, a co-solvent, can be used to enhance solubility or to significantly lower the solubility of a certain target substance. A co-solvent that over-proportionally lowers the solubility of a target substance is often referred to as an "anti-solvent".

Both thermodynamic cycles have been used to calculate solubilities in mixed solvent systems. In order to be able to evaluate the performance of the computational methods, a broad experimental study of the solubility of both chiral species of lactide and naproxen in a variety of mixed solvent systems was conducted. Solubilities have been measured according to the isothermal method presented in section 3.2.1. Primary experimental data is summarized in Appendix (Table 7.8 and Table 7.9). Calculations via the melt cycle use the corrected ΔG_{melt} from Table 4.5 and Table 4.6 in combination with ΔG^E from COSMO-RS has been used. For the sublimation cycle the $\psi_{crys+\text{COSMO-RS}}$ method because of its comparatively better performance compared to the $\psi_{mol+\text{COSMO-RS}}$ method (see Table 4.10). Furthermore, the experimental sublimation free energies, $\Delta G_{subl,exp}$, from Table 4.8 have been used in combination with ΔG_{solv} from COSMO-RS to calculate solubilities. As measurements for naproxen have been performed at 30°C the solid-state thermodynamic parameters (ΔG_{melt} and ΔG_{subl}) have been adjusted to 303 K. More details on the temperature adjustments of ΔG_{subl} (ψ_{crys}) is given in a later section 4.6.1 when discussing temperature-dependent solubility behaviour.

Figure 4.35 compares this work's measurements and calculations of the enantiopure (left) and racemic forms (right) of lactide at 25°C and naproxen at 30°C in mixtures of ethanol and toluene. For both substances, the experimental solubility is significantly increased in mixtures of the two solvents in comparison to the pure solvent systems. The maximum solubility is obtained for lactide in a 20/80 wt% EtOH/Toluene mixture and for naproxen in between 20/80 and 40/60 wt% EtOH/Toluene mixture. For naproxen there is an up to 16-fold increase in solubility in comparison to pure toluene. The trend is qualitatively reproduced by the two thermodynamic cycles but the absolute solubilities vary considerably between the various methods. There is a systematic overestimation of solvation contributions in ethanol by the COSMO-RS model which is more pronounced for lactide.
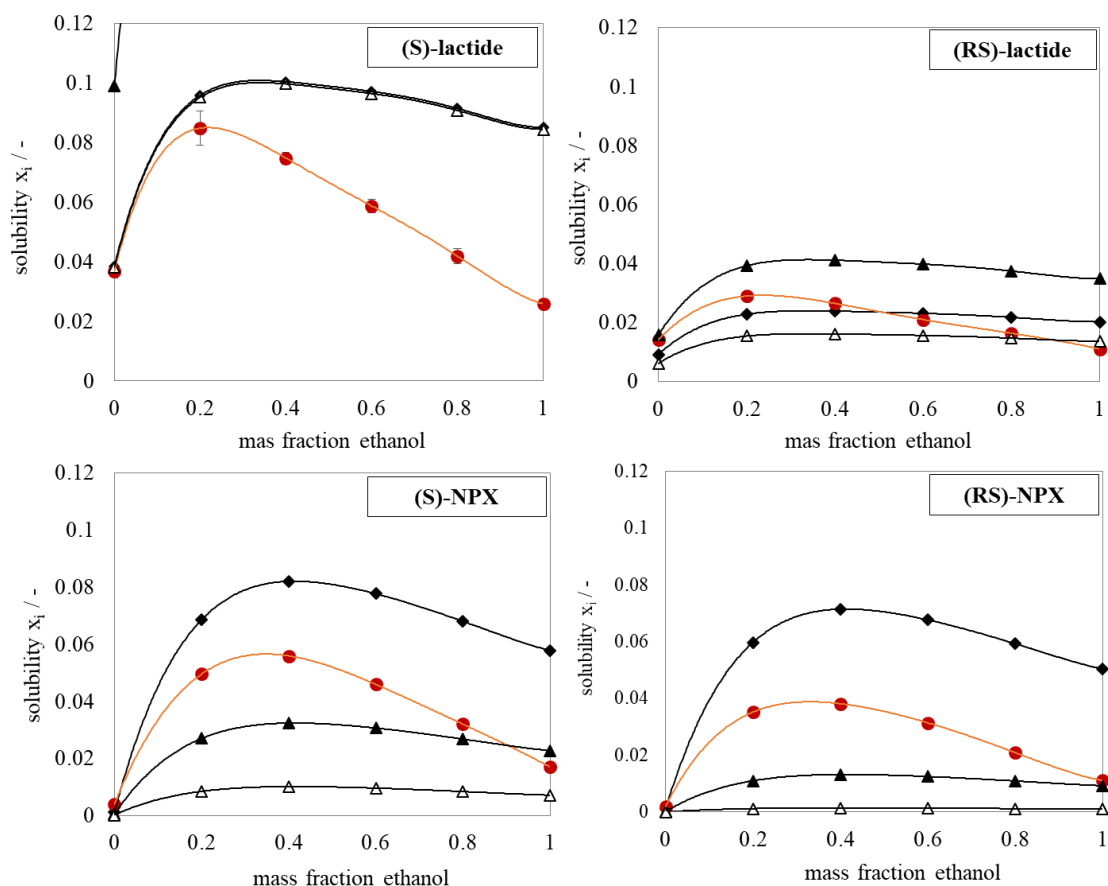
Figure 4.35: (red ●) Experimental solubilities of the enantiomer and the racemic compound of lactide (25°C) and naproxen (30°C) in mixtures of ethanol and toluene. Calculations via (◆) the melt cycle uses temperature corrected ΔG_{melt} in combination with ΔG^E from COSMO-RS; (Δ) the sublimation cycle in combination with the $\psi_{crys+COSMO-RS}$ method; (▲) the sublimation cycle in combination with $\Delta G_{subl,exp}$ from Table 4.8 and ΔG_{solv} from COSMO-RS

Calculations using the exclusively computational $\psi_{crys+COSMO-RS}$ method systematically underestimate the solubilities. This is most likely due to an overestimation of the sublimation free energies (see Table 4.9). Only for (*S*)-lactide the $\psi_{crys+COSMO-RS}$ and the melt cycle deliver nearly identical results. In contrary to the $\psi_{crys+COSMO-RS}$ method, the melt cycle overestimates the solubilities in most cases. As a consequence, there is not a clear advantage of the melt cycle over the sublimation cycle, especially if experimental sublimation free energies are used.

Further experimental and computational investigations have been conducted for (*S*)- and (*RS*)-naproxen in mixtures of ethanol with acetonitrile (ACN) and with water as shown in Figure 4.36. The experimental solubility of naproxen in mixtures of ethanol with ACN follows a similar trend as for the previously discussed ethanol-toluene mixtures. The solubility is significantly increased within solvent mixtures and is at the maximum at around 60 wt% ethanol. In contrary to that water acts as an anti-solvent by lowering the solubility over-proportionally.
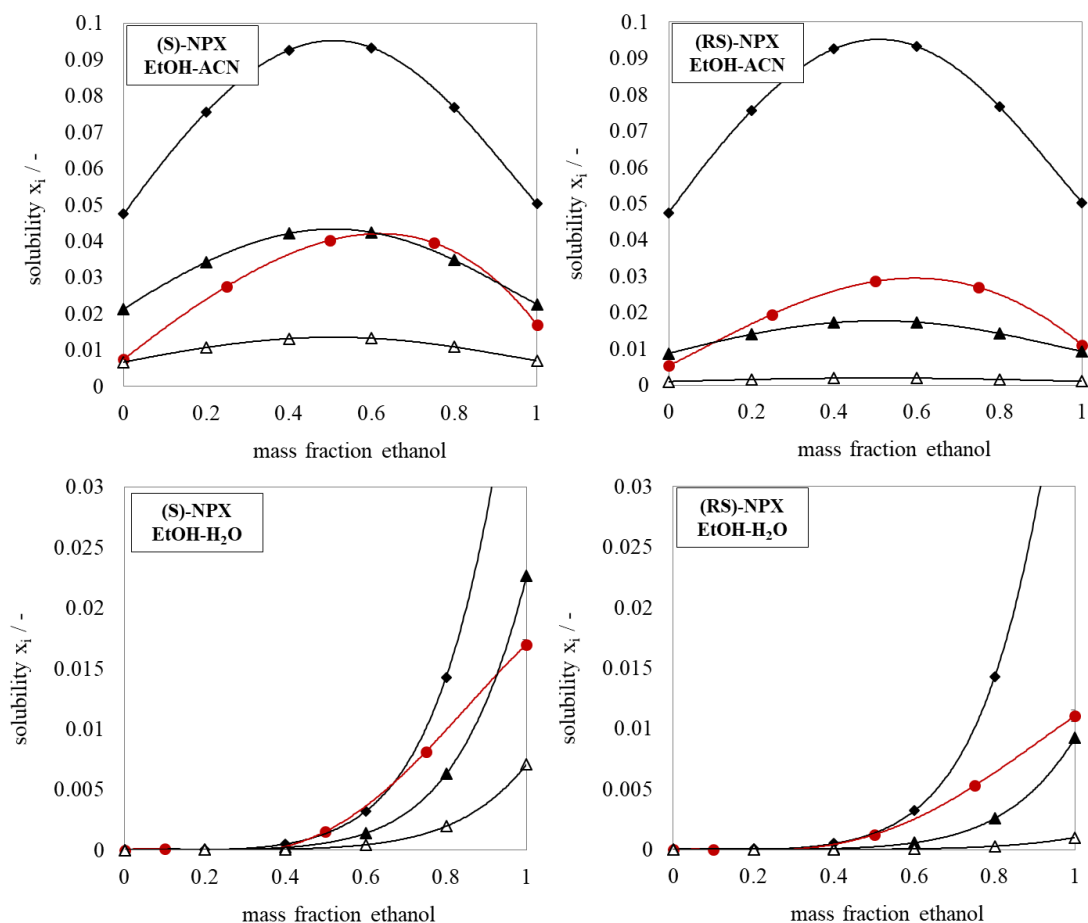
Figure 4.36: (red ●) Experimental solubilities of (*S*)-naproxen, (*RS*)-naproxen in binary solvent mixtures of ethanol and acetonitrile as well as ethanol and water each at 30°C. Calculations via (◆) the melt cycle using uncorrected ΔG_{melt} from Table 4.5 and ΔG^E from COSMO-RS; (Δ) the sublimation cycle in combination with the $\psi_{crys+COSMO-RS}$ method; (▲) the sublimation cycle in combination with $\Delta G_{subl,exp}$ from Table 4.8 and ΔG_{solv} from COSMO-RS.

Both non-linear solubility trends are captured qualitatively well by both cycles. In all cases the sublimation cycle in combination with experimental sublimation free energies gives the best results. Computational results of the melt cycle systematically overestimate the solubilities. Similar to the ethanol-toluene mixture (Figure 4.35), the $\psi_{crys+COSMO-RS}$ method underestimates the experiment. This is most likely due to the overestimation of the sublimation free energy of both (*S*)- and (*RS*)-naproxen by 3 and 5.4 kJ·mol^{-1}, respectively (see Table 4.9).

In summary, it can be concluded that the sublimation cycle provides a promising alternative to the melt cycle which performs comparably well for the studied systems. Best results are obtained if experimental Gibbs sublimation energies are used while ΔG_{subl} from $\psi_{crys+COSMO-RS}$ leads to systematic underestimations. The non-linear co-solvent behaviour within the mixed solvent systems is qualitatively captured in all cases. The absolute mole fraction solubilities, however, are not reliable enough for crystallization process design.

4.4.3   Conclusions

There is no clear advantage of the melt cycle over the sublimation cycle when using experimental melting and sublimation free energies (see Figure 4.33 and Table 4.10). The combined $\psi_{\text{crys+COSMO-RS}}$ method gives better results in comparison to the $\psi_{\text{mol+COSMO-RS}}$ method. Around 40 % of the solubilities from the $\psi_{\text{crys+COSMO-RS}}$ are within the $\pm 0.5 \log(\text{x})$ limits which has been suggested as within a recent solubility challenge[246]. The overall computational error of the $\psi_{\text{crys+COSMO-RS}}$ is equally caused by errors in the calculation of the sublimation and solvation thermodynamics. Within the $\psi_{\text{crys+COSMO-RS}}$ errors in the calculation of ΔG_{subl} prevail. These are promising results regarding that $\psi_{\text{crys+COSMO-RS}}$ is exclusively based on first-principle methods and does not rely on substance specific primary experimental data.

Solubilities of the two chiral crystals have been additionally measured within a variety of mixed organic solvent systems for naproxen and lactide. Both thermodynamic cycles are able to qualitatively reproduce the non-linear co-solvent behaviour (see Figure 4.35 and Figure 4.36). However, due to an overestimation of ΔG_{subl} by the $\psi_{\text{crys+COSMO-RS}}$ method, solubilities are systematically.

In summary, even though the absolute sublimation thermochemistry can be calculated with chemical accuracy by periodic DFT solubility predictions via the sublimation cycle are not yet reliable enough for crystallization process design.

4.5   Determination of the eutectic composition in solution

For chiral compound forming systems, the eutectic composition, x_{eu}, within the ternary solution phase diagram (see Figure 2.2) is the key parameter for chiral separation. It can depend on temperature, the nature of the solvent or both.[43, 44, 150] In this section, the two thermodynamic cycles are used to predict x_{eu} for lactide, naproxen and 3ClMA in solution using the phase transition thermodynamics from section 4.3. Experimental data of the eutectic composition of lactide[44] and 3ClMA[216, 222, 223] has been taken from literature as sufficient reliable data is available. For naproxen measurements have been performed within pure and mixed solvent systems using experimental methods according to section 3.2.1. Besides focusing on the absolute value of the eutectic composition at 298 K, its variation of x_{eu} with temperature and/or the solvent, the eutectic shift $\Delta x_{eu} = f\,(T,\,solvent)$, is crucial for enantioseparation by crystallization. The eutectic shift with temperature is evaluated in this section using theory and experiment. Furthermore, the influence of the solvent on x_{eu} is discussed.

4.5.1   Method evaluation

It was suggested before that the eutectic composition is related to the ratio between the mole fraction solubility of the racemic compound and that of the enantiomer.[43, 55] Based on this approach a general model was constructed in this work (see eq. (23) in section

2.2.4) that relates the eutectic composition to the difference in Gibbs free energy of solution between the racemic compound and the enantiomer $\Delta_{RS\text{-}S}\Delta G_{sol}$. Eq. (23) can be solved by the two thermodynamic cycles which approximate $\Delta_{RS\text{-}S}\Delta G_{sol}$ with $\Delta_{RS\text{-}S}\Delta G_{melt}$ or $\Delta_{RS\text{-}S}\Delta G_{subl}$. Based on the same principle slightly different model was established in the literature[56] that uses lattice energy difference instead of the difference in solution free energy (see eq. (24)).
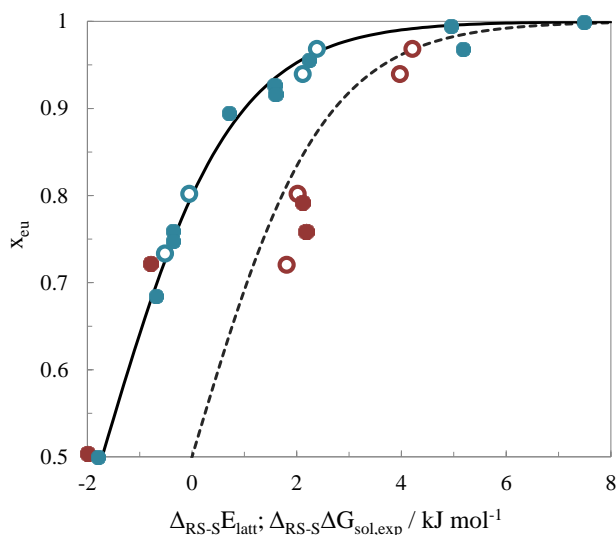
Figure 4.37: The experimental eutectic composition at 298 K for several amino acids in water plotted against the free energy difference ($\Delta_{RS\text{-}S}\Delta G_{sol}$) from ref. [55] and the lattice energy difference ($\Delta_{RS\text{-}S}E_{latt}$) from ref. [56]. This work's eutectic estimation model (thick line, eq. (23)) is compared to an alternative model by de la Otero Roza *et al.*[56] (dashed line, eq. (24)). Open symbols represent the systems evaluated in both studies.

The two slightly different models (eq. (23) and (24)) have been used in their original work[55, 56] for estimating the eutectic composition of several amino acids in water. The results of the two models are compared in Figure 4.37 where x_{eu} is plotted against the (free) energy differences between the racemate and the enantiomer (solid line: eq. (23); dashed line: eq. (24)). On one hand, the difference in Gibbs free energy of solution which which was calculated from the experimental relative solubility from ref.[55] via $\Delta_{RS\text{-}S}\Delta G_{sol} = RT \ln(x_{RS}/x_S)$ is plotted against x_{eu} (blue circles). On the other hand, x_{eu} is plotted against the lattice energy difference from ref.[56]. Primary data of the systems that have been evaluated in both studies[55, 56] are summarized in Table 4.11. Figure 4.37 clearly shows that the thermodynamic model of eqs. (23) correctly correlates the experimental x_{eu} to $\Delta_{RS\text{-}S}\Delta G_{sol}$ and thus to the experimental solubility ratios. There is a constant energy difference between the two models of $RT \cdot \ln(2)$ which is - 1.72 kJ mol^{-1} at 298 K. This results in a major difference between the two models. For eq. (24) $x_{eu} = 0.5$ which corresponds to an ideal conglomerate is obtained for a system with a lattice energy difference of $\Delta_{RS\text{-}S}E_{latt} = 0$ while eq. (23) requires energy difference of $\Delta_{RS\text{-}S}\Delta G_{sol} = - 1.72$ kJ·mol^{-1} (at 298 K). There is a negative free energy difference for alanine and valine (see Table 4.11 column 3). Such a system could not be handled within the model of eq. (24). Based on the superior representation the experimental relative solubility data, eq. (23) will be used in the following for eutectic estimations using the two thermodynamic cycles.

Table 4.11: Systems examined in two studies[55, 56] for the estimation of x_{eu} in water from (free) energy differences between the racemic compound and the enantiomer at 298 K. $\Delta_{RS-S}\Delta G_{sol}$ is obtained from the relative solubilities (columns 3 and 4) via eq. (22) and (23) and $\Delta_{RS-S}E_{latt}$ are the calculated lattice energy differences from literature.[56]

Substance	$x_{RS,exp}$[55] %	$x_{S,exp}$[55] %	$\Delta_{RS-S}\Delta G_{sol,exp}$ kJ mol^{-1}	$\Delta_{RS-S}E_{latt}$[56] kJ mol^{-1}	(4-3) kJ mol^{-1}	$\Delta_{RS-S}\Delta G_{corr}$ kJ mol^{-1}	$x_{eu,exp}$[55, 56] %
	1	**2**	**3**	**4**	**5**	**6**	**7**
serine	0.86	6.37	4.95	17.22	12.3	-1.79*	99.5
histidine	0.18	0.47	2.39	4.21	1.81	-	96.9
leucine	0.14	0.32	2.11	3.97	1.97	-	94.0
alanine	3.41	3.34	-0.05	2.02	2.07	-	80.2
valine	1.13	0.92	-0.52	1.81	2.32	0.70*	72.3 ± 0.2

*calculated from the integral of the experimental solid-state heat capacities of serine[239] and valine[238].

There are two cases within Table 4.11 where experimental solid-state heat capacities are available (serine[239] and valine[238]) between 5 K and 298 K for the racemic compound and the enantiomer. Integrals over $\Delta_{RS-S}C_{P,s}$ and $\Delta_{RS-S}C_{P,s}/T$ according to eq. (44) can be calculated in order to determine a $\Delta_{RS-S}\Delta G_{corr}$ which are 1.79 and 0.7 kJ·mol^{-1} for serine and valine, respectively. This indicates that thermal corrections to the lattice energy are required in order to accurately calculate x_{eu} via the sublimation cycle. This is discussed in more detail for lactide, naproxen and 3ClMA in the following section.

4.5.2   Eutectic composition – experiment and calculation

This section compares estimations of the eutectic composition of lactide, naproxen and 3ClMA in solution to experiment. Table 4.12 summarizes all measurements of the eutectic composition of lactide, naproxen and 3ClMA which have been partially taken from literature[44, 216, 222, 223] and, for the sake of completeness, determined in the frame of this work for naproxen. For all substances x_{eu} is in the range of 85 % to 95 % and there are some smaller deviations depending on the solvent used. For example, for lactide x_{eu} in ethyl acetate and isopropanol is around 93 % while 95 % in ethanol and acetone. For naproxen solvent specific deviations are smaller and within the experimental uncertainty. Largest differences are found for 3ClMA between water ($x_{eu} = 90$ % which drastically reduces at higher temperatures) and unpolar toluene ($x_{eu} = 93$ %)

Table 4.12. Experimental eutectic composition of lactide, naproxen and 3ClMA in various solvent systems and temperatures. The maximum and minimum values at 25°C for each substance are highlighted in bold.

Substance	Solvent	Temperature / °C	$x_{eu,exp}$ / %	Literature
Lactide	Toluene	5 to 45	94	[44]
	Isopropanol	25 to 45	93.4	[44]
	Acetone	5 to 35	**95**	[44]
	Ethanol	5 to 45 (25)	97.1 to 93.6 (**95.0**)	[44]
	Ethyl acetate	15 to 45 (25)	95.8 to 90.2 (**93.2**)	[44]
Naproxen	Ethanol	15 to 45 (25)	90.5 to 88.9 (**90.1**)	*This study*
	Toluene	15 to 45 (25)	90.5 to 88.7 (**89.9**)	*This study*
	EtOH/ACN 50/50 wt/wt	10 to 40 (25)	90.9 to 89.1 (90.0)	*This study*
3ClMA	Toluene	40 to 80	91	[216]
	Toluene/EA 80/20 v/v	25 to 45	**91.3** to 92.6	[216]
	water	5 to 25 (25)	89.4 to 89.1 (**89.1**)	[216]
	water	5 to 50	90 to 84	[222]
	water / IPA 90/10 wt/wt	20 to 40	0.88 to 0.85	[223]

As discussed before, eq. (23) is used for estimating x_{eu}. It is further assumed that the solvation is identical for the two enantiomers. In this case, the difference in excess Gibbs free energy of mixing, $\Delta_{RS-S}G^E$, and the Gibbs free energy of solvation, $\Delta_{RS-S}\Delta G_{solv}$, cancels out. As a consequence, x_{eu} can be estimated from different approximations of the melting and sublimation energy differences $\Delta_{RS-S}\Delta G_{melt}$ and $\Delta_{RS-S}\Delta G_{subl}$, respectively.

Figure 4.38 compares the maximum (solid line) and minimum (dashed line) values of the experimental x_{eu} at 298 K from Table 4.12 with the estimations via the two thermodynamic cycles (Figure 2.10) in combination with eq. (23). The "pure" ψ_{mol} and the ψ_{crys} model are evaluated along with experimental solid-state heat capacities, $C_{p,exp}$, in the frame of the "exp/theory" model using data from Table 4.9 (see section 2.7.2 for details). Experimental estimates based on the sublimation cycle (Table 4.8) are compared to those using the difference in Gibbs free energy of melting. Thermal corrections to $\Delta_{RS-S}\Delta G_{melt}$ are within 0 to -0.4 kJ·mol⁻¹ (Table 4.6) and thus negligible, uncorrected measurements have been taken from Table 4.5.

The accuracy the sublimation results cycle varies considerably and is dominated by uncertainties in lattice energy differences. They systematically overestimate the eutectic composition in comparison to experiment. This is consistent with previous findings for amino acids in water[56] (see Figure 4.37). The enthalpy correction, ΔH_{corr}, only contributes significantly to x_{eu} in the case of 3ClMA, but combined with the entropic differences the effects add up accounting for up to 4 kJ·mol⁻¹ to $\Delta_{RS-S}\Delta G_{subl}$ and thus effect the eutectic composition for all three substances (see Table 4.9 for primary data). The combination of electronic structure calculations and experimental thermal corrections within the "exp/theory" (ψ_{crys}) model, $\Delta_{RS-S}\Delta G_{subl,exp/theory}$, gives the best estimates of x_{eu} in case

thermal corrections are regarded. These results correlate well with results using experimental sublimation free energies from vapor pressure measurements, $\Delta_{RS\text{-}S}\Delta G_{subl,exp}$[41, 230]. However, the pure lattice energies of the ψ_{crys} model give the best overall accuracies which questions their precision as thermal corrections cannot be neglected for all three molecules.

The results for x_{eu} using the melt cycle and hence the difference in the free energy of melting, $\Delta_{RS\text{-}S}\Delta G_{melt}$, are comparable to the sublimation cycle for lactide only. However, for naproxen, where both the racemic and enantiopure crystals have almost the same melting temperature and enthalpies, the melt cycle significantly underestimates the energy difference and hence the eutectic composition.
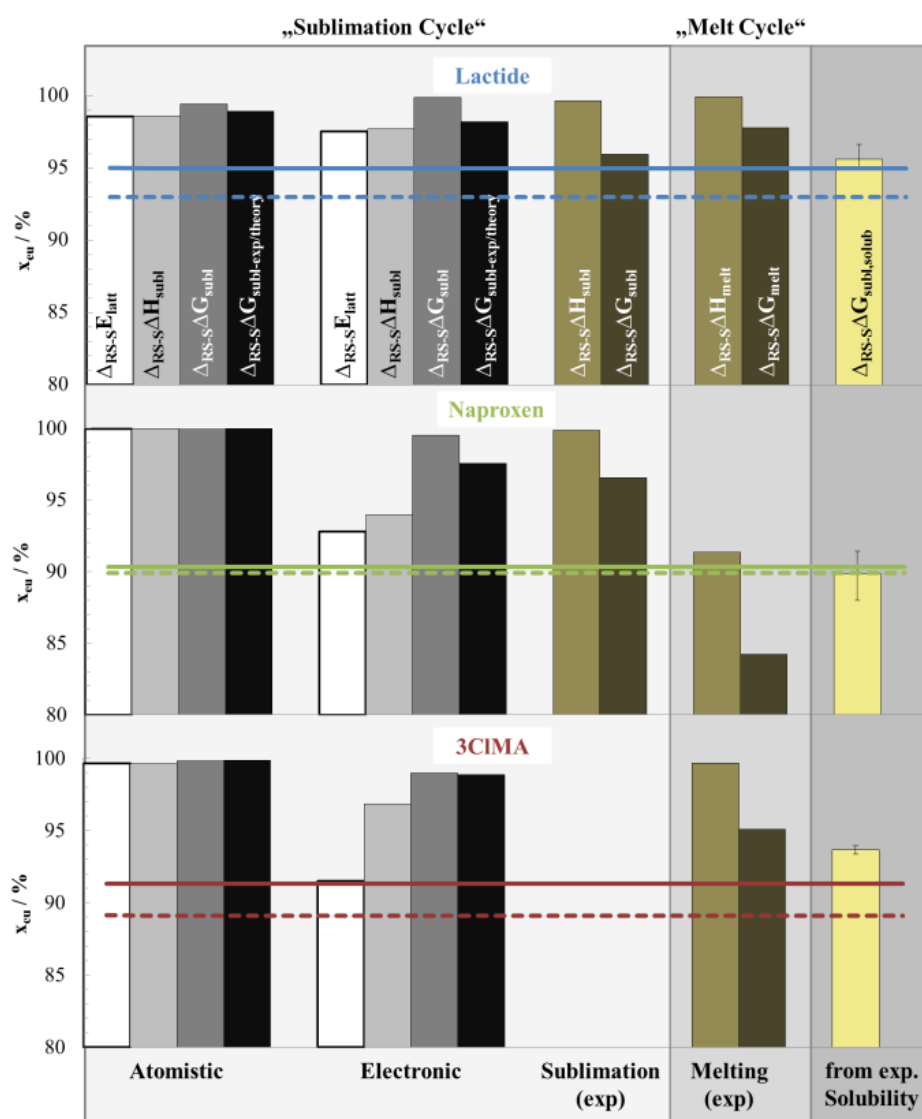
Figure 4.38: Estimation of the eutectic composition via eq. (24) using different ways to obtain $\Delta_{RS\text{-}S}\Delta G_{sol}$. Calculations of $\Delta_{RS\text{-}S}\Delta G_{subl}$ with the ψ_{mol} and ψ_{crys} model are compared to eutectic estimations using experimental sublimation and melting enthalpies and free energies as well as free energy differences that have been determined from experimental solubilities, $\Delta_{RS\text{-}S}\Delta G_{subl,solub}$ (see Appendix, Table 7.7). The coloured lines correspond to the maximum (solid line) and minimum (dashed line) values of x_{eu} measured in various solvent systems at 298 K (Table 4.12).

Estimates of x_{eu} are slightly more accurate when using free energy differences from measured solubilities of the enantiomer and the racemate, $\Delta_{RS-S}\Delta G_{sol}$. They are equivalent to the recalculated sublimation free energies, $\Delta_{RS-S}\Delta G_{subl,solub}$, from Table 4.8. The values from solubility measurements agree with the experimental value derived from vapor pressure which differ only by 0.1 kJ mol^{-1} for lactide and 1.4 kJ mol^{-1} for naproxen. However, they depend on the nature of the solvent system and vary between 0.06-0.23 kJ mol^{-1} which is indicated by error bars in Figure 4.38. The solvent effect is in the same order of magnitude as the experimental variation of x_{eu} different solvents at 298 K for lactide while it is overestimating for naproxen and 3ClMA (see Table 4.12). This indicates that there is a solvent effect on the eutectic composition, and that the solutions of the three molecules involved are not ideal.

The relatively good performance of the sublimation cycle suggests that predictions of x_{eu} via the difference in sublimation free energy can be used as a guidance for the design of enantioseparation processes. However, energy differences have to be calculated precisely and thermal corrections should not be neglected. In case energy differences are very large, the eutectic composition is likely to large and close to the pure enantiomer. If energy differences are small thermal corrections play a crucial role as in this range the thermodynamic model of eq. (23) is sensitive to errors. As a consequence, changes of the energy difference with temperature are more likely to affect x_{eu} which in could be exploited for separating enantiomers by a two-step crystallization process.[44] The variation of the eutectic composition with temperature and the solvent is discussed in more detail in the following section.

4.5.3   Variations of the eutectic composition

A variation of the eutectic composition (eutectic shift), Δx_{eu}, is of interest for separating enantiomers by crystallization. A two-step process has been suggested in literature which exploits a shift of the eutectic composition when changing the temperature or solvent system.[44, 216] Hereby, the productivity depends on the position of the eutectic and the magnitude of the shift.[44] According to eq. (23) a variation of the eutectic composition is related to a change in the Gibbs energy of solution difference between the enantiomer and the racemate, $\Delta_{RS-S}\Delta G_{sol}$ (see eq. (67)). Consequently, is a function of temperature and the solvent.

$$\Delta x_{eu} = f\left(T, solvent\right) = \cfrac{1}{1 + \cfrac{1}{4}\exp\left(-2\cfrac{\Delta^{T,solvent}\Delta_{RS-S}\Delta G_{sol}}{RT}\right)} \qquad (67)$$

The eutectic shift can be computationally estimated if $\Delta_{RS-S}\Delta G_{sol}$ is described by either one of the two thermodynamic cycles (see Figure 2.10). Consequently, if the solventdepending terms are assumed to be identical for the enantiomer and the racemic compound, Δx_{eu} can be estimated by via the sublimation cycle by $\Delta_{RS-S}\Delta G_{subl}$. According to eqs. (43) and (44) a temperature variation of $\Delta_{RS-S}\Delta G_{subl}$ is related to the temperature dependence of the solid-state heat capacity difference between the racemic and

enantiopure crystal, $\Delta_{RS\text{-}S}C_P$ (T). In the following, experimentally determined eutectic shifts with temperature are compared to calculations using this work's experimental heat capacity differences (see Figure 4.24).

Literature results of the eutectic shift of lactide and 3ClMA have been summarized before in Table 4.12 along with this works results for naproxen. The naproxen results are additionally summarized in Figure 4.39. All primary experimental data on this work's measurements are given in Appendix (Table 7.14).
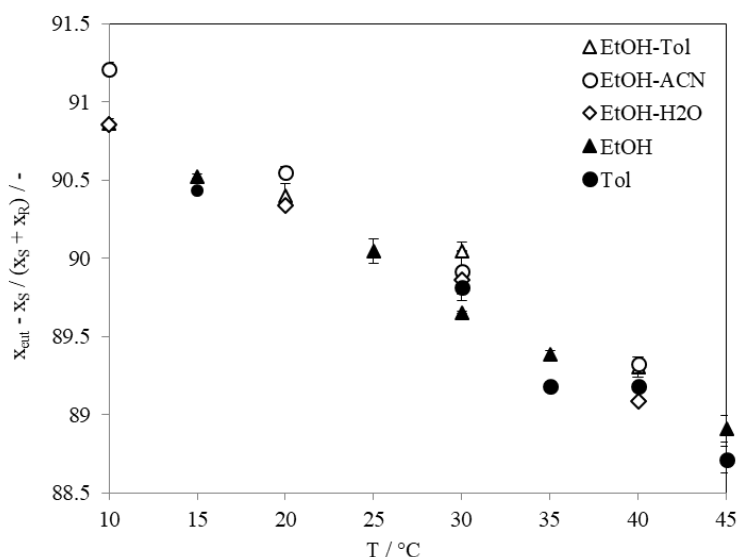
Figure 4.39: Eutectic composition of chiral naproxen in several pure solvents and binary solvent mixtures in between 10 °C and 45 °C.

For naproxen, there is a noticeable shift of x_{eu} in the temperature range of 10 °C and 45 °C which seems to be nearly independent to the solvent system (see Figure 4.39). The binary melt phase diagram suggested the formation of partial solid-solutions close to the pure enantiomer and the racemic compound (see section 4.3.2). This was obtained when mixtures of (S)- and (R)-naproxen crystallized from the melt as well as from acetone solution (see Figure 4.18). The XRPD patterns of the separated equilibrated solid phase from the measurements of the eutectic composition of naproxen show the presence of a mixture of both crystals (enantiomer and racemate) (see Appendix, Figure 7.1).

However, close-ups of parts of the spectra (see Figure 4.40) reveal slight shifts of one reflection ~23° for some of the studied mixed solvent systems. It has been previously shown in section 4.3.2 that these shifts are evoked by the formation of partial solidsolutions when crystallized from the melt (see Figure 4.20) as well as from acetone solutions (see Figure 4.19). Effects of the partial solid-solutions on the spectra within Figure 4.40 are small and difficult to identify. In any case the formation of partial solidsolutions of naproxen appears to have no significant effect on the experimental eutectic composition and its shift with temperature (Figure 4.39). However, parts of the experimental uncertainties can potentially be attributed to that.
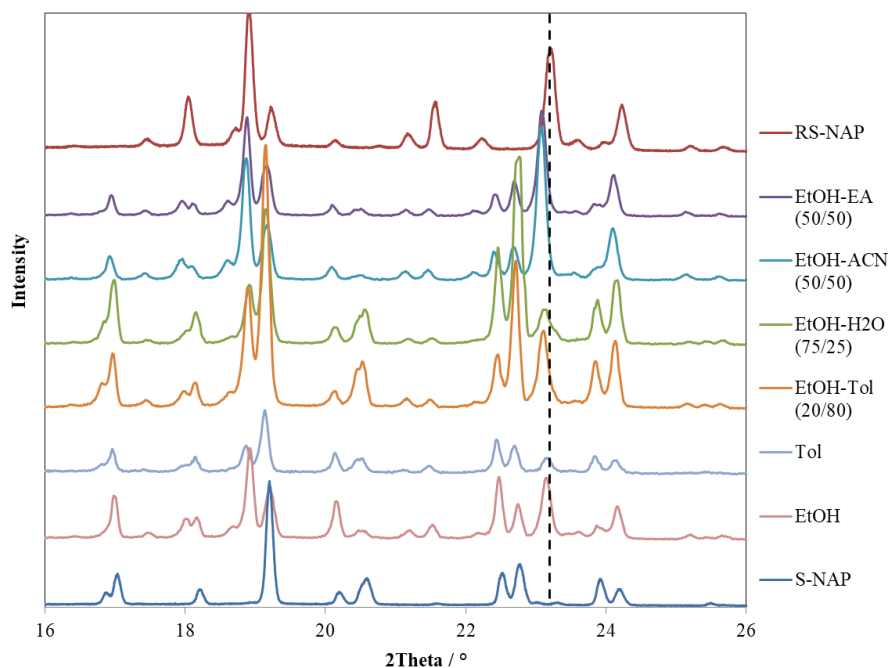
Figure 4.40: Extract of the XRPD pattern of the equilibrated solid phase from measurements of the eutectic composition reveals mixtures of (*S*)- and (*RS*)-naproxen. One peak is marked, which is shifted in some cases indicating the formation of partial solid-solutions within the racemic crystal.

In summary, a shift of x_{eu} with temperature (eutectic shift Δx_{eu}) has been estimated for all three substances (see Table 4.12). As discussed before, in theory those are related, according to eq. (67), to temperature integrals of the solid-state heat capacity difference between the racemic and enantiopure crystal, $\int \Delta_{RS-S} C_P(T) dT$. Hence, integrals of this work's high temperature DSC heat capacity measurements (Figure 4.24) were used to calculate the change of $\Delta_{RS-S}\Delta G_{subl}$ within a temperature range of 20 K. This results in a $\Delta^{T1-T2}\Delta_{RS-S}\Delta G_{subl}$ which can subsequently used to calculate $\Delta x_{eu}(T)$ via eq. (67).

There is a small temperature effect on the Gibbs free energy sublimation differences for all three substances resulting in a $\Delta^{T1-T2}\Delta_{RS-S}\Delta G_{subl}$ which is large enough to affect the eutectic composition. These calculated shifts are shown in Figure 4.41 in comparison to experimental data (see Table 4.12). Primary data on $\Delta^{T1-T2}\Delta_{RS-S}\Delta G_{subl}$ and the resulting eutectic shifts with temperature are given in Appendix Table 7.21. For all three molecules the estimations capture the trend from the experiments which shows a decreasing x_{eu} with temperature for lactide and naproxen and an increasing x_{eu} for 3ClMA. Those shifts of the eutectic cannot be estimated by any of the computationally methods (ψ_{mol} or ψ_{crys}) since they are not able to give a temperature-dependent heat capacity difference in this range of temperature (see Figure 4.24).
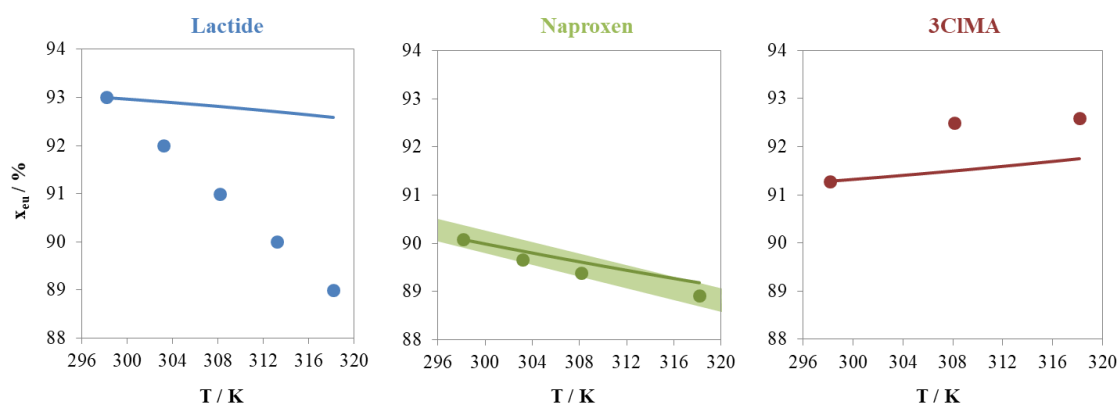
Figure 4.41: The shift of the eutectic composition with temperature, $\Delta x_{eu,calc}(T_2-T_1)$, ($T_1 = 298$ K to $T_2 = 318$ K) compared to ($\bullet$) experimentally determined eutectic shifts, $\Delta x_{eu,exp}(T_2-T_1)$. The eutectic shift is calculated for lactide in EA, 3ClMA in Toluene/EA mixture (80w%/20w%) and for naproxen in ethanol (see Table 4.12 for details). The variation of the eutectic shift of naproxen in several solvent systems is indicated by a green shaded area.

Hence, shifts of the eutectic composition with temperature can arise from differences in the heat capacities at process relevant temperatures. Those require a difference in the higher frequency "molecular modes" which are visible in the Raman spectra of the two crystals (see Figure 4.26). Besides that, $\Delta x_{eu}(T)$ can be as well evoked by a different thermal expansion of the enantiopure and racemic crystal which was neglected within this work's ψ_{mol} and ψ_{crys} calculations.

The challenge of modelling the eutectic shift is closely related to the exponential sensitivity of $\Delta_{RS-S}\Delta G_{subl}$ and x_{eu} over a small energy range. The examples studied all show similarly high values of x_{eu}. However, the same variety of changes of x_{eu} in different solvent systems and the presence and absence of a eutectic shift is found for chiral systems having lower eutectic compositions. These systems should in principle be more sensitive to a change in the free energy difference due to a change in the heat capacity difference or solvent effects. For example, even though propranolol hydrochloride has a very low eutectic composition of $x_{eu} = 55$ % it does not vary with temperature within two different solvents.[5] On the other hand for x_{eu} of 2ClMA, an isomer of this works 3ClMA which has a significantly smaller eutectic composition as 3ClMA, varies in different solvent[247]. Affected by its low eutectic composition it even forms a metastable conglomerate from both melts and solutions. In contrast to 2- and 3-ClMA, the eutectic composition of mandelic acid is stable at $x_{eu} = 69$ % and shows no variation in numerous solvents and temperatures.[5] This is especially surprising as mandelic acid has a difference in heat capacity between the racemic and enantiopure crystal which is dependent on temperature which has been shown in this work (see Figure 4.24) and in literature[235]. This has to be explained by a cancellation of different effects. Thus, for explanation of the mandelic acid examples and cases where very large shifts of the eutectic composition temperature have been found (e.g. from 0.94 to 0.85 between 1 and 60 °C for methionine in water[248]) a reliable prediction method will require great accuracy in all contributions including effects of the solvent.

As a consequence, further experimental studies have been performed for naproxen to

further study the solvent effect on x_{eu}. Therefore, x_{eu} was measured in a variety of solvent mixtures at one temperature (303 K). All primary data is summarized in Appendix (Table 7.15). It has been shown before (Figure 4.35 and Figure 4.36) that for mixtures of ethanol with toluene, acetonitrile and ethyl acetate show a maximum solubility in the binary mixture of the solvents. Water however works as an anti-solvent and decreases the solubility drastically (see Figure 4.36). The eutectic composition was measured within the same solvent mixtures. In all the cases the addition of a second solvent to ethanol only slightly effects the eutectic composition with changes of x_{eu} below $\Delta x_{eu} = 1$ %. Based on the above, it can be summarized that the eutectic composition and its shift with temperature of naproxen in solution mostly related to solid-state properties only (difference in lattice energies and thermal corrections).
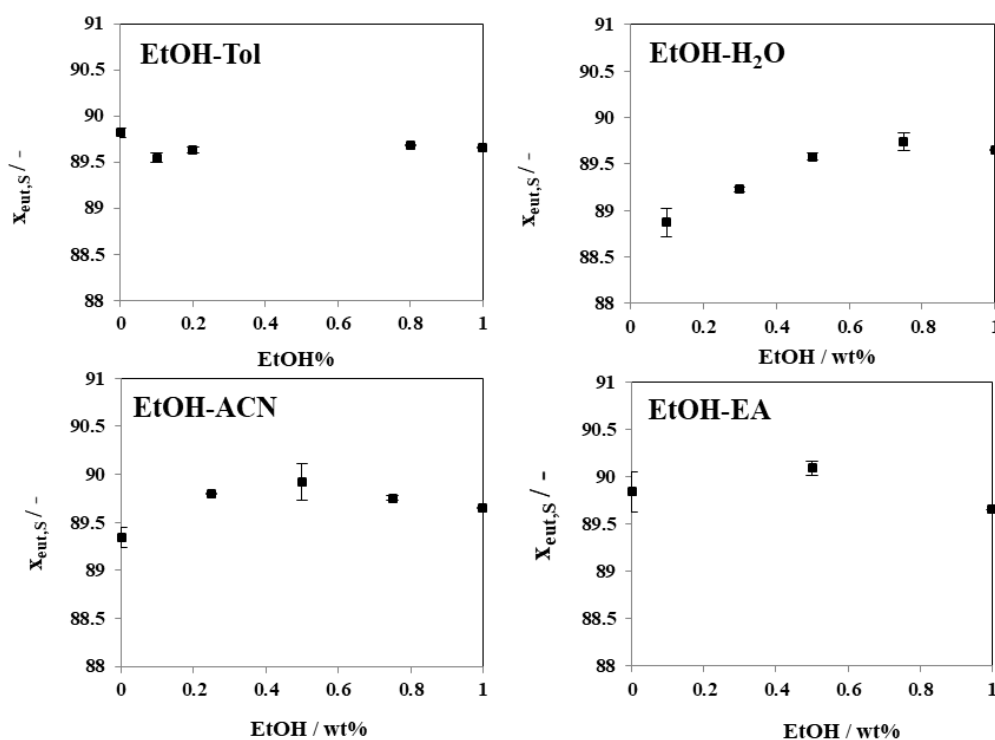
Figure 4.42: Eutectic composition of naproxen in solution with binary solvent mixtures of ethanol with toluene, acetonitrile, ethyl acetate and water.

However, it was shown before that the eutectic composition and its temperature dependence $\Delta x_{eu}(T)$ is not a solid-state property alone.[44] In that case accurate prediction models will have to consider the difference in solvation free energies in the racemic and enantiopure solution. This implies consideration of the non-ideality of the solution in terms of the specific molecule and its solvent as well as solute-solute interactions between the two enantiomers in solution. The influence of solute-solute interactions on the temperature dependency of the absolute as well as relative solubility between the racemate and enantiomer is evaluated in the following section 4.6 for lactide as well as naproxen.

4.5.4 Conclusions

The two thermodynamic cycles have been used to calculate the eutectic composition of lactide, naproxen and 3ClMA at 298 K via a rather simple thermodynamic approach which uses approximations of the solution free energy difference (see eq. (23)). Best results are obtained when the ψ_{crys} electronic structure calculations (E_{latt} and ΔE_{ZPE}) and thermal corrections within the "exp/theory" (ψ_{crys}) model are combined (Figure 4.38). However, the pure lattice energy differences of the ψ_{crys} model give surprisingly good estimated of x_{eu} even though thermal corrections are relevant for all three molecules (see Figure 4.30). The comparatively good performance of the sublimation cycle suggests that predictions of x_{eu} via the difference in sublimation free energy can be used as a guidance for the design of enantioseparation processes. Two general statements can be formulated:

(1)   A large energy difference is related to a eutectic composition close to the pure enantiomer. On the contrary, if energy differences are small, x_{eu} is likely to be closer to the racemate.

(2)   For small energy differences thermal corrections play a crucial role, because the thermodynamic model of eq. (23) is sensitive to errors.

It was shown, that temperature-dependent heat capacity differences between the enantiomer and the racemic compound $\Delta_{RS\text{-}S}C_P$ are shown to be able to stimulate shifts of the eutectic composition with temperature, Δx_{eu} (see eq. (67)). For all three substances there is a small temperature effect of $\Delta_{RS\text{-}S}C_P$ on the Gibbs free energy sublimation which is large enough to affect the eutectic composition (see Figure 4.41). All computational methods, however, fail to reproduce experimental temperature-dependent $\Delta_{RS\text{-}S}C_P$ at temperatures relevant for modelling SLE (see Figure 4.24). Besides the mentioned solidstate effects, influences of the solvent were experimentally investigated for naproxen in various solvent mixtures. Experimental studies indicate that Δx_{eu} of naproxen is almost independent of the solvent and furthermore not noticeably affected by the formation of solid-solutions (see Figure 4.39 and Figure 4.41). This supports the hypothesis that Δx_{eu} for naproxen is exclusively a solid-state property. However, there are many cases in literature where Δx_{eu} is affected by the solvent and thus not a solid-state property alone. For example, there is an influence of the solvent on the temperature dependency of Δx_{eu} for lactide (Table 4.12). This is investigated in more detail in the following section 0, along with the general temperature dependence of absolute and relative solubilities of chiral substances.

4.6   Temperature dependence of the absolute and relative solubility

For a crystallization process a given target substance should have a high solubility in order to enable high productivities. Additionally, in case crystallization is conducted by temperature variation (cooling crystallization), a strong temperature dependency of the solubility is required for achieving high yields. According to eq. (25) the temperature dependency of the solubility is characterized by its solution enthalpy. In a concentrated

solution, besides concentration-independent interactions (solute-solvent) as well concentration-dependent interactions (solute-solute) affect the solubility and its temperature dependence.

Within this section at first the accuracy of the two thermodynamic cycles to calculate the solution enthalpies was evaluated for chiral lactide and naproxen. In order to work out error sources, computations were compared results from a broad experimental investigation of solubilities in a variety of pure and mixed solvent systems at different temperatures. In a second part solvent-independent transfer energies (melting and sublimation) as well as solvent-solute and solute-solute interaction energies on the solution enthalpies were examined in detail. It was investigated, whether solute-solute interactions in solution affect the absolute as well as the relative temperature-dependent solubilities.

4.6.1   Temperature-dependent melting and sublimation free energies

For calculating temperature-dependent solubilities of naproxen and lactide, the solvent independent ΔG_{melt} (T) and ΔG_{subl} (T) within the melt and the sublimation cycle are required, respectively. They are evaluated within this section for the temperature range in which solubilities were measured.

Melting enthalpies and temperatures from Table 4.5 have been used in combination with thermal corrections, in order to determine a temperature-dependent ΔG_{melt} (T). Therefore, ΔH_{melt} and ΔS_{melt} have been corrected from melting to solution temperature using the heat capacity difference between the melt and the solid $\Delta C_P^{l\text{-}s} = C_P^l - C_P^s$ from Table 4.6, according to eq. (33). The experimental heat capacities from Table 4.6 can either be assumed to be temperature-independent, or they can be determined from the temperature-dependent solid state as well as the linearly extrapolated heat capacities of the melt. In order to account for the uncertainties within the two correction methods the average of the two methods has been used while their difference is regarded as an experimental error.

For the sublimation cycle, the ψ_{crys} method has been used to calculate the temperature-dependent sublimation free energies ΔG_{subl} (T). The sublimation enthalpies and entropies at 298 K from Table 4.9 have been adjusted to the various solution temperatures by using the ideal gas and solid-state heat capacities from the ψ_{crys} method according to section 2.7.2. As an experimental counterpart, an experimental $\Delta G_{subl,exp}$ (T) has been determined directly from the experimental vapor pressures of lactide[230] and naproxen (see Figure 4.27). For that purpose, vapor pressures have been extrapolated from measurement temperature (naproxen: 390 K and 420 K; lactide: 320 K and 380 K) to solution temperature (283 to 318 K) using eq. (66). The temperature-dependent experimental sublimation free energies are compared to the computations from the ψ_{crys} method in Figure 4.43.
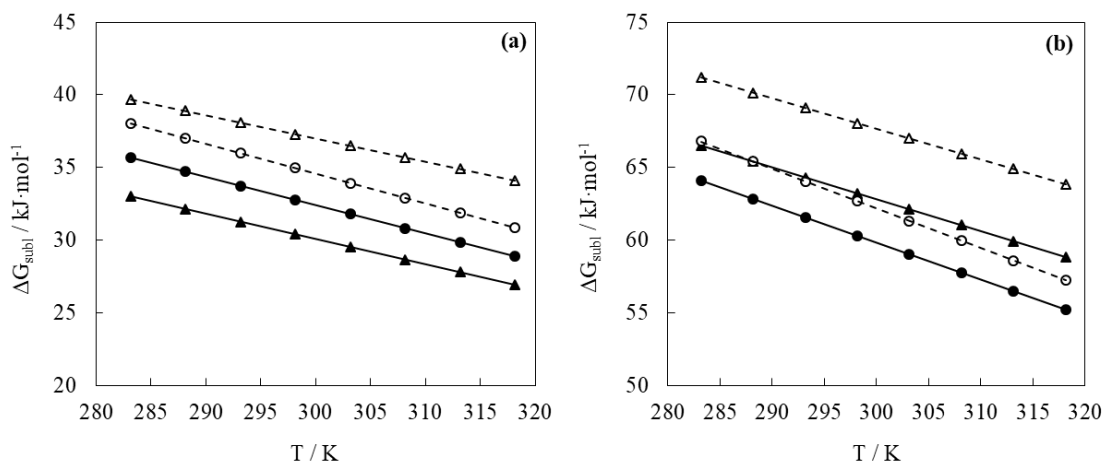
Figure 4.43: Temperature-dependent sublimation Gibbs energies for (a) lactide and (b) naproxen from (●) experimental vapor pressures[41, 230] and (▲) calculations using the ψ_{crys} method. Solid symbols and lines correspond to the enantiomer and open symbols and dashed lines to the racemic compound.

Calculations of ΔG_{subl} (T) using the ψ_{crys} method are generally in good agreement to experiment. There are larger differences for the racemic crystals. This is consistent with the comparably large differences between the calculated and experimental sublimation enthalpies for (RS)-lactide and (RS)-naproxen (see Table 4.9).

4.6.2   Solution enthalpies of lactide and naproxen

Temperature-dependent solubilities have been measured by means of isothermal solubility method according section 3.2.1. They have been performed for both chiral species of lactide as well as naproxen within a temperature range of 10 to 45 °C in a variety of pure and mixed solvent systems. All numeric values of the experimental mole fraction solubilities are summarized in Appendix (Table 7.10 and Table 7.11).

Calculations have been performed by combining the free energies of melting and sublimation from the previous section 4.6.1 with the solvent specific ΔG^E (T) and ΔG_{solv} (T) from the COSMO-RS model. The TZVPD-Fine parameterization has been used for all calculations. For rigid lactide, only one molecular conformation was considered. For naproxen, the four conformations according to Figure 4.32 have been weighted within a Boltzmann distribution according to eq. (64). For both cycles, calculations have been performed at infinite dilution, as well as at saturation concentrations. Additional information on the COSMO-RS model and its application within the two thermodynamic cycles is given in section 2.7.4.

The experimental apparent solution enthalpies, ΔH_{sol}, as well as the computational solution enthalpies at infinite dilution and at saturation concentration, $\Delta H_{sol,inf}$ and ΔH_{sol}, have been extracted from the experimental and calculated solubilities. According to Van't Hoff (see eq. (25)) the apparent solution enthalpy is related to the slope ($\Delta H_{sol} = -R \cdot$ slope) of the temperature dependency of ln x_i over the reciprocal temperature, 1/T. In order to

minimize numerical issues when extracting ΔH_{sol} via eq. (25) the computations have been performed at the same temperatures as the experimental values. The resulting ΔH_{sol} are summarized in Appendix (Table 7.10 and Table 7.11) along with the primary experimental mole fraction solubilities.

Figure 4.44 compares the calculations via the sublimation and melt cycle to the experimental solution enthalpies. The overall accuracy expressed as the root-mean-square error (RMSE) between the calculations and the experiment is 9.3 kJ·mol^{-1} for the melt cycle in case solute-solute interactions are considered and 10.7 kJ·mol^{-1} if infinite dilution is assumed. On the other hand, the sublimation cycle predicts the solution enthalpy with a RMSE of 6.5 kJ·mol^{-1} and in case solute-solute interactions are neglected with a RMSE of 8.1 kJ·mol^{-1}. Thus, the sublimation cycle calculations of the solution enthalpies are slightly more accurate in comparison to the melt cycle results. For both thermodynamic cycles the accuracy is improved if the concentration dependence of solvation terms is considered. Furthermore, there is a tendency that the melt cycle underestimates the solution enthalpy (see Figure 4.44).
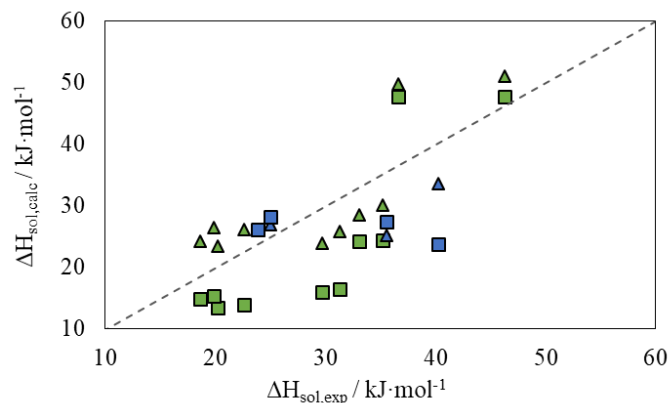
Figure 4.44: Calculated versus experimental apparent solution enthalpies for naproxen (green symbols) and lactide (blue symbols) in a variety of pure and mixed solvent systems. Calculations via the melt cycle ($\square$) and the sublimation cycle (Δ) use the temperature-dependent experimental melting and calculated sublimation free energies of the ψ_{crys} method as well as the solvent specific ΔG^E and ΔG_{solv} from the COSMO-RS model.

In order to evaluate error sources, the accuracy of the COSMO-RS model to model H^E and ΔH_{solv} was evaluated. Therefore, "experimental" H^E_{exp} and $\Delta H_{solv,exp}$ have been recalculated from the experimental solution enthalpies as well as the experimental melting and sublimation enthalpies according to eqs. (37) and (46), respectively. The corrected ΔH_{melt} (298 K) according to Table 4.5 and Table 4.6 as well as ΔH_{subl} (298 K) from Table 4.8 were used, as 298 K is approximately the average temperature of the experimental solubilities. The calculations of H^E and ΔH_{solv} are compared to the experimental values within Figure 4.45 (a) and (b), respectively. While the excess enthalpies take positive as well as negative values the solvation enthalpies are exclusively negative and significantly larger in size. The RMSE of the $\Delta H_{solv,calc}$ is 7.2 kJ·mol^{-1} which is slightly larger than the overall computational error for ΔH_{sol} (6.5 kJ·mol^{-1}). Sublimation enthalpies are calculated with an accuracy of RMSE of 3.6 kJ·mol^{-1} by the ψ_{crys} method

(see Table 4.9). Hence, the largest part of the overall computational error for calculating ΔH_{sol} via the sublimation cycle is most likely attributed to the computation of the solvation energies using COSMO-RS. Within the melt cycle, all errors are related to the calculations of H^E_{calc} as the solubilities are calculated using the same experimental melting properties as for recalculating of H^E_{exp}. Consequently, the overall RMSE of the melt cycle is the same as of the calculated excess enthalpies (RMSE = 9.3 kJ·mol^{-1}).
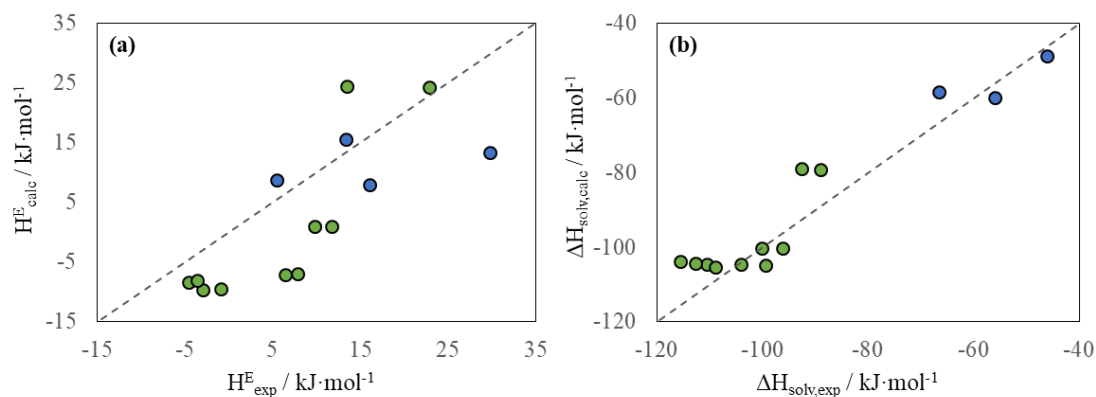
Figure 4.45: Calculated versus experimental **(a)** excess enthalpies and **(b)** solvation enthalpies for naproxen (green symbols) and lactide (blue symbols).

Additionally, methodical uncertainties can arise when extracting the apparent solution enthalpies from the experimental and calculated solubilities via the Van't Hoff equation. The Van't Hoff solution enthalpy incorporates changes of the activity coefficient of the solute with temperature but neglects the change in activity with concentration at constant temperature.[59] Hence, it is comparable but not necessarily equal to the true enthalpy of solution at saturation concentration. Especially for larger temperature ranges the temperature dependency of ln x_i can exhibit a distinct non-linear behaviour which the Van't Hoff equation is only in parts able to account for.[57] However, within the systems at hand there are no cases with a pronounced non-linear behaviour of ln x over 1/T. Effects of solution non-idealities on the temperature dependence of the absolute as well as relative solubilities are discussed in more detail in the following parts.

4.6.3   Analysis of energy contributions to the solution enthalpies

Within this section the various energy contributions to the solution enthalpies and thus to the temperature dependency of the solubilities are examined for lactide and naproxen. Experimental and calculated solution enthalpies at infinite dilution and at saturation concentration are systematically compared. This makes it possible to extract the various solvent independent and solvent specific contributions to ΔH_{sol}.

As discussed before ΔH_{sol} has been determined from the experimental as well as calculated solubilities via the equation of Van't Hoff (see eq. (25)). Calculations have been performed at infinite dilution to obtain $\Delta H_{sol,inf}$ or at saturation concentration to obtain ΔH_{sol}. As experimental counterpart to the calculated solution enthalpies at infinite

dilution, calorimetric dissolution measurements have been performed in order to extract and experimental $\Delta H_{sol,inf}$. This is discussed in the following section. They are subsequently used in order to quantify and evaluate solvent specific interaction in solution.

Solution calorimetry

Dissolution enthalpies were measured for the diluted system by solution calorimetry according to section 3.2.4 in order to extract experimental solution enthalpies at infinite dilution. Within this section measurements of $\Delta H_{sol,inf}$ are presented and discussed. All primary data on the caloric dissolution measurements and the final $\Delta H_{sol,inf}$ are summarized in Appendix (Table 7.12 and Table 7.13).

Caloric measurements of the dissolution the diluted solution have been performed at 30 °C. Three to four measurements at varying concentrations have been performed for each compound and solvent in order to extrapolate a $\Delta H_{sol,inf}$ at $x = 0$ for (S)- and (RS)- lactide as well as (S)- and (RS)-naproxen. On the one hand, sufficient amount of substance is required within the caloric measurements in order to get a reliable thermal response. On the other hand, the final solution concentrations should be significantly lower, in comparison to saturation concentrations (solubility line), to obtain solution enthalpies for the diluted system. As a consequence, it is beneficial if saturation concentrations are high. In order to perform experiments sufficiently far away from the solubility line.
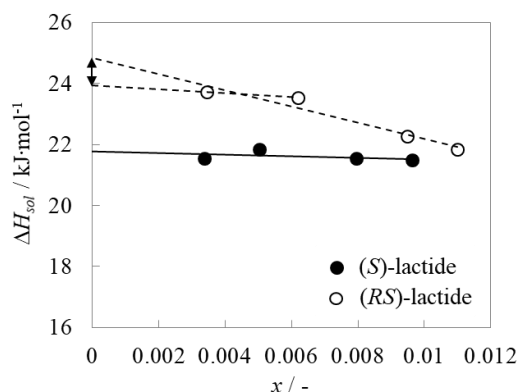
Figure 4.46: Caloric measurements of the dissolution of different amounts of (S)- and (RS)-lactide in toluene at T_{ref} = 303 K. Linear extrapolations to $x = 0$ give the solution enthalpy at infinite dilution $\Delta H_{sol,inf}$.

For lactide, calorimetric investigations have been performed for the diluted toluene system. The results of the dissolution of (S)- and (RS)-lactide in toluene at $T = 303$ K are presented in Figure 4.46. Due to the more stable crystal structure, the racemic compound has larger solution enthalpies. Additionally, the dissolution enthalpies of (RS)-lactide show a significantly larger concentration dependency. This could be due to the lower solubility of the racemic compound in comparison to the enantiomer. Thus, the caloric measurements have been evaluated once only for the linear part until 0.6 mol% and a second time for the whole concentration range. The difference between the two

extrapolated values at $x = 0$ is incorporated to the overall experimental uncertainty of $\Delta H_{sol,inf}$. For (*S*)-lactide saturation concentrations at 303 K are 4.1 mol% and thus far from the solution concentrations in the dissolution experiments (see x-axis in Figure 4.46). However, even though the measurements are linearly extrapolated to $x = 0$ it is likely that the final $\Delta H_{sol,inf}$ incorporate parts of the concentration-dependent excess enthalpies.

For chiral naproxen, measurements have been performed in pure ethanol and in solvent mixtures of ethanol with toluene (20/80 wt% EtOH/Toluene), with water (75/25 wt% EtOH/H$_2$O) and with acetonitrile (50/50 wt% EtOH/ACN). The results are summarized in Figure 4.47.
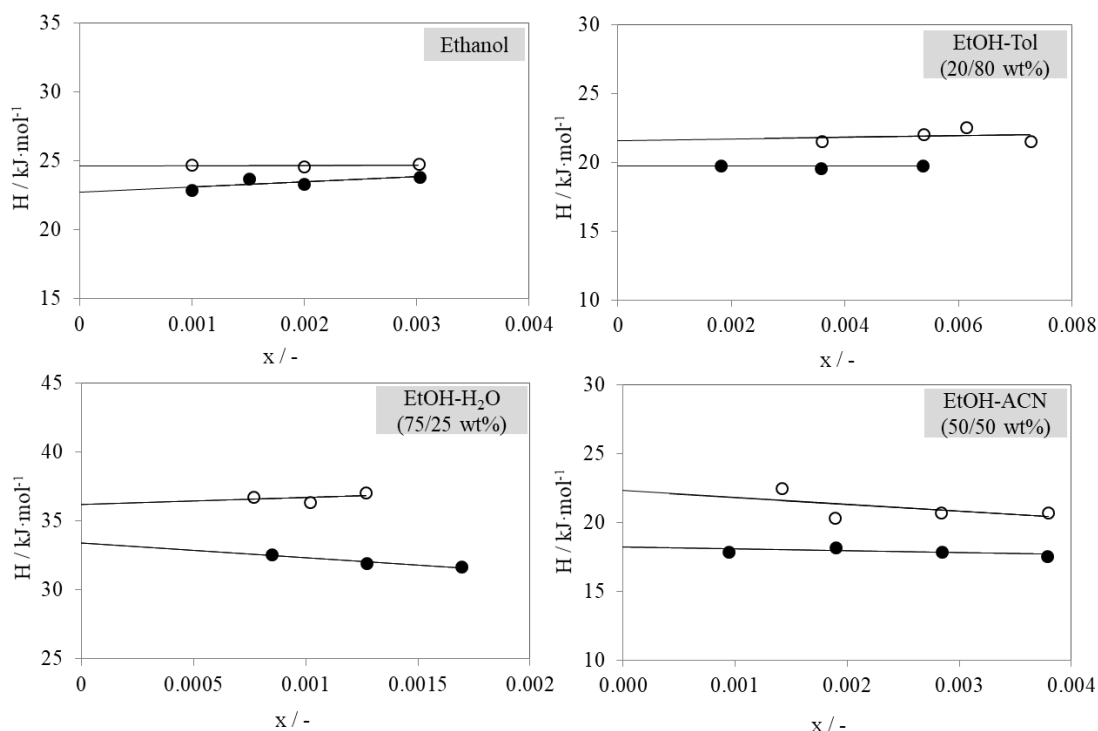
Figure 4.47: Caloric measurements of the dissolution of different amounts of (●) (*S*)- and (○) (*RS*)-naproxen in pure and mixed solvent systems at $T_{ref} = 303$ K. Linear extrapolations to $x = 0$ give the solution enthalpy at infinite dilution $\Delta H_{sol,inf}$.

All experiments have been performed for concentrations far below saturation concentrations. Within all solvent systems a linear behaviour of the concentration dependency was assumed. The extrapolations to $x = 0$ are used in the following as experimental solution enthalpies at infinite dilution, $\Delta H_{sol,inf}$. The experimental uncertainties from the linear least squares regression appear to be larger for the racemic crystal which is possibly due to the lower saturation concentrations and thus slower dissolution kinetics.

Temperature-dependent solubilities of chiral lactide

Figure 4.48 compares the experimental and calculated solubilities for lactide in ethanol as well as toluene between 10 and 45 °C. In all cases, (*RS*)-lactide has a significantly lower solubility than (*S*)-lactide. Thus, differences between the calculations at infinite dilution and saturation concentration are less obvious for the racemic system and only affect the solubilities at elevated temperatures. On the contrary, the calculated solubilities of (*S*)-lactide in ethanol and toluene are significantly affected by solute-solute interactions within both thermodynamic cycles due to higher saturation concentrations compared to (*RS*)-lactide. As a consequence, concentration dependent solute-solute interactions affect as well the relative solubilities between the enantiomer and the racemic compound.
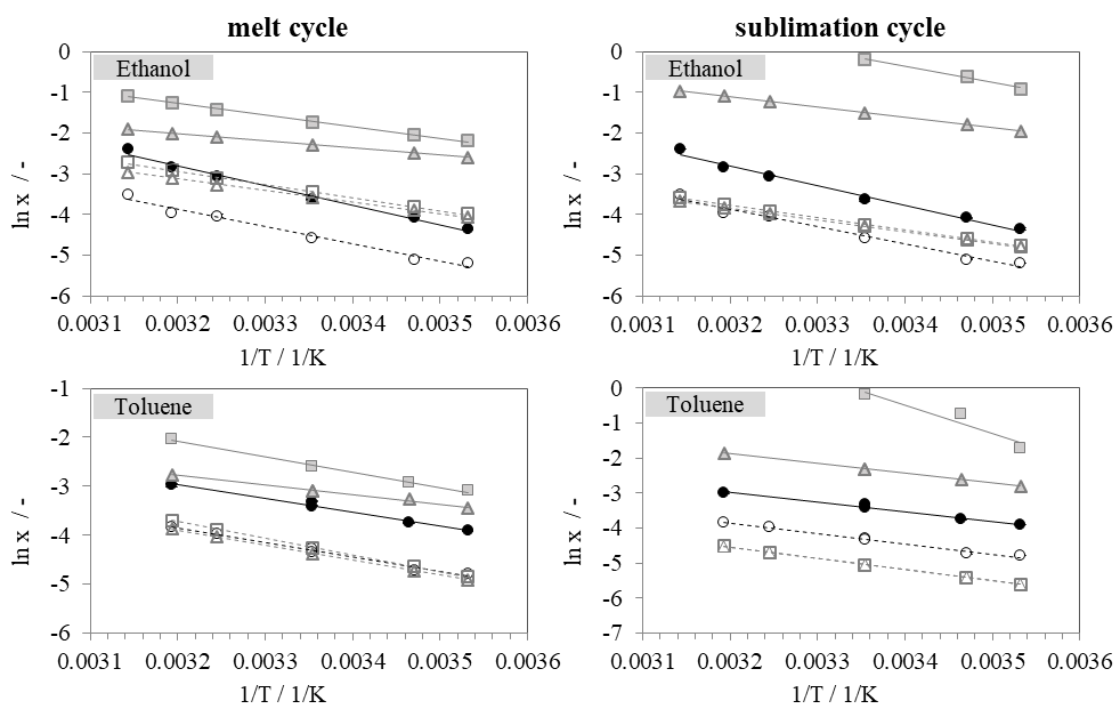
Figure 4.48 (○,●) Experimental solubilities, ln *x*, of lactide in ethanol and toluene as a function of the reciprocal temperature, 1/T, in comparison to calculations via the (left) melt cycle and (right) sublimation cycle. Calculation at (△,▲) infinite dilution and (□,■) at saturation concentration are displayed. Open symbols and dashed lines correspond to (*RS*)-lactide and solid symbols and solid lines to (*S*)-lactide.

For a quantitative evaluation, solution enthalpies have been extracted from the experimental and calculated solubilities in Figure 4.48 via the Van't Hoff method. The absolute values, as well as their differences, are summarized together with the experimental $\Delta H_{sol,inf}$ and the temperature corrected ΔH_{melt} in Table 4.13. They are compared against the experimental $\Delta H_{sol,inf}$ from solution calorimetry (see Figure 4.47) and the temperature corrected ΔH_{melt} in order to evaluate the solvent effect on the solution enthalpies.

Table 4.13: Melting enthalpies of (*S*)- and (*RS*)-lactide and their differences Δ(*RS-S*) in comparison to $\Delta H_{sol,inf}$ as well as ΔH_{sol} in ethanol and toluene from calculations and experiment.

Solvent	solute	Melt Cycle		Sublimation Cycle[a]		Experiment		
		$\Delta H_{sol,inf}$	ΔH_{sol}	$\Delta H_{sol,inf}$	ΔH_{sol}	ΔH_{melt} (30 °C)	$\Delta H_{sol,inf}{}^{b}$ (30 °C)	ΔH_{sol}
ethanol	(*S*)	14.7	23.8	20.9 (29.7)	33.6 (47.4)	10.5±0.2	n.a.	40.2
	(*RS*)	23.9	27.5	23.9 (27.5)	25.2 (42.4)	19.5±0.7	n.a.	35.6
	Δ(*RS-S*)	*9.3*	*3.6*	*2.9 (5.4)*	*-8.3 (-4.8)*	*9.0±0.5*	*-*	*-4.7*
toluene	(*S*)	16.2	26.1	22.9 (31.7)	69.1 (49.7)	10.5±0.2	21.8±0.2	25.2
	(*RS*)	25.6	28.2	25.9 (37.1)	26.9 (42.3)	19.5±0.7	24.7±1.0	24.5
	Δ(*RS-S*)	*9.4*	*2.1*	*2.9 (5.4)*	*-42.2 (-7.4)*	*9.0±0.5*	*2.9±1.0*	*-0.7*

a. Values in bracket correspond to calculation using $\Delta G_{subl,exp}$ instead of $\Delta G_{subl,calc}$ (ψ_{crys}) (see Figure 4.43) in combination with ΔG_{solv} from COSMO-RS

b. $\Delta H_{sol,inf}$ determined by solution calorimetry for the diluted system according to section 3.2.4.

There are two main conclusions that can be extracted from the experimental results in toluene. For the sake of clarity, they are additionally illustrated in Figure 4.49. On one hand, the absolute solid-liquid phase transition enthalpies steadily increase from the solvent free system via the diluted solution to saturation concentration for both (*S*)- and (*RS*)-lactide. On the contrary, the enthalpy differences Δ(*RS-S*) decrease significantly from $\Delta_{RS-S}\Delta H_{melt}$ = 10.5 kJ·mol^{-1} to $\Delta_{RS-S}\Delta H_{sol}$ = -0.7 kJ·mol^{-1}. The solution calorimetry measurements for the diluted systems give an enthalpy difference $\Delta_{RS-S}\Delta H_{sol,inf}$ of 2.6 kJ·mol^{-1} which is in between $\Delta_{RS-S}\Delta H_{melt}$ and $\Delta_{RS-S}\Delta H_{sol}$. Based on the above, it can be concluded that concentration-dependent solution non-idealities contribute to the solution enthalpies of lactide in toluene.
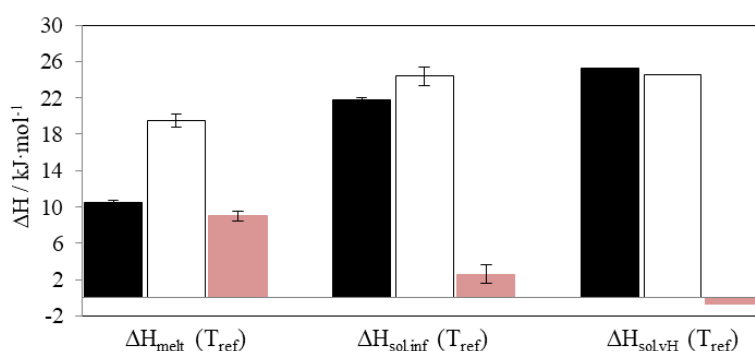
Figure 4.49: Melting enthalpies corrected to 30 °C (ΔH_{melt}) in comparison to the calorimetrically determined solution enthalpies at infinite dilution ($\Delta H_{sol,inf}$), as well as Van't Hoff solution enthalpies (ΔH_{sol}) in toluene; (black bars) (*S*)-lactide, (white bars) (*RS*)-lactide; differences Δ(*RS-S*) (red bars).

This has been qualitatively observed as well in the calculations (see Table 4.13). Within both cycles, the calculated solution enthalpies are larger at saturation concentration in comparison to the infinite dilution. Conversely, the differences decrease and, in case of

the sublimation cycle, even switch sign due to solute-solute interactions in solution. The effect of solute-solute interactions on the solution enthalpy differences between (S)- and (RS)-lactide is slightly more severe in ethanol where experimental $\Delta_{RS-S}\Delta H_{sol}$ = -4.7 kJ·mol^{-1} (see Table 4.13). T This trend is well captured by the calculations via the sublimation cycle and can be clearly attributed to modelling of solute-solute interactions in solution. The calculated saturation concentrations from the melt cycle are smaller than those of the sublimation cycle (see Figure 4.48). As a consequence, the enthalpy difference is affected slightly less and changes from 9.3 to 3.6 kJ·mol^{-1}.

As discussed before, the calorimetric measurements in toluene are likely to incorporate parts of the concentration effects. In theory, the solution enthalpy differences for the infinite dilution should be equal to the melting enthalpy differences as the studied solvents are achiral. There are other possible explanations for the rather large differences between the melting and dissolution enthalpy differences. For example, measurement errors of the experimentally determined melting enthalpies could be responsible for parts of the differences. This work's uncorrected melting enthalpy differences are $\Delta_{RS-S}\Delta H_{melt}$ (T_{melt}) = 11 kJ·mol^{-1} and thus slightly larger than the 8 kJ·mol^{-1} from literature[221] (see Table 4.5). Additionally, the thermal corrections slightly decrease the enthalpy differences from 11 kJ·mol^{-1} at T_{melt} to 9.0±0.5 kJ·mol^{-1} at T_{ref}. Yet, the accumulated uncertainties are not the only explanation for the large difference between $\Delta_{RS-S}\Delta H_{melt}$ and $\Delta_{RS-S}\Delta H_{sol,inf}$. Thus, despite several possible sources of error, there is strong evidence that solute-solute interactions affect the solution enthalpy of lactide in toluene as well as in ethanol.
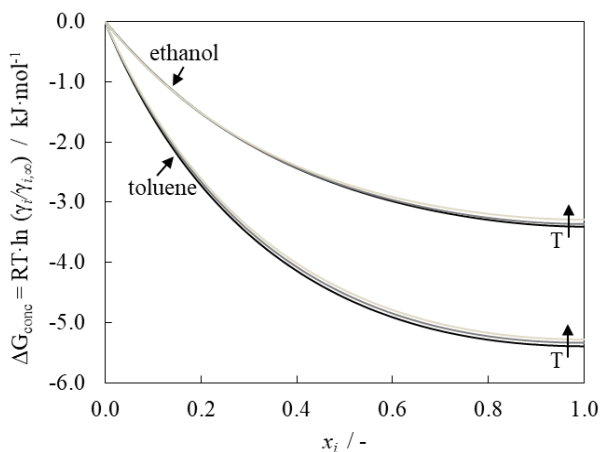
Figure 4.50: COSMO-RS calculations of the concentration and temperature dependency of the Gibbs energy difference between saturation concentration and infinite dilution, ΔG_{conc}, for lactide in ethanol and toluene. The three lines represent calculations at 15, 30 and 45 °C for each solvent.

In theory, solute-solute effects in solution require that the solvent specific terms are a function of the solution concentration. Within the COSMO-RS model the concentration dependency of the excess Gibbs free energy of mixing, ΔG^E, as well as the Gibbs free energy of solvation ΔG_{solv} is incorporated within the chemical potential in solution (see 2.7.3). The chemical potential of the solute in solution is a function of the activity coefficient in solution. Thus, the absolute concentration dependent Gibbs energy contribution to ΔG^E and ΔG_{solv} is related to the difference between the chemical potential

of the solute i at saturation concentration and at infinite dilution $\Delta G_{conc} = RT \cdot \ln (\gamma_i / \gamma_{i,inf})$. The COSMO-RS results of ΔG_{conc} for lactide in ethanol and toluene are depicted in Figure 4.50. Within both solvents ΔG_{conc} is significantly affected by the solution concentration while effects of the temperature are rather small. This strengthens the suspicion that concentration-dependent solute-solute interactions are responsible for the above discussed effects on the solution enthalpies.

In summary, within both solvent systems the calculated temperature dependence of the solubilities is affected by solute-solute interactions which could be qualitatively validated for toluene by experiment using solution calorimetry. The strong solute-solute interactions within the saturated ethanol solution which influences the relative solubility of (S)- and (RS)-lactide could be one source for the comparably large shift of the eutectic concentration with temperature that has been observed[225] in ethanol (see Table 4.12). However, such a shift has not been detected within the lactide-toluene system. This is surprising as the overall solubility of lactide in toluene is slightly larger in comparison to ethanol. This can only be explained by a cancellation of the various effects or an incorrect description of the solution interactions of lactide in toluene.

Temperature-dependent solubilities of chiral naproxen

Temperature-dependent solubilities have been studied for naproxen in pure toluene, ethanol and in a 20/80 wt% mixture of ethanol and toluene. The experimental and calculated solubilities are depicted in Figure 4.51. For all solvent systems the sublimation cycle significantly underestimates the absolute solubilities of the two chiral crystals. This is due to an overestimation of sublimation Gibbs energies by the ψ_{crys} method, especially for (RS)-naproxen (see Table 4.9). As a consequence, differences between the calculations at infinite dilution and at saturation concentration rather small in comparison to the melt cycle results. However, even though the melt cycle calculates significantly larger solubilities, the calculations at infinite dilution and at saturation concentration are hardly distinguishable at the scale in Figure 4.51. As a consequence, for both computational methods only the calculations at saturation concentration are displayed.
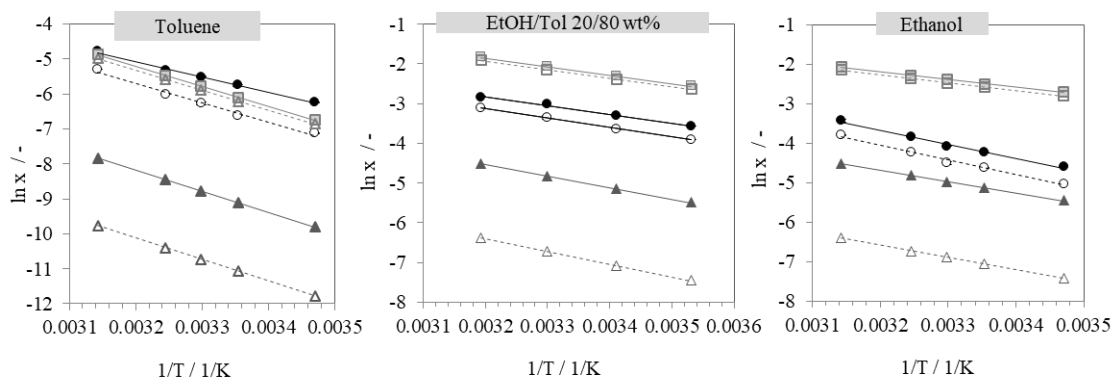
Figure 4.51: Solubilities, ln x, of naproxen in toluene, ethanol and in 20/20 wt% ethanol/toluene mixture as a function of the reciprocal temperature 1/T. (○,●) Experimental results are compared to calculations via the (□,■) melt and the (△,▲) sublimation cycle. Open symbols and dashed lines correspond to (RS)-naproxen and solid symbols and solid lines to (S)-naproxen.

The strong overestimation of the free energy difference between the racemic compound and the enantiomer by the ψ_{crys} method results in an overestimation of the calculated solubility differences. On the contrary, the melt cycle is not able to resolve the experimental solubility difference between (*S*)- and (*RS*)-naproxen due to the very similar melting behaviour of the two chiral crystals (see Table 4.5). In case solubility differences are small, the relative solubilities should be affected less by concentration-dependent effects.

For a quantitative evaluation, solution enthalpies have been extracted from the experimental and calculated solubilities in Figure 4.51 via the Van't Hoff method. The absolute values as well as their differences are summarized together with the experimental $\Delta H_{sol,inf}$ and the temperature corrected ΔH_{melt} in Table 4.14. They are compared against the experimental $\Delta H_{sol,inf}$ from solution calorimetry (see Figure 4.48) and the temperature corrected ΔH_{melt}, in order to evaluate the solvent effect on the solution enthalpies. Previously, when studying the absolute solubilities of naproxen within the toluene-ethanol system (see Figure 4.35 in section 4.4.2), it was shown that the SLE of both chiral crystals of naproxen exhibit a strong non-linear solubility behaviour. The highest solubility occurs in between 20/80 and 40/60 wt% of ethanol/toluene mixture. Conversely to the absolute solubilities, the solution enthalpy is largest within pure toluene and smallest for the 20/80 wt% ethanol/toluene solvent mixture (see Table 4.14). Nonetheless, the significant increase in solubility within the solvent mixture seems not to evoke concentration-dependent effects in solution that noticeably change the solution enthalpies.

Table 4.14: Melting enthalpies of (*S*)- and (*RS*)-naproxen and their differences $\Delta(RS\text{-}S)$ in comparison to $\Delta H_{sol,inf}$ as well as ΔH_{sol} in ethanol, toluene and mixtures of both from calculations and experiment.

Solvent	Solute	Melt Cycle		Sublimation Cycle[a]		Experiment[b]		
		$\Delta H_{sol,inf}$	ΔH_{sol}	$\Delta H_{sol,inf}$	ΔH_{sol}	ΔH_{melt} (30 °C)	$\Delta H_{sol,inf}$ (30 °C)	ΔH_{sol}
Toluene	(*S*)	42.2	47.7	49.4 (56.4)	49.8 (58.5)	23.2±0.4	n.a.	36.6
	(*RS*)	42.4	47.8	51.0 (64.9)	51.1 (66.0)	23.4±0.4	n.a.	46.3
	$\Delta(RS\text{-}S)$	*0.2*	*0.0*	*1.7 (8.5)*	*1.3 (7.4)*	*0.2±0.4*	*-*	*9.7*
Etoh/Tol (20/80)	(*S*)	17.9	14.9	24.8 (31.9)	24.2 (29.6)	23.2±0.4	19.7±0.3	18.6
	(*RS*)	18.0	15.3	26.5 (40.4)	26.4 (39.0)	23.4±0.4	21.6±1.3	19.8
	$\Delta(RS\text{-}S)$	*0.2*	*0.4*	*1.7 (8.5)*	*2.2 (9.5)*	*0.2±0.4*	*1.9±1.3*	*1.2*
Ethanol	(*S*)	17.1	16.1	24.2 (31.3)	24.0 (30.3)	23.2±0.4	22.7±0.5	29.7
	(*RS*)	17.3	16.5	25.9 (39.8)	25.9 (39.1)	23.4±0.4	24.6±0.2	31.3
	$\Delta(RS\text{-}S)$	*0.2*	*0.4*	*1.7 (8.5)*	*1.9 (8.8)*	*0.2±0.4*	*1.9±0.5*	*1.6*

a.   Values in bracket correspond to calculation using $\Delta G_{subl,exp}$ instead of $\Delta G_{subl,calc}$ (ψ_{crys}) (see Figure 4.43) in combination with ΔG_{solv} from COSMO-RS

b. $\Delta H_{sol,inf}$ determined by solution calorimetry for the diluted system according to 3.2.4.

Besides the absolute values, relative solubilities and their temperature dependence are of importance as they are related to the eutectic composition in solution (see eq. (23)). Hence, the influence of solute-solute interactions in solution on the temperature dependence of the relative solubilities is discussed in the following. For that purpose, in addition to previously evaluated toluene-ethanol solvent systems, temperature-dependent solubilities have been measured in mixtures of ethanol and acetonitrile (50/50 wt%) as well as ethanol and water (75/25 wt%). They have been used to extract the apparent Van't Hoff solution enthalpies ΔH_{sol}. Furthermore, solution enthalpies at infinite dilution have been determined by solution calorimetry (see Figure 4.47).

Figure 4.52 shows the various experimental $\Delta_{RS-S}\Delta H_{sol}$ and $\Delta_{RS-S}\Delta H_{sol,inf}$ for naproxen in comparison to calculations at infinite dilution and at saturation concentration. As previously discussed in section 4.4.2, acetonitrile increases the solubility of naproxen drastically while water acts as anti-solvent. Despite the significant changes of the absolute solubilities there are no significant effects of the solution concentration on the experimental solution enthalpy differences. This is consistent with the calculations from both thermodynamic cycles which give a constant enthalpy difference at infinite dilution and some small concentration effects within the calculations at saturation concentration. Those are largest within the solvent system with the highest solubilities (ethanol/toluene and ethanol/ACN). This is consistent to experiment and thus likely due to the fact that the solvation shell is getting less dense with increasing solution temperature and, thus, solution concentrations. Within the 50/50 wt% EtOH/ACN mixture one naproxen molecules is surrounded by 40 solvent molecuels at 10 °C and only 17 solvent molecules at 40 °C. However, differences are small and within the experimental uncertainty of determining $\Delta_{RS-S}\Delta H_{sol}$ and $\Delta_{RS-S}\Delta H_{sol,inf}$.
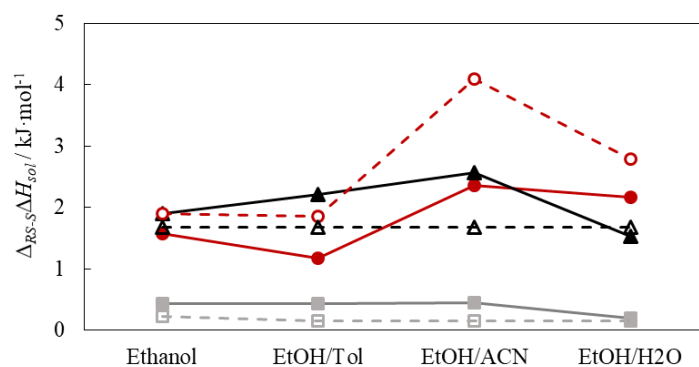
Figure 4.52: Solution enthalpy difference $\Delta_{RS-S}\Delta H_{sol}$ between (*RS*)- and (*S*)-naproxen in ethanol, a 80/20 wt% ethanol/toluene solvent mixture, a 50/50 wt% ethanol/ACN solvent mixture and a 75/25 wt% ethanol/water solvent mixture. (red ○,●) experiment and calculations via the (grey □,■) melt and the (black △,▲) sublimation cycle. Open symbols and dashed lines correspond to the infinite dilution whereas solid symbols and solid lines to saturation concentration.

In summary, the concentration effects on the absolute solution enthalpies and the differences between the enantiomer and the racemic compound are rather small within the studied solvent systems for naproxen in comparison to lactide systems (see Table 4.13). This is consistent with the previously described solvent independent eutectic

composition for naproxen (see Figure 4.41). As a consequence, this substantiate the suspicion that the shift of the eutectic composition of naproxen in solution is merely evoked by temperature-dependent solid-state properties.

4.6.4 Conclusions

The two thermodynamic cycles have been used to calculate the solution enthalpies for chiral lactide and naproxen in a variety of pure and mixed solvent systems. Calculations are compared to experimental solubilities which have been measured in the frame of this work (see Figure 4.44). The of the sublimation cycle using sublimation free energies from the ψ_{crys} method has been shown to be slightly more accurate than the melt cycle results. For both approaches the consideration of solute-solute interactions slightly enhances the calculations accuracy.

Concentration-dependent effects are especially relevant for lactide in toluene as well as in ethanol (see Table 4.13). The calculation results suggest that solute-solute interactions in solution affect the absolute as well as relative solution behaviour of lactide in both systems (see Figure 4.50). This is qualitatively in agreement with experimental findings. Experimentally, the apparent solution enthalpies were compared to caloric dissolution experiments for the diluted solution (see Table 4.13 and Figure 4.49).

Even in cases where experimental saturation concentrations of naproxen and lactide are comparable, the solution enthalpy difference between (*S*)- and (*RS*)-naproxen is not affected by concentration-dependent interactions in solution (Figure 4.52). This is consistent with the solvent-independent shift of the eutectic composition (see Figure 4.41). This is thus rather evoked by temperature-dependent solid-state properties alone. For lactide, however, a comparably large shift of the eutectic concentration with temperature has been observed in ethanol[225] which is consistent with the strong solute-solute interactions energy contributions to the solution enthalpy differences.

5 Conclusiones and Outlook

In this work, a consistent framework was derived and tested for calculating absolute mole fraction solubilities of organic molecular crystals via the so-called *melt cycle* and the so-called *sublimation cycle*. These two approaches aim to reduce labour and substance intensive experimental work. In fact, the sublimation cycle relies exclusively on first-principle computational methods. Both cycles can resolve the influence of the crystal structure and thus can distinguish between polymorphs and chiral crystals. Furthermore, they are capable of handling pure as well as mixed organic solvent systems and are not restricted to infinite solution. This thesis used a joint computational and experimental approach to evaluate the energy contributions required for calculating solid-liquid phase equilibria via the two thermodynamic cycles. We focused on three representatives of chiral compound forming systems; namely lactide, naproxen and 3-chloromandelic acid (3ClMA).

The melting and sublimation thermochemistry of chiral lactide, naproxen and 3ClMA have been studied by means of experimental and computational methods. It was shown that measurement uncertainties of the melting thermodynamics (T_{melt} and ΔH_{melt}) can be large enough to noticeably affect ΔG_{melt}. Furthermore, thermal corrections affect ΔG_{melt} by up to 1.6 kJ·mol⁻¹ in case of naproxen. Both influences are not negligible if ΔG_{melt} is used for solubility prediction within the melt cycle. Detailed experimental studies of the melting behaviour were carried out for structural clarification. In case of lactide, the determined binary melting phase diagram confirms the presence of a simple racemic compound-forming system. However, the binary melting behaviour of naproxen was found to be complicated by the formation of partial solid-solutions. This has been observed when samples were crystallized from the melt as well as from acetone solutions. Consequently, it can be concluded that for structural clarification measurements of the binary melt phase diagram are important. They can reveal substance specific phase behaviour which can also complicate the ternary solution phase diagram.

The accuracy of state-of-the-art periodic DFT was determined by the density functional, the size of the basis and as the choice of the dispersion correction. A consistent framework was used to model the separated ideal gas molecules and periodic crystal combining GGA type density functionals and atom-centered Gaussian type basis sets (riper framework). Its accuracy was tested with a frequently used benchmark set of molecular crystals (X23). This works def2-TZVP/PBE-D3 method has an overall accuracy of around 10 kJ·mol⁻¹. However, there are some methods in literature that give lattice energies close to chemical accuracy (4.2 kJ·mol⁻¹). Thermal corrections are of great importance when calculating sublimation Gibbs energies, ΔG_{subl}. Even though lattice energies make up the largest part of the absolute energy contributions to ΔG_{subl}, thermal corrections are responsible for around 40 percent. They incorporate zero-point energies as well as integrals of the solidstate and ideal gas heat capacities between 0 K and reference temperature. They have been calculated using two distinct computational methods (ψ_{mol} and ψ_{crys}) for three representatives of chiral compound forming systems: lactide, naproxen and

3-chloromandelic acid. A broad experimental investigation of the solid-state heat capacities of these three systems reveals that calculations from both methods systematically underestimate experimental solid-state heat capacities at high temperatures. This is partly due to measurement uncertainties and the neglect of thermal expansion of the crystal. Still, both the ψ_{mol} and ψ_{crys} method calculate ΔG_{subl} close to chemical accuracy. Overall, computational errors are mostly related to the calculation of E_{latt} and ΔS_{subl}. In both cases calculations are strongly method-dependent. Thus, a modified benchmark set of molecular crystals has been suggested which can be used to test computational methods to calculate ΔG_{subl} rather than E_{latt} or ΔH_{subl}.

The accuracy of calculating E_{latt} is strongly dependent on the types of prevalent intermolecular interactions within the crystal. The crystal density and thus its packing plays a less significant role. This can be exploited when aiming for energy differences between enantiopure and racemic crystals as molecule specific errors potentially cancel out. However, experimental solid-state heat capacities reveal heat capacity differences $\Delta_{RS-S}C_P$ between the racemate and the enantiomer. If large enough, they can affect the sublimation Gibbs energy difference $\Delta_{RS-S}\Delta G_{subl}$. Experimental ΔC_P are observed within the low temperature PPMS measurements and in some cases also at high temperatures. Computational methods qualitatively reproduce the low temperature ΔC_P. However, even if interactions of molecular and lattice vibrations are coupled (ψ_{crys} method), theory fails to quantitatively reproduce the high temperature ΔC_P. Those are related to differences between the high frequency modes which are detectable by Raman spectroscopy. In sum, thermal corrections contribute by 20 to 80% to the absolute energy contributions to $\Delta_{RS-S}\Delta G_{subl}$ (on average by 1.6 ± 1.5 kJ·mol^{-1} and up to 4.1 kJ·mol^{-1}). The magnitude and their method-depending variation is affected by the flexibility of the molecular structure and the crystal packing. Therefore, when modelling the thermochemistry of molecular crystals at ambient temperature, it is not always justified to simplify $\Delta_{RS-S}\Delta G_{subl}$ by considering solely the lattice energy difference.

Solubility predictions via melt and sublimation thermodynamic cycle have been at first performed and evaluated for two non-chiral model substances and finally applied for both chiral species of lactide, naproxen and 3ClMA. Hereby, absolute solubilities of the enantiomer and the racemic compound and their temperature dependence were studied within pure and mixed solvent systems. The $\psi_{crys+COSMO-RS}$ gives slightly more accurate absolute solubilities in comparison to the $\psi_{cmol+COSMO-RS}$ method. The overall accuracy of the sublimation cycle in combination with the $\psi_{crys+COSMO-RS}$ method is comparable to that of the melt cycle. Around 40 % of the solubilities from $\psi_{crys+COSMO-RS}$ are within the $\pm 0.5\log(x)$ limits which have been suggested as within a recent solubility challenge[246]. Experimental solubilities in the studied mixed solvent systems exhibit a strong non-linear behaviour. This was qualitatively well described by all calculations. The lattice energy has been identified as being the dominant energy contribution to ΔG_{sol} but thermal corrections and solvation make up around 40 to 50 % of the sum of the absolute energies. The computational error within the $\psi_{crys+COSMO-RS}$ method for calculating ΔG_{sol} (RMSE = 4.8 kJ·mol^{-1}) equally comes from ΔG_{subl} and ΔG_{solv}. Additionally, the temperature dependence of the solubilities was investigated by experiment and computation. For a

quantitative comparison, solution enthalpies, ΔH_{sol}, have been extracted from the temperature-dependent solubilities of chiral lactide and naproxen in a variety of pure and mixed solvent systems. The accuracy of the sublimation cycle in combination with the $\psi_{crys+CSOMO-RS}$ method to calculate ΔH_{sol} was slightly better in comparison to the melt cycle calculations. Concentration-dependent effects are especially relevant for lactide in toluene as well as in ethanol while less significant for the naproxen solutions. Overall, these are considered promising results for the sublimation cycle keeping in mind that the $\psi_{crys+COSMO-RS}$ is exclusively based on firstprinciple methods. It therefore does not rely on substance specific primary experimental data compared to the melt cycle which requires melting properties from experiment. Nevertheless, it must be stated that both thermodynamic cycles are still not reliable enough to be used for accurate solubility prediction required in an early stage crystallization process design.

Estimation methods of the eutectic composition x_{eu} use the melting and sublimation phase transition energy differences between the racemic compound and the enantiomer. A rather simple thermodynamic model from literature has been modified so that it can be solved consistently within both thermodynamic cycles. Calculations carried out were accompanied by broad experimental investigations of x_{eu} and its variation with temperature and solvent Δx_{eu}. The previously discussed model-dependent variation of the lattice energy differences as well as differences in thermal corrections are recognizable again when they are used for estimating x_{eu}. The combination of electronic structure calculations and experimental $C_{P,s}$ within the "exp/theory" (ψ_{crys}) model gives the most reliable estimates of x_{eu}. The good performance of the sublimation cycle in comparison to the performance of the melt cycle suggests that it can be used for predicting x_{eu} in solution as a valuable guidance during early stage enantioseparation process design.

However, the applied computational methods still have some limitations. They fail to reproduce experimentally observed temperature dependence of $\Delta_{RS-S}C_P$. Those require a differences in the higher frequency "molecular modes" which can be detected by solidsate Raman spectroscopy. The experimental $\Delta_{RS-S}C_P$ are shown to be large enough to change the Gibbs energy difference $\Delta_{RS-S}\Delta G$ which can evoke important shifts of the eutectic composition with temperature. However, shifts of x_{eu} with temperature are in many cases influenced also by the solvent and thus are not a solid-state property alone. In such cases predictive models will have to consider the difference in solvation free energies in the racemic and enantiopure solution. This aspect has been studied in this thesis in detail for naproxen and lactide. A combined experimental investigation of the temperature and solvent dependence of x_{eu} indicates that shifts for naproxen are merely a solid-state property and thus evoked by temperature-dependent $\Delta_{RS-S}C_P$. In contrast, for lactide the solvent system plays an important role. Lactide shows a comparatively large shift of x_{eu} with temperature in ethanol.[225] This is consistent with the strong solute-solute interactions which affect the absolute as well as relative solution behaviour. This has been identified by a combined experimental and computational analysis of solution enthalpy differences at infinite dilution and at saturation concentration. In general, the combined investigation of $\Delta_{RS-S}C_P$ and of solution effects on $\Delta x_{eu}(T)$ provides a valuable methodology to investigate the physiochemical roots of the eutectic shift.

Outlook

The reported results suggest further study of the effect of thermal corrections on the sublimation thermodynamics. A modified benchmark set of molecular crystals has been suggested. Besides a combined treatment of the molecular and lattice vibrations, a more complete model of the thermal corrections should be used to quantify effects of the thermal expansion of the crystal. A potential theoretical framework for this purpose is the quasi-harmonic approximation.[234] Precise Gibbs energy differences and their temperature dependence should be used to further study the physio-chemical origin of the eutectic shift with temperature. It would be of value to investigate if there is a correlation between the magnitude of the energy differences between the enantiopure and racemic crystal and the variability of the eutectic composition in solution. Based on eq. (23) a small value of $\Delta_{RS-S}\Delta G_{subl}$ should result in a eutectic composition with a low enantiomeric excess, which is more likely to be affected by changes of $\Delta_{RS-S}C_P$ with temperature. For example, 2ClMA, an isomer of this works 3ClMA, has a eutectic composition close to the racemic mixture that is solvent-depending[247].

Another promising area of future work is the combination of the sublimation cycle with crystal structure prediction methods[11] in order to establish solubility prediction tools that are exclusively based on information on the molecular structures. Within this work the initial crystal structure still originates from experimental investigations. In future, the applicability of explicit solvation methods which consider the 3D molecular structure should be evaluated for chiral systems. Even though force-field based methods are not yet precise enough to calculate absolute solvation energies they are capable to calculate solvation energy differences.[249, 250] Explicit methods should be further applied to model solution non-idealities which can be related to general solute-solute interactions or evoked by the chirality of the molecules.

6   Literature

1.   Cefic, European Chemistry for Growth. Cefic - The European Chemical Industry Council: www.cefic.org, 2013.

2.   Pollak, P., *Fine Chemicals: The Industry and the Business*. 2nd ed.; John Wiley & Sons, Inc.: 2011.

3.   Cybulski, A.; Moulijn, J. A.; Sharma, M. M.; Sheldon, R. A., *Fine Chemicals Manufacture Technology and Engineering*. Elsevier Science: Amsterdam, 2001.

4.   Murakami, H., From Racemates to Single Enantiomers - Chiral Synthetic Drugs over the last 20 Years. *Top Curr Chem* **2007,** *269*, 273-99.

5.   Lorenz, H.; Seidel-Morgenstern, A., Processes To Separate Enantiomers. *Angewandte Chemie-International Edition* **2014,** *53* (5), 1218-1250.

6.   Jorgensen, W. L.; Duffy, E. M., Prediction of drug solubility from structure. *Advanced Drug Delivery Reviews* **2002,** *54* (3), 355 - 366.

7.   Katritzky, A. R.; Kuanar, M.; Slavov, S.; Hall, C. D.; Karelson, M.; Kahn, I.; Dobchev, D. A., Quantitative Correlation of Physical and Chemical Properties with Chemical Structure: Utility for Prediction. *Chemical Reviews* **2010,** *110* (10), 5714-5789.

8.   McDonagh, J. L.; Nath, N.; De Ferrari, L.; van Mourik, T.; Mitchell, J. B. O., Uniting Cheminformatics and Chemical Theory To Predict the Intrinsic Aqueous Solubility of Crystalline Druglike Molecules. *Journal of Chemical Information and Modeling* **2014,** *54* (3), 844-856.

9.   Adler, S., *Vision 2020: 2000 separations roadmap*. Published by the Center for Waste Reduction Technologies of the AIChE in cooperation with the U.S. Dept. of Energy, Office of Industrial Technologies: 2000.

10.   Palmer, D. S.; McDonagh, J. L.; Mitchell, J. B. O.; van Mourik, T.; Fedorov, M. V., First-Principles Calculation of the Intrinsic Aqueous Solubility of Crystalline Druglike Molecules. *Journal of Chemical Theory and Computation* **2012,** *8* (9), 3322-3337.

11.   Price, S. L., Predicting crystal structures of organic compounds. *Chem Soc Rev* **2014,** *43* (7), 2098-2111.

12.   Cross, L. C.; Klyne, W., *Rules for the Nomenclature of Organic Chemistry: Section E: Stereochemistry (Recommendations 1974)*. Elsevier Science: 2013.

13.   Nguyen, L. A.; He, H.; Pham-Huy, C., Chiral Drugs: An Overview. *International Journal of Biomedical Science : IJBS* **2006,** *2* (2), 85-100.

14.   Wei, Y.; Wang, S.; Chao, J.; Wang, S.; Dong, C.; Shuang, S.; Paau, M. C.; Choi, M. M. F., An Evidence for the Chiral Discrimination of Naproxen Enantiomers: A Combined Experimental and Theoretical Study. *The Journal of Physical Chemistry C* **2011,** *115* (10), 4033-4040.

15.   Caron, G.; Tseng, W.-M.; Kazlauskas, R. J., Kinetic resolutions concentrate the minor enantiomer and aid measurement of high enantiomeric purity. *Tetrahedron: Asymmetry* **1994,** *5* (1), 83 - 92.

16.   McNaught, A. D.; Wilkinson, A., IUPAC. Compendium of Chemical

Terminology. Blackwell Scientific Publications: Oxford, 1997.

17.   FDA'S policy statement for the development of new stereoisomeric drugs. *Chirality* **1992,** *4* (5), 338--340.

18.   Agranat, I.; Caner, H.; Caldwell, J., Putting chirality to work: the strategy of chiral switches. *Nat Rev Drug Discov* **2002,** *1* (10), 753-768.

19.   Christmann, M.; Bräse, S., *Asymmetric Synthesis: The Essentials*. Wiley: Weinheim, 2007.

20.   Soloshonok, V. A.; Ueki, H.; Yasumoto, M.; Mekala, S.; Hirschi, J. S.; Singleton, D. A., Phenomenon of Optical Self-Purification of Chiral Non-Racemic Compounds. *Journal of the American Chemical Society* **2007,** *129* (40), 12112-12113.

21.   Eicke, M. Process Strategies for Batch Preferential Crystallization. Shaker Verlag Aachen, 2016.

22.   Bergström, C. A. S.; Norinder, U.; Luthman, K.; Artursson, P., Molecular Descriptors Influencing Melting Point and Their Role in Classification of Solid Drugs. *Journal of Chemical Information and Computer Sciences* **2003,** *43* (4), 1177-1185.

23.   Jaques, J.; Collet, A.; Wilen, S., *Enantiomers, Racemates, and Resolutions*. Wiley and Sons Inc.: New York, 1981.

24.   Tabora, J. E.; Corry, J.; Osifchin, R.; Lepore, J. V.; Davidson, O.; Thien, M. P., Identification and characterization of an anomalous racemate. *Fluid Phase Equilibria* **2007,** *258* (2), 140-147.

25.   Kotelnikova, E. N.; Isakov, A. I.; Lorenz, H., Non-equimolar discrete compounds in binary chiral systems of organic substances. *Crystengcomm* **2017,** *19* (14), 1851-1869.

26.   Isakov, A. I.; Kotelnikova, E. N.; Lorenz, H., Non-Equimolar Discrete Phases Formed in the System of Malic Acid Enantiomers. *Chemical Engineering & Technology* **2015,** *38* (6), 1047-1052.

27.   Lorenz, H.; von Langermann, J.; Sadiq, G.; Seaton, C. C.; Davey, R. J.; Seidel-Morgenstern, A., The Phase Behavior and Crystallization of 2-Chloromandelic Acid: The Crystal Structure of the Pure Enantiomer and the Behavior of Its Metastable Conglomerate. *Crystal Growth \& Design* **2011,** *11* (5), 1549-1556.

28.   Cruz-Cabeza, A. J.; Reutzel-Edens, S. M.; Bernstein, J., Facts and fictions about polymorphism. *Chemical Society Reviews* **2015,** *44* (23), 8619-8635.

29.   Ibach, H.; Lüth, H., *Solid-State Physics - An Introduction to Principles of Materials Science*. 4 ed.; Springer-Verlag: Berlin, 2009.

30.   Mighell, A. D.; Ondik, H. M.; Molino, B. B., Crystal Data Space-Group Tables. *J Phys Chem Ref Data* **1977,** *6* (3), 675-829.

31.   Brock, C. P., High-Z ' structures of organic molecules: their diversity and organizing principles. *Acta Crystallogr B* **2016,** *72*, 807-821.

32.   Brittain, H. G., *Polymorphism in pharmaceutical solids*. Informa Healthcare USA: New York, NY, 2016.

33.   Day, G. M.; Cooper, T. G.; Cruz-Cabeza, A. J.; Hejczyk, K. E.; Ammon, H. L.; Boerrigter, S. X. M.; Tan, J. S.; Della Valle, R. G.; Venuti, E.; Jose, J.; Gadre, S. R.; Desiraju, G. R.; Thakur, T. S.; van Eijck, B. P.; Facelli, J. C.; Bazterra, V. E.; Ferraro, M. B.; Hofmann, D. W. M.; Neumann, M. A.; Leusen, F. J. J.; Kendrick, J.; Price, S. L.; Misquitta, A. J.; Karamertzanis, P. G.; Welch, G. W. A.; Scheraga, H. A.; Arnautova, Y.

A.; Schmidt, M. U.; van de Streek, J.; Wolf, A. K.; Schweizer, B., Significant progress in predicting the crystal structures of small organic molecules - a report on the fourth blind test. *Acta Crystallographica Section B* **2009,** *65* (2), 107-125.

34. Reilly, A. M.; Cooper, R. I.; Adjiman, C. S.; Bhattacharya, S.; Boese, A. D.; Brandenburg, J. G.; Bygrave, P. J.; Bylsma, R.; Campbell, J. E.; Car, R.; Case, D. H.; Chadha, R.; Cole, J. C.; Cosburn, K.; Cuppen, H. M.; Curtis, F.; Day, G. M.; DiStasio, R. A.; Dzyabchenko, A.; van Eijck, B. P.; Elking, D. M.; van den Ende, J. A.; Facelli, J. C.; Ferraro, M. B.; Fusti-Molnar, L.; Gatsiou, C. A.; Gee, T. S.; de Gelder, R.; Ghiringhelli, L. M.; Goto, H.; Grimme, S.; Guo, R.; Hofmann, D. W. M.; Hoja, J.; Hylton, R. K.; Iuzzolino, L.; Jankiewicz, W.; de Jong, D. T.; Kendrick, J.; de Klerk, N. J. J.; Ko, H. Y.; Kuleshova, L. N.; Li, X. Y.; Lohani, S.; Leusen, F. J. J.; Lund, A. M.; Lv, J.; Ma, Y. M.; Marom, N.; Masunov, A. E.; McCabe, P.; McMahon, D. P.; Meekes, H.; Metz, M. P.; Misquitta, A. J.; Mohamed, S.; Monserrat, B.; Needs, R. J.; Neumann, M. A.; Nyman, J.; Obata, S.; Oberhofer, H.; Oganov, A. R.; Orendt, A. M.; Pagola, G. I.; Pantelides, C. C.; Pickard, C. J.; Podeszwa, R.; Price, L. S.; Price, S. L.; Pulido, A.; Read, M. G.; Reuter, K.; Schneider, E.; Schober, C.; Shields, G. P.; Singh, P.; Sugden, I. J.; Szalewicz, K.; Taylor, C. R.; Tkatchenko, A.; Tuckerman, M. E.; Vacarro, F.; Vasileiadis, M.; Vazquez-Mayagoitia, A.; Vogt, L.; Wang, Y. C.; Watson, R. E.; de Wijs, G. A.; Yang, J.; Zhu, Q.; Groom, C. R., Report on the sixth blind test of organic crystal structure prediction methods. *Acta Crystallographica Section B-Structural Science Crystal Engineering and Materials* **2016,** *72*, 439-459.

35. Sun, C., Thermal Expansion of Organic Crystals and Precision of Calculated Crystal Density: A Survey of Cambridge Crystal Database. *Journal of Pharmaceutical Sciences* **2007,** *96* (5), 1043 - 1052.

36. Bondi, A., Thermal Properties of Molecular Crystals. I. Heat Capacity and Thermal Expansion. *Journal of Applied Physics* **1966,** *37* (13), 4643-4647.

37. Galan, K.; Eicke, M. J.; Elsner, M. P.; Lorenz, H.; Seidel-Morgenstern, A., Continuous Preferential Crystallization of Chiral Molecules in Single and Coupled Mixed-Suspension Mixed-Product-Removal Crystallizers. *Crystal Growth \& Design* **2015,** *15* (4), 1808-1818.

38. Binev, D.; Seidel-Morgenstern, A.; Lorenz, H., Continuous Separation of Isomers in Fluidized Bed Crystallizers. *Crystal Growth \& Design* **2016,** *16* (3), 1409-1419.

39. Lu, Y.; Wang, X.; Ching, C. B., Application of Preferential Crystallization for Different Types of Racemic Compounds. *Industrial \& Engineering Chemistry Research* **2009,** *48* (15), 7266-7275.

40. Lorenz, H.; Polenske, D.; Seidel-Morgenstern, A., Application of preferential crystallization to resolve racemic compounds in a hybrid process. *Chirality* **2006,** *18* (10), 828--840.

41. Buchholz, H.; Emel'yanenko, V. N.; Lorenz, H.; Verevkin, S. P., An Examination of the Phase Transition Thermodynamics of (S)- and (RS)-Naproxen as a Basis for the Design of Enantioselective Crystallization Processes. *Journal of Pharmaceutical Sciences* **2016,** *105* (5), 1676-1683.

42. Piotr, M.; João, A. P. C.; Urszula, D., High pressure (solid+liquid) equilibria of n-alkane mixtures: experimental results, correlation and prediction. *Fluid Phase Equilibria* **2005,** *230* (1), 72 - 80.

43. Wang, Y. L.; LoBrutto, R.; Wenslow, R. W.; Santos, I., Eutectic composition of a chiral mixture containing a racemic compound. *Organic Process Research &*

Development **2005,** *9* (5), 670-676.

44.   Lorenz, H.; Le Minh, T.; Kaemmerer, H.; Buchholz, H.; Seidel-Morgenstern, A., Exploitation of shifts of eutectic compositions in crystallization-based enantioseparation. *Chemical Engineering Research & Design* **2013,** *91* (10), 1890-1902.

45.   Fayzullin, R. R.; Lorenz, H.; Bredikhina, Z. A.; Bredikhin, A. A.; Seidel-Morgenstern, A., Solubility and Some Crystallization Properties of Conglomerate Forming Chiral Drug Guaifenesin in Water. *Journal of Pharmaceutical Sciences* **2014,** *103* (10), 3176--3182.

46.   Lorenz, H.; Sapoundjiev, D.; Seidel-Morgenstern, A., Enantiomeric mandelic acid system-melting point phase diagram and solubility in water. *Journal of Chemical and Engineering Data* **2002,** *47* (5), 1280-1284.

47.   Freiser, H.; Nancollas, G. H., *IUPAC Compendium of Analytical Nomenclature*. 2 ed.; Blackwell Scientific Publications: Oxford, 1987.

48.   Gibson, R. E., On the effect of pressure on the solubility of solids in liquids. *American Journal of Science* **1938,** *35*, 49-69.

49.   Prausnitz, J. M.; Lichtenthaler, R. N.; Azevedo de, E. G., *Molecular Thermodynamics of Fluid-Phase Equilibira*. 3 ed.; Prentice Hall PTR: Upper Saddle River, New Jersey, 1999.

50.   Haase, R., *Thermodynamik der Mischphasen*. Springer Berlin: Heidelberg, 1956.

51.   Ben-Naim, A., *Solvation Thermodynamics*. Plenum Press: New York, NY, 1987.

52.   Klamt, A., *COSMO-RS: From Quantum Chemistry to Fluid Phase Thermodynamics and Drug Design*. 1 ed.; Elsevier: Amsterdam, 2005.

53.   Ploetz, E. A.; Smith, P. E., Local Fluctuations in Solution: Theory and Applications. *Advances in Chemical Physics, Vol 153* **2013,** *153*, 311-372.

54.   Prigogine, I.; Defay, R., *Chemical Thermodynamics*. John Wiley & Sons Inc.: New York, 1962.

55.   Klussmann, M.; White, A. J. R.; Armstrong, A.; Blackmond, D. G., Rationalization and prediction of solution enantiomeric excess in ternary phase systems. *Angew Chem Int Edit* **2006,** *45* (47), 7985-7989.

56.   Otero-de-la-Roza, A.; Cao, B. H.; Price, I. K.; Hein, J. E.; Johnson, E. R., Predicting the Relative Solubilities of Racemic and Enantiopure Crystals by Density-Functional Theory. *Angewandte Chemie-International Edition* **2014,** *53* (30), 7879-7882.

57.   Grant, D. J. W.; Mehdizadeh, M.; Chow, A. H. L.; Fairbrother, J. E., Non-linear van't Hoff solubility-temperature plots and their pharmaceutical interpretation. *International Journal of Pharmaceutics* **1984,** *18* (1-2), 25-38.

58.   Krug, R. R.; Hunter, W. G.; Grieger, R. A., Enthalpy-entropy compensation. 2. Separation of the chemical from the statistical effect. *The Journal of Physical Chemistry* **1976,** *80* (21), 2341-2351.

59.   Nordstrom, F. L.; Rasmuson, A. C., Determination of the activity of a molecular solute in saturated solution. *J Chem Thermodyn* **2008,** *40* (12), 1684-1692.

60.   Solomonov, B. N.; Novikov, V. B., Solution calorimetry of organic nonelectrolytes as a tool for investigation of intermolecular interactions. *Journal of Physical Organic Chemistry* **2008,** *21* (1), 2-13.

61.   Ivanov, E. V.; Batov, D. V., Temperature-dependent behavior of enthalpies and heat capacities of solution in water for thiourea and its N,N′-dimethylsubstituted derivative. *Thermochimica Acta* **2013,** *558,* 10 - 15.

62.   Kustov, A. V.; Smirnova, N. L., Standard Enthalpies and Heat Capacities of Solution of Urea and Tetramethylurea in Water. *Journal of Chemical & Engineering Data* **2010,** *55* (9), 3055-3058.

63.   Dallos, A.; Hajós-Szikszay, É.; Liszi, J., Enthalpies of solution and crystallization ofL-ascorbic acid in aqueous solution. *The Journal of Chemical Thermodynamics* **1998,** *30* (2), 263-270.

64.   O'Neill, M. A. A.; Gaisford, S., Application and use of isothermal calorimetry in pharmaceutical development. *International Journal of Pharmaceutics* **2011,** *417* (1-2), 83-93.

65.   Chen, J.; Sarma, B.; Evans, J. M. B.; Myerson, A. S., Pharmaceutical Crystallization. *Crystal Growth & Design* **2011,** *11* (4), 887-895.

66.   Lee, A. Y.; Erdemir, D.; Myerson, A. S., Crystal Polymorphism in Chemical Process Development. *Annual Review of Chemical and Biomolecular Engineering, Vol 2* **2011,** *2,* 259-280.

67.   Elder, D. P.; Patterson, J. E.; Holm, R., The solid-state continuum: a perspective on the interrelationships between different solid-state forms in drug substance and drug product. *Journal of Pharmacy and Pharmacology* **2015,** *67* (6), 757-772.

68.   Abramov, Y. A., Major Source of Error in QSPR Prediction of Intrinsic Thermodynamic Solubility of Drugs: Solid vs Nonsolid State Contributions? *Molecular Pharmaceutics* **2015,** *12,* 2126−2141.

69.   Docherty, R.; Pencheva, K.; Abramov, Y. A., Low solubility in drug development: de-convoluting the relative importance of solvation and crystal packing. *Journal of Pharmacy and Pharmacology* **2015,** *67* (6), 847-856.

70.   Skyner, R. E.; McDonagh, J. L.; Groom, C. R.; van Mourik, T.; Mitchell, J. B. O., A review of methods for the calculation of solution free energies and the modelling of systems in solution. *Phys. Chem. Chem. Phys.* **2015,** *17,* 6174.

71.   Bordwell, F. G., Equilibrium acidities in dimethyl sulfoxide solution. *Accounts of Chemical Research* **2002,** *21* (12), 456-463.

72.   Grant, D. J. W.; Higuchi, T., *Solubility Behavior of Organic Compounds*. John Wiley and Sons: New York, 1990.

73.   Chu, K. A.; Yalkowsky, S. H., Predicting Aqueous Solubility: The Role of Crystallinity. *Curr Drug Metab* **2009,** *10* (10), 1184-1191.

74.   Ran, Y. Q.; Jain, N.; Yalkowsky, S. H., Prediction of aqueous solubility of organic compounds by the general solubility equation (GSE). *J Chem Inf Comp Sci* **2001,** *41* (5), 1208-1217.

75.   Yalkowsky, S. H.; Wu, M., Estimation of the Ideal Solubility (Crystal-Liquid Fugacity Ratio) of Organic Compounds. *Journal of Pharmaceutical Sciences* **2010,** *99* (3), 1100-1106.

76.   Hughes, L. D.; Palmer, D. S.; Nigsch, F.; Mitchell, J. B. O., Why Are Some Properties More Difficult To Predict than Others? A Study of QSPR Models of Solubility, Melting Point, and Log P. *Journal of Chemical Information and Modeling* **2008,** *48* (1), 220-232.

77. Palmer, D. S.; Llinàs, A.; Morao, I.; Day, G. M.; Goodman, J. M.; Glen, R. C.; Mitchell, J. B. O., Predicting Intrinsic Aqueous Solubility by a Thermodynamic Cycle. *Molecular Pharmaceutics* **2008,** *5* (2), 266-279.

78. Tetko, I. V.; Sushko, Y.; Novotarskyi, S.; Patiny, L.; Kondratov, I.; Petrenko, A. E.; Charochkina, L.; Asiri, A. M., How Accurately Can We Predict the Melting Points of Drug-like Compounds? *Journal of Chemical Information and Modeling* **2014,** *54* (12), 3320-3329.

79. Zhang, Y.; Edward, J. M., A comparison of methods for melting point calculation using molecular dynamics simulations. *The Journal of Chemical Physics* **2012,** *136* (14), 144116.

80. Gharagheizi, F.; Salehi, G. R., Prediction of enthalpy of fusion of pure compounds using an Artificial Neural Network-Group Contribution method. *Thermochimica Acta* **2011,** *521* (1-2), 37-40.

81. Gharagheizi, F.; Gohar, M. R. S.; Vayeghan, M. G., A quantitative structure–property relationship for determination of enthalpy of fusion of pure compounds. *J Therm Anal Calorim* **2011,** *109* (1), 501-506.

82. Neau, S. H.; Bhandarkar, S. V.; Hellmuth, E. W., Differential Molar Heat Capacities to Test Ideal Solubility Estimations. *Pharmaceutical Research* **1997,** *14* (5), 601-605.

83. Chickos, J. S.; Hosseini, S.; Hesse, D. G.; Liebman, J. F., Heat capacity corrections to a standard state: a comparison of new and some literature methods for organic liquids and solids. *Structural Chemistry* **1993,** *4* (4), 271-278.

84. Hasnip, P. J.; Refson, K.; Probert, M. I. J.; Yates, J. R.; Clark, S. J.; Pickard, C. J., Density functional theory in the solid state. *Phil. Trans. R. Soc. A* **2014,** *372*, 20130270.

85. Otero-de-la-Roza, A.; Johnson, E. R., A benchmark for non-covalent interactions in solids. *J Chem Phys* **2012,** *137* (5), 054103.

86. Yang, J.; Hu, W. F.; Usvyat, D.; Matthews, D.; Schutz, M.; Chan, G. K. L., Ab initio determination of the crystalline benzene lattice energy to sub-kilojoule/mole accuracy. *Science* **2014,** *345* (6197), 640-643.

87. William Acree Jr. and James, S. C., Phase Transition Enthalpy Measurements of Organic and Organometallic Compounds. Sublimation, Vaporization and Fusion Enthalpies From 1880 to 2010. *Journal of Physical and Chemical Reference Data* **2010,** *39* (4), 043101.

88. Griesser, U. J.; Szelagiewicz, M.; Hofmeier, U. C.; Pitt, C.; Cianferani, S., Vapor Pressure and Heat of Sublimation of Crystal Polymorphs. *Journal of Thermal Analysis and Calorimetry* **1999,** *57* (1), 45-60.

89. Price, S. L.; Leslie, M.; Welch, G. W. A.; Habgood, M.; Price, L. S.; Karamertzanis, P. G.; Day, G. M., Modelling organic crystal structures using distributed multipole and polarizability-based model intermolecular potentials. *Physical Chemistry Chemical Physics* **2010,** *12* (30), 8478-8490.

90. Gavezzotti, A., *Moleczular Aggregation - Structure Analysis and Molecular Simulation of Crystals and Liquids*. Oxford University Press: Oxford NewYork, 2007.

91. Gavezzotti, A., Computational contributions to crystal engineering. *CrystEngComm* **2008,** *10*, 367-367.

92. Moellmann, J.; Grimme, S., DFT-D3 Study of Some Molecular Crystals. *J Phys*

Chem C **2014,** *118* (14), 7615-7621.

93. Reilly, A. M.; Tkatchenko, A., Seamless and Accurate Modeling of Organic Molecular Materials. *J Phys Chem Lett* **2013,** *4* (6), 1028-1033.

94. Chickos, J. S., Enthalpies of Sublimation after a Century of Measurement: A View as Seen through the Eyes of a Collector. *Netsu Sokutei* **2003,** *30* (3), 116-124.

95. Gavezzotti, A.; Rizzato, S., Are Racemic Crystals Favored over Homochiral Crystals by Higher Stability or by Kinetics? Insights from Comparative Studies of Crystalline Stereoisomers. *Journal of Organic Chemistry* **2014,** *79*, 4809-4816.

96. Gavezzotti, A., *Molecular Aggregation - Structure Analysis and Molecular Simulation of Crystals and Liquids*. Oxford University Press: Oxford NewYork, 2007.

97. Reilly, A. M.; Tkatchenko, A., Understanding the role of vibrations, exact exchange, and many-body van der Waals interactions in the cohesive properties of molecular crystals. *Journal of Chemical Physics* **2013,** *139* (2), 024705-024705.

98. Maitland, G. C.; Rigby, M.; Smith, E. B.; Wakeham, W. A., *Intermolecular Forces - their origin and determination*. Oxford University Press: 1981.

99. Hoja, J.; Reilly, A. M.; Tkatchenko, A., First-principles modeling of molecular crystals: structures and stabilities, temperature and pressure. *Wiley Interdisciplinary Reviews: Computational Molecular Science* **2017,** *7* (1), e1294.

100. Jensen, F., *Introduction to Computational Chemistry*. 2 ed.; John Wiley & Sons Ltd: The Atrium, Southern Gate, Chichester, 2007.

101. Gavezzotti, A., Computational contributions to crystal engineering. *CrystEngComm* **2008**.

102. Cohen, A. J.; Mori-Sánchez, P.; Yang, W., Challenges for Density Functional Theory. *Chemical Reviews* **2012,** *112* (1), 289-320.

103. Hohenberg, P.; Kohn, W., Inhomogeneous Electron Gas. *Physical Review* **1964,** *136* (3B), B864-B871.

104. Drissi, M.; Benhalima, N.; Megrouss, Y.; Rachida, R.; Chouaih, A.; Hamzaoui, F., Theoretical and Experimental Electrostatic Potential around the m-Nitrophenol Molecule. *Molecules* **2015,** *20* (3), 4042-4054.

105. Marques, M. A. L.; Oliveira, M. J. T.; Burnus, T., Libxc: A library of exchange and correlation functionals for density functional theory. *Computer Physics Communications* **2012,** *183* (10), 2272-2281.

106. Grimme, S., Density functional theory with London dispersion corrections. *Wiley Interdisciplinary Reviews: Computational Molecular Science* **2011,** *1* (2), 211-228.

107. Grimme, S.; Hansen, A.; Brandenburg, J. G.; Bannwarth, C., Dispersion-Corrected Mean-Field Electronic Structure Methods. *Chemical Reviews* **2016,** *116* (9), 5105-5154.

108. Hermann, J.; DiStasio, R. A.; Tkatchenko, A., First-Principles Models for van der Waals Interactions in Molecules and Materials: Concepts, Theory, and Applications. *Chemical Reviews* **2017,** *117* (6), 4714-4758.

109. Johnson, E. R.; Mackie, I. D.; DiLabio, G. A., Dispersion interactions in density-functional theory. *Journal of Physical Organic Chemistry* **2009,** *22* (12), 1127-1135.

110. Jensen, F., Atomic orbital basis sets. *Wiley Interdisciplinary Reviews:*

Computational Molecular Science **2013,** *3* (3), 273--295.

111.   Hafner, J., Ab-initio simulations of materials using VASP: Density-functional theory and beyond. *Journal of Computational Chemistry* **2008,** *29* (13), 2044-2078.

112.   Blaha, P.; Schwarz, K.; Sorantin, P.; Trickey, S. B., Full-potential, linearized augmented plane wave programs for crystalline systems. *Computer Physics Communications* **1990,** *59* (2), 399-415.

113.   Lippert, B. G.; Parrinello, J. H.; Michele, A hybrid Gaussian and plane wave density functional scheme. *Molecular Physics* **1997,** *92* (3), 477-488.

114.   Dovesi, R.; Civalleri, B.; Orlando, R.; Roetti, C.; Saunders, V. R., Ab inito quantum simulation in solid state chemistry. In *Reviews in Computational Chemistry*, Lipkowitz, K. B.; Larter, R.; Cundari, T. R., Eds. John Wiley & Sons: Hoboken, New Jersey, 2005; Vol. 21.

115.   Kittel, C., *Introduction to Solid State Physics*. Wiley: New York, 1996.

116.   Löwdin, P.-O., On the state of the art of quantum chemistry. *International Journal of Quantum Chemistry* **1986,** *29* (5), 1651-1683.

117.   Irikura, K. K.; Frurip, D. J., *Computational Thermochemistry: Prediction and Estimation of Molecular Thermodynamics*. American Chemical Society: Washington DC, 1998.

118.   Diedrichs, A.; Gmehling, J., Solubility Calculation of Active Pharmaceutical Ingredients in Alkanes, Alcohols, Water and their Mixtures Using Various Activity Coefficient Models. *Ind Eng Chem Res* **2011,** *50* (3), 1757-1769.

119.   Chen, C.-C.; Mathias, P. M., Applied thermodynamics for process modeling. *AIChE Journal* **2002,** *48* (2), 194-200.

120.   Gross, J.; Sadowski, G., Perturbed-Chain SAFT: An Equation of State Based on a Perturbation Theory for Chain Molecules. *Industrial \& Engineering Chemistry Research* **2001,** *40* (4), 1244-1260.

121.   Klamt, A., Conductor-Like Screening Model for Real Solvents - a New Approach to the Quantitative Calculation of Solvation Phenomena. *J Phys Chem-Us* **1995,** *99* (7), 2224-2235.

122.   Xiong, R. C.; Sandler, S. I.; Burnett, R. I., An Improvement to COSMO-SAC for Predicting Thermodynamic Properties. *Industrial & Engineering Chemistry Research* **2014,** *53* (19), 8265-8278.

123.   Tomasi, J.; Mennucci, B.; Cammi, R., Quantum Mechanical Continuum Solvation Models. *Chemical Reviews* **2005,** *105* (8), 2999-3094.

124.   Klamt, A.; Schüürmann, G., COSMO: a new approach to dielectric screening in solvents with explicit expressions for the screening energy and its gradient. *J. Chem. Soc., Perkin Trans.* **1993,** *2*.

125.   Ashcraft, R. W.; Raman, S.; Green, W. H., Ab Initio Aqueous Thermochemistry: Application to the Oxidation of Hydroxylamine in Nitric Acid Solution. *The Journal of Physical Chemistry B* **2007,** *111* (41), 11968-11983.

126.   Klamt, A.; Jonas, V.; Bürger, T.; Lohrenz, J. C. W., Refinement and Parametrization of COSMO-RS. *The Journal of Physical Chemistry A* **1998,** *102* (26), 5074-5085.

127.   Reinisch, J.; Klamt, A., Prediction of free energies of hydration with COSMO-RS

on the SAMPL4 data set. *Journal of Computer-Aided Molecular Design* **2014,** *28* (3), 169-173.

128.   Bronneberg, R.; Pfennig, A., MOQUAC, a new expression for the excess Gibbs energy based on molecular orientations. *Fluid Phase Equilibria* **2013,** *338*, 63 - 77.

129.   Gutiérrez-Sevillano, J. J.; Leonhard, K.; van der Eerden, J. P. J. M.; Vlugt, T. J. H.; Krooshof, G. J. P., COSMO-3D: Incorporating Three-Dimensional Contact Information into the COSMO-SAC Model. *Industrial \& Engineering Chemistry Research* **2015,** *54* (7), 2214-2226.

130.   Mobley, D. L.; Wymer, K. L.; Lim, N. M.; Guthrie, J. P., Blind prediction of solvation free energies from the SAMPL4 challenge. *Journal of Computer-Aided Molecular Design* **2014,** *28* (3), 135-150.

131.   Weininger, D., SMILES, a chemical language and information system. 1. Introduction to methodology and encoding rules. *Journal of Chemical Information and Computer Sciences* **1988,** *28* (1), 31-36.

132.   Turbomole; GmbH, *TURBOMOLE V7.1 2016, a development of University of Karlsruhe and Forschungszentrum Karlsruhe GmbH, 1989-2007, TURBOMOLE GmbH, since 2007; available from http://www.turbomole.com.* Turbomole GmbH: Karlsruhe, 2016.

133.   Weigend, F.; Ahlrichs, R., Balanced basis sets of split valence, triple zeta valence and quadruple zeta valence quality for H to Rn: Design and assessment of accuracy. *Physical Chemistry Chemical Physics* **2005,** *7* (18), 3297.

134.   Perdew, J. P., Density-functional approximation for the correlation energy of the inhomogeneous electron gas. *Phys. Rev. B* **1986,** *33* (12), 8822-8824.

135.   Becke, A. D., Density-functional exchange-energy approximation with correct asymptotic behavior. *Phys. Rev. A* **1988,** *38* (6), 3098-3100.

136.   Joachim Paier and Robin Hirschl and Martijn Marsman and Georg, K., The Perdew–Burke–Ernzerhof exchange-correlation functional applied to the G2-1 test set using a plane-wave basis set. *The Journal of Chemical Physics* **2005,** *122* (23), 234102.

137.   Grimme, S.; Antony, J.; Ehrlich, S.; Krieg, H., A consistent and accurate ab initio parametrization of density functional dispersion correction (DFT-D) for the 94 elements H-Pu. *J Chem Phys* **2010,** *132* (15), 154104.

138.   Sierka, M.; Hogekamp, A.; Ahlrichs, R., Fast evaluation of the Coulomb potential for electron densities using multipole accelerated resolution of identity approximation. *J Chem Phys* **2003,** *118* (20), 9136-9148.

139.   TURBOMOLE V7.0 2015 a development of University of Karlsruhe and Forschungszentrum Karlsruhe GmbH, -., TURBOMOLE GmbH, since 2007 available from http://www.turbomole.com.

140.   Burow, A. M.; Sierka, M.; Mohamed, F., Resolution of identity approximation for the Coulomb term in molecular and periodic systems. *The Journal of Chemical Physics* **2009,** *131* (21), 214101.

141.   Łazarski, R.; Burow, A. M.; Sierka, M., Density Functional Theory for Molecular and Periodic Systems Using Density Fitting and Continuous Fast Multipole Methods. *Journal of Chemical Theory and Computation* **2015,** *11* (7), 3029-3041.

142.   Hasnip, P. J.; Refson, K.; Probert, M. I. J.; Yates, J. R.; Clark, S. J.; Pickard, C. J., Density functional theory in the solid state. *Philosophical Transactions of the Royal*

Society A: Mathematical, Physical and Engineering Sciences **2014,** *372* (2011), 20130270-20130270.

143.   Kazantsev, A. V.; Karamertzanis, P. G.; Adjiman, C. S.; Pantelides, C. C., Efficient Handling of Molecular Flexibility in Lattice Energy Minimization of Organic Crystals. *Journal of Chemical Theory and Computation* **2011,** *7* (6), 1998-2016.

144.   Frisch, M. J.; Trucks, G. W.; Schlegel, H. B.; Scuseria, G. E.; Robb, M. A.; Cheeseman, J. R.; Scalmani, G.; Barone, V.; Mennucci, B.; Petersson, G. A.; Nakatsuji, H.; Caricato, M.; Li, X.; Hratchian, H. P.; Izmaylov, A. F.; Bloino, J.; Zheng, G.; Sonnenberg, J. L.; Hada, M.; Ehara, M.; Toyota, K.; Fukuda, R.; Hasegawa, J.; Ishida, M.; Nakajima, T.; Honda, Y.; Kitao, O.; Nakai, H.; Vreven, T.; Montgomery Jr., J. A.; Peralta, J. E.; Ogliaro, F.; Bearpark, M. J.; Heyd, J.; Brothers, E. N.; Kudin, K. N.; Staroverov, V. N.; Kobayashi, R.; Normand, J.; Raghavachari, K.; Rendell, A. P.; Burant, J. C.; Iyengar, S. S.; Tomasi, J.; Cossi, M.; Rega, N.; Millam, N. J.; Klene, M.; Knox, J. E.; Cross, J. B.; Bakken, V.; Adamo, C.; Jaramillo, J.; Gomperts, R.; Stratmann, R. E.; Yazyev, O.; Austin, A. J.; Cammi, R.; Pomelli, C.; Ochterski, J. W.; Martin, R. L.; Morokuma, K.; Zakrzewski, V. G.; Voth, G. A.; Salvador, P.; Dannenberg, J. J.; Dapprich, S.; Daniels, A. D.; Farkas, Ö.; Foresman, J. B.; Ortiz, J. V.; Cioslowski, J.; Fox, D. J. *Gaussian 09*, Gaussian, Inc.: Wallingford, CT, USA, 2009.

145.   Stone, A. J., Distributed multipole analysis: Stability for large basis sets. *Journal of Chemical Theory and Computation* **2005,** *1* (6), 1128-1132.

146.   Stone, A. J. *GDMA: A Program for Performing Distributed Multipole Analysis of Wave Functions Calculated Using the Gaussian Program System*, 2.2; University of Cambridge: Cambridge, United Kingdom, 2010.

147.   Day, G. M.; Price, S. L.; Leslie, M., Atomistic calculations of phonon frequencies and thermodynamic quantities for crystals of rigid organic molecules. *Journal of Physical Chemistry B* **2003,** *107* (39), 10919-10933.

148.   Anghel, A. T.; Day, G. M.; Price, S. L., A study of the known and hypothetical crystal structures of pyridine: why are there four molecules in the asymmetric unit cell? *CrystEngComm* **2002,** *4* (62), 348-355.

149.   Day, G. M.; Price, S. L., A nonempirical anisotropic atom-atom model potential for chlorobenzene crystals. *Journal of the American Chemical Society* **2003,** *125* (52), 16434-16443.

150.   Buchholz, H. K.; Hylton, R. K.; Brandenburg, J. G.; Seidel-Morgenstern, A.; Lorenz, H.; Stein, M.; Price, S. L., Thermochemistry of Racemic and Enantiopure Organic Crystals for Predicting Enantiomer Separation. *Crystal Growth & Design* **2017,** *17* (9), 4676-4686.

151.   Dovesi, R.; Orlando, R.; Erba, A.; Zicovich-Wilson, C. M.; Civalleri, B.; Casassa, S.; Maschio, L.; Ferrabone, M.; De La Pierre, M.; D'Arco, P.; Noel, Y.; Causa, M.; Rerat, M.; Kirtman, B., CRYSTAL14: A Program for the Ab Initio Investigation of Crystalline Solids. *Int J Quantum Chem* **2014,** *114* (19), 1287-1317.

152.   Orlando, R.; De La Pierre, M.; Zicovich-Wilson, C. M.; Erba, A.; Dovesi, R., On the full exploitation of symmetry in periodic (as well as molecular) self-consistent-field ab initio calculations. *J Chem Phys* **2014,** *141* (10), 104-108.

153.   Sure, R.; Grimme, S., Corrected small basis set Hartree-Fock method for large systems. *Journal of Computational Chemistry* **2013,** *34* (19), 1672-1685.

154.   Brandenburg, J. G.; Grimme, S., Dispersion corrected hartree-fock and density

functional theory for organic crystal structure prediction. *Top Curr Chem* **2014,** *345*, 1-23.

155.   Grimme, S.; Ehrlich, S.; Goerigk, L., Effect of the damping function in dispersion corrected density functional theory. *Journal of Computational Chemistry* **2011,** *32* (7), 1456-1465.

156.   Brandenburg, J. G.; Alessio, M.; Civalleri, B.; Peintinger, M. F.; Bredow, T.; Grimme, S., Geometrical Correction for the Inter- and Intramolecular Basis Set Superposition Error in Periodic Density Functional Theory Calculations. *The Journal of Physical Chemistry A* **2013,** *117* (38), 9282-9292.

157.   Kruse, H.; Grimme, S., A geometrical correction for the inter- and intra-molecular basis set superposition error in Hartree-Fock and density functional theory calculations for large systems. *The Journal of Chemical Physics* **2012,** *136* (15), 154101.

158.   Sanahuja, A.; Cesari, E., Heat of Solution of Kcl in Water at 303.15 K. *Thermochimica Acta* **1985,** *85* (Apr), 163-166.

159.   Lorenz, H., Solubility and Solution Equilibria in Crystallization. In *Crystallization: Basic Concepts and Industrial Applications*, Beckmann, W., Ed. Wiley-VCH: Weinheim, 2013; pp 35-74.

160.   Verevkin, S. P.; Emel'yanenko, V. N., Transpiration method: Vapor pressures and enthalpies of vaporization of some low-boiling esters. *Fluid Phase Equilibria* **2008,** *266* (1–2), 64 - 75.

161.   Verevkin, S. P.; Sazonova, A. Y.; Emel'yanenko, V. N.; Zaitsau, D. H.; Varfolomeev, M. A.; Solomonov, B. N.; Zherikova, K. V., Thermochemistry of Halogen-Substituted Methylbenzenes. *Journal of Chemical & Engineering Data* **2015,** *60* (1), 89-103.

162.   Verevkin, S. P.; Ralys, R. V.; Zaitsau, D. H.; Emel'yanenko, V. N. S., C., Express thermo-gravimetric method for the vaporization enthalpies appraisal for very low volatile molecular and ionic compounds. *Thermochimica Acta* **2012,** *538*, 55 - 62.

163.   Kennedy, C. A.; Stancescu, M.; Marriott, R. A.; White, M. A., Recommendations for accurate heat capacity measurements using a Quantum Design physical property measurement system. *Cryogenics* **2007,** *47* (2), 107-112.

164.   Lashley, J. C.; Hundley, M. F.; Migliori, A.; Sarrao, J. L.; Pagliuso, P. G.; Darling, T. W.; Jaime, M.; Cooley, J. C.; Hults, W. L.; Morales, L.; Thoma, D. J.; Smith, J. L.; Boerio-Goates, J.; Woodfield, B. F.; Stewart, G. R.; Fisher, R. A.; Phillips, N. E., Critical examination of heat capacity measurements made on a Quantum Design physical property measurement system. *Cryogenics* **2003,** *43* (6), 369-378.

165.   Hwang, J. S.; Lin, K. J.; Tien, C., Measurement of heat capacity by fitting the whole temperature response of a heat-pulse calorimeter. *Rev Sci Instrum* **1997,** *68* (1), 94–101.

166.   Le Parlouër, P., Simultaneous TG-DSC: a new technique for thermal analysis. *Thermochimica Acta* **1987,** *121*, 307-322.

167.   Ditmars, D. A.; Ishihara, S.; Chang, S. S.; Bernstein, G., Measurement of the relative enthalpy of pure a-Al2O3 (NBS heat capacity and enthalpy Standard Reference Material No. 720) from 273 to 1173. *Journal of Research of the National Bureau of Stondards* **1982,** *87*, 159-163.

168.   Robie, R. A.; Hemingway, B., Apparatus and Methods for Low Temperature Heat

Capacity Measurements. The Heat Capacity of Standard Benzoic Acid. *Geological Survey Professional Paper* **1972,** *755*.

169.   Buchholz, H.; Seidel-Morgenstern, A.; Lorenz, H., A Contribution to the Solution Thermodynamics of Chiral Lactide. *Chemical Engineering & Technology* **2017,** *40* (7), 1268-1275.

170.   Buchholz, H. K.; Stein, M., Accurate lattice energies of organic molecular crystals from periodic turbomole calculations. *Journal of Computational Chemistry* **2018**.

171.   De Kruif, C. G.; Blok, J. G., The vapour pressure of benzoic acid. *Journal of Chemical Thermodynamics* **1982,** *14* (3), 201-206.

172.   Ruzicka, K.; Fulem, M.; Ruzicka, V., Recommended vapor pressure of solid naphthalene. *Journal of Chemical and Engineering Data* **2005,** *50* (6), 1956-1970.

173.   Acree, W.; Chickos, J. S., Phase Transition Enthalpy Measurements of Organic and Organometallic Compounds and Ionic Liquids. Sublimation, Vaporization, and Fusion Enthalpies from 1880 to 2015. Part 2. C11–C192. *Journal of Physical and Chemical Reference Data* **2017,** *46* (1), 013104.

174.   Chirico, R. D.; Knipmeyer, S. E.; Steele, W. V., Heat capacities, enthalpy increments, and derived thermodynamic functions for naphthalene between the temperatures 5K and 440K. *The Journal of Chemical Thermodynamics* **2002,** *34* (11), 1873-1884.

175.   Gamsjäger, H.; Lorimer John, W.; Salomon, M.; Shaw David, G.; Tomkins Reginald, P. T., The IUPAC-NIST Solubility Data Series: A guide to preparation and use of compilations and evaluations (IUPAC Technical Report). In *Pure and Applied Chemistry*, 2010; Vol. 82, pp 1137--1159.

176.   Acree, W. E., IUPAC-NIST Solubility Data Series. 98. Solubility of Polycyclic Aromatic Hydrocarbons in Pure and Organic Solvent Mixtures: Revised and Updated. Part 1. Binary Solvent Mixtures. *Journal of Physical and Chemical Reference Data* **2013,** *42* (1).

177.   Acree, W. E., IUPAC-NIST Solubility Data Series. 99. Solubility of Benzoic Acid and Substituted Benzoic Acids in Both Neat Organic Solvents and Organic Solvent Mixtures. *Journal of Physical and Chemical Reference Data* **2013,** *42* (3).

178.   Dickhut, R. M.; Andren, A. W.; Armstrong, D. E., Naphthalene Solubility in Selected Organic Solvent-Water Mixtures. *Journal of Chemical and Engineering Data* **1989,** *34* (4), 438-443.

179.   Yalkowsky, S. H., *Handbook of Aqueous Solubility Data*. CRC Press: Boca Raton, FL, 2003.

180.   Maryott, A. A.; Smith, E. R. *Table of dielectric constants of pure liquids*; National Bureau of Standards: Gaithersbur, MD, 1951.

181.   Li, R.; Zeitler, J. A.; Tomerini, D.; Parrott, E. P. J.; Gladden, L. F.; Day, G. M., A study into the effect of subtle structural details and disorder on the terahertz spectrum of crystalline benzoic acid. *Physical Chemistry Chemical Physics* **2010,** *12* (20), 5329-5340.

182.   Cysewski, P., Pressure-imposed changes of benzoic acid crystals. *Journal of Molecular Modeling* **2015,** *21* (4), 83.

183.   McCullough, J. P.; Finke, H. L.; Messerly, J. F.; Todd, S. S.; Kincheloe, T. C.; Waddington, G., The Low-Temperature Thermodynamic Properties of Naphthalene, l-Methylnaphthalene,   2-Methylnaphthalene,   1,2,3,4-Tetrahydronaphthalene,trans-

Decahydronaphthalene and cis-Decahydronaphthalene. *The Journal of Physical Chemistry* **1957,** *61* (8), 1105-1116.

184.   Lee, C.; Yang, W.; Parr, R. G., Development of the Colle-Salvetti correlation-energy formula into a functional of the electron density. *Physical Review B* **1988,** *37* (2), 785-789.

185.   Grimme, S., Semiempirical GGA-type density functional constructed with a long-range dispersion correction. *Journal of Computational Chemistry* **2006,** *27* (15), 1787-1799.

186.   Ponomarev, V. I.; Filipenko, O. S.; Atovmyan, L. O., Crystal and Molecular Structure of Naphthalene at -150 degrees. *Kristallografiya* **1976,** *21* (2), 392-394.

187.   Feld, R.; Lehmann, M. S.; Muir, K. W.; Speakman, J. C., The crystal structure of Benzoic Acid: a redetermination with X-rays at room temperature; a summary of neutron-diffraction work at temperatures down to 5 K. *Zeitschrift für Kristallographie - Crystalline Materials* **1981,** *157*, 215.

188.   Fedorov, I. A.; Zhuravlev, Y. N.; Berveno, V. P., Electronic structure and chemical bond in naphthalene and anthracene. *Physical Chemistry Chemical Physics* **2011,** *13* (13), 5679-5686.

189.   Sure, R.; Brandenburg, J. G.; Grimme, S., Small Atomic Orbital Basis Set First-Principles Quantum Chemical Methods for Large Molecular and Periodic Systems: A Critical Analysis of Error Sources. *ChemistryOpen* **2016,** *5* (2), 94-109.

190.   Capelli, S. C.; Albinati, A.; Mason, S. A.; Willis, B. T. M., Molecular Motion in Crystalline Naphthalene: Analysis of Multi-Temperature X-Ray and Neutron Diffraction Data. *The Journal of Physical Chemistry A* **2006,** *110* (41), 11695-11703.

191.   Bruno, G.; Randaccio, L., A refinement of the benzoic acid structure at room temperature. *Acta Crystallographica Section B* **1980,** *36* (7), 1711-1712.

192.   Kampermann, S. P.; Ruble, J. R.; Craven, B. M., The Charge-Density Distribution in *Hexamethylenetetramine at 120 K*. *Acta Crystallographica Section B-Structural Science* **1994,** *50*, 737-741.

193.   Leviel, J. L.; Auvert, G.; Savariault, J. M., Hydrogen-Bon Studies - A Neutron-Diffraction Study of the Structures of Succinic Acid at 300 and 77 K. *Acta Crystallographica Section B-Structural Science* **1981,** *37* (DEC), 2185-2189.

194.   Brandenburg, J. G.; Grimme, S., Accurate Modeling of Organic Molecular Crystals by Dispersion-Corrected Density Functional Tight Binding (DFTB). *J Phys Chem Lett* **2014,** *5* (11), 1785-1789.

195.   Riley, K. E.; Op't Holt, B. T.; Merz, K. M., Critical Assessment of the Performance of Density Functional Methods for Several Atomic and Molecular Properties. *Journal of Chemical Theory and Computation* **2007,** *3* (2), 407-433.

196.   Bučko, T.; Lebègue, S.; Gould, T.; Ángyán, J. G., Many-body dispersion corrections for periodic systems: an efficient reciprocal space implementation. *Journal of Physics: Condensed Matter* **2016,** *28* (4), 045201.

197.   Emel'yanenko, V. N.; Zaitsau, D. H.; Shoifet, E.; Meurer, F.; Verevkin, S. P.; Schick, C.; Held, C., Benchmark Thermochemistry for Biologically Relevant Adenine and Cytosine. A Combined Experimental and Theoretical Study. *Journal of Physical Chemistry A* **2015,** *119* (37), 9680-9691.

198.   Sonnefeld, W. J.; Zoller, W. H.; May, W. E., Dynamic Coupled-Column Liquid-

Chromatrographic Determination of Ambient-Temperature Vapor-Pressures of Polynuclear Aromatic-Hydrocarbons. *Analytical Chemistry* **1983,** *55* (2), 275-280.

199. Bazyleva, A. B.; Blokhin, A. V.; Kabo, G. J.; Charapennikau, M. B.; Emel'yanenko, V. N.; Verevkin, S. P.; Diky, V., Thermodynamic Properties of Adamantane Revisited. *Journal of Physical Chemistry B* **2011,** *115* (33), 10064-10072.

200. De Wit, H. G. M.; Van Miltenburg, J. C.; De Kruif, C. G., Thermodynamic properties of molecular organic crystals containing nitrogen, oxygen, and sulphur 1. Vapour pressures and enthalpies of sublimation. *The Journal of Chemical Thermodynamics* **1983,** *15* (7), 651-663.

201. Verevkin, S. P.; Emel'yanenko, V. N.; Notario, R.; Roux, M. V.; Chickos, J. S.; Liebman, J. F., Rediscovering the Wheel. Thermochemical Analysis of Energetics of the Aromatic Diazines. *Journal of Physical Chemistry Letters* **2012,** *3* (23), 3454-3459.

202. Jimenez, P.; Roux, M. V.; Turrion, C.; Gomis, F., Thermochemical Properties of N-Heterocyclic Compounds 1. Enthalpies of Combustion, Vapor-Pressures and Enthalpies of Sublimation, and Enthalpies of Formation of Pyrazole, Imadizole, Indazole and Benzimidazole. *Journal of Chemical Thermodynamics* **1987,** *19* (9), 985-992.

203. Brunetti, B.; Piacente, V.; Portalone, G., Sublimation enthalpies of some methyl derivatives of uracil from vapor pressure measurements. *Journal of Chemical and Engineering Data* **2000,** *45* (2), 242-246.

204. Davies, M.; Jones, A. H., Lattice Energies of some N-Methyl Amides and of some Carbamates. *Transactions of the Faraday Society* **1959,** *55* (8), 1329-1332.

205. Booth, A. M.; Markus, T.; McFiggans, G.; Percival, C. J.; McGillen, M. R.; Topping, D. O., Design and construction of a simple Knudsen Effusion Mass Spectrometer (KEMS) system for vapour pressure measurements of low volatility organics. *Atmospheric Measurement Techniques* **2009,** *2* (2), 355-361.

206. Dewit, H. G. M.; Bouwstra, J. A.; Blok, J. G.; Dekruif, C. G., Vapor-Pressures and Lattice Energies of Oxalic-Acid, Mesotartaric Acid, Phloroglucinol, Myoinositol, and their Hydrates. *Journal of Chemical Physics* **1983,** *78* (3), 1470-1475.

207. Bradley, R. S.; Cotson, S., The Vapor Pressure and Lattice Energy of Hydrogen-Bonded Crystals. 2. Alpha-Anhydrous and Beta-Anhydrous Oxalic Acid and Tetragonal Pentaerythritol. *Journal of the Chemical Society* **1953,** (JUN), 1684-1688.

208. Cappa, C. D.; Lovejoy, E. R.; Ravishankara, A. R., Determination of evaporation rates and vapor pressures of very low volatility compounds: A study of the C-4-C-10 and C-12 dicarboxylic acids. *Journal of Physical Chemistry A* **2007,** *111* (16), 3099-3109.

209. Emel'yanenko, V. N.; Kabo, G. J.; Verevkin, S. P., Measurement and prediction of thermochemical properties: Improved increments for the estimation of enthalpies of sublimation and standard enthalpies of formation of alkyl derivatives of urea. *Journal of Chemical and Engineering Data* **2006,** *51* (1), 79-87.

210. McDonagh, J. L.; Palmer, D. S.; Mourik, T. v.; Mitchell, J. B. O., Are the Sublimation Thermodynamics of Organic Molecules Predictable? *Journal of Chemical Information and Modeling* **2016,** *56* (11), 2162-2179.

211. Ouchi, T.; Ohya, Y., Design of lactide copolymers as biomaterials. *Journal of Polymer Science Part A: Polymer Chemistry* **2004,** *42* (3), 453-462.

212. Hylton, R. K.; Tizzard, G. J.; Threlfall, T. L.; Ellis, A. L.; Coles, S. J.; Seaton, C. C.; Schulze, E.; Lorenz, H.; Seidel-Morgenstern, A.; Stein, M.; Price, S. L., Are the

Crystal Structures of Enantiopure and Racemic Mandelic Acids Determined by Kinetics or Thermodynamics? *Journal of the American Chemical Society* **2015,** *137* (34), 11095-11104.

213.   Le Minh, T.; Langermann, J. v.; Lorenz, H.; Seidel-Morgenstern, A., Enantiomeric 3-Chloromandelic Acid System: Binary Melting Point Phase Diagram, Ternary Solubility Phase Diagrams and Polymorphism. *Journal of Pharmaceutical Sciences* **2010,** *99* (9), 4084-4095.

214.   Braun, D. E.; McMahon, J. A.; Koztecki, L. H.; Price, S. L.; Reutzel-Edens, S. M., Contrasting Polymorphism of Related Small Molecule Drugs Correlated and Guided by the Computed Crystal Energy Landscape. *Crystal Growth & Design* **2014,** *14* (4), 2056-2072.

215.   Braun, D. E.; Ardid-Candel, M.; D'Oria, E.; Karamertzanis, P. G.; Arlin, J. B.; Florence, A. J.; Jones, A. G.; Price, S. L., Racemic Naproxen: A Multidisciplinary Structural and Thermodynamic Comparison with the Enantiopure Form. *Crystal Growth & Design* **2011,** *11* (12), 5659-5669.

216.   Le Minh, T.; Lorenz, H.; Seidel-Morgenstern, A., Enantioselective Crystallization Exploiting the Shift of Eutectic Compositions in Solid-Liquid Phase Diagrams. *Chemical Engineering & Technology* **2012,** *35* (6), 1003-1008.

217.   Belen'kaya, B. G.; Bel'skii, V. K.; Dement'ev, A. I.; Sakharova, V. I.; Chernikova, N. Y., Crystal and Molecular Structures of Glycolide and Lactide: Association through CH...O Hydrogen Bonds. *Crystallography Reports* **1997,** *42* (3), 449-452.

218.   van Hummel, G. J.; Harkema, S.; Kohn, F. E.; Feijen, J., Structure of 3,6-dimethyl-1,4-dioxane-2,5-dione [D-,D-(L-,L-)lactide]. *Acta Crystallographica Section B Structural Crystallography and Crystal Chemistry* **1982,** *38* (5), 1679-1681.

219.   Ravikumar, K.; Rajan, S. S.; Pattabhi, V., Structure of Naproxen, C14h14o3. *Acta Crystallogr C* **1985,** *41* (Feb), 280-282.

220.   Coles, S. J.; Threlfall, T. L.; Tizzard, G. J., The Same but Different: Isostructural Polymorphs and the Case of 3-Chloromandelic Acid. *Crystal Growth & Design* **2014,** *14* (4), 1623-1628.

221.   Lebedev, B. V.; Kulagina, T. G.; Kiparisova, E. G., The thermodynamic properties of L-lactide in the temperature range 0-430 K. *Zhurnal Fizicheskoi Khimii* **1999,** *73* (4), 609-616.

222.   Le Minh, T.; Von Langermann, J.; Lorenz, H.; Seidel-Morgenstern, A., Enantiomeric 3-Chloromandelic Acid System: Binary Melting Point Phase Diagram, Ternary Solubility Phase Diagrams and Polymorphism. *Journal of Pharmaceutical Sciences* **2010,** *99* (9), 4084-4095.

223.   Zhang, Y.; Ray, A.; Rohani, S., Measurement and prediction of phase diagrams of the enantiomeric 3-chloromandelic acid system. *Chemical Engineering Science* **2009,** *64* (2), 192-197.

224.   Bergström, C. A. S. a. N. U. a. L. K. a. A. P., Molecular Descriptors Influencing Melting Point and Their Role in Classification of Solid Drugs. *Journal of Chemical Information and Computer Sciences* **2003,** *43* (4), 1177-1185.

225.   Le Minh, T. Designing crystallization based-enantiomeric separation for chiral compound-forming systems in consideration of polymorphism and solvate formation. PhD Thesis, Dr. Hut, München, 2014.

226. Kalugina, T. G.; Lebedev, Y. G.; Lyudvig, Y. B.; Barskaya, I. G., Thermodynamics of dl-Lactide, Polylactide and Polymerization of dl-Lactide in the range of 0-430 K. *Polymer Science U.S.S.R.* **1982,** *24* (7), 1702-1708.

227. de Barros, T. M. V. R.; Santos, R. C.; Fernandes, A. C.; da Piedade, M. E. M., Accuracy and precision of heat capacity measurements using a heat flux differential scanning calorimeter. *Thermochimica Acta* **1995,** *269-270*, 51-60.

228. Nyman, J.; Day, G. M., Static and lattice vibrational energy differences between polymorphs. *Crystengcomm* **2015,** *17* (28), 5154-5165.

229. Abdulla, M.; Refson, K.; Friend, R. H.; Haynes, P. D., A first-principles study of the vibrational properties of crystalline tetracene under pressure. *J Phys-Condens Mat* **2015,** *27* (37).

230. Emel'yanenko, V. N.; Verevkin, S. P.; Pimerzin, A. A., The thermodynamic properties of DL- and L-lactides. *Russ J Phys Chem a+* **2009,** *83* (12), 2013-2021.

231. Červinka, C.; Fulem, M.; Stoffel, R. P.; Dronskowski, R., Thermodynamic Properties of Molecular Crystals Calculated within the Quasi-Harmonic Approximation. *The Journal of Physical Chemistry A* **2016,** *120* (12), 2022-2034.

232. Quantum Design, S. V. R., San Diego, CA 92121.

233. Dachs, E.; Benisek, A., A sample-saving method for heat capacity measurements on powders using relaxation calorimetry. *Cryogenics* **2011,** *51* (8), 460-464.

234. Heit, Y. N.; Beran, G. J. O., How important is thermal expansion for predicting molecular crystal structures and thermochemistry at finite temperatures? *Acta Crystallographica Section B Structural Science, Crystal Engineering and Materials* **2016,** *72* (4), 514-529.

235. Leclercq, M.; Collet, A.; Jacques, J., Etude des Melanges d'Antipodes Optiques - XII. *Tetrahedron* **1976,** *32*, 821-828.

236. Nyman, J.; Day, G. M., Modelling temperature-dependent properties of polymorphic organic molecular crystals. *Phys. Chem. Chem. Phys.* **2016,** *18* (45), 31132-31143.

237. Paukov, I. E.; Kovalevskaya, Y. A.; Boldyreva, E. V., Low-temperature heat capacity of L- and DL-phenylglycines. *J Therm Anal Calorim* **2012,** *108* (3), 1311-1316.

238. Paukov, I. E.; Kovalevskaya, Y. A.; Boldyreva, E. V., Low-temperature thermodynamic properties of L- and DL-valines. *Journal of Thermal Analysis and Calorimetry* **2013,** *111* (1), 905-910.

239. Drebushchak, V. A.; Kovalevskaya, Y. A.; Paukov, I. E.; Boldyreva, E. V., Heat capacity of D- and DL-serine in a temperature range of 5.5 to 300 K. *J Therm Anal Calorim* **2007,** *89* (2), 649-654.

240. Makhatadze, G. I., Heat capacities of amino acids, peptides and proteins. *Biophysical Chemistry* **1998,** *71* (2-3), 133-156.

241. Paukov, I. E.; Kovalevskaya, Y. A.; Boldyreva, E. V., Low-temperature thermodynamic properties of L-cysteine. *J Therm Anal Calorim* **2008,** *93* (2), 423-428.

242. Paukov, I. E.; Kovalevskaya, Y. A.; Boldyreva, E. V., Low-temperature thermodynamic properties of dl-cysteine. *J Therm Anal Calorim* **2010,** *100* (1), 295-301.

243. Donahue, M.; Botonjic-Sehic, E.; Wells, D.; Brown, C. W., Understanding Infrared and Raman Spectra of Pharmaceutical Polymorphs. *American Pharmaceutical*

Review **2011,** *14* (2).

244.   Perlovich, G. L.; Kurkov, S. V.; Kinchin, A. N.; Bauer-Brandl, A., Thermodynamics of solutions III: comparison of the solvation of (+)-naproxen with other NSAIDs. *European Journal of Pharmaceutics and Biopharmaceutics* **2004,** *57* (2), 411-420.

245.   Klamt, A.; Mennucci, B.; Tomasi, J.; Barone, V.; Curutchet, C.; Orozco, M.; Luque, F. J., On the Performance of Continuum Solvation Methods. A Comment on "Universal Approaches to Solvation Modeling". *Accounts of Chemical Research* **2009,** *42*, 489-492.

246.   Hopfinger, A. J.; Esposito, E. X.; Llinas, A.; Glen, R. C.; Goodman, J. M., Findings of the Challenge To Predict Aqueous Solubility. *Journal of Chemical Information and Modeling* **2009,** *49* (1), 1-5.

247.   Gilks, S. E.; Davey, R. J.; Mughal, R. K.; Sadiq, G.; Black, L., Crystallization of 2-Chloromandelic Acid: Solubility, Formation of the Metastable Conglomerate, and Use of a Nonaqueous Emulsion To Prepare an Enantiomerically Enriched Product. *Crystal Growth & Design* **2013,** *13* (10), 4323-4329.

248.   Polenske, D.; Lorenz, H., Solubility and Metastable Zone Width of the Methionine Enantiomers and Their Mixtures in Water. *Journal of Chemical & Engineering Data,* **2009,** *54* (8), 2277–2280.

249.   Paluch, A. S.; Parameswaran, S.; Liu, S.; Kolavennu, A.; Mobley, D. L., Predicting the excess solubility of acetanilide, acetaminophen, phenacetin, benzocaine, and caffeine in binary water/ethanol mixtures via molecular simulation. *Journal of Chemical Physics* **2015,** *142* (4).

250.   Liu, S.; Cao, S.; Hoang, K.; Young, K. L.; Paluch, A. S.; Mobley, D. L., Using MD Simulations To Calculate How Solvents Modulate Solubility. *Journal of Chemical Theory and Computation* **2016,** *12* (4), 1930-1941.

251.   Furche, F.; Ahlrichs, R.; Hattig, C.; Klopper, W.; Sierka, M.; Weigend, F., Turbomole. *Wiley Interdisciplinary Reviews-Computational Molecular Science* **2014,** *4* (2), 91-100.

7   Appendix

7.1   Primary experimental data

7.1.1   Heat capacities at high temperatures (DSC)

Table 7.1: Experimental high temperature (DSC) heat capacities of lactide.

(S)-lactide			(RS)-lactide		
T	$C_{P,exp}$	Abs dev.	T	$C_{P,exp}$	Abs dev.
/ K	/ J·mol⁻¹·K⁻¹	/ J·mol⁻¹·K⁻¹	/ K	/ J·mol⁻¹·K⁻¹	/ J·mol⁻¹·K⁻¹
Heat capacities of the crystalline solid					
298.2	*189.0*		*298.2*	*289.6*	
297.3	187.4	0.3	298.8	190.2	0.2
304.4	193.4	0.5	308.8	194.2	0.2
311.4	194.8	0.6	318.8	200.2	0.3
318.4	201.3	0.7	328.8	204.6	0.1
325.3	203.3	0.5	338.8	206.5	0.1
332.3	206.3	0.5	348.8	213.5	0.0
339.3	208.6	0.6	358.8	215.9	0.2
346.3	212.8	0.7	368.8	223.1	0.2
353.3	218.7	0.2	378.8	228.1	0.2
Heat capacities of the melt					
380.0	282.3	0.7	408.7	291.1	3.2
390.0	288.4	0.8	418.7	293.1	2.2
398.8	291.6	0.4	428.8	294.1	3.0
408.7	297.0	-			
418.7	296.3	-			
428.7	301.9	-			

Table 7.2: Experimental high temperature (DSC) heat capacities of naproxen.

(S)-naproxen			(RS)-naproxen		
T	$C_{P,exp}$	Abs dev.	T	$C_{P,exp}$	Abs dev.
/ K	/ J·mol⁻¹·K⁻¹	/ J·mol⁻¹·K⁻¹	/ K	/ J·mol⁻¹·K⁻¹	/ J·mol⁻¹·K⁻¹
Heat capacities of the crystalline solid					
298.2	*295.6*		*298.2*	*296.9*	
298.4	296.3	4.1	298.4	297.4	1.6

307.8	303.2	3.1	307.8	304.9	1.6
317.0	314.3	3.7	317.1	316.8	1.5
326.3	320.7	3.2	326.3	322.9	1.5
335.6	329.7	4.9	335.6	331.0	1.7
344.9	335.2	4.1	344.9	338.1	1.5
354.2	346.4	3.7	354.2	349.5	1.4
363.5	353.5	3.9	363.5	356.8	1.4
372.7	362.1	5.7	372.7	366.2	1.5
382.0	366.7	5.3	382.0	372.2	1.0
391.3	379.5	5.0	391.3	383.5	1.5
400.6	389.6	6.7	400.6	393.0	1.0

Heat capacities of the melt

436.7	490.8	0.7	436.6	488.3	1.4
442.4	504.4	1.2	442.2	497.9	1.3
448.1	509.3	0.8	447.7	505.2	0.8
453.8	509.7	1.2	452.1	501.7	2.0
465.2	519.1	0.6	453.8	504.6	0.5
			461.7	516.9	1.1
			465.2	516.0	0.2
			470.9	526.8	1.0
			480.0	534.4	0.5
			489.2	541.4	0.4

Table 7.3: Experimental high temperature (DSC) heat capacities of 3-chloromandelic acid (3ClMA).

(R)-3ClMA			(RS)-3ClMA		
T	$C_{P,exp}$	Abs dev.	T	$C_{P,exp}$	Abs dev.
/ K	/ $J \cdot mol^{-1} \cdot K^{-1}$	/ $J \cdot mol^{-1} \cdot K^{-1}$	/ K	/ $J \cdot mol^{-1} \cdot K^{-1}$	/ $J \cdot mol^{-1} \cdot K^{-1}$
Heat capacities of the crystalline solid					
298.2	*211.1*		*298.2*	*201.9*	
305.1	216.2	1.4	298.4	202.2	1.2
312.6	218.9	1.6	307.6	206.6	1.2
320.1	220.2	1.7	316.7	211.8	1.2
327.6	225.1	1.6	325.9	216.6	1.3
335.1	229.8	1.7	335.1	220.2	1.7
342.6	233.8	1.7	344.2	225.9	1.6
350	238.2	1.8	351.7	229.5	1.8
357.6	241.8	1.5	360.9	233.8	1.4
			370.1	239.9	1.7
Heat capacities of the melt					
297.5	309.1	-	360.1	331.5	1.4
305.1	314.0	-	369.6	333.9	-
320.1	329.4	-	379.1	333.7	1.0

350.0	657.4	-	388.8	333.8	0.0
357.6	334.7	-	396.3	334.6	4.7
365.1	330.9	-	400.1	338.6	3.0
386.3	343.6	4.6	407.6	335.8	2.1
391.3	349.9	2.2	411.3	344.1	2.1
396.3	349.8	1.7	417.2	340.3	2.3
401.3	348.8	3.2	428.8	341.1	-
406.3	343.8	3.7			
411.3	345.6	6.3			

Table 7.4: Experimental high temperature (DSC) heat capacities of mandelic acid.

(S)-mandelic acid			(RS)-mandelic acid		
T	$C_{P,exp}$	Abs dev.	T	$C_{P,exp}$	Abs dev.
/ K	/ J·mol^{-1}·K^{-1}	/ J·mol^{-1}·K^{-1}	/ K	/ J·mol^{-1}·K^{-1}	/ J·mol^{-1}·K^{-1}
Heat capacities of the crystalline solid					
298.2	*187.0*		*298.2*	*182.4*	
298.7	186.9	0.7	298.7	182.2	0.6
306.7	192.8	0.5	306.7	187.3	0.8
314.7	197.4	0.4	314.7	192.4	0.1
322.7	202.2	0.2	322.7	196.4	0.9
330.7	207.4	0.4	330.7	199.7	1.0
338.7	211.7	0.3	338.7	204.7	0.9
346.7	216.9	0.2	346.7	208.4	0.2
354.7	221.6	0.5	354.7	213.9	1.1
362.7	226.9	0.5	362.7	218.6	1.1
370.7	232.6	0.7	370.7	222.5	1.0

7.1.2 Solid-state heat capacities at low temperatures (DHCP)

Table 7.5: Experimental low temperature (DHCP) heat capacities of naproxen.

(S)-naproxen			(RS)-naproxen		
T	$C_{P,exp}$	Abs dev.	T	$C_{P,exp}$	Abs dev.
/ K	/ J·mol^{-1}·K^{-1}	/ J·mol^{-1}·K^{-1}	/ K	/ J·mol^{-1}·K^{-1}	/ J·mol^{-1}·K^{-1}
1.83	0.03	0.00	1.82	0.04	0.00
2.94	0.11	0.00	2.93	0.14	0.00
4.04	0.28	0.00	4.02	0.34	0.00
5.13	0.58	0.00	5.11	0.69	0.00
6.21	1.05	0.01	6.18	1.20	0.00
7.29	1.70	0.00	7.26	1.88	0.00
8.36	2.51	0.01	8.33	2.70	0.00

9.43	3.48	0.03	9.39	3.65	0.01
10.48	4.57	0.01	10.44	4.69	0.01
11.55	5.84	0.02	11.52	5.86	0.02
12.64	7.15	0.02	12.61	7.16	0.02
13.70	8.59	0.03	13.67	8.48	0.02
14.80	10.16	0.03	14.76	10.00	0.05
15.89	11.71	0.04	15.87	11.40	0.02
16.99	13.38	0.03	16.94	12.84	0.06
18.08	15.08	0.10	18.04	14.51	0.03
19.19	16.63	0.02	19.12	16.00	0.04
20.31	18.34	0.05	20.23	17.62	0.01
28.25	30.36	0.07	28.15	29.42	0.02
36.20	41.82	0.02	36.01	41.64	0.08
44.12	52.72	0.01	43.99	52.48	0.32
52.05	62.68	0.25	51.89	62.67	0.28
59.81	71.98	0.05	59.65	71.94	0.18
67.68	80.50	0.01	67.46	81.09	0.21
75.52	88.71	0.04	75.32	89.56	0.30
83.38	96.22	0.47	83.18	97.53	0.29
91.31	103.50	0.47	91.13	104.96	0.39
99.22	110.43	0.45	99.06	111.88	0.23
107.14	117.25	0.33	106.90	119.31	0.21
115.05	123.76	0.02	114.80	126.01	0.21
122.91	130.27	0.06	122.66	133.11	0.52
130.74	136.46	0.54	130.51	139.82	0.54
138.62	142.56	0.51	138.43	145.84	0.11
146.49	148.78	0.33	146.29	152.20	0.10
154.39	154.37	0.59	154.19	158.74	0.47
162.25	160.46	0.15	162.10	165.16	0.84
170.22	166.40	0.73	169.98	170.91	1.70
178.05	172.75	0.13	177.89	178.23	0.65
185.93	178.46	0.15	185.74	184.44	1.92
193.76	184.66	0.48	193.57	190.82	1.55
201.61	190.72	0.48	201.34	198.48	0.05

Table 7.6: Experimental low temperature (DHCP) heat capacities of 3-chloromandelic acid (3ClMA).

(*R*)-3ClMA			(*RS*)-3ClMA		
T	$C_{P,exp}$	Abs dev.	T	$C_{P,exp}$	Abs dev.
/ K	/ J·mol^{-1}·K^{-1}	/ J·mol^{-1}·K^{-1}	/ K	/ J·mol^{-1}·K^{-1}	/ J·mol^{-1}·K^{-1}
1.83	0.02	0.00	1.83	0.04	0.00
2.94	0.09	0.00	2.93	0.18	0.00
4.04	0.25	0.00	4.03	0.50	0.01
5.14	0.56	0.00	5.12	1.05	0.01
6.23	1.01	0.02	6.20	1.81	0.00

7.30	1.61	0.02	7.28	2.74	0.02
8.37	2.34	0.00	8.35	3.78	0.00
9.44	3.17	0.02	9.43	4.94	0.02
10.50	4.10	0.01	10.50	6.11	0.03
11.57	5.13	0.04	11.58	7.40	0.05
12.65	6.28	0.00	12.66	8.78	0.01
13.72	7.44	0.02	13.71	10.16	0.01
14.86	8.78	0.01	14.84	11.62	0.01
15.92	10.08	0.01	15.91	12.97	0.01
17.03	11.38	0.14	16.99	14.41	0.02
18.12	12.79	0.01	18.09	15.78	0.03
19.19	14.16	0.01	19.18	17.20	0.01
20.28	15.50	0.04	20.27	18.60	0.02
28.20	25.62	0.08	28.18	28.46	0.02
36.07	35.27	0.12	36.13	36.77	0.11
43.95	43.32	0.06	44.01	44.40	0.06
51.84	50.66	0.04	51.92	51.36	0.08
59.73	57.26	0.02	59.75	57.40	0.01
67.61	63.42	0.15	67.63	63.05	0.11
75.52	69.08	0.11	75.54	68.04	0.08
83.42	74.21	0.11	83.46	72.68	0.04
91.31	79.36	0.02	91.34	77.47	0.04
99.19	84.29	0.11	99.23	81.98	0.05
107.07	89.20	0.19	107.12	86.57	0.08
114.96	93.76	0.08	115.02	90.99	0.12
122.83	98.40	0.19	122.87	95.19	0.09
130.70	102.86	0.05	130.75	99.65	0.06
138.60	107.18	0.13	138.66	104.26	0.06
146.48	111.44	0.20	146.56	108.05	0.17
154.36	116.12	0.16	154.43	112.67	0.20
162.24	119.85	0.05	162.30	117.12	0.26
170.12	124.48	0.58	170.18	120.82	0.12
178.00	128.70	0.12	178.08	125.13	0.44
185.86	133.40	0.14	185.93	129.72	0.34
193.67	137.77	0.28	193.78	133.53	0.18
201.48	141.69	0.26	201.56	138.03	0.27

7.1.3 Solubilities in pure solvents

Table 7.7: (1) Experimental solubilities (mole fraction) and (3) ΔG_{sol} at 298 K, (4) experimental ΔG_{solv} and (5) calculated ΔG_{solv} via the COMSO-RS model. Furthermore, recalculations of the sublimation free energies $\Delta G_{subl,sol}$ from the experimental solution free energies and calculated solvation free energies ($\Delta G_{subl,sol} = \Delta G_{sol} - \Delta G_{solv,inf}$).

		x_{exp} / molar	refs	ΔG_{sol} (-RT ln x) / kJ mol^{-1}	ΔG_{solv} (exp) / kJ mol^{-1}	ΔG_{solv} (inf) / kJ mol^{-1}	$\Delta G_{subl.sol}$ / kJ mol^{-1}
Lactide		**1**	**2**	**3**	**4**	**5**	**6**
Toluene	S	0.034		8.35	-24.4	-24.66	33.01
	RS	0.013		10.68	-24.3	-24.66	35.34
Acetone	S	0.293	225	3.04	-29.7	-31.13	34.17
	RS	0.144	225	4.81	-30.2	-31.13	35.94
2-propanol	S	0.021	225	9.53	-23.2	-26.43	35.96
	RS	0.010	225	11.50	-23.46	-26.43	37.93
Ethanol	S	0.028		8.83	-23.9	-26.89	35.72
	RS	0.011		11.18	-23.8	-26.89	38.07
Ethyl acetate	S	0.191	225	4.11	-28.7	-26.72	30.83
	RS	0.082	225	6.21	-28.9	-26.72	32.93
Average	**S**						**33.94±2.66**
	RS						**36.04±1.89**
Naproxen		**1**	**2**	**3**	**4**	**5**	
Ethanol	S	0.015		10.48	-49.8	-50.53	61.00
	RS	0.010		11.45	-51.2	-50.53	61.97
Heptane	S	5.3E-05		24.41	-35.8	-35.53	59.95
	RS	3.0E-05		25.79	-36.8	-35.53	61.33
ACN	S	0.0065		12.49	-47.7	-50.32	62.82
	RS	0.0045		13.37	-49.2	-50.32	63.70
Ethyl actetate	S	0.026		9.05	-51.2	-55.12	64.17
	RS	0.018		9.95	.52.7	-55.12	65.07
Average	**S**						**61.98±1.63**
	RS						**63.02±1.47**
3ClMA		**1**	**2**	**3**	**4**	**5**	
water	R	0.0003	225	20.39	n.a.	-26.44	46.83
	RS	0.0001	225	22.08	n.a.	-26.44	48.51
Tol/EA (80/20 wt%)	R	0.050	225	7.43	n.a.	-41.11	48.54
	RS	0.027	225	8.98	n.a.	-41.11	50.09
Average	**R**						**47.68±0.85**
	RS						**49.30±0.79**

7.1.4 Solubilities in solvent mixtures

Table 7.8: Mole fraction solubility, x_i, of lactide in mixtures of ethanol and toluene at 25 °C

EtOH / wt	(S)-lactide / x_i	err	(RS)-lactide / x_i	err
0	0.0368	0.0024	0.0141	0.0003
0.2	0.0848	0.0057	0.0289	0.0003
0.4	0.0748	0.0020	0.0264	0.0003
0.6	0.0587	0.0023	0.0209	0.0016
0.8	0.0419	0.0025	0.0163	0.0003
1	0.0258	0.0014	0.0110	0.0007

Table 7.9: Mole fraction solubility, x_i, of naproxen in mixtures of ethanol and toluene, water and acetonitrile at 30 °C.

EtOH / wt	(S)-naproxen / x_i	err	(RS)-naproxen / x_i	err
Mixtures of ethanol and toluene				
0	0.0040	0.0000	0.0019	0.0000
0.2	0.0495	0.0003	0.0352	0.0001
0.4	0.0559	0.0002	0.0381	0.0004
0.6	0.0459	0.0009	0.0314	0.0004
0.6	0.0319	0.0004	0.0209	0.0001
1	0.0170	0.0004	0.0111	0.0005
Mixtures of ethanol and water				
0	-	-	-	-
0.1	0.0001	0.0001	0.0000	0.0000
0.5	0.0015	0.0000	0.0012	0.0000
0.75	0.0081	0.0001	0.0053	0.0001
1	0.0170	0.0004	0.0111	0.0005
Mixtures of ethanol and acetonitrile (ACN)				
0	0.0074	0.0000	0.0053	0.0000
0.25	0.0276	0.0001	0.0195	0.0001
0.5	0.0402	0.0001	0.0286	0.0001
0.75	0.0396	0.0000	0.0269	0.0000
1	0.0170	0.0004	0.0111	0.0005

7.1.5   Solubilities at varying temperatures

Table 7.10: Temperature variation of the mole fraction solubility, x_i, of lactide in pure ethanol and toluene. The apparent solution enthalpies, ΔH_{sol}, are additionally given.

Temp / °C	(S)-naproxen / x_i	err	Temp / °C	(RS)-naproxen / x_i	err
Ethanol					
15	0.0168	-	15	0.0061	-
25	0.0263	0.0003	25	0.0104	-
35	0.0462	-	35	0.0175	0.0175
45	0.0912	0.0045	45	0.0297	0.0297
10	0.0129	-	10	0.0055	0.0055
40	0.0591	-	40	0.0193	0.0193
ΔH_{sol} / kJ·mol^{-1}	**40.2**	**2.2**		**35.6**	**2.4**
Toluene					
10	0.0200	-	10	0.0083	-
15.5	0.0238	-	25	0.0138	-
25	0.0359	-	15	0.0089	-
25	0.0331	-	25	0.0130	-
40	0.0510	-	35	0.0188	-
40	0.0614	-	40	0.0216	-
ΔH_{sol} / kJ·mol^{-1}	**25.6**	**2.0**		**24.8**	**1.3**

Table 7.11: Temperature variation of the mole fraction solubility, x_i, of naproxen in pure ethanol and toluene as well as in mixtures of ethanol and toluene, water and acetonitrile. The apparent solution enthalpies, ΔH_{sol}, are additionally given.

Temp / °C	(S)-naproxen / x_i	err	(RS)-naproxen / x_i	err
Toluene				
15	0.0019	0.0000	0.0008	0.0000
25	0.0032	0.0001	0.0013	0.0001
30	0.0040	0.0000	0.0019	0.0000
35	0.0048	0.0000	0.0024	0.0001
45	0.0084	0.0003	0.0050	0.0003
ΔH_{sol} / kJ·mol^{-1}	**36.6**	**1.6**	**46.3**	**2.9**
Ethanol				
15	0.0101	0.0000	0.0065	0.0000
25	0.0146	0.0000	0.0099	0.0001
30	0.0170	0.0004	0.0111	0.0005
35	0.0217	0.0002	0.0147	0.0001
45	0.0324	0.0008	0.0225	0.0002
ΔH_{sol} / kJ·mol^{-1}	**29.7**	**1.5**	**31.3**	**2.0**
20/80 wt% ethanol/ toluene				
10	0.0281	0.0001	0.0201	0.0009
20	0.0371	0.0006	0.0262	0.0005

30	0.0495	0.0003	0.0352	0.0001
40	0.0592	0.0000	0.0445	0.0000
ΔH_{sol} / kJ·mol^{-1}	**18.6**	**1.0**	**19.8**	**0.5**
75/25 wt% ethanol water				
10	0.0035	0.0000	0.0023	0.0000
20	0.0052	0.0000	0.0034	0.0000
30	0.0081	0.0001	0.0053	0.0001
35	0.0107	0.0001	0.0072	0.0000
40	0.0135	0.0001	0.0100	0.0005
ΔH_{sol} / kJ·mol^{-1}	**33.0**	**1.6**	**35.2**	**3.0**
50/50 wt% ethanol/acetonitrile				
10	0.0241	0.0004	0.0156	0.0008
20	0.0312	0.0002	0.0207	0.0004
30	0.0402	0.0001	0.0286	0.0001
40	0.0554	0.0001	0.0390	0.0001
ΔH_{sol} / kJ·mol^{-1}	**20.2**	**1.2**	**22.6**	**0.8**

7.1.6 Solution calorimetry

Table 7.12: Caloric measurements of the dissolution of (*S*)- and (*RS*)-lactide in toluene and the extrapolated solution enthalpies at infinite dilution (x = 0), $\Delta Hsol,inf$.

(*S*)-lactide		(*RS*)-lactide	
x mol/mol	H / kJ/mol	x mol/mol	H / kJ/mol
0.0034	21.56	0.0034	23.71
0.0050	21.83	0.0062	23.53
0.0080	21.56	0.0095	22.27
0.0096	21.49	0.0110	21.85
	$\Delta Hsol,inf$		$\Delta Hsol,inf$
	21.8±0.2		**24.7±1.0**

Table 7.13: Caloric measurements of the dissolution of (*S*)- and (*RS*)-naproxen in toluene and the extrapolated solution enthalpies at infinite dilution (x = 0), $\Delta Hsol,inf$.

(*S*)-naproxen		(*RS*)-naproxen	
x mol/mol	H / kJ/mol	x mol/mol	H / kJ/mol
Ethanol (30°C)			
0.0010	22.88	0.0010	24.71
0.0015	23.73	0.0020	24.57
0.0020	23.35	0.0030	24.75
0.0030	23.86		
$\Delta Hsol,inf$		$\Delta Hsol,inf$	
22.7±0.5		**24.6±0.2**	

20/80 wt% ethanol/toluene (30°C)

0.0018	19.78	0.0036	21.52
0.0036	19.57	0.0054	22.05
0.0054	19.77	0.0061	22.54
		0.0073	21.51
	$\Delta Hsol,inf$		$\Delta Hsol,inf$
	19.7±0.3		**21.6±1.3**

75/25 wt% ethanol/water (30°C)

0.00085	32.57	0.00076	36.77
0.00127	31.92	0.00102	36.37
0.00169	31.68	0.00127	37.04
	$\Delta Hsol,inf$		$\Delta Hsol,inf$
	33.4±0.4		**36.2±1.3**

50/50 wt% ethanol/acetonitrile (30°C)

0.0009	17.90	0.0014	22.46
0.0019	18.19	0.0019	20.36
0.0028	17.88	0.0028	20.72
0.0038	17.56	0.0038	20.71
	$\Delta Hsol,inf$		$\Delta Hsol,inf$
	18.2±0.3		**22.3±1.4**

7.1.7 Eutectic composition in solution

Table 7.14: Temperature variation of the eutectic composition (eutectic shift), Δx_{eu}, of naproxen in pure ethanol and toluene as well as in mixtures of ethanol with toluene, water and acetonitrile.

Temp / °C	x_{eu}	err
Toluene		
15	90.4	0.0
25	89.8	0.0
30	89.2	0.0
35	89.2	0.0
45	88.7	0.1
Ethanol		
15	90.5	0.0
25	90.0	0.1
30	89.7	0.0
35	89.4	0.0
45	88.9	0.1
20/80 wt% ethanol/toluene		
10	90.9	0.0
20	90.4	0.1

| 30 | 90.0 | 0.0 |
| 40 | 89.3 | 0.1 |

75/25 wt% ethanol/water		
10	90.9	0.0
20	90.3	0.1
30	89.9	0.1
35	89.1	0.0
40	90.9	0.0

50/50 wt% ethanol/acetonitrile		
10	91.2	0.0
20	90.5	0.0
30	89.9	0.2
40	89.3	0.0

Table 7.15: Variation of the eutectic composition as a function of the solvent composition (eutectic shift), Δx_{eu}, for naproxen in mixtures of ethanol with toluene, water and acetonitrile at 30 °C.

EtOH / wt %	x_{eu}	err
ethanol / toluene mixtures		
0	89.8	0.0
0.2	89.6	0.0
0.4	-	-
0.6	-	-
0.8	89.7	0.0
1	89.7	0.0
ethanol / water mixtures		
0		-
0.1	88.9	0.1
0.3	89.2	0.0
0.5	89.6	0.0
0.75	89.7	0.1
1	89.7	0.0
Ethanol / ACN mixtures		
0	89.3	0.0
0.25	89.8	0.0
0.50	89.9	0.2
0.75	89.8	0.0
1	89.7	0.1
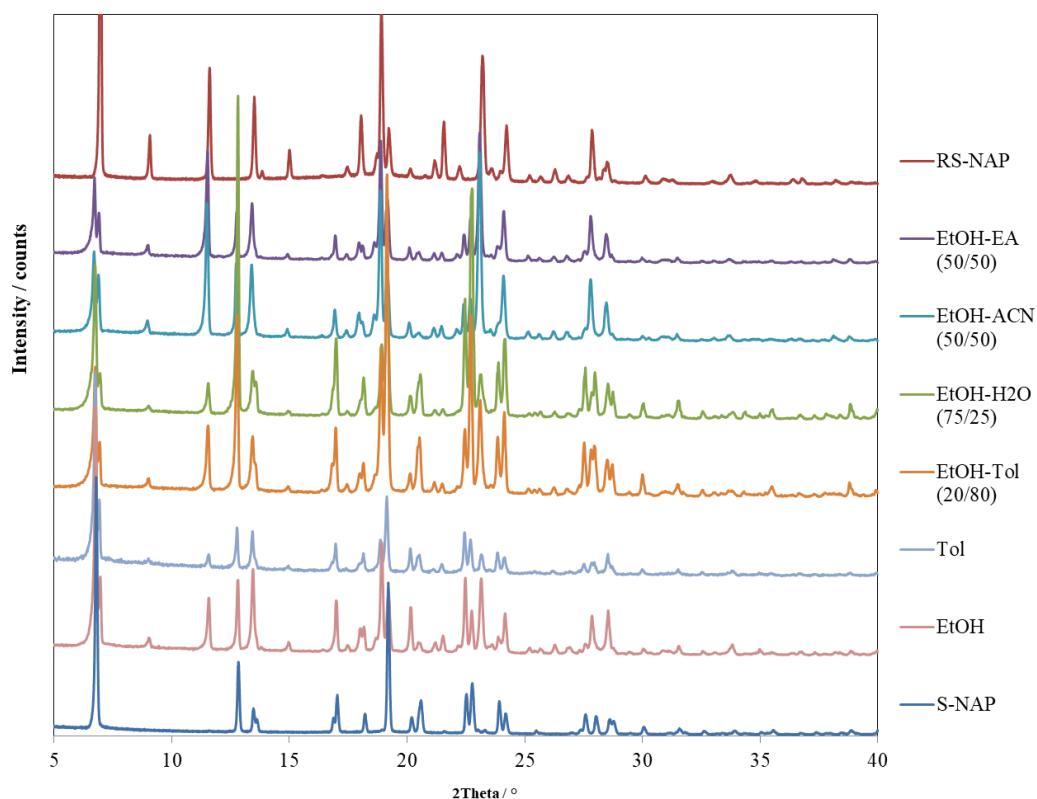
Figure 7.1: XRPD patterns of mixtures of (*S*)- and (*RS*)-naproxen. Samples correspond to the equilibrated solid phases from the isothermal solubility measurements for determining the eutectic composition in Table 7.15.

7.2 Primary computational data

7.2.1 Unit cell dimensions

Table 7.16: Specification of the unit cell of the two naphthalene (NAPHTA04 and NAPHTA23) and benzoic acid (BENZAC01 and BENZAC02) crystals.

	Length of lattice vectors			Lattice angles		Z
		Å	bohr		[°]	[-]
NAPHTA04[186]	a	8.098	15.303	alpha	90	
	b	5.953	11.249	beta	124.4	2
	c	8.652	16.350	gamma	90	
NAPHTA23[190]	a	8.085	15.278	alpha	90	
	b	5.938	11.221	beta	124.7	2
	c	8.633	16.314	gamma	90	
BENZAC01[191]	a	5.510	10.412	alpha	90	

		Å	bohr			Z
	b	5.157	9.745	beta	97.41	2
	c	21.973	41.523	gamma	90	
BENZAC02[187]	a	5.4996	10.393	alpha	90	
	b	5.1283	9.691	beta	97.37	2
	c	21.950	41.479	gamma	90	

Table 7.17: Specification of the unit cells of the enantiopure crystal and the corresponding racemic compound of lactide. naproxen and 3ClMA.

		Length of lattice vectors		Lattice angles		Z
		Å	bohr		[°]	[-]
BICVIS[218]	a	8.046	15.205	alpha	90	
(*RS*)-lactide	b	9.081	17.161	beta	103.06	4
	c	9.711	18.351	gamma	90	
NAHNOZ[217]	a	9.2439	17.468	alpha	90	
(*S*)-lactide	b	13.467	25.449	beta	90	12
	c	16.669	31.500	gamma	90	
PAPTUX[215]	a	25.830	48.812	alpha	90	
(*RS*)-naproxen	b	15.494	29.279	beta	90	8
	c	5.947	11.237	gamma	90	
COYRUD[219]	a	13.375	25.275	alpha	90	
(*S*)-naproxen	b	5.793	10.947	beta	93.91	2
	c	7.914	14.955	gamma	90	
FIZPEL03[212]	a	8.675	16.393	alpha	90	
(*RS*)-3ClMA	b	8.9404	16.895	beta	90.99	4
	c	10.7831	20.377	gamma	90	
TUYBIA[212]	a	8.316	15.715	alpha	90	
(*S*)-3ClMA	b	11.855	22.403	beta	93.82	4
	c	8.4526	15.973	gamma	90	

Table 7.18: Specification of the unit cell of the molecular crystals within the X23-benchmark set according to refs. [85, 97].

		Length of lattice vectors	Lattice angles		Z
		Å	[°]		[-]
anthracene	a	84.144	alpha	90	
	b	59.903	beta	125.293	2
	c	110.953	gamma	90	
urea	a	5.565	alpha	90	
	b	5.565	beta	90	2

	c	4.684	gamma	90	
oxalic acid (a)	a	6.548	alpha	90	
	b	7.844	beta	90	4
	c	6.086	gamma	90	
oxalic acid (b)	a	5.33	alpha	90	
	b	6.015	beta	115.83	2
	c	5.436	gamma	90	
CO2	a	5.624	alpha	90	
	b	5.624	beta	90	4
	c	5.624	gamma	90	
ethylcarbamate	a	5.051	alpha	101.37	
	b	7.011	beta	104.58	2
	c	7.543	gamma	76.65	
pyracine	a	9.325	alpha	90	
	b	5.85	beta	90	2
	c	3.733	gamma	90	
1.4-cyclohexanedione	a	6.65	alpha	90	
	b	6.21	beta	99.82	2
	c	6.87	gamma	90	
acetic acid	a	13.151	alpha	90	
	b	3.923	beta	90	4
	c	5.762	gamma	90	
adamantane	a	6.639	alpha	90	
	b	6.639	beta	90	2
	c	8.918	gamma	90	
ammonia	a	51.305	alpha	90	
	b	51.305	beta	90	4
	c	51.305	gamma	90	
benzene	a	7.39	alpha	90	
	b	9.42	beta	90	4
	c	6.81	gamma	90	
cyanamide	a	6.856	alpha	90	
	b	6.628	beta	90	8
	c	9.147	gamma	90	
cytosine	a	13.044	alpha	90	
	b	9.496	beta	90	4
	c	3.814	gamma	90	
formamide	a	3.604	alpha	90	
	b	9.041	beta	100.5	4
	c	6.994	gamma	90	
pyrazole	a	8.19	alpha	90	
	b	12.588	beta	90	8
	c	6.773	gamma	90	
hexamine	a	6.954	alpha	90	
	b	6.954	beta	90	2
	c	6.954	gamma	90	
succinic acid	a	5.466	alpha	90	
	b	8.740	beta	91.7	2

	c	5.108	gamma	90	
triazine	a	9.647	alpha	90	
	b	9.647	beta	90	6
	c	7.281	gamma	120	
trioxane	a	9.32	alpha	90	
	b	9.32	beta	90	6
	c	8.196	gamma	120	
imidazole	a	7.582	alpha	90	
	b	5.371	beta	119.0	4
	c	9.790	gamma	90	
uracil	a	11.938	alpha	90	
	b	12.376	beta	120.9	4
	c	3.655	gamma	90	
naphthalene	a	8.085	alpha	90	
	b	5.938	beta	124.7	2
	c	8.633	gamma	90	

7.2.2   Sublimation thermodynamics of lactide. naproxen and 3ClMA

Table 7.19: Thermodynamics of lactide. naproxen and 3ClMA evaluated at 298.15 K.

Lattice energy and thermal corrections (main manuscript)									
	Lactide			Naproxen			3ClMA		
	RS	S	RS-S	RS	S	RS-S	RS	S	RS-S
Lattice Energy: E_{latt} / kJ mol^{-1}									
Separated (Ψ_{mol})	-86.17	-82.64	-3.53	-133.48	-125.41	-8.07	-110.40	-105.11	-5.28
Electronic (Ψ_{crys})	-90.1	-87.25	-2.85	-135.71	-134.26	-1.45	-127.43	-126.20	-1.23
Zero Point Energy $\left(E_{ZPE}^{g} - E_{ZPE}^{s} \right)$ / kJ mol^{-1}									
Separated (Ψ_{mol})	-2.40	-2.59	0.19	-2.83	-2.76	-0.07	-2.90	-2.95	0.05
Electronic (Ψ_{crys})	-2.75	-2.99	0.24	-4.45	-5.39	0.94	-6.04	-7.38	1.34
Heat capacity correction to enthalpy: $\int\limits_{T'=0}^{T} \left(C_P^g(T') - C_P^s(T') \right) dT'$ / kJ mol^{-1}									
Separated (Ψ_{mol})	-2.72	-2.55	-0.17	-2.37	-2.55	0.18	-2.31	-2.25	-0.06
Electronic (Ψ_{crys})	-2.18	-2.02	-0.16	-0.92	-0.21	-0.71	0.60	0.65	-0.05
Experimental	-3.11	-2.73	-0.37	-1.84	-1.55	-0.29	-0.61	-1.52	0.91

Entropic correction: $T\Delta S_{subl} = T \int\limits_{T'=0}^{T} \left(C_P^g(T')/T' - C_P^s(T')/T' \right) dT'$ / kJ mol-1

Separated (Ψ_{mol})	51.55	52.72	-1.17	59.78	58.64	1.14	57.00	57.93	-0.94
Electronic (Ψ_{crys})	47.88	51.85	-3.97	62.30	65.44	-3.14	63.19	64.62	-1.43
Experimental	56.53	57.07	-0.54	69.76	70.50	-0.74	65.80	66.14	-0.33

summarized sublimation thermodynamic quantities

	Lactide			Naproxen			3ClMA		
	RS	S	RS-S		RS	S	RS-S		RS

Sublimation enthalpies: $\Delta H_{subl} = -E_{latt} - \left(E_{ZPE}^g - E_{ZPE}^s \right) + \int\limits_{T'=0}^{T} \left(C_P^g(T') - C_P^s(T') \right) dT'$ / kJ mol^{-1}

Separated (Ψ_{mol})	81.05	77.5	3.55	128.28	120.1	8.18	105.19	99.91	5.27
Electronic (Ψ_{crys})	85.17	82.24	2.93	130.34	128.66	1.68	121.99	119.47	2.52
Exp/Separated	80.66	77.32	3.35	128.81	121.1	7.71	106.89	100.64	6.24
Exp/ Electronic	84.24	81.53	2.72	129.42	127.32	2.1	120.78	117.3	3.48

Thermal correction: $\left(E_{ZPE}^g - E_{ZPE}^s \right) + \int\limits_{T'=0}^{T} \left(C_P^g(T') - C_P^s(T') \right) dT'$ / kJ mol-1

Separated (Ψ_{mol})	-5.12	-5.14	0.02	-5.2	-5.31	0.11	-5.21	-5.2	-0.01
Electronic (Ψ_{crys})	-4.93	-5.01	0.08	-5.37	-5.6	0.23	-5.44	-6.73	1.29
Exp/Separated	-5.51	-5.32	-0.18	-4.67	-4.31	-0.36	-3.51	-4.47	0.96
Exp/ Electronic	-5.86	-5.72	-0.13	-6.29	-6.94	0.65	-6.65	-8.9	2.25

Gibbs free energies: $\Delta G_{subl} = \Delta H_{subl} - T\Delta S_{subl}$ / kJ mol^{-1}

Separated (Ψ_{mol})	29.5	24.78	4.72	68.5	61.46	7.04	48.19	41.98	6.21
Electronic (Ψ_{crys})	37.29	30.39	6.9	68.04	63.22	4.82	58.8	54.85	3.95
Exp/Separated	24.13	20.25	3.89	59.05	50.6	8.45	41.09	34.5	6.57
Exp/ Electronic	27.71	24.46	3.26	59.66	56.82	2.84	54.98	51.16	3.81

Gibbs free energy corrections: $\Delta G_{corr} = \Delta H_{corr} - T\Delta S_{subl}$ / kJ mol^{-1}

Separated (Ψ_{mol})	-56.67	-57.86	1.19	-64.98	-63.95	-1.03	-62.21	-63.13	0.93
Electronic (Ψ_{crys})	-52.81	-56.86	4.05	-67.67	-71.04	3.37	-68.63	-71.35	2.72
Exp/Separated	-62.04	-62.39	0.36	-74.43	-74.81	0.38	-69.31	-70.61	1.29

| *Exp/ Electronic* | -62.39 | -62.79 | 0.41 | -76.05 | -77.44 | 1.39 | -72.45 | -75.04 | 2.58 |

7.2.3 Temperature variation of the sublimation Gibbs energy

Table 7.20: Gibbs free energy of sublimation at temperatures between 283 K and 318 K. Experimental values are compared to computations using the ψ_{crys} method.

T	(*RS*)-lactide	(*S*)-lactide	(*RS*)-naproxen	(*S*)-naproxen
	Experiment			
283.15	39.7	33.0	71.2	66.5
288.15	38.9	32.1	70.1	65.4
293.15	38.2	31.3	69.1	64.3
298.15	37.3	30.4	68.0	63.2
303.15	36.5	29.5	67.0	62.1
308.15	35.7	28.7	65.0	61.0
313.15	34.9	27.8	64.9	59.9
318.15	34.1	26.9	63.9	58.8
	Computation (ψ_{crys})			
283.15	38.05	35.70	66.80	64.07
288.15	37.02	34.72	65.43	62.80
293.15	35.99	33.74	64.06	61.54
298.15	34.95	32.76	62.69	60.27
303.15	33.92	31.79	61.32	59.01
308.15	32.89	30.81	59.96	57.74
313.15	31.87	29.84	58.59	56.48
318.15	30.84	28.87	57.23	55.22

7.2.4 Estimation of the eutectic composition

Table 7.21: Free energy differences $\Delta^{T2-T1}\Delta_{RS-S}\Delta G_{subl}$, obtained from integrating experimental heat capacity differences (see Figure 4.24) between the racemic and enantiopure crystals from T1= 298.15 K to T2= 318.15 K, and its effect on the eutectic composition in solution, $\Delta x_{eu,calc}(T_2-T_1)$, compared to experimentally determined eutectic shifts, $\Delta x_{eu,exp}$ (T_2-T_1). The eutectic shift is calculated from the maximum and minimum experimental $x_{eu,exp}$ in various solvent systems from literature[44, 216, 222, 223] for lactide and naproxen and measured in this work for 3ClMA.

	Unit	Lactide max / min	Naproxen max / min	3ClMA max / min
$x_{eu,exp}$ (T_1)*	mol%	93.2 / 95.0	89.9 / 90.3	89.1 / 91.3
$\Delta_{RS-S}\Delta G$ (T_1)**	kJ·mol⁻¹	1.49 / 1.93	0.99 / 1.05	0.99 / 1.30
$\Delta^{T2-T1}\Delta_{RS-S}\Delta G_{subl}$	kJ·mol⁻¹	0.02	-0.06	0.16

$\Delta^{T2\text{-}T1}x_{eu.exp}$*	mol%	0 / -3.0	-1.2	0 to 1.3
$\Delta^{T2\text{-}T1}x_{eu.calc}$***	mol%	-0.4 / -0.41	-0.9 / -0.9	0.6 / 0.5

*Experimental eutectic composition. $x_{eu.exp.}$ at 298.15 K and its dependence on temperature Δx_{eu} (T_2-T_1) of lactide. naproxen (determined in this work) and 3ClMA in a variety of solvent systems[44, 216, 222, 223] (see Table 4.12 for details).

**$\Delta_{RS\text{-}S}\Delta G_{subl}$(T1) calculated from the maximum and minimum $x_{eu.exp}$ (T_1).

7.2.5   Lattice energies for benzoic acid and naphthalene

Table 7.22: *k*-point sampling for a selected crystal structure of benzoic acid and naphthalene (BENZAC01[191] and NAPHTA04[186]).

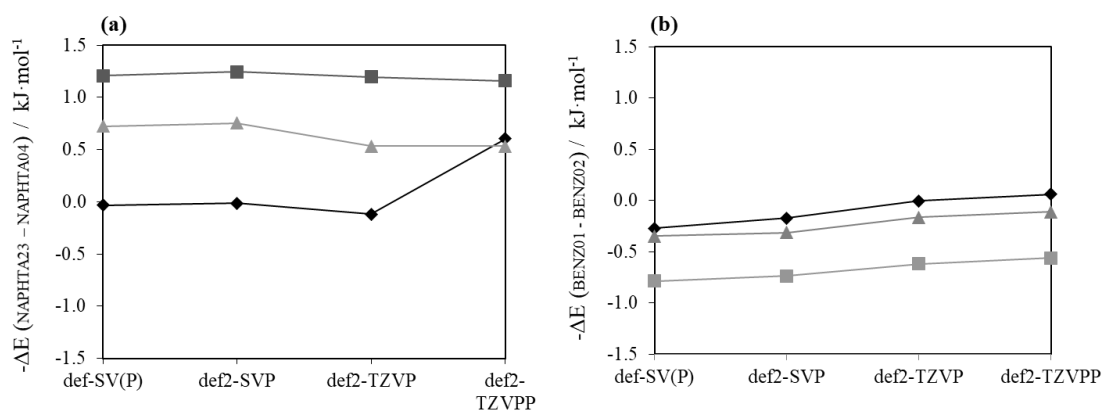| Crystal	Method	k-point mesh	Elatt / kJ mol-1
NAPHTA04	def2-TZVP PBE-D3	1x1x1	-95.1
		3x3x3	-84.1
		5x5x5	-84.1
		7x7x7	-84.1
		21x21x21	-84.1
BENZAC01	def2-TZVP PBE-D3	1x1x1	-153.0
		3x3x3	-108.9
		5x5x5	-108.9
		7x7x7	-108.9
		21x21x21	-108.9

Figure 7.2: Lattice energy *difference*s between different crystal structures of (a) naphthalene (NAPHTA04 and NAPHTA23) and (b) benzoic acid (BENZAC01 and BENZAC02), respectively. Details on the unit cell dimensions are given in Table 7.16.

7.2.6 Lattice energies for the X23 benchmark

Table 7.23: Calculated lattice energies. -E_{latt}. of the X23 benchmark set using the "riper" module within TURBOMOLE[251] version 7.1[132] and a k-point mesh of 3x3x3. The experimental lattice energy represents the average value of refs. [85, 97]. All energies are in kJ·mol^{-1}.

	PBE-D3 def2-SVP	PBE-D3 def2-TZVP	-$E_{latt.exp}$	err
Anthracene	128.84	112.19[a]	106.9	5.0
Naphthalene	97.17	83.94	79.1	2.2
Benzene	68.19	58.41	50.9	0.6
Adamantane	87.59	79.33	65.7	2.9
Hexamine	129.91	99.19	84.0	2.2
Pyrazine	91.21	70.00	62.8	1.6
Pyrazole	107.06	86.28	77.5	0.5
14-cyclohexanedione	135.82	100.11	87.4	0.9
CO_2	41.52	27.27	29.1	1.4
Triazine	87.48	65.08	61.6	0.8
Trioxane	107.48	70.89	63.7	1.9
Cytosine	213.45	170.14	168.9	0.7
Imidazole	120.41	97.48	88.0	2.4
Uracil	186.12	146.20	135.0	1.5
Acetic acid	113.61	82.60	72.5	0.5
Ammonia	70.03	50.74	36.5	1.3
Cyanamide	118.27	96.00	80.3	1.2
Ethylcarbamate	131.37	97.75	85.2	0.9
Formamide	118.22	89.47	79.0	0.2
Oxalic acid (α)	148.33	102.60	98.2	1.8
Oxalic acid (β)	151.30	105.19	97.8	2.6
$\Delta_{\alpha-\beta}$	-2.96	-2.59	-0.49	1.5
Succinic acid	201.58	145.24	126.7	3.6
Urea	153.33	117.58	101.2	1.3

[a] Calculated with the TZP basis set due to convergence issues with the larger def2-TZVP basis set.

Table 7.24: Determination of an average calculations value from literature. denoted as "average calculation". and its standard deviation. σ. for the lattice energies of the X23 benchmark from refs. [85, 97]. Hexamine and succinic acid have only been studied in ref.[97]. All energies are in kJ·mol^{-1}.

Substances	B86b XDM	PBE D	PBE TS	PBE XDM	vdW DF1	vdW DF2	EPBE +TS	EPBE0 +TS	EPBE +MBD	EPBE0 +MBD	DFTB3 D3	"average calculation"	σ
Anthracene	101.23	106.22	135.46	96.29	116.98	108.55	134.4	133.5	121.8	119.1	112.2	116.0	*13.3*
Naphthalene	75.74	80.4	100.53	72.24	88.06	81.44	99.9	98.4	87.4	85.4	71.6	85.0	*10.2*
Benzene	51.23	56.32	66.51	49.49	59.94	55.87	66.3	62	55	51	56.0	57.0	*5.7*
Adamantane	72.8	83.94	108.92	69.83	82.56	79.48	108	105	81	78.6	81.1	85.9	*13.5*
Hexamine	-	-	-	-	-	-	114.9	109.8	86.9	83.4	70.8	92.6	*16.7*
Pyrazine	59.66	64.47	74.9	58.48	69.09	67.75	76.2	72	67.3	63	55.9	65.9	*6.4*
Pyrazole	75.99	83.65	87.69	75.76	79.4	79.18	88.5	83.1	82.8	77.6	59.3	79.6	*7.6*
14-cyclohexanedione	85.81	97.32	107.22	84.64	104.39	103.33	105.9	101.2	92.2	88.2	100.7	97.0	*8.0*
CO$_2$	21.55	24.37	25.72	22.63	35.76	33.81	25.2	24.4	21.7	21.2	23.1	25.2	*4.7*
Triazine	54.73	61.2	67.98	53.93	68.38	66.5	68.9	65.6	58.7	55.7	51.7	60.9	*6.3*
Trioxane	57.95	67.23	75.78	57.34	77.64	79.31	75.9	72	62.4	59.3	65.2	67.8	*8.0*
Cytosine	151.25	163.83	172.82	150.25	153.92	157.53	172.6	167.9	170	164.5	147.1	161.2	*9.0*
Imidazole	87.54	94.46	100.76	87.32	89.99	89.58	101.9	96.3	97.1	91.4	104.7	94.5	*5.7*
Uracil	130.42	138.21	150.21	130.19	137.31	140.01	149	144.6	145.9	140.4	148.7	141.3	*6.7*
Acetic acid	71.76	77.6	83.66	72.52	77.38	78.1	82.6	79	78.3	74.6	77.8	77.7	*3.5*
Ammonia	38.56	46.23	44.03	39.15	37.47	40.31	45.4	42.4	42.9	40.2	32.2	41.0	*3.9*
Cyanamide	87.24	92.43	94.1	87.75	84.58	88.4	94.3	88.8	94.3	88.8	66.4	88.4	*7.7*
Ethylcarbamate	83.76	92.82	99.49	84.18	95.96	95.92	99.2	94	92.1	87.1	96.4	92.8	*5.3*
Formamide	77.95	84.12	86.79	78.65	79.22	82.56	86.3	84	82.8	80.7	76.9	82.0	*3.3*
Oxalic acid (α)	111.28	119.65	125.17	112.12	120.25	125.43	100.7	98.5	98.1	95.7	114.3	110.1	*11.1*
Oxalic acid (β)	113.81	122.95	128.2	114.99	120.77	124.7	104.3	100.1	98.6	94.8	112.3	111.4	*11.3*
Succinic acid	-	-	-	-	-	-	147.1	143.4	138.7	135.3	139.9	140.6	*4.1*
Urea	101.91	112.02	112.62	102.51	101.93	108.28	113.1	111.4	111.2	109.7	113.7	109.5	*4.9*